Low-Angle X-Band Radar Ground Clutter Spatial Amplitude Statistics

J.B. Billingsley

Lincoln Laboratory

MASSACHUSETTS INSTITUTE OF TECHNOLOGY

LEXINGTON, MASSACHUSETTS

20030123 062

This technical report has been reviewed and is approved for publication.

FOR THE COMMANDER

Gary Tutungian
Administrative Contracting Officer
Plans and Programs Directorate
Contracted Support Management

Massachusetts Institute of Technology
Lincoln Laboratory

Low-Angle X-Band Radar Ground Clutter
Spatial Amplitude Statistics

J.B. Billingsley
Group 48

Technical Report 958

20 December 2002

Lexington   Massachusetts

ABSTRACT

A large volume of X-band radar ground clutter measurement data was collected from many sites widely dispersed over the North American continent. This program of measurements involved a wide variety of terrain types, where at each site backscatter was recorded from all of the terrain within the field of view, through 360 degrees in azimuth and to ranges typically extending to 25 or 50 km. As a result, in most of these measurements the angle of illumination of the earth's surface was usually very low, typically within a degree or so of grazing incidence, with much intermittent shadowing of low regions occurring within the field of view. This report examines the nature of low-angle radar ground clutter as it has come to be understood through analysis of this extensive base of measurements. Depression angle, that is, the angle below the horizontal at which the backscattering terrain point is observed at the radar antenna, is shown to be the principal parametric influence on clutter amplitude statistics, even for the very low angles and small (typically fractional) variations in angle that occur in surface-sited radar. This principal role of depression angle is the result of its effect on shadowing in a sea of patchy visibility and discrete or localized scattering sources. Following this understanding, a general predictive model for X-band ground clutter spatial amplitude statistics is developed based on specific computation of depression angle but on only relatively general specification of terrain type. The report goes on to illustrate how increasing information about terrain type allows more precise prediction of clutter statistics.

PREFACE

The Lincoln Laboratory project of radar ground clutter measurements went forward in two phases: Phase Zero, a pilot phase that was noncoherent and at X-band only, followed by Phase One, the full-scale coherent program at five frequencies (VHF, UHF, L-, S-, and X-bands). This current technical report presents Phase Zero results and findings. It revises and updates for public release much earlier reported project material of limited distribution. This report is the basis of Chapter 2 of the recently published clutter reference book [1] that summarizes the Lincoln Laboratory Phase Zero and Phase One clutter project in its entirety.

A major objective of the Laboratory clutter project was to uncover fundamental parametric trends in the distributions of clutter amplitudes over kilometer-sized macroregions or patches of geometrically visible terrain. Low-angle ground clutter is a complex phenomenon, primarily because of the essentially infinite variety of terrain. As a result, there are many influences at work in any specific measurement. Thus, the objective became one of attempting to discern fundamental trends through a fog of obscuring detail. It was believed there was a science to be winnowed out through statistical combination of many similar measurements (i.e., measurements from like-classified patches of terrain at similar illumination angles).

This brings the discussion to technical statistical issues concerning combination of measured data. Simply put, an individual resolution cell (from which a single sample of clutter strength is obtained) may be regarded as the elemental spatial statistical quantity; or the complete terrain patch (from which an amplitude distribution is formed from the clutter returns from the many resolution cells comprising the patch) may be regarded as the elemental spatial statistical quantity. The former approach leads to ensemble amplitude distributions in which measured data from many similar patches are aggregated, sample by sample. The word "ensemble" distinguishes such results obtained by combining individual cell values— many values per patch—from many patches. The latter approach leads to the generation of many statistical attributes for the amplitude distribution of a given patch, the subsequent combination of a given attribute (e.g., mean strength) into a distribution of that attribute from many similar patches, and the final determination of a best expected value of the attribute from its distribution. The words "expected value" distinguish such results obtained by combining patch values—one value per patch—from many patches.

The advantage of the cell-by-cell histogram-additive ensemble approach is that it not only allows quick determination of trends in amplitude distributions, but also allows simple and straightforward actual specification of resultant general distributions. This is the major approach followed in this report. The report also contains a few expected value results of an adjunct nature. Trends seen in ensemble distributions also occur in expected values; fine adjustment of ensemble numbers to best expected values appropriate to a patch is a higher-order technical issue to which quantitative consideration is given in this report.

A considerable amount of ensemble modeling information is provided in this report within the context of approximating Weibull coefficients, reflecting the web of basic parametric trends in amplitude distributions that was found. There are simpler approaches to ground clutter modeling available, involving, for example, at one extreme in scale, propagation physics on a spherical earth, or, as another example, at an opposite extreme in scale, grazing angle on terrain facets specified by digitized terrain elevation data. Realistic and useful models of the low-angle clutter phenomenon need to include the sorts of complex parametric variation such as presented in this report. The Laboratory-derived empirical modeling information presented here and elsewhere [1] for describing low-angle clutter amplitude distributions captures the fundamental characteristics of these variations and allows the understanding and quantitative prediction of the limiting effects of clutter on the system performance of surface-sited radar.

ACKNOWLEDGMENTS

TABLE OF CONTENTS

TABLE OF CONTENTS (Continued)

LIST OF ILLUSTRATIONS

LIST OF ILLUSTRATIONS (Continued)

LIST OF ILLUSTRATIONS (Continued)

LIST OF ILLUSTRATIONS (Continued)

LIST OF ILLUSTRATIONS (Continued)

LIST OF TABLES

LIST OF TABLES (Continued)

1. INTRODUCTION

The subject of this report is the measurement and empirical modeling of low-angle radar land clutter. Interest is in land clutter as it occurs in surface-sited surveillance or tracking radars typically operating in clutter over ranges reaching to 25 or 50 kilometers, and against stressing targets that can present low radar cross sections and fly at low altitudes. In such circumstances, modern radar is often clutter limited even after state-of-the-art Doppler-discriminatory clutter cancellation is performed. Historically, the clutter-limited performance of surface-sited radar has been extremely variable and highly unpredictable. This report provides general information describing X-band spatial amplitude distributions of clutter returns received from regions of visible ground, based on Lincoln Laboratory Phase Zero measurements at many sites. Other available publications based on Phase One measurements extend the information to lower radar frequencies [1–5]. In addition to modeling land clutter spatial amplitude statistics, Phase One investigations have also addressed the intrinsic Doppler spectral spreading in land clutter and its effects on radar systems [6–8].

In presenting ground clutter data and results, this report attempts both to do justice to describing an extremely complex phenomenon and also to efficiently provide useful and easily accessible modeling information. The result is a report that provides increasing insight into the clutter phenomenon by cyclically building up an understanding of the many complex and interacting influences affecting clutter amplitude statistics. These developing insights are accompanied with easy-to-use modeling information that generalizes such influences at various levels of fidelity. Some guidance in using this report is provided in the following two subsections. First, Section 1.1 briefly describes the scope within which the subject of low-angle clutter amplitude statistics is taken up. Next, Section 1.2 provides an outline of the important modeling results of this report.

1.1 SCOPE

This section briefly discusses questions concerning context and usage for the modeling information provided in this report. First and foremost, low-angle ground clutter is a patchy phenomenon. Areas of the ground that are geometrically visible to the radar usually cause relatively strong clutter returns, and areas of the ground that are geometrically shadowed or masked to the radar usually cause relatively weak clutter returns often below the sensitivity of the radar. Use of digitized terrain elevation data (DTED) allows, at gross level, the deterministic prediction of and distinction between macroregions of general visibility and macroregions of shadow, where the prefix "macro" implies kilometer-sized regions encompassing hundreds or thousands of spatial resolution cells. Such specific prediction of the gross pattern of spatial occurrence of ground clutter at a given site is essentially what is meant here by site-specific study.

Predicting, in this manner, the existence of a macropatch of clutter at some site, a description is subsequently needed of the statistics of the clutter returns that are expected from within the patch. Thus, this report provides modeling information for describing clutter amplitude distributions occurring over

1

macro-sized spatial regions of visible terrain. These distributions are characterized by broad spread. The degree of spread in the distribution is fundamentally controlled by depression angle; that is, the angle below the horizontal at which the patch is observed at the radar. Depression angle is a quantity that can be computed relatively rigorously and unambiguously from DTED, depending as it does simply on range and relative elevation difference between the radar antenna and the patch. The fundamental dependence of spread in the clutter amplitude distribution on depression angle is significant even for the very low depression angles (i.e., typically <1°) and small patch-to-patch differences in depression angle (i.e., typically fractions of 1°) that occur in surface-sited radar. The modeling information for ground clutter amplitudes presented in this report is tied tightly to this basic dependence on depression angle, such that amplitude distributions are specified in terms of small and precise gradations of depression angle for various terrain types.

Let us reflect on this approach to modeling low-angle ground clutter. As a physical phenomenon, the two most salient attributes of low-angle ground clutter are patchiness in spatial occurrence and extremely wide cell-to-cell statistical fluctuation in strength within a patch. Concerning spatial patchiness, it is emphasized that clutter does not exist in all spatial cells, and it is the patch-specific on-again, off-again macrobehavior of clutter that at first level determines the performance of a given radar against a given low-altitude aircraft at a given site. Concerning wide cell-to-cell variations of clutter strength within macropatches, it is emphasized that what appears at first consideration to be a phenomenon of extreme variability and little predictability turns out in the end, after analyzing much data, to be generally dependent on very fine differences in depression angle. Use of site-specific DTED allows the capture of both these basic attributes of low-angle ground clutter, its spatial patchiness (approximately computed simply as geometric visibility), and (through depression angle) its expected range of amplitudes within a patch. Furthermore, a specific clutter patch is a proper subject for quantitative study (i.e., it can be both predicted and measured, and the prediction can be quantitatively compared with the measurement). Therefore, this approach to modeling low-angle clutter is regarded as a major advance over more general non-spatially-patchy approaches that do not distinguish between macroregions of clutter occurrence and macroregions of shadow. This approach allows an analyst to predict, within macroregions, where a surface-sited radar can be expected to encounter clutter interference and where the radar will be free of such interference, and, given that the radar is experiencing clutter, what, on the average, the expected statistics of signal-to-clutter ratio will be across the macroregion of clutter.

Clutter returns within patches are often highly spatially correlated. This report discusses the fact that the dominant clutter sources within macroregions of general geometric visibility are usually spatially localized or discrete, such that groups of cells providing strong returns are often separated by cells providing weak or noise-level returns. The occurrence of noise-level returns sprinkled within macroregions of general geometric visibility is referred to ás microshadowing, where the prefix "*micro*" implies resolution-cell-sized areas. The high degree of spatial microcorrelation of strong discrete sources within macropatches results from the fact that such sources exist as vertical features of discontinuity in landscape that often occur in definite patterns, for example, along the leading edge of a tree line or the clustering of vertical objects along roads and field boundaries. If an analyst is interested in the actual microstatistics, for example, of break-lock in a surface radar tracking a target across a given clutter patch,

the information in this report does not go that far. The kind of detail and fidelity in terrain description that is required to predict microstatistics of spatial correlation of clutter amplitudes within macropatches is regarded as a second sequential major hurdle to cross in clutter modeling. Limitations encountered in attempting this second advance are severe. The prediction of microspatial correlation is a very challenging task that takes exploratory operations to the limits of currently available terrain-descriptive information. In contrast, the first major advance in low-angle clutter fidelity, which is the field-of-investigation of this report, comes relatively easily once the DTED is in play.

As an alternative to predicting microspatial correlation in full fidelity, actual measured $\sigma°F^4$ data can be used in analysis. That is, it is very difficult to statistically predict the detailed spatial nature of clutter at microlevel, but it is relatively easy to use actual measured $\sigma°F^4$ clutter data with all of its sample-to-sample and cell-to-cell statistical variations intact, at a level that no degree of modeling could ever achieve. This approach to clutter modeling involves canonical sites. By canonical site is meant a clutter measurement site that has been selected to be generally representative in a straightforward way of a general class of sites (e.g., a high-relief forested site, a low-relief agricultural site, a mountain site, a desert site, etc.). A number of insightful system analyses have resulted from this canonical site approach using measured clutter maps. But can any particular measured clutter map really be considered a model? Useful results are obtained in this approach, but the mainstream modeling effort at Lincoln Laboratory involves *a priori* site- and patch-specific prediction of clutter, not *a posterior* use of measured clutter maps.

In alluding to general non-site-specific approaches to clutter modeling, it is not meant to imply that such approaches are without value. Although the main thrust of this report is site-specific clutter modeling involving specification of visible clutter patches and the depression angles at which they are illuminated, some non-angle-specific modeling information is also provided based only on relatively general parameters such as terrain relief, and terrain type (e.g., wetland, urban, etc.).

It is true, however, that clutter models without spatial patchiness are, indeed, relatively abstract and conceptually vague in quantitative study involving experimental data. This is the logical penalty that non-specific approaches must pay as the price for generality. This penalty comes about because, instead of aggregating system performance measures after realistic clutter computations at many individual sites, as per the site-specific approach of this report, non-site-specific approaches attempt to aggregate and generalize clutter influences before a one-time assessment of system performance. That is, non-site-specific approaches attempt to *a priori* average the clutter first, whereas the site-specific approach takes the more computationally intensive way of *a posterior* averaging actual site-specific performance measures over many sites to reach generality. The validity of the former approach can only be tested by comparison with the latter.

Although the discussion throughout Section 1.1 has focused on the use of the clutter amplitude modeling information of this report within the context of computer operations involving DTED, the modeling information provided is generally applicable to describing clutter amplitude statistics in surface-sited radar whatever the context of interest.

Ground clutter results in this report are based on Phase Zero measurements from 106 sites widely dispersed over the North American continent and hence covering a variety of terrain types and terrain relief. Modeling information is provided for general rural terrain and various specific terrain types. Ranges at which clutter was measured are relatively long (>>1 km) and patch sizes are relatively large (median size = 5 km^2). Thus the scale at which the clutter results in this report apply is appropriate to surface-sited surveillance and tracking radar typically operating with cell sizes of thousands of square meters in composite, discrete-dominated, heterogeneous terrain over long ranges and low angles. In contrast, much of the existing ground clutter literature is not relevant to this situation, but rather is concerned with measurements at shorter ranges (<1 km), higher angles, and homogeneous conditions over much smaller areas of ground.

1.2 OUTLINE

The major results of this report are briefly listed below. The list is not comprehensive, and additional information descriptive of low-angle ground clutter occurs throughout the report. Most of the general clutter modeling information, in contrast to specific examples of measured clutter, is presented in Section 4.

1.2.1 Basic Model

The basic model describing X-band clutter amplitude distributions over macropatches of visible terrain as a function of depression angle for three comprehensive terrain types is provided in Table 5. The Weibull coefficients tabulated in Table 5 are graphically plotted in Figures 25 and 26. Table 5 allows an analyst to quantitatively predict low-angle X-band ground clutter strengths. The remainder of the report expands upon the nature of low-angle clutter as basically encoded within the numbers of Table 5.

Traditionally, a clutter model has often been thought of as being a simple characteristic of clutter strength versus illumination angle. Such a simple model is provided in this report in Figure 48, which represents a generalization of all of the Phase Zero measurements. However, ground clutter is inherently a statistical phenomenon in which large statistical variation occurs. Thus, this simple angle-characteristic model shows two characteristics of clutter strength, mean and median, versus angle. Together, these two characteristics keep the important fact that clutter is statistical before us, and give us not only a measure of central tendency (i.e., mean, median) of clutter strength with angle, but also the extent of variation (i.e., mean-to-median ratio) of clutter strength to be expected at any given angle.

1.2.2 Worst-Case Situations

The basic clutter model provides general information. Beyond this, we may wish to set upper bounds on how strong ground clutter can become in exceptional circumstances. Figure 33 compares the amplitude distribution from the single strongest Phase Zero clutter patch, which was urban clutter, and the amplitude

4

distributions from the four strongest Phase Zero mountain clutter patches with the general rural regime of the basic model.

1.2.3 Fine-Scaled Variations with Terrain

The basic clutter model separates terrain into just three categories, which, simply interpreted, imply that only "mountains" (i.e., rural/high-relief terrain) and "cities" (i.e., urban terrain) warrant separation from all other terrain types (i.e., rural/low-relief terrain). This three-class categorization is based on gross differences in Phase Zero clutter amplitude statistics. However, with decreasing significance finer trends occur in the data with more specific description of terrain type. Within the overall realm of general rural low-relief terrain, fine-scaled differences in clutter amplitude statistics between wetland, forest, and agricultural land are shown in Figures 40, 41, and 42, respectively. Fine-scaled differences in clutter amplitude statistics between urban terrain of residential (i.e., low-rise) character versus urban terrain of commercial (i.e., high-rise) character are shown in Figure 38. The effect of trees as discrete scattering sources is discussed throughout this report. General modeling information illustrating that, on low-relief open terrain, trees are, indeed, the predominant X-band discrete scattering source, and illustrating how clutter amplitude distributions vary with the relative incidence of occurrence of trees (i.e., percent tree cover) is shown in Figure 43.

1.2.4 Higher-Order Attributes

The important central parts of the clutter amplitude distributions of the basic model and its variations as discussed above can usually be reasonably well approximated by a single-piece Weibull approximation. However, in these amplitude distributions, there is usually a high tail of significantly increased spread caused by relatively infrequent, very strong discrete scatterers of widely varying strength. Modeling information describing this high-side tail of discretes is provided in Section 4.1.2.

Furthermore, in rural/high-relief terrain, the clutter amplitude distributions are bi-modal, in that not only do they show a relatively tight primary region in the distribution over the important, relatively strong clutter levels controlling the mean, but, in addition, they show a secondary, relatively spread out region in the distribution across a wide extent of weaker clutter levels. Modeling information describing this secondary mode of relatively weak clutter in rural/high-relief terrain is provided in Figure 35.

Both of these higher order attributes of clutter amplitude distributions, namely, the high-side tail of increased spread and the secondary mode in high-relief terrain of increased spread over relatively weak levels of clutter, are modeled in this report within the context of Weibull approximation as being piece-part Weibull in several parts.

5

1.2.5 Negative Depression Angle

This report discusses the difficulties attendant in attempting to use grazing angle above the local terrain surface, rather than depression angle below the local horizontal at the antenna, as the appropriate measure of illumination angle for characterizing low-angle ground clutter. The difficulties are in finding any significant correlation of clutter strength with grazing angle, as opposed to the highly significant correlation of clutter strength that occurs with depression angle (see Ref. [1], Appendix 4.D). Enthusiasts of grazing angle tend to be undeterred by such difficulties. However, empirical clutter model development must rest on actual parametric dependencies that can be shown to exist in the measured clutter data, not preconceptions that cannot be validated. In formulating clutter modeling information in terms of depression angle rather than grazing angle, negative depression angles need contending with. This is a practical complication arising with the use of depression angle that does not intrude with the use of grazing angle. Negative depression angle occurs when relatively steep terrain is observed by the radar at elevations above the antenna. General information describing clutter amplitude distributions occurring at negative depression angle is provided in Figure 44.

1.2.6 Non-Angle-Specific Modeling Information

A major purpose of this report is to provide modeling information for X-band clutter amplitude statistics as a function of depression angle suitable for use in site-specific studies in which the clutter is spatially patchy and the depression angle to each patch is specifiable. However, some non-angle-specific modeling information is also provided in this report. For example, Figure 29 shows the distribution that results from combining all of the Phase Zero measured clutter samples, irrespective of terrain type and depression angle, into one all-encompassing distribution. This distribution represents complete generality. For the analyst who does not wish to be concerned with "ground-truth" at all, a considerable amount of information concerning frequency of occurrence of various levels of low-angle clutter strength is contained in this overall distribution, as measured from 2,177 macropatches of geometrically visible terrain at 96 different sites. The high-side tail of increased spread is very evident in this distribution. This overall distribution is subsequently separated into component terrain types of rural/low-relief, rural/high-relief, and urban, in Figure 30. These non-angle-specific ensemble distributions of Figures 29 and 30 are obtained by combining clutter measurements at the individual sample level.

In contrast to ensemble information, some other non-angle-specific expected value clutter modeling information is also provided by combining results obtained at the patch level. Thus, Figure 23 shows distributions of mean patch clutter strength by landform. To the extent that the overall terrain at a given radar site may be classified as being of one category of terrain relief, the information in Figure 23 may be used non-specifically with respect to illumination angle to assign an expected or most-likely mean clutter strength to the whole site. In addition to most-likely values, the information in Figure 23 may also be used to allow an analyst to specify typical "worst-case" (strong clutter) and "best-case" (weak clutter) values for mean clutter strength at that site. Similar non-specific information with respect to illumination angle for mountain, wetland, urban, and general rural terrain types is provided in Figure 39.

6

1.2.7 Appendices

This report illustrates the nature of the low-angle clutter phenomenon through examples of measurement data (Section 3) and provides general modeling information for low-angle clutter amplitude statistics (Section 4). Relevant and necessary information for understanding the results presented is confined to appendices. That is, the body of the report is largely limited to discussing the low-angle clutter phenomenon, whereas the appendices define the terminology and framework within which that discussion is conducted. The appendices include stand-alone discussions of the following subjects: Phase Zero measurement equipment and calibration; clutter measurement database and terrain classification; formulation of clutter statistics; and numerical computation of depression angle.

2. CLUTTER MEASUREMENTS

During the approximately five-year period of time from late 1979 to late 1984, large amounts of radar ground clutter measurement data were collected from many sites. These sites are listed and described in Appendix A. Photographs of the terrain at two of the measurement sites are shown in Figure 1. Figure 1(a) shows low-relief undulating prairie farmland at the Beiseker site located 75 km northeast of Calgary. Figure 1(b) shows high-relief mountainous terrain at the Plateau Mountain site located 120 km southwest of Calgary deep in the Canadian Rockies. Both Figures 1(a) and 1(b) are airborne views looking west. The level terrain in the foreground of Figure 1(b) is the top of Plateau Mt. The lower part of Figure 1(b) shows how the terrain drops off precipitously on the east side of Plateau Mt. Significantly different backscatter characteristics would be expected, and indeed were measured, from the terrain in Figure 1(a) compared with that of Figure 1(b). This report shows that a useful first step in clutter prediction is to simply distinguish terrain type by whether it is simply low-relief as pictured in Figure 1(a) or high-relief as in Figure 1(b).

Clutter measurements were made with two measurement radars. The Phase Zero program utilized an X-band only, noncoherent measurement radar which was employed in a pilot or precursor role preceding the full-scale multifrequency measurement program, which was denoted Phase One. Brief summaries of the measurement parameters available from both the Phase Zero and Phase One instruments are provided in Table 1.

This report is based on clutter measurements obtained with the X-band Phase Zero radar. The Phase Zero equipment was self-contained and mobile on a one-ton truck platform. Its antenna was mounted on a 50-ft erectable tower and had a relatively wide elevation beam (23°) which was fixed horizontally at zero degrees depression angle. That is, no control was provided on the position of the elevation beam. For most sites and landscapes, the terrain at all ranges from one to many kilometers was usually illuminated within the 3-dB points of the fixed elevation beamwidth. At each site, terrain backscatter was measured by steering the azimuth beam through 360 degrees, and selecting a maximum range setting such that all discernible clutter within the field-of-view, typically from one to about 25 or 50 km in range, was recorded.

The Phase Zero radar utilized uncoded, pulsed waveforms. It was internally calibrated for every clutter measurement and utilized balloon-borne spheres to provide several external calibrations. More detailed information concerning the schedule, equipment, and calibration of the Phase Zero measurement instrument is provided in Appendix B. Some ancillary information describing the Phase One radar and its measurement program is also provided in Appendix B.

The most important result of the analyses of Phase Zero clutter measurements is the strong general effect of illumination angle on spatial amplitude distributions of clutter. This report provides general information concerning this effect. Corresponding results observed across the complete Phase One frequency regime are reported elsewhere [1–4].

9

(a)

(b)

Figure 1. Two clutter measurement sites in Alberta, Canada. (a) Low-relief farmland at Beiseker. (b) High-relief mountainous terrain at Plateau Mt.

TABLE 1

Clutter Measurement Parameters

	Phase Zero	Phase One				
Frequency						
Band	X-Band	VHF	UHF	L-Band	S-Band	X-Band
MHz	9375	165	435	1230	3240	9200
Polarization	HH	VV or HH				
Resolution						
Range	9, 75, 150 m	15, 36, 150 m				
Azimuth	0.9°	13°	5°	3°	1°	1°
Peak Power	50 kW	10 kW (50 kW at X-Band)				
10 km Sensitivity	$\sigma°F^4 = -45$ dB	$\sigma°F^4 = -60$ dB				
Antenna Control	Continuous Azimuth Scan	Step or Scan through Azimuth Sector (<185°)				
Tower Height	50'	60' or 100'				
Data						
Volume	2 Tapes/Site (800 bpi)	$\approx$ 25 Tapes/Site (6250 bpi)				
Acquisition Time	1/2 Day/Site	2 Weeks/Site				

11

3. THE NATURE OF LOW ANGLE CLUTTER

3.1 CLUTTER PHYSICS

The major elements involved in low-angle clutter are shown in Figure 2. Attention is focused on directly illuminated clutter from large kilometer-sized patches of visible terrain. Within such patches, at the low angles of ground-based radars, the clutter sources are all of the vertical features of discontinuity (i.e., things that rise up) on the landscape, either objects associated with the land cover, such as trees or buildings, or just the high points of the terrain itself. Such sources are usually spatially localized or discrete in nature, with regions of microshadow occurring between them where the receiver is at its noise floor. As the angle of illumination increases, the amount of microshadowing decreases. As a result, strengths[1] in clutter amplitude distributions increase, and spreads[1] in clutter amplitude distributions decrease with increasing angle. These effects with angle constitute the single strongest parametric dependence that exists in the Phase Zero X-band low-angle clutter data. This dependence tends to wash out other dependencies such as terrain type. As a result, this dependence with angle is emphasized in the modeling information presented in this report.
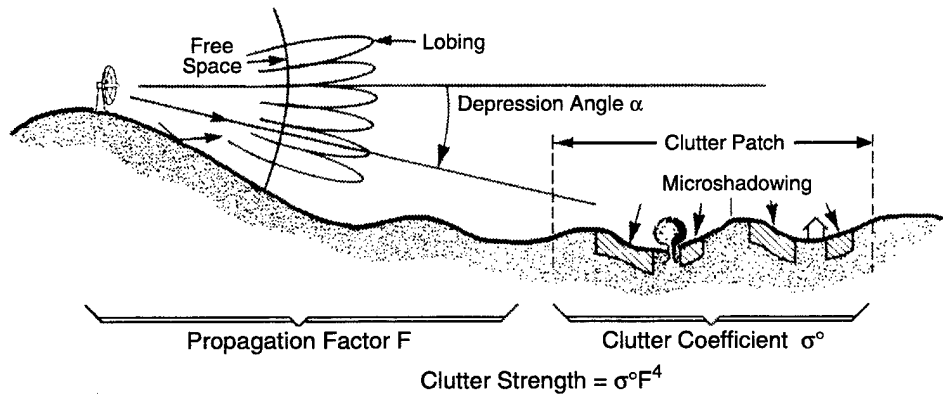
Figure 2. Clutter physics (X-band).

The terrain between the radar and the clutter patch influences the illumination of the clutter patch. For example, multipath reflections can interfere with the direct illumination and cause lobing on the free-space antenna pattern. All such propagation effects are included within the pattern propagation factor F,

---

[1] Any statistical distribution has two basic parameters, which specify its central tendency (e.g., mean) and its dispersion (e.g., variance), respectively. In this report, in describing clutter amplitude distributions, we often use "strength" to mean "central strength" and "spread" to mean dispersion.

13

which is defined to be the ratio of the incident field that actually exists at the clutter cell being measured to the incident field that would exist there if the clutter cell existed by itself in free space and on the axis of the antenna beam. What is measured as clutter strength is the product of the clutter coefficient itself, $\sigma°$, defined to be radar cross section per unit ground area in the resolution cell, and the fourth power of the propagation factor. At X-band, terrain reflection coefficients are often lower, and hence multipath effects diminished, from those that can exist at lower radar frequencies. When they exist at X-band, propagation lobes are usually relatively narrow. Typical clutter sources such as trees and buildings over most visible terrain often subtend a number of such lobes when they exist.[2] As a result, the effects of propagation are diminished, and they tend to average out at X-band, compared with lower frequencies, where they can dominate. Throughout this report, clutter strength is given by $\sigma°F^4$, in units of m^2/m^2. Further discussion defining $\sigma°F^4$ is given in Appendix B.

3.2 MEASURED GROUND CLUTTER MAPS

Figure 3 shows Phase Zero X-band measurements of ground clutter in PPI format at six Canadian sites.[3] The maximum range in all cases is 47 km. These data are shown at close to full Phase Zero sensitivity, so that cells with discernible clutter return from the ground are shown as white, and cells where the receiver is at its noise floor are shown as black. Range resolution is 150 m, azimuth resolution (i.e., 3-dB beamwidth) is 0.9°. Capsule descriptions of the six sites shown in Figure 3 are given in Table A-1.

At Altona, the terrain is very level cropland in Manitoba. Clutter is measured there only from discrete vertical objects (such as barns, silos, telephone poles, isolated trees, etc.) out to a spherical earth horizon nominally given by 16 km for the 50 ft Phase Zero antenna mast, except for the terrain feature (Pembina Hills) that rises to the far southwest. Only on such level sites is a spherical earth model of terrain very applicable in understanding low-angle microwave clutter, and at such level sites, dominant clutter sources are often very high[4] cultural or natural discretes distributed over the spherical surface.

At most other sites, even relatively low-relief sites, specific terrain features dominate in low-angle clutter measurements over what would be measured on a spherical earth. Thus, in moving across Saskatchewan (Dana) and into Alberta (Penhold and Beiseker), the terrain becomes more undulating and rolling, and the influence of specific large-scale terrain features dominates over spherical earth effects in the clutter maps for these sites in Figure 3. For example, even in the relatively low-relief terrain at Beiseker, it is the terrain surfaces inclined toward the radar (e.g., to the north and south) from which clutter is received; these surfaces are shadowed (i.e., black) on their far sides. A spherical earth clutter model is not very applicable to clutter visibility at Beiseker.

---

[2] However, there can be a region at long enough range where strengths from even relatively high clutter sources are generally reduced because of illumination from the underside of just the first propagation lobe.

[3] Ground clutter maps of Figure 3, and, looking ahead, also of Figure 4, were obtained by photographing the face of the 16" diameter Phase Zero PPI scope indicator (i.e., analog data, see Table B-1). All other PPI clutter maps in this report were computer generated (i.e., digital data).

[4] Of extended vertical dimension with respect to radar transmission wavelength λ. For Phase Zero, $\lambda = 3.2$ cm.

14
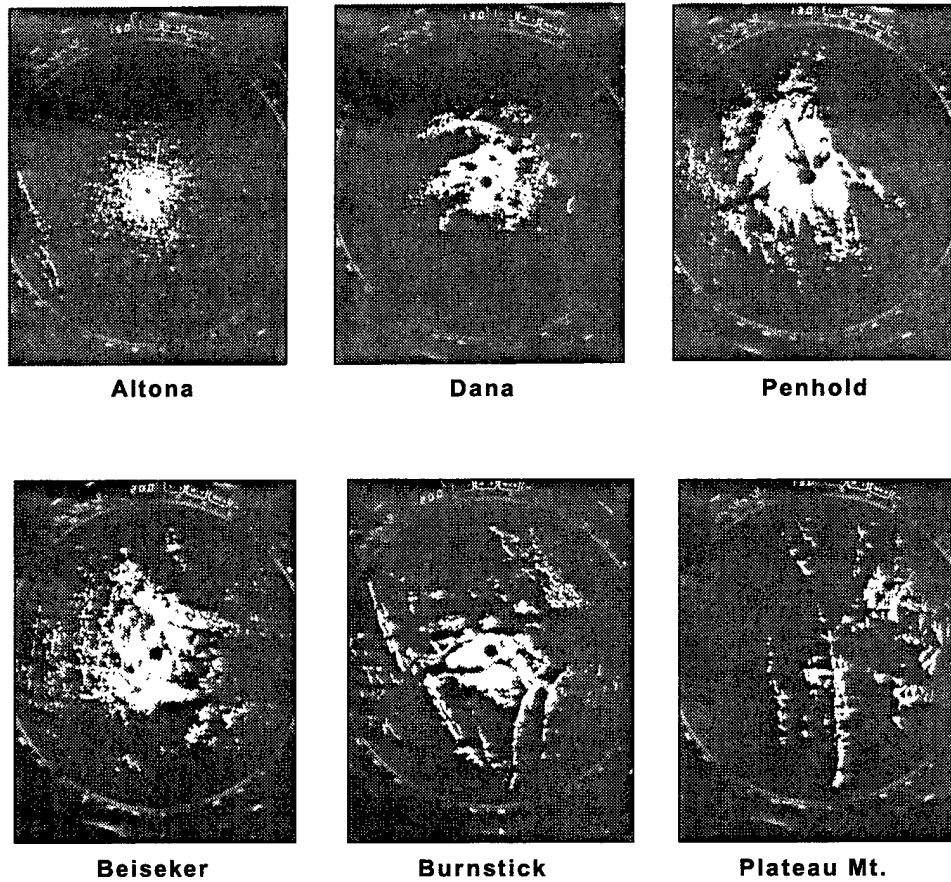
Figure 3. Ground clutter maps at six sites. Phase Zero X-band data, 150-m range resolution, horizontal polarization. In each map, maximum range = 47 km, north is zenith, clutter is white, clutter threshold is 3 dB from full sensitivity. PPI scope photos.

Moving on in Figure 3, Burnstick is a forested site in the foothills of the Rocky Mountains, and Plateau Mountain is a site high in the Rockies themselves. To the west at Plateau Mountain, clutter is measured from barren rock faces of some high peaks in the Rockies, and to the east clutter is measured looking down at the prairie. In all cases in Figure 3, the patterns of spatial occurrence of clutter are very patchy and granular. The nature of the clutter is on-again, off-again as it arises from discrete sources distributed on surfaces within line-of-sight visibility. The details of each pattern are specific to the terrain features at that site. However, two general observations may be made about all such patterns. First, the amount of clutter that occurs gradually diminishes with increasing range from the site. Second, where

15

clutter occurs (i.e., white patches), its strength is relatively independent of range. Elsewhere, the development of simple non-site-specific modeling information is based on these two observations [3]. In this report, attention is focused on the following question—Where clutter occurs (i.e., spatial regions largely within geometric line-of-sight visibility in which a relatively high[5] percentage of resolution cells contain discernible clutter), what are the amplitude distributions of clutter strengths that occur there?

The prediction or modeling of where clutter occurs is not in itself a subject for study in this report. However, digitized terrain elevation data (DTED) available from various sources are directly applicable and useful for geometrically predicting and modeling the gross nature of the spatial patterns of occurrence of clutter such as are shown in Figure 3. Prediction of such patterns with DTED is essentially what is meant herein by site-specific investigation.

In Figure 3, the range resolution is 150 m. Figure 4 shows similar measurements at six sites at higher resolution, namely, 9 m. At this increased resolution (and shorter maximum range, namely, 5.88 km), the discrete or localized nature of the actual clutter sources within regions of general terrain visibility is very evident. The pattern of vertical cultural objects on the level cropland at Altona is obvious. On the undulating terrain at Beiseker, terrain features are evident in the clutter map, but a rectangular pattern of cultural discretes is seen overlaying them. At ranges within 6 km, Dundurn is a military wasteland area of shrub and brush-covered sand dunes, typically 20 to 30 feet high, but without a road grid or cultural overlay. There, however, the clutter pattern is observed to be of very granular texture, where the top of each sand dune gives rise to a discrete or localized clutter return. In observing this very granular clutter map for Dundurn, an investigator is not very inclined to want to bring detailed terrain slope and grazing angle to bear to explain or predict the strength from each individual dune.

In totality, the high resolution plots of Figure 4 amply illustrate what was stated earlier, that within directly illuminated clutter regions, the clutter sources are all of the discrete objects that rise up above the mean level of the surface. These discrete sources are densely distributed within illuminated regions. Clutter returns from the areally-extensive terrain surfaces themselves, as opposed to the discrete objects rising above these surfaces, are much weaker and, in fact, are often below the sensitivity of the receiver. In viewing the clutter maps of Figure 4, one is inclined to envisage a sea of discretes as an appropriate physical model for low angle ground clutter, in contrast to the historical tendency in clutter modeling to associate the phenomenon primarily with area-extensive $\sigma°$. Of course, the discrete clutter sources that high resolution reveals in Figure 4 are also the dominant clutter sources at work at lower resolution. The discrete nature of the dominant clutter sources is just less noticeable at lower resolutions.

---

[5] The meaning of "relatively high" depends on the terrain type and corresponding nature of microshadow in the clutter map. Typically, "relatively high" might mean about 50%, but for high sites and/or steep terrain in which relatively full illumination exists, it can approach 100%, and in level terrain in which only isolated discretes are illuminated it can be as low as about 10%. Appendix C provides examples of illuminated patches for a variety of terrain types with differing degrees of percentage of cells in discernible clutter.
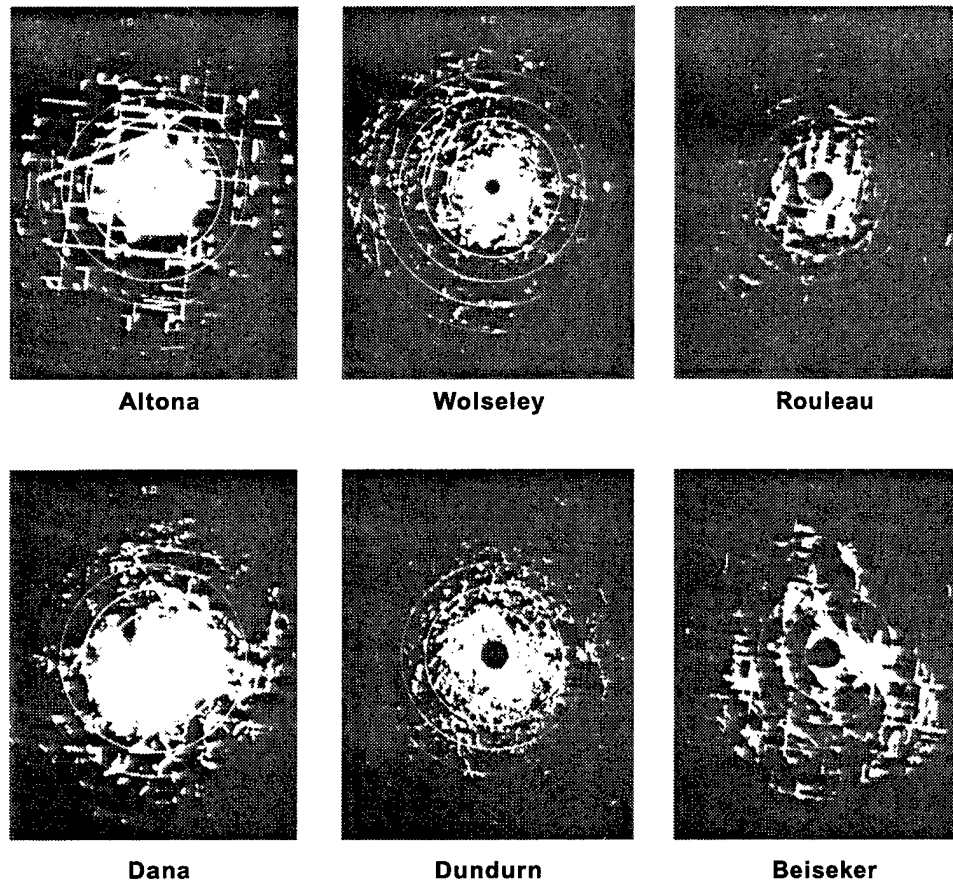
Figure 4. High resolution ground clutter maps at six sites. Phase Zero X-band data, 9-m range resolution, horizontal polarization. In each map, maximum range is 5.9 km, north is zenith, clutter is white, clutter threshold is reduced by 6 dB to 18 dB from full sensitivity in order to show strong clutter cells. PPI scope photos.

3.3 CLUTTER PATCHES AT GULL LAKE WEST

The approach taken to modeling clutter amplitude statistics in this report is as follows. Within the PPI clutter map measured at each site, macropatches of clutter were selected within spatial regions generally within line-of-sight illumination in which a relatively high percentage of resolution cells contained discernible clutter.

Overlaying and registering clutter maps onto stereo aerial photographs and topographic maps also ensured in patch specification that the terrain within each patch was, in large measure, uniform.

17

Interpretation of the air photos and topographic maps provided descriptive information of the terrain within the patch. For each clutter patch, the distribution of clutter strengths occurring within the patch was obtained and stored in a computer file together with the applicable terrain descriptors of the patch. Altogether 2,177 clutter patches were selected from the Phase Zero 11.8 km maximum range experiment at 96 different sites. The modeling task then became one of attempting to establish general correlative properties between the 2,177 stored distributions of measured clutter strength and the corresponding terrain descriptions.

Next are shown some typical clutter patches and measured clutter patch spatial amplitude distribution from the Gull Lake West site in Manitoba. Figure 5 shows the Phase Zero equipment and a view to the northwest at Gull Lake West. Figure 6 shows a terrain characterization map of 30 km radius for the Gull Lake area. Site centers for both the Gull Lake West site and the Gull Lake East site are shown as crosses in this map. Figure 7 shows a measured clutter map of 12-km radius for Gull Lake West, with six selected clutter patches. An overview of the terrain classification system that was utilized is also shown in Figure 7. Figure 8 shows the measured amplitude distributions for the six Gull Lake patches shown in Figure 7. Appendix C provides similar information as that shown in Figures 7 and 8 for six other sites, together with detailed definitions of all of the statistical quantities indicated in Figures 7 and 8. The terrain classifications shown in Figures 6, 7, and 8 are defined in Appendix A.
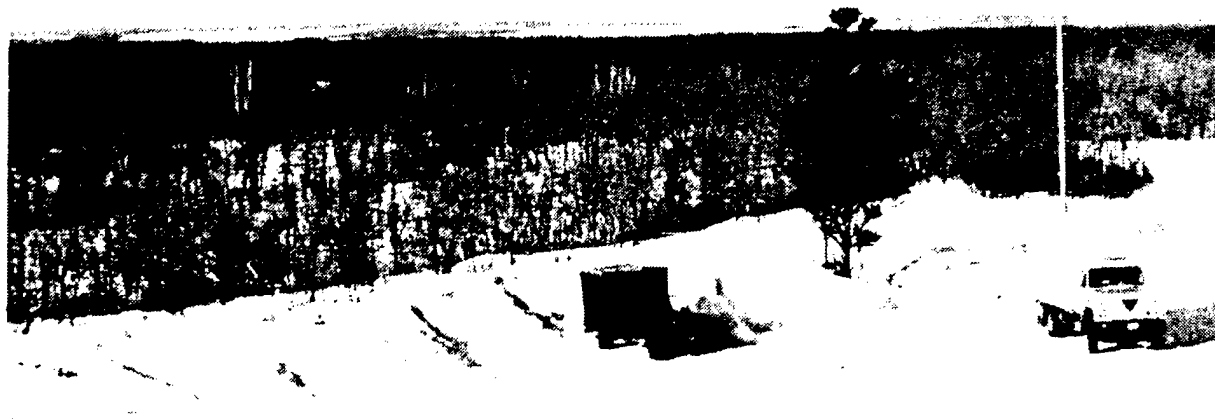
Figure 5. Phase Zero equipment at Gull Lake West, Manitoba. Date: 23 February. Camera viewing direction is northwest. Lake ice is visible at horizon.

18
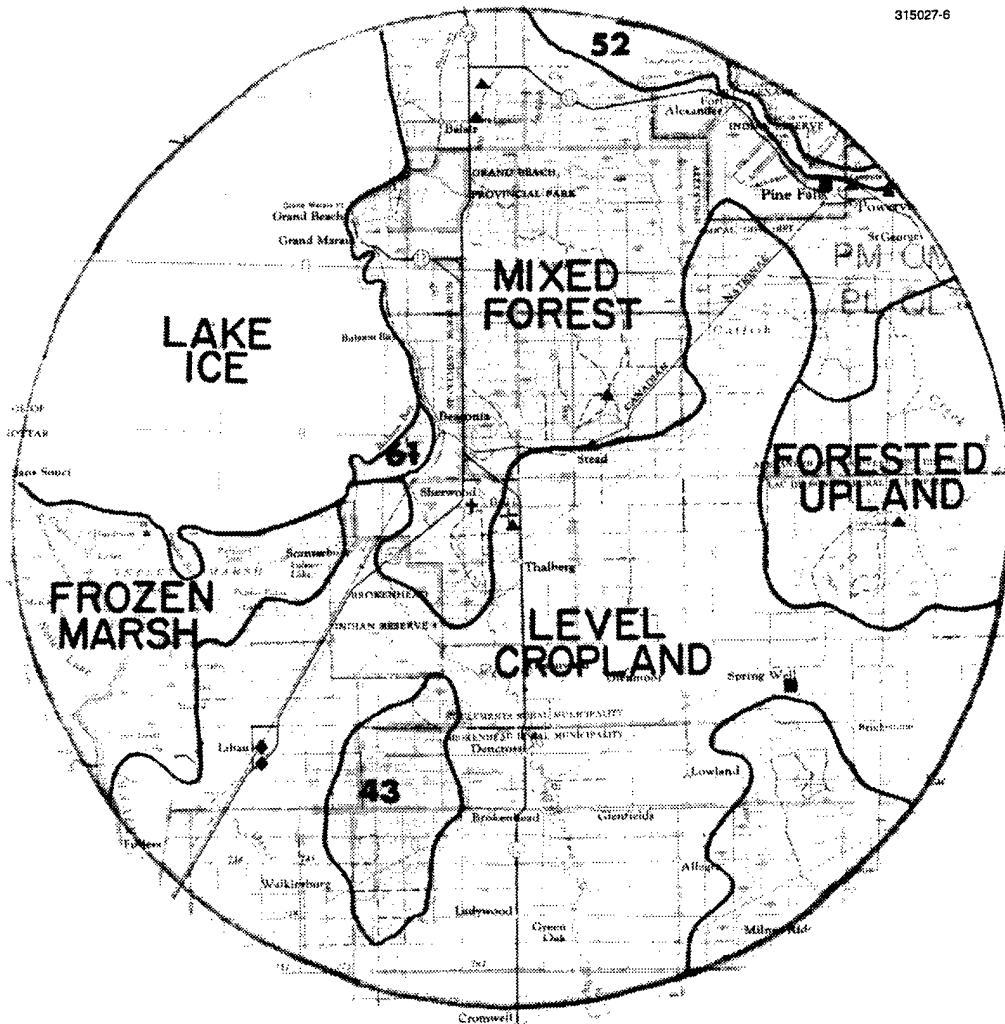
Figure 6. Terrain characterization map at Gull Lake, Manitoba. Map radius = 30 km.

The six measured clutter patch amplitude distributions at Gull Lake West shown in Figure 8 are now discussed in more detail. The terrain from which clutter was measured at Gull Lake lies in the valley of the Red River and is, in general, extremely level. The radar site itself at Gull Lake West lay on the western brow of a north-south situated ridge about 100 feet above the level terrain to the west which the site overlooks. The effect of the ridge was to extend the Phase Zero antenna mast height from its nominal 50-foot value to a higher elevation of about 150 feet.

315027-7B

Land Cover Map

1. Urban
2. Agricultural
3. Rangeland
4. Forest
5. Water
6. Wetland
7. Barren

Landform Map

1. Level
2. Inclined
3. Undulating
4. Rolling
5. Hummocky
6. Ridged
7. Moderately steep
8. Steep
9. Broken

Phase Zero PPI Display
Received Power: 3-dB attenuation
Radius: 12 km
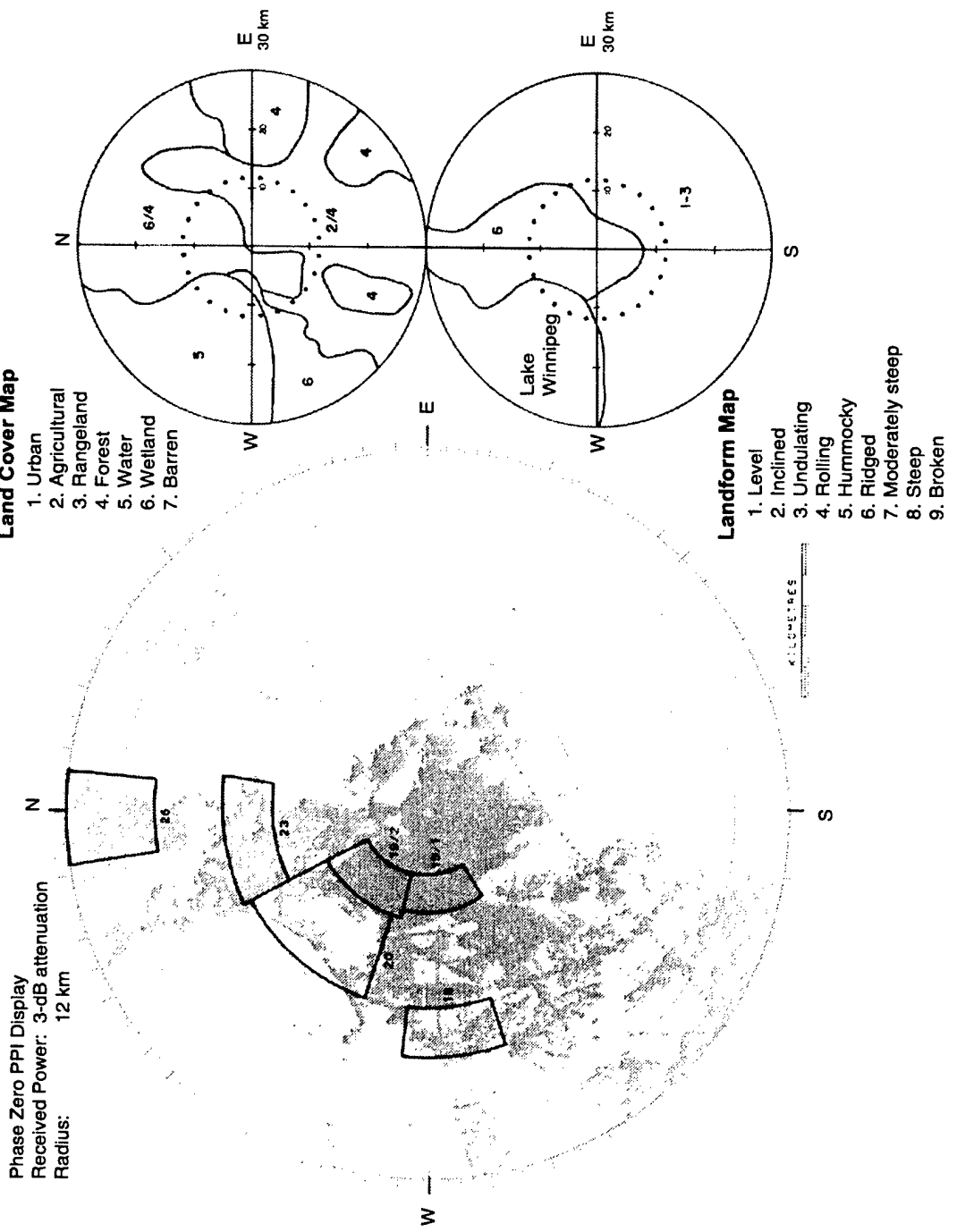
Figure 7. Radar ground clutter visibility and terrain classification maps with selected clutter patches for Gull Lake West site.

20

Y = m•$\sigma°F^4$ (dB) + b

Lognormal Scale

Linear Scale

Probability That $\sigma°F^4$ (dB) ≤ Abscissa

Weibull Scale

Rayleigh Slope

Linear Scale

$\sigma°F^4$ (dB)

$\sigma°F^4$ (dB)

23	7176 Samples	26	5070 Samples
19/2	8651 Samples	20	14440 Samples
18	4708 Samples	19/1	6666 Samples

Percent

Patch Number	Terrain Classification		Depression Angle (deg)	Tree Cover (%)	Supplementary Terrain Descriptors
	Land Cover	Landform			
18	43-21	1	0.45	>50	Continuous forested wetland
19/1	61	1	1.07	>50	Continuous forested wetland
19/2	61	1	1.11	>50	
20	52-61	1	0.68	4-10	Backwater area, shrubs on sandy bars
23	43-21	3-1	0.38	>50	Dense tree cover, lakeshore road, minor cottages
26	43-21	3	0.11	>50	Road, cleared fields

Patch Number	$\sigma°F^4$ (dB)*				Percentiles			Regression Coefficients†			
	Mean	Standard Deviation	Skewness	Kurtosis	50	90	99	Y = m•$\sigma°F^4$ (dB)+b		Coefficient of Determination	Sum of Squared Deviations
								Slope (m)	Intercept (b)		
18	-35.7 (-43.6)	-30.6 (8.3)	10.9 (0.52)	23.6 (2.09)	-45	-32	-25	0.040 (0.084)	1.65 (3.73)	0.997 (0.979)	0.013 (0.377)
19/1	-30.9 (-34.2)	-29.9 (6.7)	5.4 (-1.30)	14.2 (5.52)	-33	-27	-23	0.087 (0.149)	2.75 (5.13)	0.996 (0.975)	0.012 (0.507)
19/2	-31.4 (-35.6)	-29.9 (8.3)	7.1 (-1.50)	17.8 (5.49)	-34	-27	-23	0.077 (0.125)	2.50 (4.50)	0.997 (0.967)	0.026 (0.777)
20	-34.9 (-50.1)	-27.0 (9.7)	13.4 (1.36)	28.8 (3.89)	-54 ††	-34	-22	0.022 (0.051)	1.16 (2.77)	0.988 (0.958)	0.022 (0.405)
23	-34.1 (-43.4)	-26.3 (9.2)	16.6 (0.29)	34.6 (2.03)	-43	-31	-23	0.038 (0.077)	1.54 (3.43)	0.995 (0.998)	0.027 (0.287)
26	-34.9 (-41.2)	-30.7 (6.9)	9.3 (0.73)	20.7 (2.41)	-44	-31	-24	0.043 (0.093)	1.71 (3.94)	0.997 (0.979)	0.007 (0.244)

* Of Linear Values (of dB Values)   † Weibull (Lognormal)   †† Upper Bound

Figure 8. Phase Zero clutter statistics and terrain classification for selected patches at Gull Lake West site, February visit.

The very level terrain at Gull Lake West in many respects represents a canonical situation in which complicating effects of various and specific realizations of terrain relief, so often present at most sites, are absent. Thus, the specific effects observed in the clutter distributions at Gull Lake West are largely caused by variation and complexity in land cover. Consideration of these effects can help provide a deeper understanding of the general low-angle clutter amplitude distributions presented subsequently in this report.

In discussing these effects, first consider patches 19/1 and 19/2. These patches are level forested wetland. Such patches are referred to as "pure" patches (27% of the Phase Zero patches lying between 2 and 12 km range from the radar are "pure"), since they do not require second and third levels of landform and land cover classification as do most mixed patches. In other words, patches 19/1 and 19/2 are homogeneous and continuous level forested wetland relatively uncomplicated by the presence of roads running through them, clearings, cultural discretes, and shadowing caused by variations in terrain elevation. The radar overlooked these patches from its nearby ridge location at a depression angle of about one degree.

The situation is illustrated in the photographs shown in Figure 9. The bottom photograph in Figure 9 was taken looking southeast from a position just northwest of the area of level forested wetland, which is seen extending from right to left across the center of the photograph. The 100-ft ridge upon which the radar was located is seen in the far background to the left center in the photograph. A closer view of the species of trees making up this forested wetland is shown in the top photograph of Figure 9. Many of the taller trees were larch or tamarack. The other major component of the forested wetland was spruce, shown as shorter, darker trees in the photograph. Also present was an understory of willow. Clearly, at an X-band wavelength of 3.2 cm, this forest represents a complex scattering medium which is far from homogeneous, 75-m cell to 75-m cell. Yet over large enough sampling areas, results next to be discussed indicate that it does generate near-Rayleigh backscatter statistics.

The forested wetland was illuminated at a depression angle of about one degree. At first consideration, one degree may not seem to provide much in the way of illumination angle, but it is enough to make all the difference in causing these patches to be fully illuminated obliquely from above rather than from the side at grazing incidence, as they would have been if the radar position had not had its 100 ft terrain elevation advantage. As a result, observe first that the clutter histograms for patches 19/1 and 19/2 in Figure 8 are uncontaminated by cells at radar noise level (i.e., $\sigma°F^4$ bins containing one or more cells at radar noise level are double underlined in Figure 8; such bins appear to the left side of the histograms for the other four patches in Figure 8 and indicate the sensitivity limit of the radar in these histograms). That is, every cell in patches 19/1 and 19/2 provides a discernible clutter return, which is not the case for most low-angle clutter patches.

22

315027-9

(a)
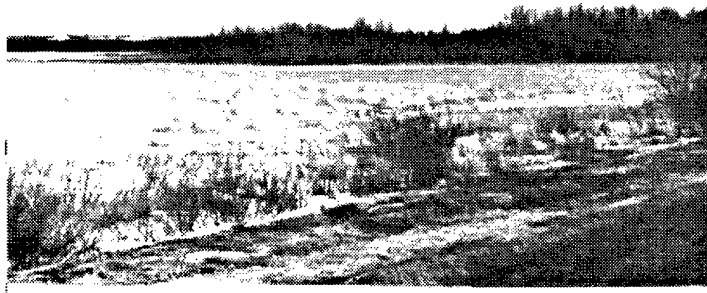
(b)

Figure 9. Photos of level forested wetland at Gull Lake West. (a) Tree species. (b) Northern extent.

Second, observe that patches 19/1 and 19/2 provide relatively well behaved histograms of traditional bell shape. In fact, and as would be expected for full illumination of relatively homogeneous tree foliage, the amplitude distributions for patches 19/1 and 19/2 are very Rayleigh. This is ascertained from their close match to the Rayleigh slope in the Weibull cumulative plot (bottom right graph) in Figure 8, as well as from the relative values[6] of $\sigma°F^4$ moments and percentiles listed (bottom table) in Figure 8.

23

Few clutter patches provide such approximately Rayleigh statistics as do patches 19/1 and 19/2. Over large extents of composite landscape, most sites provide little homogeneous terrain. For example, consider patch 18 at Gull Lake West. Although the terrain is level, the land cover is mixed between forest and cropland. At a depression angle of about 0.5°, the clutter from the agricultural field surfaces is either masked by the surrounding trees or below sensitivity at this low angle. As a result, a considerable number of samples in the distribution are at radar noise level (spike at left side of histogram). To the right of the noise samples, the histogram is less bell-shaped and more spread out than those of patches 19/1 and 19/2 (dotted vertical lines indicating 50, 90, and 99 percentiles are more separated). The cumulative distribution for patch 18 plotted on the Weibull scale (bottom right graph) in Figure 8 is of considerably lesser slope than Rayleigh. Patches 23 and 26 are relatively similar to patch 18, both in terrain description, depression angle, and clutter amplitude distribution. These three patch distributions as a set (bottom graph, Figure 8) characterize much of the clutter producing terrain at Gull Lake West. Note that these cumulative distributions are shown only to the right of their regions of noise contamination. Thus, as shown in Figure 8, these distributions are not affected by the sensitivity limit of the radar and are what would be measured there by an infinitely sensitive radar. Even on canonically level terrain with an artificially high antenna mast, complexity and heterogeneity in land cover have introduced a considerable extra degree of spread in these three distributions, compared with those for the homogeneous land cover patches 19/1 and 19/2.

Most (73%) of the patches making up the Phase Zero clutter database between 2- and 12-km range from the radar are of mixed terrain type such as patches 18, 23, and 26 at Gull Lake West. Why are mixed patches specified? Why not constrain patch specifications to smaller homogeneous regions? The argument often advanced for such an approach is that, if one could separately understand backscatter from homogeneous trees versus that from homogeneous discrete-free cropland, one could work up from a pixel level view of the world in which every pixel contains homogeneous clutter of a known type to synthesize and predict more complex distributions. Shadowed pixels and pixels containing discretes could be layered in subsequently in this building block approach. Aside from insurmountable practical difficulties with respect to detail and accuracy of terrain descriptive information required, there is a basic theoretical difficulty with this approach. In Figure 7, the spatial pattern of clutter in patch 18 and east of it, in the region of patch 17, indicates that the radar is observing the edges of many land cover features (tree lines) in this area. The strengths of the returns from these features are shown in Figure 10, which shows clutter strength versus range looking west at Gull Lake West. Between 2 and 3 km in range, a relatively constant level of return is received from the level forested wetland. In this region, only small-scale fluctuation is observed from range gate to range gate, indicative of local heterogeneity in the forest over such small areas. As previously indicated, averaging over larger areas in this forested area yields approximately Rayleigh statistics. Beyond 3.3 km in Figure 10, the nature of the clutter phenomenon changes dramatically. This region is characterized by extreme and rapid fluctuations in clutter strength as the various features of vertical discontinuity, many of which are tree lines, are encountered. For example, between range gates 118 and 128, a distance of 370 meters, mean clutter strength rises from the noise floor

---

[6] "Rayleigh" implies a Rayleigh (voltage) distribution for $\sqrt{\sigma°}$. In the corresponding exponential (power) distribution for $\sigma°$, mean = standard deviation, skewness = 3 dB, kurtosis = 9.5 dB, mean/median = 1.6 dB, 90 percentile/median = 5.2 dB, 99 percentile/median = 8.2 dB; also see Table C-3 and Section 4.2.1.

in gate 118 to –17 dB in gate 123, an increase of 42 dB, and then drops back down to the noise floor in gate 128. Knowing how homogeneous tree pixels backscatter and how homogeneous cropland pixels backscatter does not provide information on how important boundary pixels backscatter in transition zones where forest meets cropland. Clearly, even for this canonically level terrain, a pixel-specific predictive approach would require an enormous amount of land cover information to be able to accurately predict the deterministic clutter strength profile shown across patches 17 and 18 in Figure 10. Such an approach would be expected to be easier to apply if more terrain was, like patch 19/1 in Figure 10, relatively homogeneous.
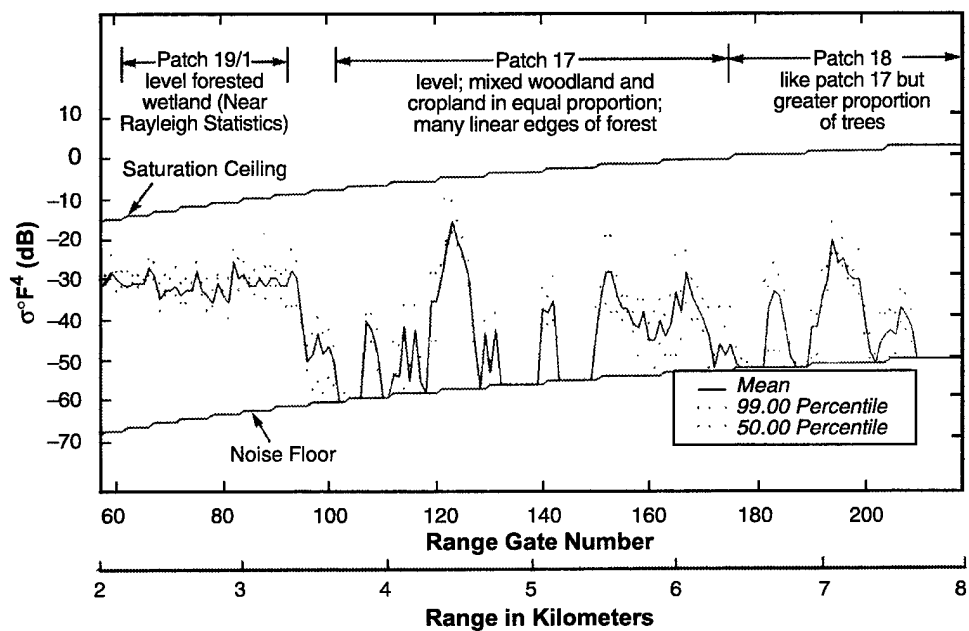
• Data shown for individual range gate positions, averaged over a 2° sector, 271.5° to 273.5° (10 azimuth samples/gate).

• Measurement date, 23 February; leafless deciduous trees, snow-covered field surfaces; see Figure 5.

Figure 10. Clutter strength versus range looking west at Gull Lake West. Phase Zero X-band data, 75-m range resolution. Compare with Figure 7.

25

Referring back to Figure 4, to a large extent most of the dominant backscatter sources in low-angle ground clutter are the myriad features of vertical discontinuity that exist on landscape. The correct empirical approach in dealing with all of these edges of features is to collect meaningful numbers of them together within macropatches (like patches 17 and 18), and let the terrain classification system carry the burden of statistically describing the attributes of the discontinuous clutter sources within the patch at a gross overall level of description. Only through study of mixed patches, like patches 17 and 18 at Gull Lake West, is one led to a general understanding of the clutter spatial amplitude distributions occurring in surface-sited radar receivers as their beams sweep over large extents of composite landscape.

As an example of backscatter from the edge of a particular clutter feature, Figure 11 shows backscatter from a tree line measured at relatively long range, 14.7 km, at Gull Lake East. This feature was sought out and photographed in the field as shown in Figure 12(a). The radar beam was directed across intervening level cropland as shown in Figure 12(b), where the radar is positioned at the horizon in the center of the photograph at 15-km range (the tree line is directly behind the photographer). The data in Figure 11 show that for this situation, in the transition region between farmland and forest, a very strong specular-like return is received from the leading edge of the tree zone, which rapidly decays in the next few range gates as the wavefront penetrates further into the forest. The trees of this forest are predominantly aspen. Leaves and branches extend to the ground, and trunks are relatively thin. As the trees are first encountered at the edge of the farmland, they are short but rapidly grow in height to 30 or 40 feet in the interior of the forest. Thus, the backscatter from the edge of the forest is not from an abrupt line of major tree trunks, but from the beginning of a tree foliage zone. It is overly simplistic to associate the strong leading-edge backscatter in Figure 13 with a substantial line of visible tree trunks at the forest edge. What is visually apparent looking at the forest edges is largely leaves and branches rather than a line of trunks.

Figure 13 shows Phase Zero backscatter from another tree line measured at closer range at the Lincoln Laboratory outdoor antenna range in Bedford, Massachusetts. Again a strong return from the leading edge of the trees is observed in the transition zone between the level grass of the antenna range and the forest, which rapidly decays with increasing penetration of the wavefront into the forest. Information is provided in Section 4.2.5 which generalizes the effect of varying incidences of occurrence of trees on clutter amplitude distributions.

It is the edges of many tree lines and other vertical features that constitute the dominant clutter sources on much composite landscape. The collection of all of the singular returns from such discrete features within local regions strongly influences measured clutter spatial amplitude distributions. Low-angle clutter comes predominantly from the edges of vertical discontinuities in landscape. Following this line of thought, a theoretical problem directly related to low-angle clutter is electromagnetic backscattering from a step discontinuity at grazing incidence, as illustrated in Figure 14(a). This problem of a step geometry has been taken up in other contexts in the electromagnetic literature [9]. Backscattering from a vegetative step at radar frequencies can be formulated in terms of volume scattering from a random medium [10]. Any rigorous formulation at grazing incidence needs to incorporate shadowing effects. The solution to such a problem should show the dominant characteristics of backscatter from tree lines indicated in Figures 11 and 13, namely a strong impulse-like leading edge return followed by a subsequent

26

decay. A low-angle clutter model for general composite landscape could be statistically synthesized from appropriate spatial distributions of step discontinuities. Such a model would be more realistic than one attempting to deal with low-angle clutter in terms of homogeneous pixels. For example, a Poisson distribution of discrete landscape elements leads to a K-distribution of clutter amplitudes. The same effects of decreasing spread with increasing illumination angle modeled empirically in this report with Weibull distributions are seen in theoretical investigations of low-angle clutter involving K-distributions [11].
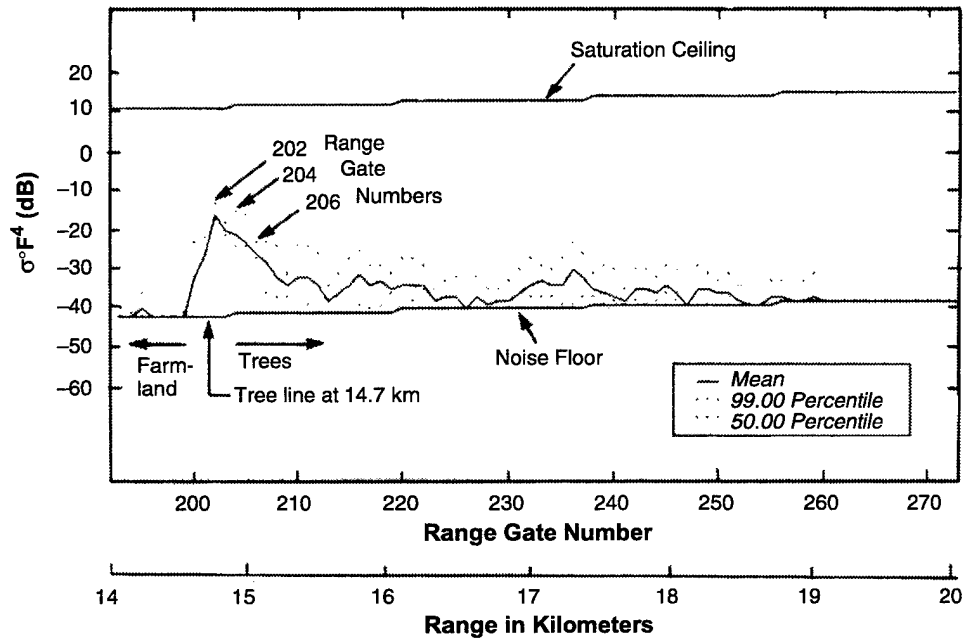
- Data shown for individual range gate positions, averaged over a 5° sector, 85° to 90° (22 azimuth samples/gate).

- Measurement date, 24 February; leafless deciduous trees, snow-covered field surfaces; see Fig. 12.

Range Gate Number	$\sigma°F^4$ (dB)		
	Mean	Median	Maximum
202	−16	−16	−13
204	−21	−24	−15
206	−26	−27	−23

Figure 11. Backscatter from a tree line at 15-km range at Gull Lake East, Manitoba. Phase Zero X-band data, 75-m range resolution, horizontal polarization, 23.5-km maximum range experiment, 74.2-m sampling interval.

27

(a)
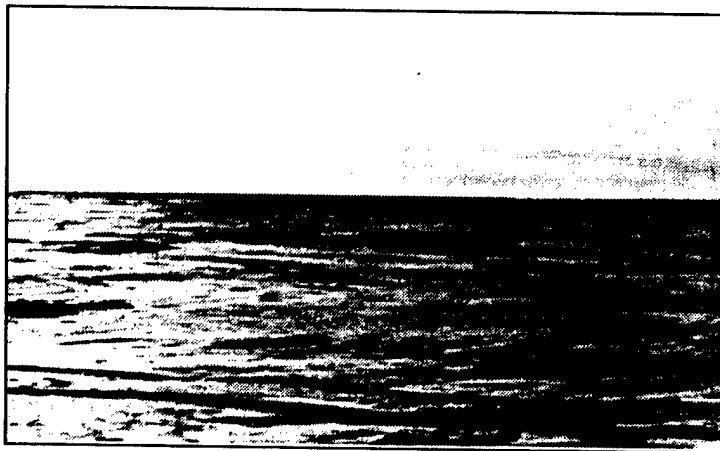
(b)

Figure 12. *Terrain photos at edge of forest at Gull Lake East. (a) Edge of forest. (b) Level cropland between radar and forest.*
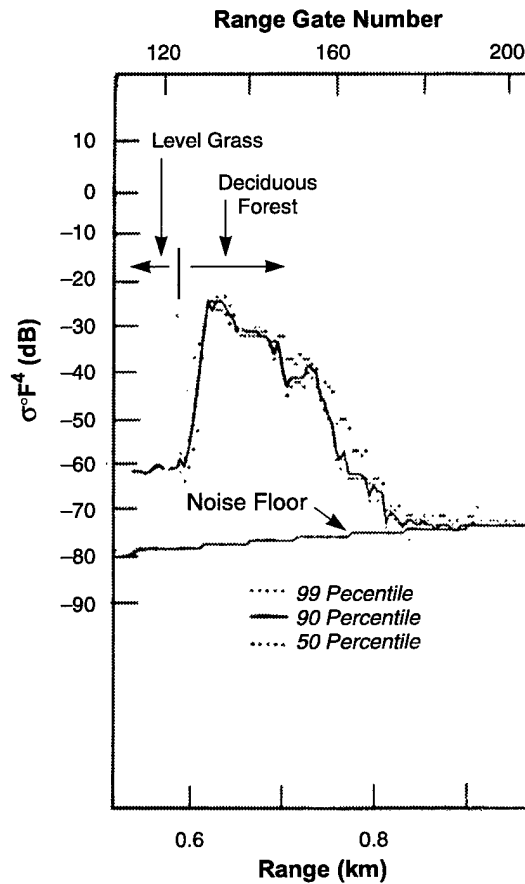
Figure 13. Backscatter from a tree line at Bedford, Massachusetts. Phase Zero X-band data, 9-m range resolution, horizontal polarization, 1.47-km maximum range setting, 4.6-m sampling interval.

Next, consider clutter patch 20 at Gull Lake West (see Figures 7 and 8). Patch 20 occurs at the edge of Lake Winnipeg and is basically a "water" patch. The clutter sources in patch 20 are shrub-covered sandy bars. The clutter amplitude distributions for patch 20 shown in Figure 8 are characterized by extreme spread. The histogram above noise level shows a long, gradually decreasing, high-side tail, and the cumulative plotted on the Weibull scale, in agreement with the histogram, shows a very low slope. The amplitude distribution of patch 20, for which the depression angle is 0.7°, is very similar to distributions

29

measured at much lower depression angles, typically between 0.1° to 0.3°, on cropland. The reason that the water patch at higher angle looks like cropland at lower angle is that, in both cases, there exists a relatively low incidence of discrete clutter sources of widely varying strength rising up from a non-backscattering medium. With increasing angle on cropland, the intervening terrain between discretes begins to contribute more and more discernible clutter to the distribution, but for the water patch, the intervening water remains at noise level.
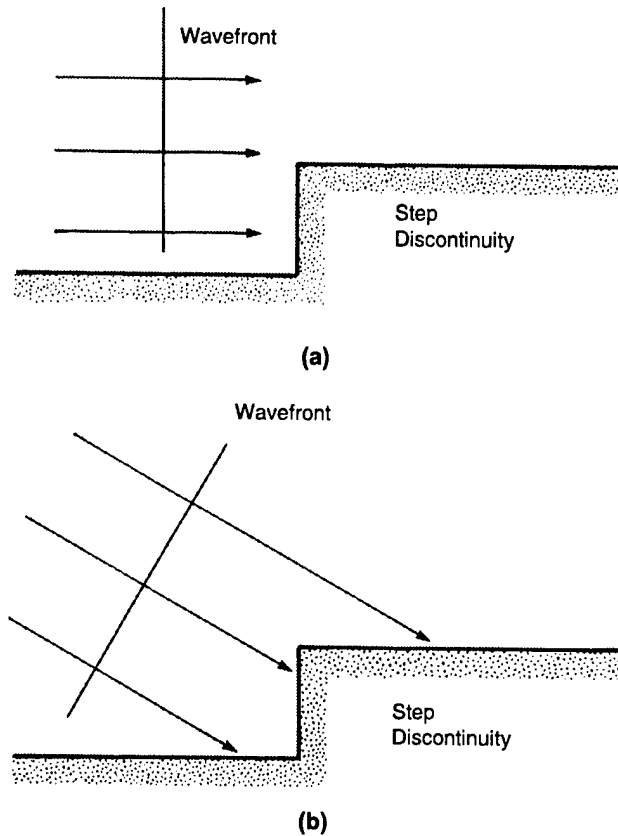
Figure 14. Cartoon illustrating backscatter from a dielectric step discontinuity.

Patch 20 is useful to illustrate a general point in ground clutter modeling. Ever increasing detail and specificity in terrain description can lead to more accuracy in analyzing measured clutter amplitudes, but at the same time the generality and simplicity that are necessary features in a basic model are lost. Taken to the extreme, every clutter patch is different (terrain is essentially infinitely variable), but an archival file of

many specific measurements does not constitute a useful model. The purpose of this report is to develop a useful empirical clutter model based on general trend analysis in the measurement data.

These considerations of measured clutter at Gull Lake West clearly illustrate that a simple general model will not rigorously and accurately predict every specific situation within a phenomenon as complex as terrain clutter. Thus, in Figure 8, although the cumulative amplitude distributions on the Weibull scale together show model-like behavior in that the distributions progressively move from low to moderate to high slopes, in fact application of the basic model of Section 4 to Gull Lake West results in substantial deviation from these measured results. The reasons for this have to do with the specific terrain at Gull Lake West. Particularly because this terrain is so level, the distributions in general have less spread and steeper slopes than would typically occur in more general low-relief terrain. For the same reason, a depression angle only as large as one degree is sufficient to provide full enough illumination to cause near-Rayleigh backscatter for patches 19/1 and 19/2. In forested terrain of higher and more complex relief, higher angles are required for this to occur. Note that some modeling information specific to level terrain is provided in Section 4.2.4, but such information burdens the analyst with describing terrain to this degree of specificity. Specificity of land cover (water patch) rather than specificity of landform (level) is the reason that the cumulative distribution for patch 20 has more spread and lower slope than would typically occur at one degree depression angle in low-relief terrain. Note that application of the more specific modeling information for level terrain in Section 4.2.4 starts to fall in more closely with the actual measured patches at Gull Lake West. If the objective is, as it is in this report, for a simple general model that is not overly demanding in terms of terrain representation but presents fundamental trends in clutter statistics, such a model will lack some degree of higher specificity in terrain representation. This fact as it pertains to realistic heterogeneous terrain has contributed historically to differences in results between different clutter modeling approaches. The basic model of this report does not predict every clutter patch exactly correctly, but over many patches and many sites it exhibits correct general trends.

In Figure 8, the cumulative distributions plotted on the Weibull scale appear more linear than those plotted on the lognormal scale. This is often the case. Weibull formulations usually (but not without exception) represent better engineering approximations to clutter spatial amplitude distributions than do lognormal formulations. Lognormal formulations of clutter amplitude statistics tend to somewhat over-predict the amount of spread in the high tails. The measured clutter amplitude distributions almost never pass rigorous statistical hypothesis tests for belonging to Weibull, lognormal, or any other theoretical distributions that were attempted over the full extent of the measured distributions. Hypothesis testing in just the high tails of measured Phase One distributions is discussed elsewhere [1, 5].

3.4 DEPRESSION ANGLE

As is shown in Figure 2, depression angle is the angle below the horizontal at which a clutter patch is observed at the radar. More specifically, depression angle is defined to be the complement of incidence angle at the terrain point under consideration. Incidence angle equals the angle between the projection of the earth's radius at the terrain point and the direction of illumination at that point, assuming a 4/3 earth

radius to account for nominal atmospheric refraction. Thus, the rigorous definition of depression angle is in a reference frame centered at the terrain point, not at the antenna. This definition of depression angle includes the effect of earth curvature on the angle of illumination, but does not include any effect of the local terrain slope. Grazing angle is the angle between the tangent to the local terrain surface at the back-scattering terrain point and the direction of illumination (see Figure 20). Thus, grazing angle does take into account the local terrain slope. The effects of grazing angle on clutter strength are discussed more fully in Section 3.5. The formula used for rigorous computation of depression angle is given in Appendix D. At short enough ranges that earth curvature is insignificant, depression angle simplifies to be the angle below the horizontal at which the terrain point is viewed from the antenna.

To illustrate the effect of depression angle on low-angle clutter, results are shown from two sites. First, results are shown from Shilo, Manitoba at very low depression angle, 0.1° or 0.2°. Then results are shown from Cazenovia, New York at a depression angle of about 9° which is a very high depression angle for surface-sited radar. Figure 15 shows a sector of a measured Phase Zero ground clutter map looking out 11.76 km to the southwest at Shilo, overlain and registered on an aerial photograph of this site. Shilo is a low relief site. Figure 16 shows photographs of some of the terrain features existing in this Shilo sector. Figure 17 shows terrain profiles in eight symmetrically disposed, radial directions away from site center at Shilo. Figure 18 shows clutter strength versus range in the southwest sector at Shilo.

The clutter measured to the southwest at Shilo is dominated by discrete clutter sources. The agricultural fields to the far southwest as shown in Figure 15 are within geometric line-of-sight and thus under direct illumination by the radar. Yet it is clear from the clutter map overlaying the aerial photograph that the radar is not sensitive to the backscatter from the field surfaces themselves. Rather, the clutter sources in these fields are all vertical discrete objects. Such objects include individual farmsteads (usually surrounded by trees as windbreaks) and other vertical features such as fence lines, telephone poles, bushes, and buildings that often show up in a rectilinear spatial pattern because such objects tend to cluster along roads and field boundaries.

Some examples of typical vertical landscape features in the southwest sector at Shilo are shown in Figure 16. At Shilo, the measurement equipment was set up on the native prairie grassland of a military base, Camp Shilo, as shown in the top left of Figure 16, where the viewing direction is to the southwest and, in the far background beyond the Phase One equipment, trees along the Assiniboine River are seen along the horizon. Between the radar and the river, some of the fields are under irrigation by 1/4 mile long, center-pivot, irrigation equipment, shown in the top right photo of Figure 16. Trees line the upper edges, slopes, and breaks of the river valley, as shown in the center left photo in Figure 16. These trees mask the terrain immediately beyond the river valley, but a treed farmstead in this depressional area as shown at the center right is high enough to stick up into the radar beam, which is directed left to right in this photograph, and constitutes a strong discrete clutter source. Beyond the depressional area, a belt of scrub is first encountered, through which runs a power transmission line, shown to the lower left in Figure 16, beyond which are the well-illuminated fields, as shown to the lower right, where the radar position is centered on the horizon in this photograph for which the viewing direction is northeast.
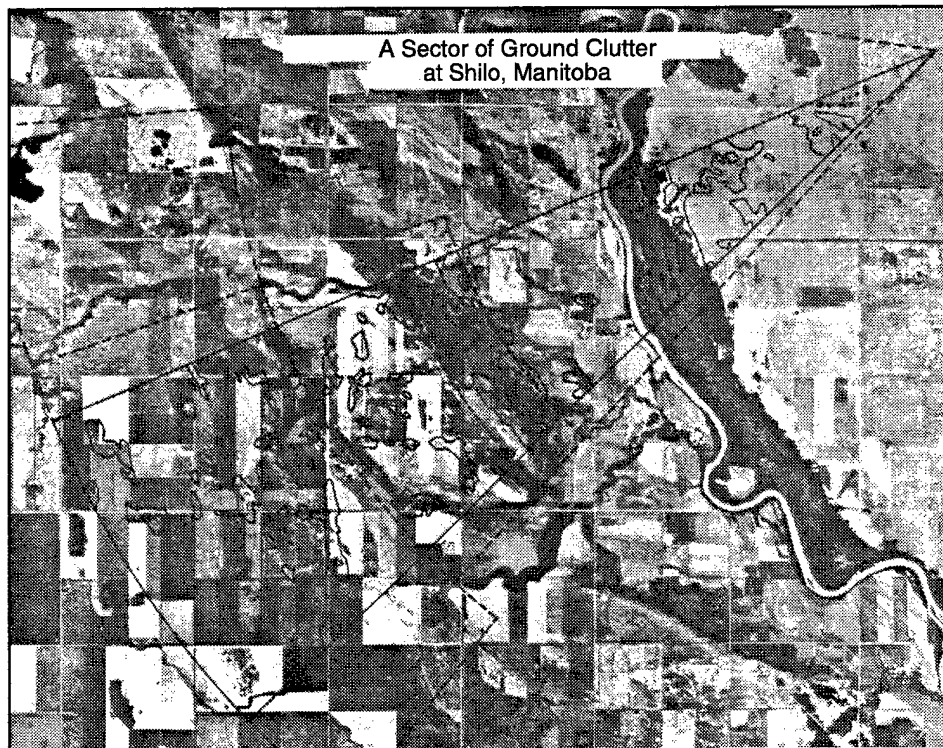
Figure 15. A sector of ground clutter at Shilo, Manitoba. Within the sector, microregions of terrain generating discernible Phase Zero clutter are circumscribed with a heavy black line. Within each such microregion, some vertical feature can be identified in the air photo. Much of the area within the sector, including most open field surfaces, is at the Phase Zero noise floor (i.e., not circumscribed). The radial extent of the sector shown is 12 km.

Now consider the terrain elevation profile to the southwest at Shilo shown in Figure 17 (as the third profile from the bottom). These profiles were produced manually from 1:50,000 scale topographic maps with 25-foot contour intervals. They incorporate the curvature of a 4/3 radius spherical earth. At 20 km this effect is 23.5 m. The vertical scale increment in Figure 17 is 20 m. Geometrical masking is also shown in Figure 17 as follows. The terrain profile itself is shown lightly dotted. For terrain that is within geometric line of sight of the radar, the dotted terrain profile line is overscribed with a heavy solid line. In the southwest terrain profile, the river valley lies about 4.5 km from the radar. From 5.2 to 13.4 km, the terrain gradually rises out of the river valley at an average terrain slope of 0.26°. This small angle is more than sufficient to bring this terrain into full visibility from the radar position. (For now, consideration is being given just to the geometric terrain elevation data, neglecting the effect of trees along the near bank of the river valley to shadow the terrain in the first few kilometers beyond the river valley.) Small changes in

terrain slope to the southwest at Shilo, for example, in the region from 13.4 to 15.1 km, and in the region beyond 17.3 km, are enough to cause these regions to be masked.

315027-16
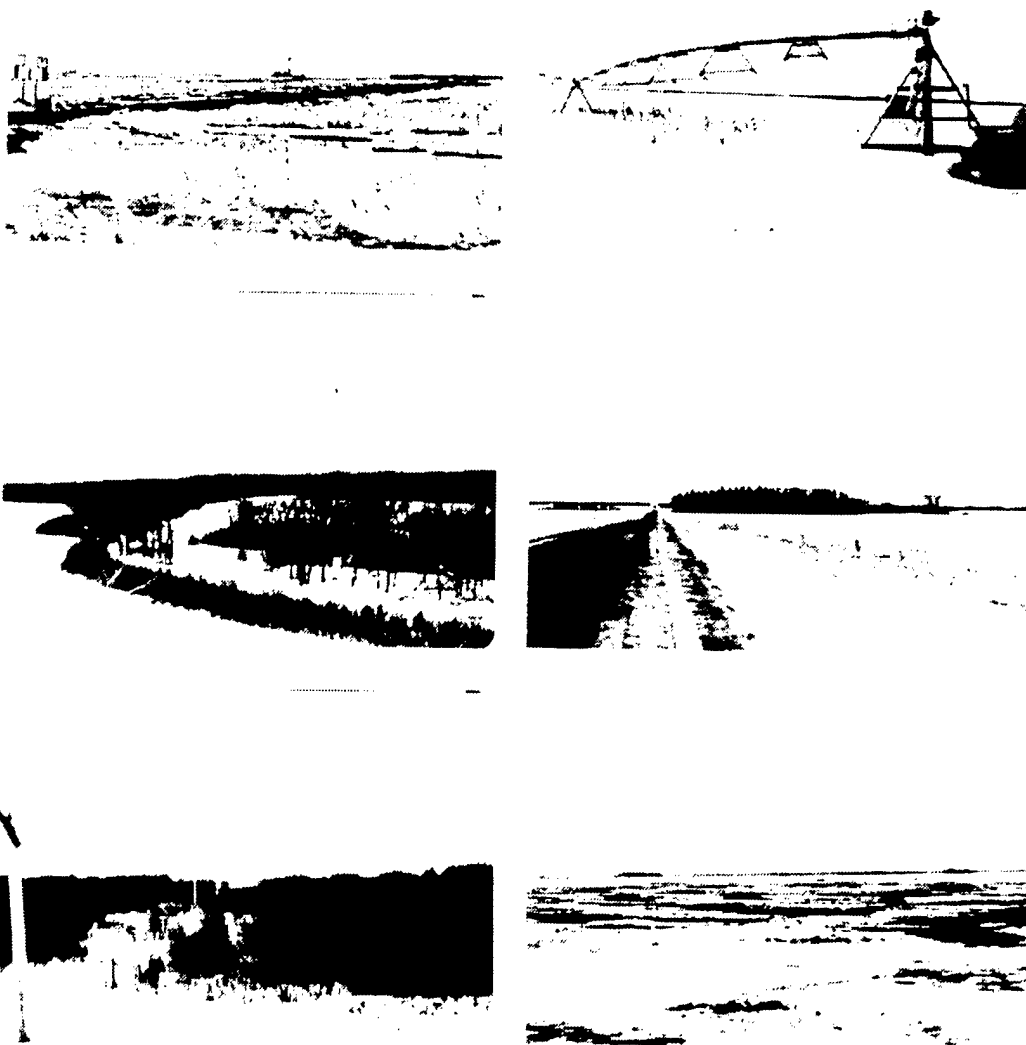
Figure 16. Ground truth in the southwest sector at Shilo (February). Compare with Figure 15.

34
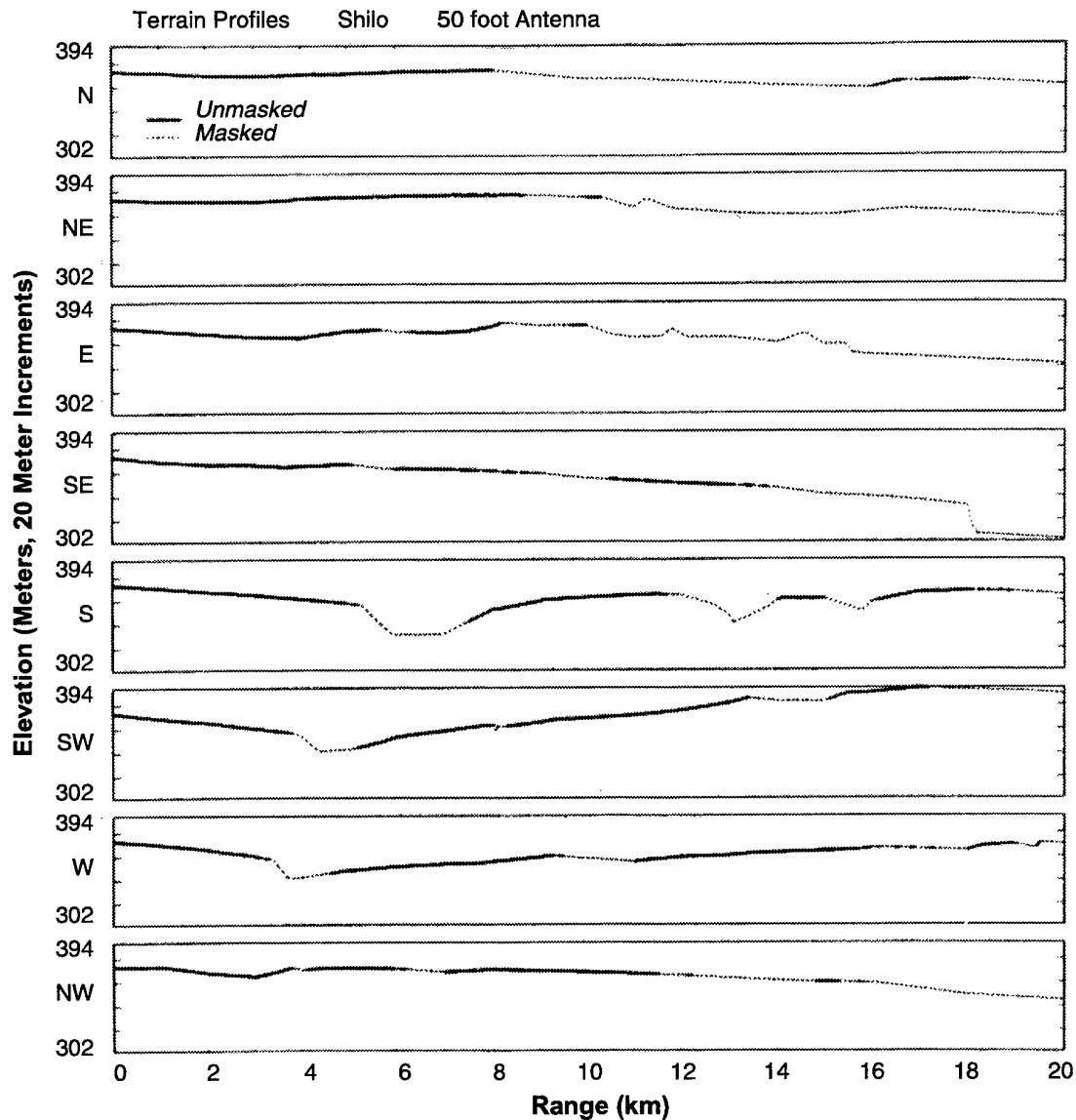
Figure 17. Terrain elevations and masking at Shilo. Antenna mast height = 50 ft. Effective site height = 3 m. Terrain elevation data are based on 1:50,000 scale topographic maps and include earth curvature for an earth of 4/3 radius of the actual earth to account for nominal atmospheric refraction. Thus these terrain profiles do not show height above mean sea level, but rather height with respect to a horizontal plane through site center and tangent there to a 4/3 earth.

This leads to an important point that is often misconstrued at first consideration. Terrain slope, and changes in terrain slope, even when quite small, are very important in how they directly and deterministically affect clutter visibility. The effect of terrain slope on clutter strength, however, is an entirely different matter, which is discussed in Section 3.5. When measured clutter maps such as those in Figure 3 are being viewed, what is being observed are the effects of terrain slope and elevation on the spatial patterns of occurrence of the clutter, or, in other words, on where the clutter is, not on the strength of the clutter. This does not imply that terrain slope has no effect on clutter strength. Section 3.5 shows that, indeed, terrain slope does affect clutter strength, but the effect is readily observable only statistically by averaging over many individual measurements and is very difficult to see within any particular measurement. On the other hand, the effect of terrain slope on clutter visibility is direct and deterministic and readily observable in any measured clutter map. This brings out more fully the importance of distinguishing between where clutter exists, and the strength of clutter given that it exists, as stated previously in Section 3.2.

Figure 18 shows clutter strength versus range in a narrow azimuth sector to the southwest at Shilo. The available dynamic range between the noise floor and the saturation ceiling of the Phase Zero receiver is shown in the figure. Only in the first 2 km on the relatively discrete-free prairie grassland of Camp Shilo is seen anything approaching a traditional deterministic effect between area-extensive $\sigma°$ from the terrain surface itself and grazing angle. This close to the radar, the antenna mast height is sufficient to provide grazing angles greater than 0.5°. Thus, as range decreases from 2 km, grazing angle increases from 0.5°, and clutter strengths rise. Even in this near-in region, the nature of the increase of $\sigma°$ with grazing angle is not smooth and monotonic but shows wide fluctuations.

Beyond 2 km, the clutter strengths in Figure 18 are dominated by discrete clutter sources. Where there are trees existing on this primarily agricultural terrain (between 2 km and 7.5 km), they tend to dominate as clutter sources. But where there are no trees (beyond 7.5 km), other vertical features are revealed on the landscape which take over as the dominant clutter sources. Again, Section 4.2.5 provides general information of the effect of various incidences of tree cover on clutter amplitude statistics.

The nature of the low-angle clutter amplitude phenomenon shown in Figure 18 shows extreme and rapid variation of clutter strength from range gate to range gate. These variations easily encompass 30 dB or more at a given percentile level of strength. The overall picture is not one of well-behaved or easy-to-describe statistics. Rather, there is patchiness and heterogeneity. An investigator would not start out being overly optimistic about capturing the effects shown here in a traditional grazing angle model based on terrain slope. This, however, is the phenomenon that requires description even though it is highly terrain-profile-specific and discrete-dominated.

Figure 18 plot showing σ°F⁴ (dB) versus Range (km):

- Y-axis: σ°F⁴ (dB), with marks at −3, −23, −43, −63
- X-axis: Range (km), 0 to 12
- Labels on plot: Increasing Grazing Angle, 0.5°, Irrigation Equipment, Trees, River Valley, Treed Farmstead, Scrub Belt, Treeless Cropland
- Legend:
  - · · · 99 Percentile
  - —— 90 Percentile
  - · · · 50 Percentile
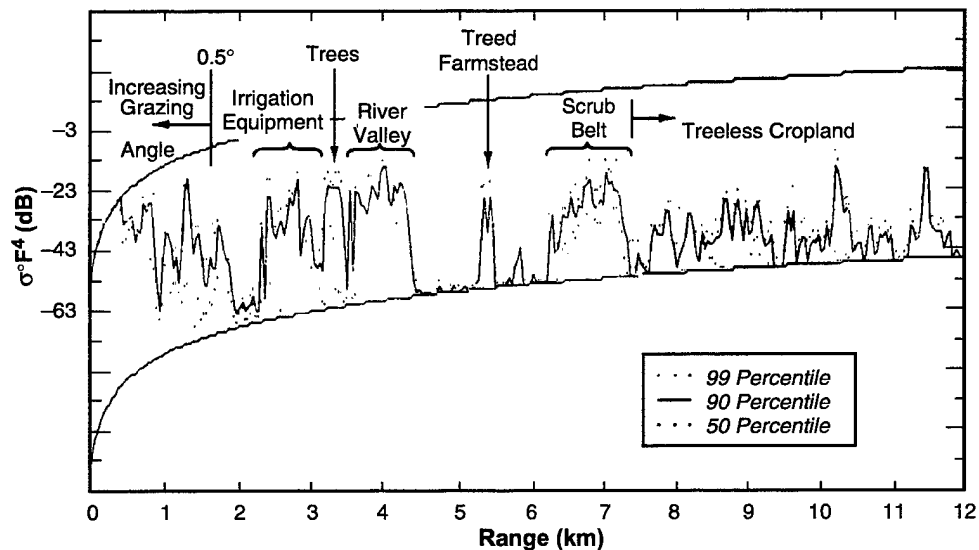
• Data shown for individual range gate positions, averaged over a 7° sector, 232° to 239° (31 azimuth samples/gate).

• Measurement date, 3 March; leafless deciduous trees, snow-covered field surfaces.

Figure 18. Clutter strength versus range to the southwest at Shilo, Manitoba. Phase Zero X-band data, 11.8-km maximum range experiment, 75-m range resolution.

Considered next is similar clutter strength versus range data from a much higher site at Cazenovia, New York. At Cazenovia the radar is set up high on the side of a steep valley, as shown in the top sketch in Figure 19. The radar looks down into the valley at high airborne-like depression angles. Beneath the terrain profile in Figure 19 are $\sigma°F^4$ data versus range shown in the same manner as in Figure 18 for Shilo, averaged azimuthally over an azimuth sector in individual range gate positions. The dashed lines between the upper terrain profile and the lower clutter data trace are included merely to aid the eye in associating particular points within the data window on the terrain profile with corresponding points in the clutter data.

The data in Figure 19 seem to belong to a completely different phenomenological regime than the data of Figure 18. The fluctuations of clutter strength with range are much less at the higher depression angle, more on the order of 6 dB than the 30 dB swings shown in Figure 18. The variation of clutter strength with range at high depression angle in Figure 19 is much less patchy, more homogeneous, and gives much more indication of being of a continuous process rather than the discrete-dominated process of Figure 18. The amount of shadowing (i.e., noise level cells) is dramatically reduced from Figure 18 to Figure 19. Thus, the most remarkable feature in the high angle data of Figure 19 is the reduction of spread

37

in clutter amplitudes exhibited at the higher illumination angle. Besides reduction in spread, the overall strength has increased with depression angle also, from about $\sigma°F^4 \approx -33$ dB on the average in Figure 18 to about $\sigma°F^4 \approx -24$ dB on the average in Figure 19. These two major effects of decreasing spread and increasing strength in clutter amplitude distributions as depression angle increases and shadowing decreases are basic effects in low-angle clutter around which is formulated the basic clutter model of Table 5.
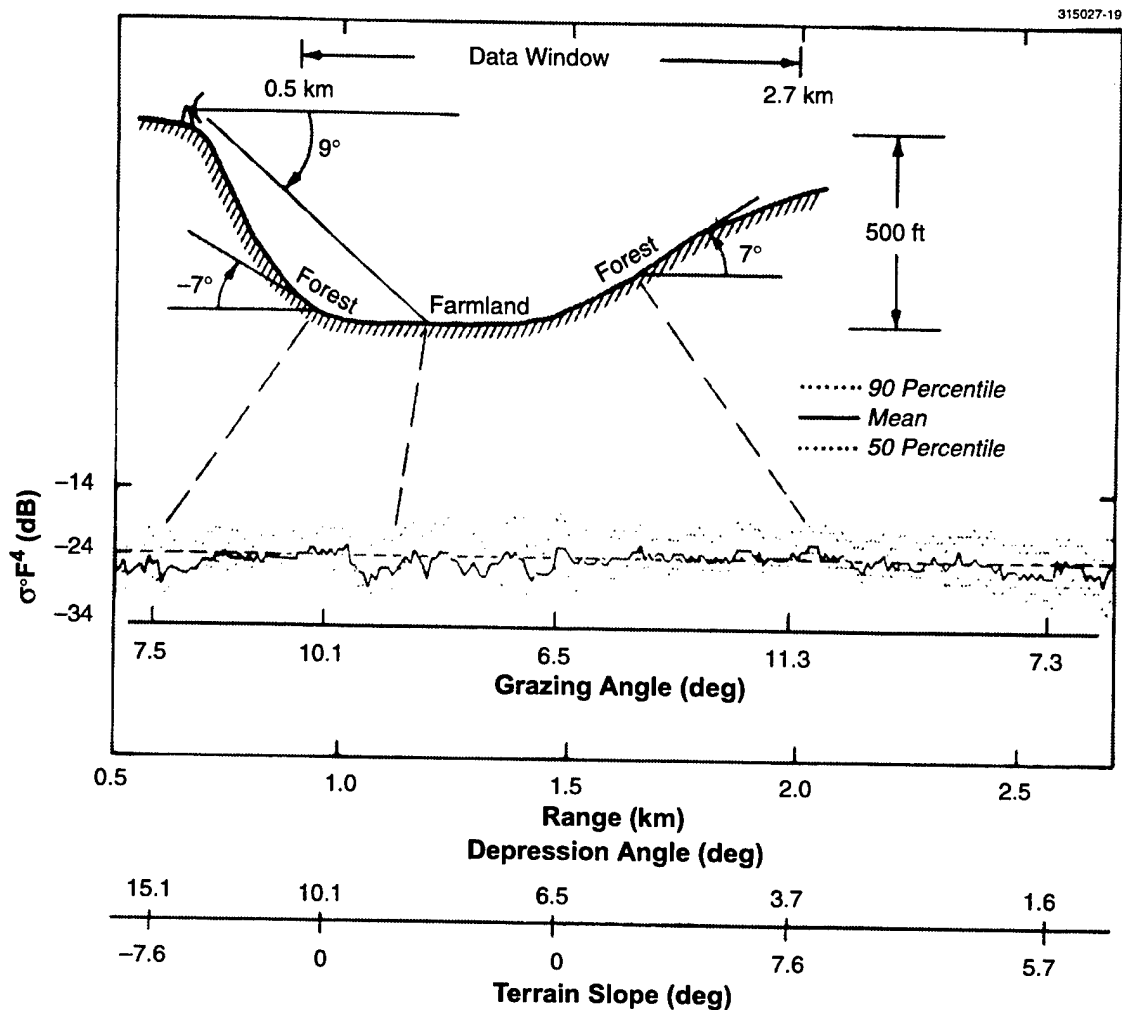
- Data shown for individual range gate positions, averaged over a 58° azimuth sector (9248 azimuth samples/gate)
- Measurement date, 12 June
- Grazing angle = depression angle + terrain slope, see Figure 20

Figure 19. Clutter strength versus range at high depression angle at Cazenovia, NY. Phase Zero X-band data, 3-km maximum range experiment, 9-m range resolution.

Next consider more closely the clutter data in Figure 19. The terrain on the valley floor is agricultural, with some trees scattered around in woodlots, around farmsteads, and along roads. As the terrain slopes increase on the valley walls, however, the terrain becomes more completely forest covered. The effects of the variations in land cover are seen in the clutter data of Figure 19. There is more fluctuation in clutter strength from the farmland on the valley floor between 1.0 and 1.5 km in range. From the forested surfaces, between 0.75 and 1.0 km and between 1.75 km and 2.25 km, there is less fluctuation, and the amplitude distributions appear to be close to Rayleigh in these regions.

Also shown in Figure 19 are approximate indications of depression angle, terrain slope, and grazing angle (see Figure 20), as a function of range. Depression angle decreases strongly and monotonically from 15.1° to 1.6° with increasing range across the data window. Looking ahead to the general clutter model of Table 5, mean clutter strength might be expected to strongly decrease with increasing range by many dB as the depression angle decreases with increasing range in Figure 19. Why is not a strong monotonic decreasing trend in mean clutter strength with increasing range seen in Figure 19? The answer has to do with the terrain slopes and grazing angles involved. Because terrain slope varies from large and negative to zero to large and positive with increasing range in Figure 19, the variation of grazing angle with increasing range in Figure 19 is non-monotonic. The lowest values of grazing angle occur in the center of the data window on the valley floor and at each end of the data window high on the valley walls. The highest values of grazing angle occur mid-way on the valley walls. A traditional way to model higher angle ground clutter is by means of a constant-γ model, where clutter strength varies directly with the sine of the grazing angle, the constant of proportionality being γ. Under such a model, with increasing range through the data window of Figure 19, the following variations in mean clutter strength would be expected: 1) a 1.3 dB increase as grazing angle increases from 7.5° to 10.1°; 2) a 1.9 dB decrease as grazing angle decreases from 10.1° to 6.5°; 3) a 2.4 dB increase as grazing angle increases from 6.5° to 11.3°; and 4) a 1.9-dB decrease as grazing angle decreases from 11.3° to 7.3°. The mean clutter strength data in Figure 19 indeed show each of these rises and drops, with the changes being of about the expected order of magnitude (i.e., 2 or 3 dB, not many dB). Thus, the data of Figure 19 support a constant-γ grazing angle model for mean clutter strength at high angle as being quite realistic. The value of γ suggested by the data of Figure 19 is 0.023. Furthermore, it would appear from Figure 19 that γ is relatively independent of terrain type, at least between farmland and forest, a conclusion supported by Lincoln Laboratory airborne clutter measurements. In all of this, however, it requires quite extreme terrain slopes and grazing angle variations caused by an unusual, close-range, large-scale terrain feature (i.e., deep linear valley) to result in barely discernible 2- or 3-dB changes in mean clutter strength with grazing angle in Figure 19.

At the beginning of this discussion of the Cazenovia data of Figure 19, it was observed that these high-angle data seem to belong to a completely different phenomenological regime than the low-angle Shilo data of Figure 18. In fact, the grazing angles of Figure 19 are so high as to be much more typical of airborne radar than general ground-based radar. Certainly a constant-γ model has no applicability to the lower angle regimes of ground-based radar which constitute the major subject of interest in this report (i.e., at grazing incidence, a constant-γ model predicts vanishing clutter strength). The data of Figure 19 are included here for several reasons, one of which is to indicate what kind of a stressing or unusual terrain geometry is required in a ground-based measurement for grazing angle and constant-γ to start to be useful.

Data were included within a wide azimuth sector in Figure 19 to help move to a constant-γ situation and further the distinction between floodlit illumination over large regions of relatively homogeneous and shadow-free terrain backscattering relatively strongly in all cells as in an airborne situation, and the more typical patchy ground-based situation dominated by microshadow and discrete sources.

If the Cazenovia data in Figure 19 were the only clutter measurements available, a different sort of basic clutter model than that of Table 5 might have been developed. Indeed, similar situations occur through much of the early clutter literature, where generalizations had to be attempted on the basis of little data. It is instructive to consider how the Phase Zero patch world deals with the Cazenovia terrain, because such an exercise helps bring home the scale at which a clutter model is sought in this report. Again, the scale of interest here is in the clutter seen by typical ground-based radars as it emanates from large extents of composite landscape extending many kilometers in range from the radar. In particular, this Phase Zero study is based on measured clutter between 2- and 12-km range from many sites.

First, note in Figure 19 that 2 km is towards the far end of the data window, and in thinking of all of the clutter at Cazenovia between 2- and 12-km range, it is realized that the data of Figure 19 really focus on one particular close-in terrain feature, rather than material from which to attempt a general model at longer range. Within the data window in Figure 19, two Phase Zero clutter patches were specified, patch 15 from 1.0 to 2.0 km in range and 133° in azimuth extent, and patch 2/2 from 2.0 to 3.9 km in range and 52° in azimuth extent. Applying the basic model of Table 5 to patch 15, the highest depression angle regime in rural/low-relief terrain is selected from the model and its mean clutter strength, –27 dB, is augmented by a dB or so to account for the 6° depression angle of patch 15. This results in a mean strength very comparable to that shown on the valley floor in Figure 19. But again, patch 15 is too close to be of general interest in Phase Zero modeling activities. It is only because of its closeness that radar visibility exists into this deep valley at all. Similar valleys at longer ranges are typically screened to ground-based radar. Only one percent of all measured Phase Zero patches between 2- and 12-km range occurred at depression angles greater than 5 degrees.

Patch 2/2, however, extending in range from 2.0 to 3.9 km, is just within the Phase Zero 2- to 12-km general range of interest. Beyond 2 km in the terrain profile shown in Figure 19, the terrain continues to rise up the side of a gullied forested hillslope to elevations at the top of the hill about 50 feet higher than the measurement site elevation itself, at a range of about 3.4 km; beyond this, the elevation starts to fall off into the next valley in this generally rolling terrain. Applying the basic model of Table 5 to patch 2/2, the second depression angle regime in high-relief terrain is applicable providing a mean clutter strength of –26 dB, relatively close to the values indicated between 2.0 and 2.7 km in Figure 19.

In considering the Cazenovia data of Figure 19 within the context of the basic Phase Zero model of Table 5, a better feel is obtained for how the model works and the terrain scale at which it is meant to work. Although the very local close-in data of Figure 19 can be sorted out through grazing angle, the model works more globally and sorts out the data of Figure 19, not in fine steps, range gate by range gate, but in large patches for which terrain slope and depression angle enter separately (terrain slope enters in via low-

and high-relief). Thus, patch 15 on the valley floor involves high depression angle and low-relief terrain, whereas patch 2/2 on the valley wall and beyond involves low depression angle and high-relief terrain.

The discussion of the Cazenovia data of Figure 19 has acted as an introduction to Section 3.5 on grazing angle. There efforts to bring grazing angle and terrain slope quantitatively to bear in clutter modeling are pursued. The difficulties attendant in usefully quantifying grazing angle are illustrated. Only in special circumstances, such as looking down into and across a single deep linear valley at close range such as occurs at Cazenovia, can direct and specific causative influences of grazing angle on clutter strength be shown. Section 3.5 does show, however, that on the statistical average terrain slope has a strong causative influence in measured clutter data.

Finally, return briefly to Figure 14 illustrating backscatter from a step discontinuity. At very low angles of illumination (Figure 14(a)), vertical surfaces are illuminated at normal incidence and give rise to strong returns, whereas horizontal surfaces are illuminated at grazing incidence and give rise to weak returns. This is the situation obtained in the Shilo data of Figure 18. However, at higher angles of illumination (Figure 14(b)), both vertical and horizontal surfaces are illuminated at angles in between normal and grazing and give rise to returns of more nearly equivalent strength. This is the situation obtained in the Cazenovia data of Figure 19. That is, at higher angles vertical features are less obtrusive and tend to "melt into" the horizontal background. As discussed throughout Section 3, low returns at grazing incidence from horizontal surfaces are more the result of microshadowing on these rough surfaces than the result of an intrinsic strong angular dependence of $\sigma°$ at low angles. Once angle is high enough to obviate micro-shadowing, both horizontal and vertical surfaces are expected to backscatter at roughly equivalent strengths (i.e., constant-γ regime). The simplistic model of a step discontinuity as shown in Figure 14 and this qualitative discussion concerning it represent a heuristic explanation to help account for some of the difference between the low-angle clutter phenomenon of Figure 18 and the higher angle phenomenon of Figure 19.

3.5   GRAZING ANGLE

Grazing angle is defined herein to be the angle between the tangent to the local terrain surface at the backscattering terrain point and the direction of illumination (see Figure 20). Whereas depression angle does not depend on the local terrain slope at the backscattering terrain point, grazing angle does depend on the local terrain slope. Consequently, if depression angle is a useful modeling parameter of low-angle clutter, should not grazing angle be a better parameter? Intuition strongly suggests that the best measure of illumination angle in considering backscattering from a rough surface is the angle between the direction of illumination and the plane of the surface.

41

Grazing angle ψ = Depression angle α + terrain slope ξ
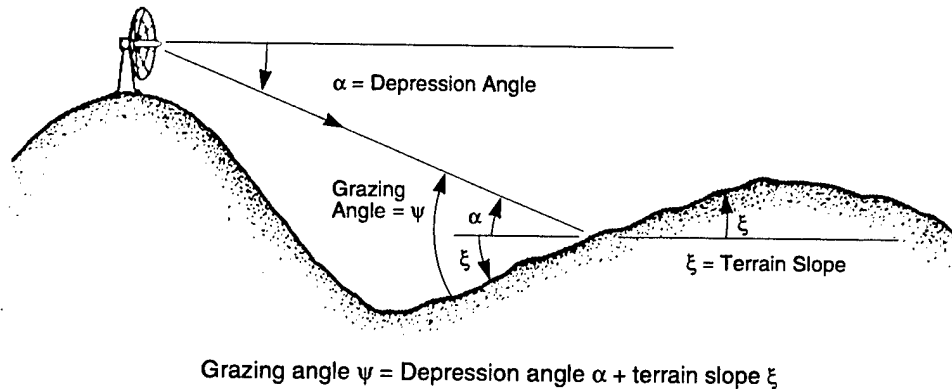
Figure 20. Cartoon showing relationship of grazing to depression angle and terrain slope.

Discrete vertical land cover features often dominate as clutter sources in low-angle clutter. For example, if a tree exists in a spatial resolution cell, the slope of the ground under the tree is not expected to be very significant in affecting the backscatter from the cell. Trees and other vertical landscape features are vertical irrespective of the underlying terrain slope. Thus discrete land cover features, which are often the dominant low-angle clutter sources, act to downplay terrain slope and grazing angle and up-play depression angle as the fundamental measure of illumination angle.

Set aside for the moment the issue of discrete vertical features in land cover and assume that over and above such dispersive factors terrain slope will still act as a dominant parameter in low-angle clutter. How should these important terrain slopes be computed or measured? At this point, consider that digitized terrain elevation data are available from various services. Hereafter in this report, digitized terrain elevation data will be referred to as "DTED." DTED are often provided as points of terrain elevation precise to ~1 m on an approximately 100-m grid. In clutter modeling, can grazing angle be brought to bear to predict clutter strength, pixel by pixel in the DTED, based on the elemental terrain slopes provided by these data? If such an approach were successful, the DTED could carry the burden of describing terrain, which is the root cause of difficulty in clutter modeling. A clutter model could merely be the direct relationship between pixel-level grazing angle and clutter strength.

An example of pixel-level correlation between measured clutter strength and DTED-predicted grazing angle is shown in Figure 21. The site for which the data of Figure 21 apply is Brazeau, a forested site of significant relief in Alberta, Canada. A forested site was selected first in order to have a more spatially continuous scattering medium and to minimize the effects of the strong discretes occurring on more open or agricultural landscapes. Thus, selecting a forested site potentially gives grazing angle a better chance to work (i.e., less a sea of discretes, more area-extensive $\sigma°$). For the same reason, a site of significant relief was selected in order to provide significant variation in terrain slope. For each resolution

cell within 20 km maximum range at Brazeau, terrain slope and grazing angle at the cell were computed from DTED and registered with the measured Phase Zero clutter strength for the cell. Then, for each cell that was within geometric visibility and for which Phase Zero measured discernible clutter return, a single point in Figure 21 was plotted indicating clutter strength versus grazing angle. Doing so for all such points resulted in the scatter plot of Figure 21.
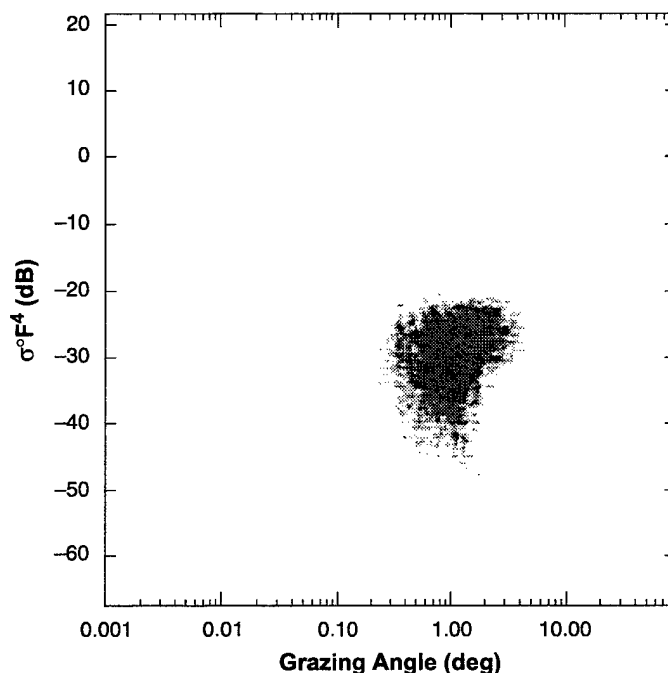
Figure 21. Cell level scatter diagram of measured $\sigma°F^4$ versus grazing angle at Brazeau, Alta. Range interval = 1 to 20 km. Azimuth interval = 1.0° to 360°. Phase Zero X-band clutter data, horizontal polarization, 75-m range resolution. Terrain slope at each cell computed from DTED.

Very little useful correlation is seen between clutter strength and grazing angle in Figure 21. The correlation coefficient computed for these data is 0.21. Scatter plots similar to Figure 21 were generated for six different sites of widely varying terrain type. The largest correlation coefficient obtained was 0.23. In general, negative correlation between grazing angle and clutter strength was equally likely to positive correlation. The original source material from which these DTED data were generated was 1:250,000 scale topographic maps. At one site, additional DTED based on 1:50,000 scale maps, a five-fold improvement in scale, were utilized but no improvement in the results occurred. Based on these investigations, the idea of a simple clutter model based on statistically significant direct correlation between pixel-level estimates of grazing angle using DTED and measured clutter strength falls into the realm of wishful thinking. The

complexities of real terrain will not disappear so easily. Any usefulness in such correlative associations need to be earned at the price of more sophisticated analyses looking for more subtle effects (e.g., after first separating strong discretes).

Why is so little correlation seen between clutter strength and grazing angle predicted from DTED? First recall that DTED describes only a bare earth and contains no information describing land cover, edges of land cover features, or discrete land cover objects that so often dominate the measurements. Beyond this, however, the results shown in Figure 22 provide more insight. These results were obtained in propagation studies at Lincoln Laboratory. They apply to forested terrain in eastern Massachusetts. In Figure 22, terrain elevations are shown based on two sources, DTED and quadrangle topographic maps. The original source for the DTED in Figure 22 was 1:250,000 scale maps with 50-ft contour intervals. The quadrangle maps from which information was plotted directly in Figure 22 were of 1:24,000 scale with 10 foot contour intervals. Both the quadrangle data and DTED data of Figure 22 were additionally interpolated every 10 m as plotted in the figure. In overall measure, the two terrain profiles in Figure 22, quadrangle and DTED, show some similarity. Use of such DTED to grossly predict macroscale regions of terrain visibility and shadow is expected, on the basis of Figure 22, to provide useful information. Indeed, DTED are routinely used in this manner to predict visibility in site-specific radar system studies at Lincoln Laboratory. However, it is another matter to consider correlating local terrain slopes with clutter strength cell by cell in the data of Figure 22. If the quadrangle data are regarded as accurate, it is evident that many DTED cells provide markedly inaccurate estimates of terrain slope. The fact that the DTED source material is 1:250,000 scale maps implies that the DTED (at about a 100-meter sampling interval) are themselves interpolated values at a sampling interval of about every 0.015 inches on the source map. Thus, many interpolated elevation values occur between map contour lines. Furthermore, consider that the DTED, quantized to 1-m precision, can only provide terrain slope on a 100-m grid quantized to about 0.5°. Clearly these data do not contain fine enough information to provide accurate terrain slope detail at the scale of radar carrier-frequency wavelength, which after all is the scale at which the mechanisms of electromagnetic backscattering take place.

The data of Figure 22 are shown here merely as an example around which to discuss what is really required in expecting a pixel-level grazing angle clutter model to work. It is not implied that the DTED used in Figure 22 are representative of all DTED. Left unaddressed are questions of accuracy or sufficiency in the quadrangle data. Although the quadrangle map is of ten times greater scale than the original source map from which DTED were generated, it is still a map and thus still a gross simplification of reality. Specification of scale, accuracy, precision, and sampling interval in a digitized terrain elevation database suitable for clutter strength prediction would result in much more stringent requirements than those of currently available DTED. Of course the availability of DTED invites its use; however, DTED cannot be faulted if, as here, it is applied to more demanding problems than it was designed to face.
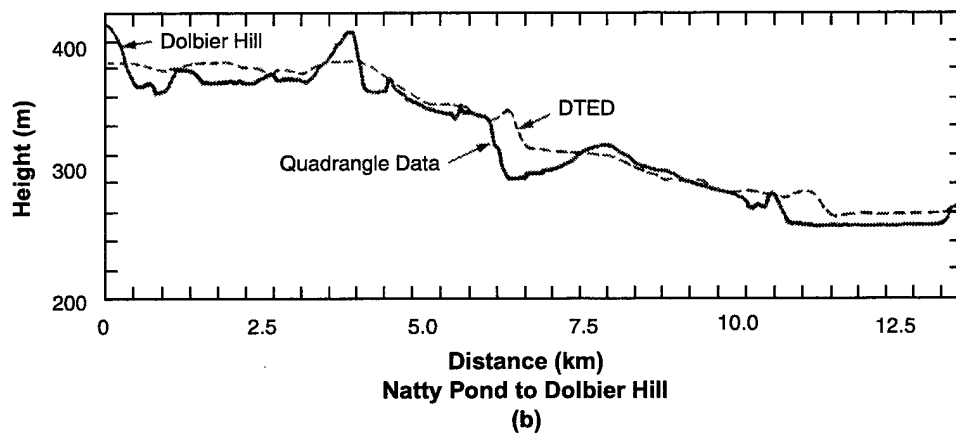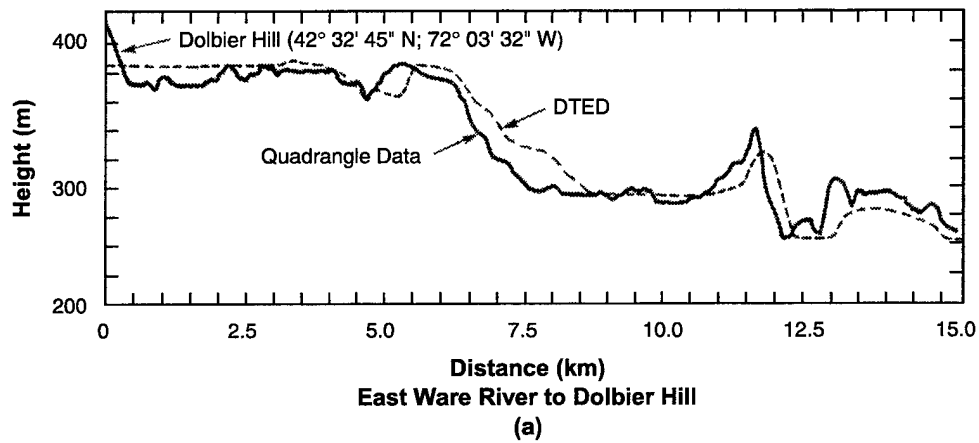
Figure 22. Terrain elevation profile along two paths in Massachusetts, comparing digitized terrain elevation data (DTED) and data derived from quadrangle topographic maps. The topographic maps were 1:24,000 USGS quadrangle sheets with 10' contour intervals. The original source for the DTED was 1:250,000 scale topographic maps with 50' contour intervals. Both quadrangle data and DTED were interpolated every 10 m.

The discussion now returns to the implicit idea that, at some level or some scale, terrain slope must strongly affect clutter strength. In contrast to DTED pixels, consider the Phase Zero clutter patches, typically sized to be several kilometers on a side. Such sizes are macroscale in comparison with microscale DTED pixels. Recall that the landform within each patch is classified through interpretation of stereo aerial photographs and topographic maps. In this classification, terrain slope is the principal criterion. Of course any patch several kilometers on a side presents various slopes to the radar, so one must think in terms of a distribution of slopes over each patch (attempts to use the slope of the best-fit plane through the patch as a

45

modeling parameter were not fruitful). Further, realize that this distribution of slopes over a patch depends on the measurement scale employed. That is, increasing magnification is expected to always reveal increasing detail and new structure in the surface (i.e., fractal phenomenon).[7] Thus, the actual distribution of slopes over a patch is regarded as an indeterminate quantity. As has been observed elsewhere, "... in typical agricultural and rolling terrain... the grazing angle is not readily definable [13]."

Through subjective interpretation of air photos and maps, however, one can at least roughly bound or set limits to the slopes existing within each patch and subsequently bin patches within classes defined by these slope limits. Table 2 shows six categories of landform in increasing order of terrain slope. More detailed descriptive definitions of these landform categories are provided in Appendix A. Within the category of level terrain, the first category in Table 2, there exist Phase Zero measurements from 524 different patches lying between 2 and 12 km from the radar. For each level patch there exists a corresponding Phase Zero measured mean clutter strength. Figure 23 shows the distribution of mean clutter strengths from all 524 patches of level terrain, plotted cumulatively on a normal probability scale. A great deal of spread is observed in this distribution of mean clutter strength measured from level patches. From maximum to minimum measured mean values, there is over 30 dB of variation. The cumulative distributions of mean clutter strength from the five remaining terrain types of Table 2 are also shown in Figure 23. If the median level in each distribution of mean clutter strength in Figure 23 (indicated by the horizontal dashed line) is selected as a measure of centrality, then a statistically significant monotonic increase in mean clutter strength is seen with terrain slope. That is, at the median level the distributions are displaced increasingly to the right with increasing terrain slope over a range of 11 dB from minimum to maximum. Hence, intuition is justified. These data unequivocally illustrate that clutter strength depends on terrain slope. The effect is strong enough to be observed through dispersive influences of land cover, terrain heterogeneity, and depression angle. Two other important facts are also observed: 1) there is much spread within the distribution of mean clutter strength for any given class of landform, and 2) although significant, there is relatively little separation between adjacent classes.

---

[7] Some theoretical investigations of land and sea clutter which lead to K-distributions of amplitudes are based on a hierarchy of models covering 1) a single-scale "smooth" model (differentiable); 2) a multiscale "fractal" model (nondifferentiable); and 3) a multi-scale "fractal slope" model (once differentiable) [12].

TABLE 2

Six Categories of Landform in Increasing Order of Terrain Slope

Landform*	Terrain Slope (deg)	Relative Incidence** (%)
Level (LEV)	< 1	26
Undulating (UND)	< 1	26
Inclined (INC)	1-2	16
Rolling (ROL)	2-5	10
Moderately Steep (MST)	2-10	7
Steep (STP)	10-35	4

*For more detailed descriptions of landform classes, see Appendix A.

**Ratio (times 100) of the number of rural (i.e., non-urban land cover) patches of the indicated landform class to 2177, the total number of Phase Zero patches (including urban) from 96 sites between 2- and 12-km range from the radar.

Information such as that provided in Figure 23 is very useful in application to non-site-specific modeling, where the overall terrain of a site can be uniformly classified as one category, and the varying terrain elevations and illumination angles from point to point over the site are suppressed. Note that Figure 23 displays one attribute of a clutter patch amplitude distribution, namely, mean patch strength, as that attribute is distributed over many patches, and from the distribution, extracts a best "expected value." This expected-value approach gives the patch the status of elemental statistical quantity, in contrast to the ensemble approach which gives the individual clutter sample that status. These matters are discussed further in Section 4.3.

47
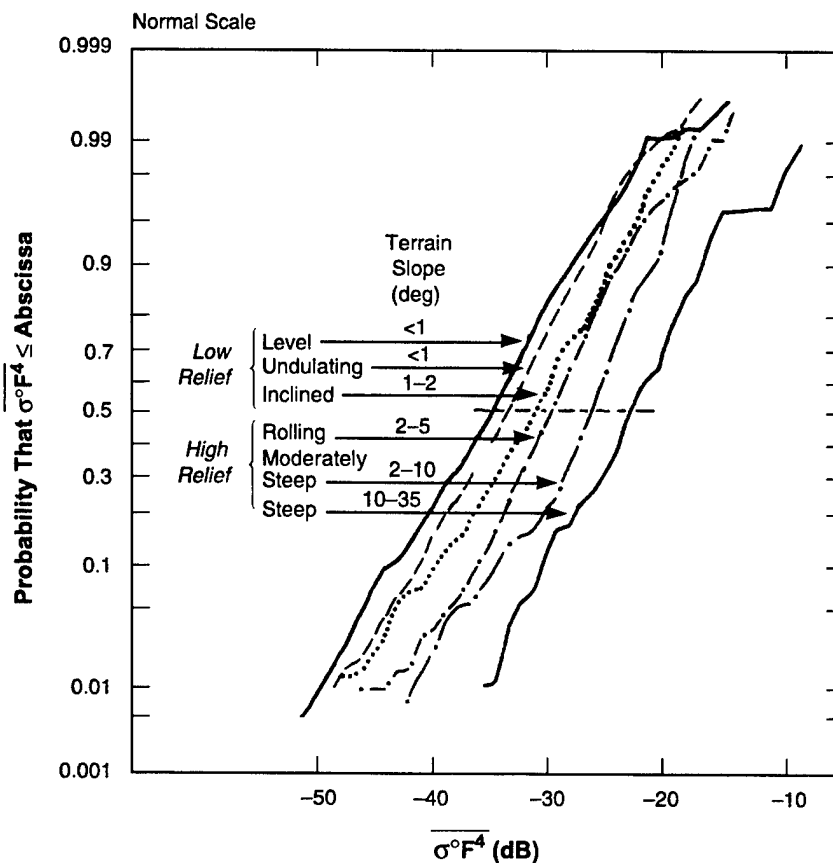
Figure 23. Cumulative distributions of mean ground clutter strength by landform in rural terrain. Phase Zero X-band data, 75 m range resolution, horizontal polarization, 2- to 12-km range, 1809 patches, 96 sites. Each curve shows the cumulative distribution of mean clutter strengths from all patches of a given landform class, one value of mean strength (see Appendix C, Equations C-3 and C-8) per patch. Patches of urban land cover classification are not included in these data.

3.6 CLUTTER MODELING

Assume that DTED are available for the site that is required to be modeled. The DTED can be used to define kilometer-sized clutter patches as regions of general geometric visibility. This is an appropriate use of DTED, well matched to the information content of the database. Within these macroregions of visibility, one cannot accurately predict clutter strength pixel by pixel simply by association with the local terrain slope and grazing angle at the pixel. This is an inappropriate use of DTED because the sought-after information is at a scale, accuracy, and precision not contained within the data.

48

Still, illumination angle is of major importance in its effects on low-angle clutter strength. Rather than grazing angle, results in this report are based on depression angle. Depression angle is a quantity that can be computed relatively rigorously and unambiguously from available information. For example, within a macropatch of visible terrain in DTED, depression angle (which depends only on the pixel-level elevations over the patch and not the detailed rates of change of these elevations) is a quantity that varies relatively slowly over the patch. If the mean depression angle over the patch is computed, this mean value is relatively insensitive to the questions of accuracy, precision, and scale that plague grazing angle.

But in using depression angle, how are the important effects of terrain slope incorporated? Reconsider the data in Figure 23 that statistically show how mean clutter strength increases with terrain slope. As shown there, terrain is simply separated into two categories, low relief and high relief. Low-relief terrain provides slopes of <2°; high-relief terrain provides slopes of >2°. Thus, in Figure 23, level, inclined, and undulating terrain categories are all low relief; whereas rolling, moderately steep, and steep terrain categories are all high relief. This simple landform-descriptive scheme consisting of two, relatively general classes captures much of the statistical significance in the dependency of clutter strength on terrain slope, given the large spread within and little separation between more specific classes. In addition, this simple twofold scheme has the attendant advantage of liberating the user of these results from providing highly detailed descriptions of terrain. Such a simple twofold scheme is appropriate to a clutter model that aims to provide fundamental parametric trends on middle ground between the overly simple, in which preconceived ideas can lead to unrealistic parametric dependencies, and the overly complex, which can lead to much information without much significance and the loss of underlying unifying trends. Further implications of what lies behind this seemingly simple partition into low- and high-relief are discussed in Section 4.2.1.

Superficially, it may appear that terrain slope enters the current results only through specification of terrain relief as low or high. However, the further quantitative dependence of these results on depression angle also carries with it an implicit dependence on terrain slope. This implicit dependence is shown in the results of Figure 24, which plots terrain slope and depression angle for each of the six landform classes of Table 2. The terrain slope for each landform class shown in Figure 24 is the mid-range value between the minimum and maximum slopes allowed for that landform class. The depression angle for each landform class in Figure 24 is the mean of the depression angles from the set of Phase Zero patches of that landform class. It is apparent in Figure 24 that depression angle is positively correlated with terrain slope. That is, on the average, higher terrain slopes occur at higher depression angles. This results from the fact that steeper terrain provides higher positions at which to site the radar. This implicit relationship helps account for the strong dependence of clutter amplitude statistics on depression angle seen in the Phase Zero data. Discussion of this matter is continued in Section 4.1. Thus, results in this report take into account terrain slope, not in simplistic or idealized ways, but in practicable ways that have stood the test of trial in the empirical data of this study.

49

315027-24
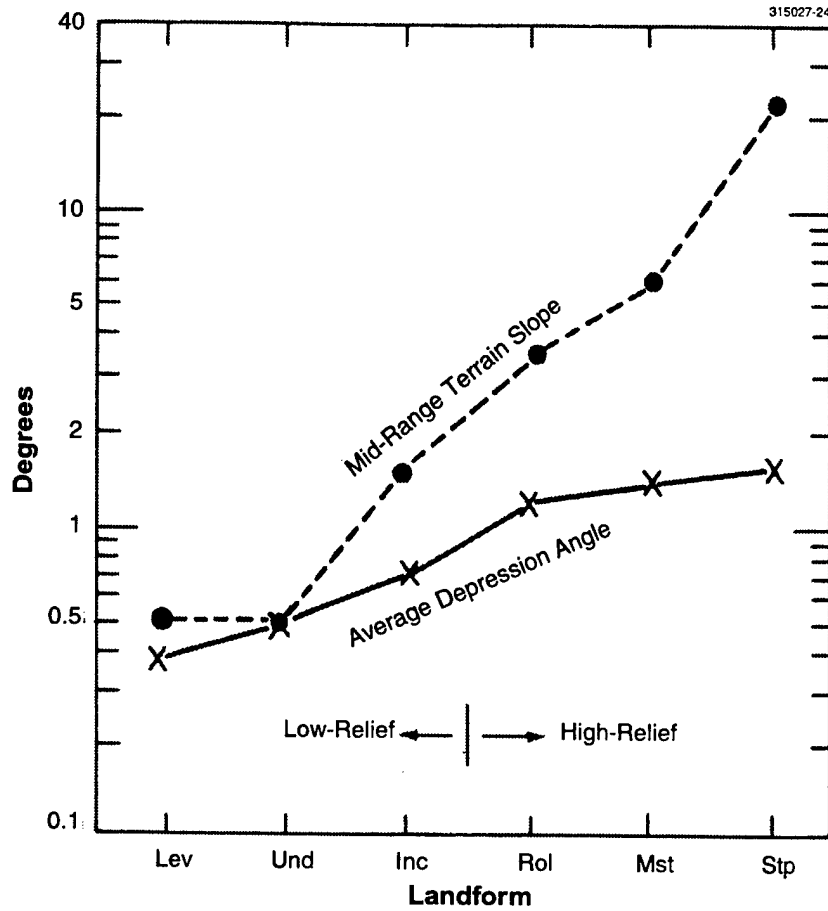
Notes: 1. See Table 2.
2. Based on 1850 Phase Zero (rural; positive
depression angle) patches from 86 sites, at ranges
between 2 and 12 km from the radar.

Figure 24. Average depression angle dependency on landform and terrain slope.

50

4. X-BAND CLUTTER SPATIAL AMPLITUDE STATISTICS

Section 4 provides modeling information for predicting ground clutter amplitude statistics applicable to spatial distribution over patches of visible terrain as seen by a surface-sited X-band radar. This information is arrived at by combining measurements from many similar Phase Zero patches into ensemble distributions of clutter amplitude statistics. By similar is meant patches of like-classified terrain type that are viewed at closely similar depression angles. Section 4 provides clutter strength modeling information for both general and various detailed levels of terrain classification.

In combining data from like-classified patches, the criterion for like-classification extends only to the primary or first-level classifier. The variations that occur in higher-order (second and third level) classifiers act as a cause of dispersion in the clutter statistics. Significant and useful parametric trends emerge over and above these complicating higher order terrain effects. Of course, one can occasionally choose to work only within the subset of pure patches that have only a primary classifier and do not require higher orders of classification; such studies can help in understanding specific influences. However, even when such influences are uncovered, the measure of their importance is whether they are generally observable. Thus, the main line of enquiry in Section 4 is inclusive of all the measured terrain as it realistically occurred, subsuming effects of terrain heterogeneity and higher-order classification.

In Section 4, empirical ensemble clutter amplitude distributions are plotted cumulatively against a nonlinear Weibull probability scale. Many of the resultant distributions are, to an engineering approximation, relatively linear as plotted on the Weibull scale, indicating that a Weibull distribution often provides a useful approximation to the measured data. Therefore, modeling information is provided in Section 4 in terms of Weibull coefficients defining the approximating Weibull distributions.

Modeling information is presented in Section 4 within a standard tabular format involving 1) terrain type, 2) depression angle, 3) Weibull coefficients of the approximating Weibull amplitude distribution, 4) measured mean strength of the ensemble amplitude distribution, 5) the percent of microshadowed cells (i.e., percent of cells at radar noise level) within the ensemble distribution, and 6) the number of clutter patches included in the ensemble. The three Weibull coefficients presented (any two of which define the distribution) are the Weibull shape parameter a_w, the Weibull median clutter strength $\sigma°_{50}$, and the Weibull mean clutter strength $\overline{\sigma°_w}$. The important characteristic of spread in the approximating Weibull distribution may therefore be readily observed, either directly in the a_w-parameter or in the mean-to-median ratio. The characteristic of average strength in the approximating Weibull distribution is directly observable as either the Weibull median or Weibull mean. In presenting the modeling information in terms of these three coefficients, one may directly observe what is regarded as the fundamental process in low-angle clutter, whereby with increasing depression angle and decreasing shadowing, spreads rapidly decrease and average strengths increase. The inclusion of measured ensemble mean strength in the tabularized modeling information allows an immediate first assessment of goodness-of-fit of the Weibull

51

approximating distribution to the actual distribution. The inclusion of number of patches in the ensemble allows a first assessment of how general the result might be.

The Weibull distribution has no intrinsic theoretical significance with respect to low-angle clutter amplitude distributions. It is used here because it provides a simple way to describe many of the effects observed in these distributions. For example, the Weibull distribution can accommodate very wide spread. Another useful characteristic of the Weibull distribution is that it degenerates to Rayleigh in the limiting case when its shape parameter becomes unity. This mirrors the behavior of actual measured clutter where, with increasing angle (up into airborne-like regimes) and decreasing shadowing (approaching zero at airborne-like angles), measured amplitude statistics also approach Rayleigh. This behavior also mirrors that of K-distributions arising out of theoretical investigations of low-angle clutter [12, 14]. For describing these amplitude distributions, which is the purpose here, Weibull distributions serve the purpose as well as K-distributions and are simpler to use.

The cumulative distributions presented in Section 4 are based on all the cells within patches including those at radar noise level[8] but are shown only for clutter strength levels above radar noise level. As a result, where shown these distributions accurately represent absolute percentile levels in clutter strength distributions independent of measurement radar sensitivity. Further discussion of this important matter is provided in Sections 4.1.1 and 4.2.1.

The results obtained in Section 4 depend somewhat on the techniques utilized for combining the individual measurements. Different ways exist for combining the data, each with advantages and disadvantages that need to be understood. This matter is discussed in Section 4.3.

Spatial amplitude statistics should ideally be based on a temporal mean clutter strength from each spatial resolution cell and the distribution of such temporal mean strengths over the many cells comprising a clutter patch. The Phase Zero instrument provided some temporal averaging for each spatial clutter sample, but it did not provide a well-defined temporal mean. Further information on how temporal variation enters Phase Zero processing is provided in Appendix B. The differences between temporal and spatial variations in low-angle clutter are profound, but the lack of a well-defined temporal mean in the Phase Zero data is of little statistical significance in the results.

A random process is stationary if it does not change its statistical properties in time. The amplitude of the clutter echo signal in the radar receiver is often highly nonstationary, both with increasing echo delay time for a given transmitted pulse and with increasing azimuth angle from pulse to pulse. This nonstationary behavior of the echo signal is the direct consequence of the heterogeneous character of landscape such that the physical nature of the actual backscattering clutter sources within a resolution cell vary considerably from cell to cell. These nonstationary variations of the echo signal in time occur because the spatial position of the active resolution cell is constantly changing in range and angle. Such spatially

---

[8] A few specific exceptions to this occur in Section 4.2.1. These exceptional results, which do not include cells within patches at radar noise level, are conspicuously labeled "shadowless."

induced variations of the received echo signal as the radar beam scans over the landscape are the basic subject of this report.

In contrast, one can consider the echo signal resulting from receiving the returns of many pulses from one fixed resolution cell. Temporal variation in this signal occurs only because of physical changes occurring with time in that particular cell (e.g., wind induced motion of leaves). Such temporally- induced variations of the received echo signal are often more stationary than spatially-induced variations, although they occasionally show evidence of singular major events in time separated by relatively event-free periods. The subject of temporally-induced variations in the received echo signal is not taken up in this report. Subsequent investigations of the subject based on Phase One data are reported elsewhere [1, 4–8].

The information provided in Section 4 is applicable for X-band at 75-m range resolution. Resolution is a fundamental parameter in low-angle clutter. Effects of resolution in the Phase Zero data are introduced in Section 4.5. In results based on Phase One data, resolution enters as a basic modeling parameter [1–4].

4.1 AMPLITUDE DISTRIBUTIONS BY DEPRESSION ANGLE FOR THREE GENERAL TERRAIN TYPES

Specified here is a basic model for spatial amplitude distributions of low-angle X-band ground clutter involving three general terrain types: 1) rural/low-relief, 2) rural/high-relief, and 3) urban. These three terrain types are described in Table 3 along with their relative incidences of occurrence. These terrain types comprehensively include all terrain, that is, any patch of terrain must be classified as one and only one of these three types. Thus, rural terrain includes such diverse specific terrain types as agricultural, forest, rangeland, wetland, and barren. Urban terrain includes any kind of built-up land, such as commercial, industrial, and residential. In terms of degrees of roughness of terrain surface, the classification system utilized incorporates the following specific categories: level, undulating, hummocky, inclined, broken, rolling, ridged, moderately steep, and steep. Low relief encompasses the first five categories, and high relief encompasses the last four. Note that the actual distributing of slopes that exist within a macroscale clutter patch is specified, not the overall slope of the best-fit plane through the patch.

In data reduction and analysis, X-band clutter amplitude distributions were formed from 2,177 clutter patches, each generally several kilometers on a side. For each patch detailed terrain descriptions at the specific level just described were determined. However, it was found that in the separation of clutter amplitude data into such specific terrain-descriptive classes, spread within class was broad, and separation between similar or neighboring classes was narrow. Thus, these findings led to the three general terrain classes of Table 3, which do provide significant and useful separation of X-band clutter data. A simple way of interpreting these three general terrain types is that only "mountains" (rural/high-relief) and "cities" (urban) grossly warrant separation from all other terrain types (rural/low-relief).

53

TABLE 3

Clutter Model Terrain Types and Relative Incidence

Terrain Type*	Relative Incidence* (Percent)
1. **Rural/Low Relief** (Slope <2°; relief <100 ft) Landform classes: 1, 2, 3, 5, 9 Land cover classes: 2, 3, 4, 5, 6, 7	72
2. **Rural/High Relief** (Slopes >2°; relief >100 ft) Landform classes: 4, 6, 7, 8 Land cover classes: 2, 3, 4, 7	22
3. **Urban** Land cover class: 1	6
*See Tables A-2 and A-3 for land cover and landform classes. **The relative incidence indicated is that of primary patch classification within the Phase Zero database of 2177 clutter patches at range between 2 and 12 km from the radar.	

Empirical ground clutter spatial amplitude distributions are presented in Figure 25 by depression angle for rural/low-relief terrain and rural/high-relief terrain. Similar results are presented in Figure 26 for urban terrain (in which the regime of the rural distributions is also shown lightly shaded for comparison). These distributions include all spatial samples within patches including cells at radar noise level, but are only shown over $\sigma°F^4$ regimes to the right of the highest noise-contaminated bin. Thus, where shown, these distributions are independent of Phase Zero sensitivity and represent what a theoretically infinitely sensitive radar would measure. It is seen that, within each of these three terrain types, the shape of the spatial amplitude distribution is strongly dependent on depression angle, such that there is a continuous rapid decrease in the spread of the distribution with increasing depression angle, even over the very small depression angles (usually <1.5° in low-relief terrain) associated with surface-sited radar. The distributions in Figures 25 and 26 are formed by combining like-classified clutter data from a large data set altogether comprising 2,177 clutter patch amplitude distributions obtained from measurements at 106 sites at ranges from 2 to 12 km from the radar. It is only by means of such extensive averaging that the smooth monotonic dependence of both strength (the distributions gradually move to the right with increasing angle) and spread (the slopes of the distributions gradually increase with increasing angle) emerge in these empirical

distributions to provide a general predictive modeling capability.[9] These underlying fundamental trends are often obscured by specific effects in individual measurements.

Weibull Scale
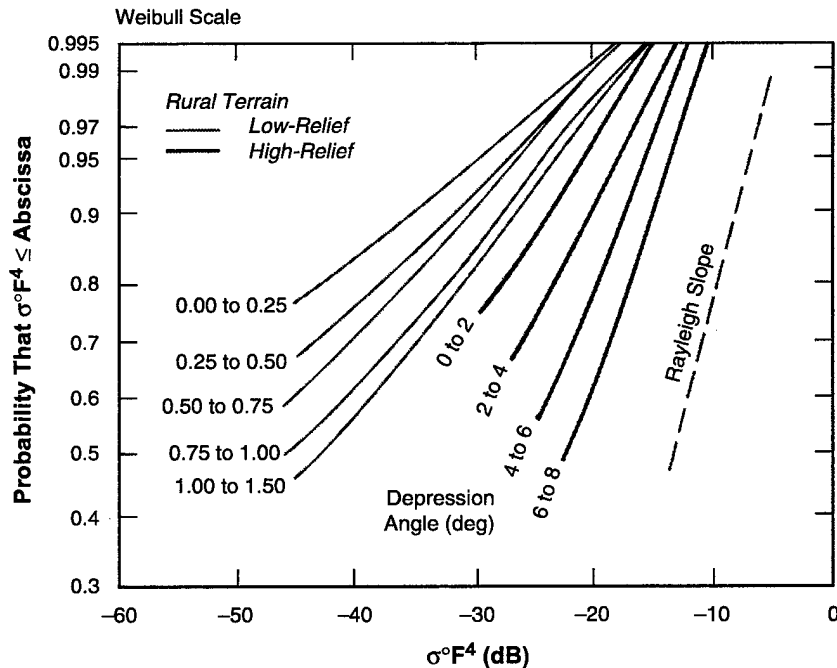
Figure 25. Cumulative ground clutter amplitude distributions by depression angle for rural terrain of low- and high-relief. Phase Zero X-band data, 75-m range resolution, horizontal polarization, 2- to 12-km range, 1743 patches, 87 sites.

Most (72% percent) of these measured data are contained in the rural/low-relief distributions of Figure 25. It is this parametric regime that is applicable to most surface radar situations and has traditionally been least well understood. The set of rural/low-relief distributions is extended in the rural/high-relief distributions (the latter accounting for 22% of the data), where higher depression angles are realized in high-relief terrain through higher site locations. Across the rural data set as a whole, the effect of continuously decreasing spread in the distributions with increasing angle is at the heart of understanding low-angle clutter as a physical phenomenon dominated by microshadowing. The highest angle distribution (6° to 8° depression angle) almost achieves the Rayleigh slope, which indicates that the amount of microshadowing is relatively small at such high airborne-like angles. The resultant nearly full illumination, as expected, provides approximately Rayleigh statistics. The urban distributions of Figure 26 (which contain 6% of the measured data) also show monotonically decreasing spread with increasing angle, but contain significantly stronger clutter than the corresponding rural/low-relief distributions. Ten percent of clutter patches were measured at negative depression angles; these data are discussed in Section 4.2.6.

---

[9] By "strength" is meant central tendency; by "spread" is meant statistical dispersion.
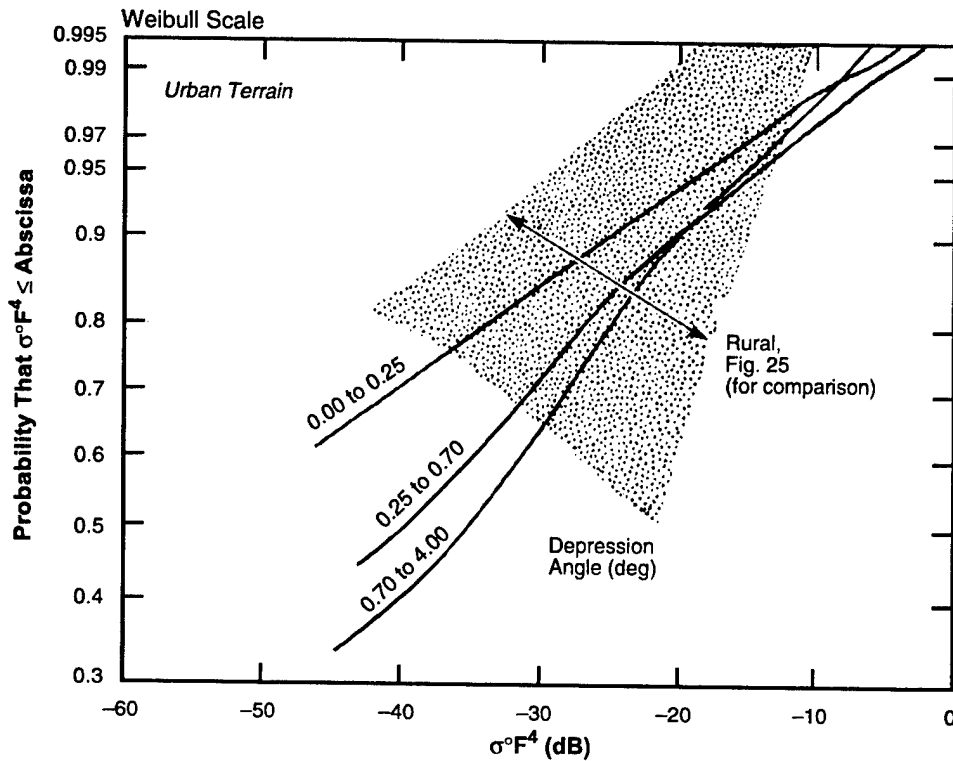
Figure 26. Cumulative ground clutter amplitude distributions by depression angle for urban terrain. Phase Zero X-band data, 75-m range resolution, horizontal polarization, 2- to 12-km range, 109 patches, 33 sites.

Note in Figure 25 that there is much less variation (less than 10 dB) in clutter strength from rural terrain with relief and depression angle at the cumulative probability level of 0.995 than at lower probability levels. As the cumulative distribution curves approach one another at high probability levels in Figure 25, they seem to be tending to closely coalesce at some high value beyond the graph, indicating that such strong low-occurrence clutter in rural terrain is relatively insensitive to relief and depression angle as it might be if it were emanating from large isolated discretes. If the distributions of Figure 25 simply continued on the plot linearly to very high clutter values, they would diverge again after their region of close coalescence, but in fact these distributions tend to roll to the right in the very high cumulative probability region beyond the graph of Figure 25. The matter of high-side tails in these distributions is further discussed in Section 4.1.3.

The high-relief distributions in Figure 25 are shown only in regions of relatively strong clutter. The shapes of the high-relief distributions in left-hand regions of relatively weak clutter depend on the accuracy of patch boundary specification. If DTED is assumed accurate enough to correctly distinguish between

56

visible and masked cells near patch boundaries in high-relief terrain, the high-relief distributions shown for regions of relatively strong clutter in Figure 25 are continued linearly to the left at the same slopes as are shown in Figure 25 to also cover regions of relatively weak clutter. The Weibull approximations given in the next section apply to such high-relief distributions covering both the relatively strong regions shown in Figure 25 and weaker regions to the left. If, however, DTED predicts high-relief visibility such that some cells near patch boundaries are actually shadowed and thus at radar noise level, the parts of high-relief distributions not shown in Figure 25 covering weaker clutter to the left have much shallower slopes than the parts for the strong clutter regions shown in this figure. This matter is further discussed in Section 4.2.1.

The distributions of depression angle at which Phase Zero clutter patches were measured, and separated into rural/low-relief, rural/high-relief, and urban components, are shown in Figure 27. For each of these four distributions, the maximum, 90-percentile, median, and minimum values of depression angle are also shown. Depression angle is a fundamental parameter in Phase Zero modeling investigations. It is the distributions shown in Figure 27, partitioned into appropriate contiguous intervals, that exert controlling influence on the data in Figures 25 and 26. The data in Figure 27 clearly indicate that depression angles to visible terrain for surface-sited radars are usually quite low (95, 90, and 50% of all depression angles at which Phase Zero patches were measured at ranges from 2 to 12 km occurred at less than 2.6°, 1.7°, and 0.43°, respectively). But the data of Figure 27 also show that depression angles in high-relief terrain range over significantly higher values than those in low-relief terrain (e.g., 95-, 90-, and 50-percentile values of 4.9°, 3.6°, and 0.89° versus 1.5°, 1.2°, and 0.38°, respectively).
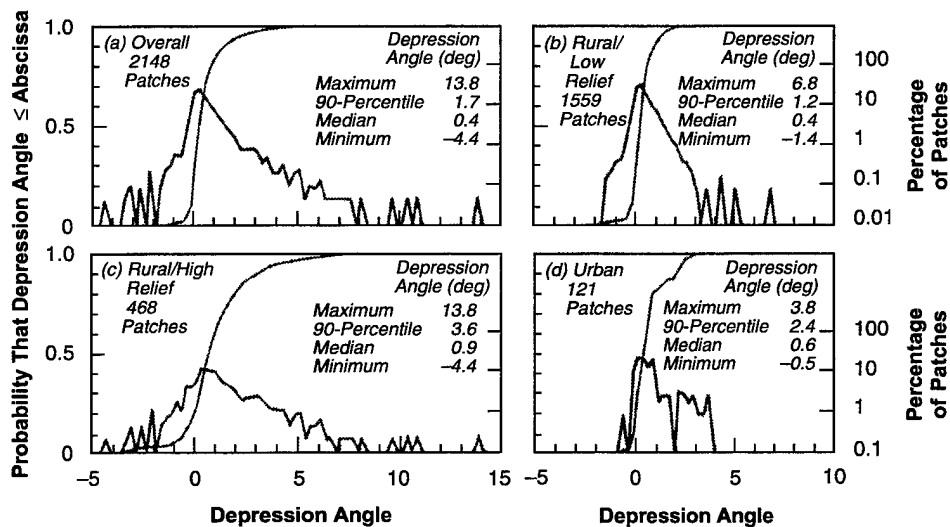
Figure 27. Distributions of depression angle at which clutter patches were measured. Phase Zero measurements, 96 sites, 2- to 12-km range.

57

The single highest depression angle at which a Phase Zero clutter patch was measured was 13.8° at the Equinox Mountain site in Vermont. The largest negative depression angle at which a Phase Zero clutter patch was measured was –4.4°, at the Waterton site in Alberta. The four highest depression angles at which urban patches were measured were between 3.4° and 3.7° at the Scranton, Pennsylvania site. Such extreme depression angles for surface radar represent relatively unusual situations.

Table 4 shows the relative frequency of occurrence of various primary landform classes within the depression angle regimes of the basic Phase Zero clutter model shown in Figure 25. In low-relief terrain, Table 4(a) shows that most patches present terrain slopes of less than 1°, but the percentage of patches presenting terrain slopes of up to 2° rises monotonically with depression angle, from 23 to 42 percent. In low-relief terrain, the discussion here is of differences in terrain slope on the order of 1° within depression angles of up to 1.5°. This is certainly a regime of small angles. In high-relief terrain, the angles increase, and the influence of terrain slope in the trend of clutter amplitude statistics with depression angle is stronger. Thus in high-relief terrain, Table 4(b) shows that even in the lowest depression angle regime, relatively high terrain slopes occur within 47% of patches. This proportion of patches with high terrain slopes increases strongly and monotonically with depression angle until it reaches 88% of patches in the highest depression angle regime. Thus, the data of Table 4 help provide understanding of the implicit effects of terrain slope in the Phase Zero clutter model, where high terrain slopes are more likely to occur at higher depression angles. This is not to say that a level patch cannot be observed at high depression angle, or that a steeply sloped patch cannot be observed at low depression angle. For example, the highest depression angle at which a "level" patch was measured was at the high Booker Mountain, Nevada site, where the radar looked down at a depression angle of 2.9° to a level desert valley floor. As a second example, the lowest positive depression angle at which a "steep" patch was measured was 0.006°, at the Dutch Corner, Pennsylvania site in the high ridges of the Allegheny Mountains, where the radar was on a relatively high site and looked out at grazing incidence to the high-relief forested upper slopes of the next ridge about 6.5 km away. Such limiting situations are of relatively infrequent occurrence. Section 4.4 shows strong parametric effects of depression angle on generalized mean and median land clutter strengths.

TABLE 4

Relative Frequency of Occurrence of Low and High Terrain Slopes* in Rural/Low-Relief Terrain and in Rural/High-Relief Terrain, by Depression Angle

a) Rural/Low-Relief Terrain (1325 patches)			b) Rural/High-Relief Terrain (391 patches)		
Depression Angle (Deg)	Terrain Slopes		Depression Angle (Deg)	Terrain Slopes	
	<1° (LEV or UND)	<2° (INC or HUM)**		2° to 5° (ROL)	2° to 35° (RID, MST, or STP)
0 to 0.25	.77	.23	0 to 2	.53	.47
0.25 to 0.5	.72	.26	2 to 4	.41	.59
0.5 to 0.75	.66	.30	4 to 6	.32	.68
0.75 to 1	.61	.37	6 to 8	.12	.88
1 to 1.5	.55	.42			

*As determined from primary landform classification; see Table A-3.

**A few (21) low-relief patches of primary landform classification equal to BRK, with terrain slopes between 1° and 5°, are deleted.

4.1.1 Weibull Parameters

The cumulative clutter amplitude distributions by depression angle for rural terrain of low- and high-relief and urban terrain shown in Figures 25 and 26 are to an engineering approximation observed to be relatively linear as plotted on the Weibull probability scale of these figures. A theoretical Weibull distribution plots as a straight line in these figures. The Weibull distribution is discussed in Appendix C, as is the methodology utilized here for obtaining Weibull approximations to measured distributions. The Weibull probability density function is given by Equation C-18 in Appendix C, which leads to the Weibull cumulative distribution function shown in Equation C-19. In Appendix C, x is used to represent $\sigma°F^4$ in units of m^2/m^2, and y is used to represent $10 \log_{10}x$ (see Equation C-1). Thus median and mean values of clutter strength are x_{50} and $\bar{x}$, respectively. In Section 4, in order to help the notation be self-interpretable, $\sigma°_{50}$ (dB) is used to represent the Weibull median value of clutter strength, i.e., $\sigma°_{50}$ (dB) = 10 $\log_{10}(x_{50})$, and, similarly, $\overline{\sigma°_w}$ (dB) is used to represent the Weibull mean value of clutter strength, i.e., $\overline{\sigma°_w}$ (dB) = 10 $\log_{10}(\bar{x})$. For Weibull statistics, the median $\sigma°_{50}$ and mean $\overline{\sigma°_w}$ are directly related as shown by Equation C-34. The Weibull shape parameter, a_w, is a dimensionless quantity indicative of the spread of the distribution. The shape parameter is sometimes referred to as the Weibull parameter, the slope

parameter, the spread parameter, or the skewness parameter. Occasionally in the technical literature, the inverse of a_w is used rather than a_w. For $a_w = 1$, the Weibull distribution degenerates to a Rayleigh distribution, which represents a lower bound on spread in clutter spatial amplitude statistics. Most of the Phase Zero empirical spatial amplitude distributions are approximated by values of shape parameter such that $a_w > 1$. The technical literature discussing Weibull distributions can be confusing, as a result of some authors discussing voltage distributions and others power distributions ($\sigma°$ is a power-like quantity), and also because a_w, $2a_w$, and $1/a_w$ are used similarly by different authors. The Weibull notation used here follows that of Boothe [15].

Section 4 characterizes or models measured Phase Zero empirical clutter amplitude distributions by means of the two Weibull coefficients, the Weibull shape parameter a_w and the Weibull median value of clutter strength $\sigma°_{50}$ (dB). These two coefficients entirely characterize the modeled distribution; from them the distribution can be easily visualized or sketched, and Weibull random numbers belonging to the modeled distribution can be generated. In addition, Section 4 provides $\overline{\sigma°}_w$ (dB), the value of mean strength in the modeled distribution. The Weibull mean strength $\overline{\sigma°}_w$ (dB) is provided to compare with the mean strength in the actual measured ensemble distribution as a first simple engineering measure of goodness-of-fit of the Weibull model to the measured data. Also, by including $\overline{\sigma°}_w$, the spread in the approximating distribution may be assessed by mean-to-median ratio, $\overline{\sigma°}_w$ (dB) minus $\sigma°_{50}$ (dB), as well as by the shape parameter a_w: Median levels of measured ensemble distributions may be read or estimated from their graphed cumulative distributions. Almost none of the measured distributions passed rigorous statistical hypothesis tests for Weibull on any other analytically representable statistical distribution that was tried.

Figure 28 shows five theoretical Weibull distributions plotted in the same manner as are plotted the empirical Phase Zero ensemble clutter amplitude distributions of Figures 25 and 26. All five of these theoretical distributions have the same median clutter strength, $\sigma°_{50}$ (dB) = –40, but have values of shape parameter a_w ranging from $a_w = 1$ to $a_w = 5$. Comparison of similar percentile levels over these five distributions indicates their extreme differences. For example, for the distribution with $a_w = 5$, one in a thousand samples is 50 dB stronger than $\sigma°_{50}$ (dB), whereas for the distribution with $a_w = 1$ (the Rayleigh degenerative case), one in a thousand samples is only 10 dB stronger than $\sigma°_{50}$ (dB). Clearly the shape parameter a_w of a ground clutter spatial amplitude distribution must strongly affect the false alarm statistics of a radar operating in that clutter. Use of equation C-34 shows that the distribution for $a_w = 5$ has a mean strength $\overline{\sigma°}_w$ (dB) of –11.25 dB, whereas the distribution for $a_w = 1$ has a mean strength of $\overline{\sigma°}_w$ (dB) of –38.41 dB, which is 27 dB weaker. In what follows, measured Phase Zero clutter amplitude distributions are characterized with the Weibull coefficients a_w and $\sigma°_{50}$ (dB). The modeled distributions so characterized may be quickly plotted as indicated in Figure 28.
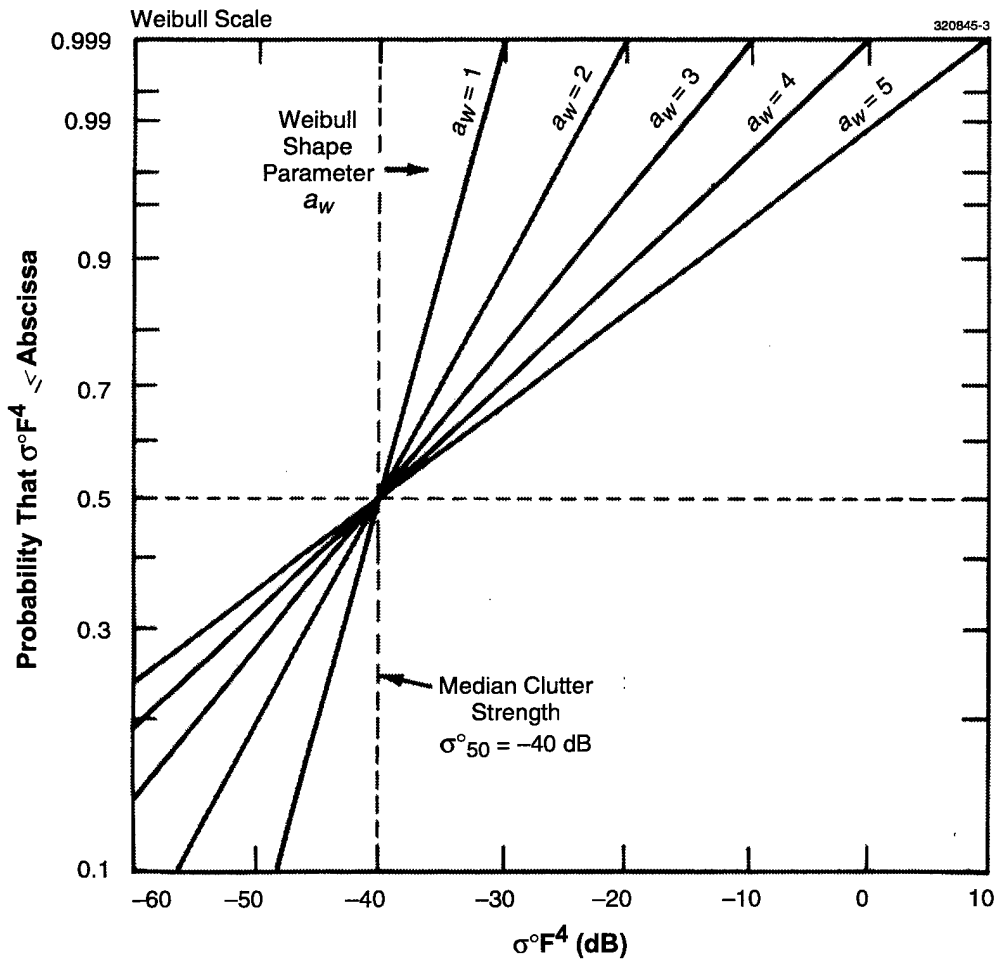
Figure 28. Five theoretical Weibull distributions.

Much of the information contained in the distributions of Figures 25 and 26 can be usefully approximated with Weibull statistics. Specific Weibull approximations for these ground clutter amplitude distributions are presented in Table 5, by depression angle for each of the three general terrain types. The table shows that large shape parameters at low angles rapidly diminish with increasing angle, approaching the Rayleigh value of unity at the highest angles. At the same time, median clutter strengths rapidly increase with increasing angle. Mean clutter strengths increase more gradually with increasing angle, so spread in terms of mean-to-median ratio is also observed to rapidly decrease with increasing angle. The measured mean clutter strength for each ensemble distribution is observed to closely match the mean

61

strength of the approximating Weibull distribution, a first engineering indication that laying a best-fitting Weibull straight line over central parts of each measured distribution of Figures 25 and 26 produces approximating distributions of reasonable mean strength. However, the measured ensemble mean strength is usually one or two dB stronger than the approximating Weibull mean strength. This is the result of the measured distributions of Figures 25 and 26 generally bending to the right at very high probability levels. The relatively few, very strong values of clutter that thus occur at a higher rate in reality than in their Weibull approximations are usually enough to increase measured mean strength by one or two dB. Also, Table 5 strongly indicates that shadowing is a major cause of the variations that are observed with depression angle. That is, the incidence of microshadowed cells varies from as much as 64% at grazing incidence in low-relief terrain to as little as 14% at high angle in high-relief terrain. The condensation and codification of properties of low-angle ground clutter within Weibull coefficients as presented in Table 5 represents the fulfillment of much of what was initially sought to be understood about the low angle clutter phenomenon.

In Table 5, rural/low-relief Weibull coefficients at high angle transition smoothly to rural/high-relief coefficients at low angle (e.g., compare a_w = 2.8 and $\sigma°_{50}$ = –40 dB at depression angle from 1.25° to 1.5° in low-relief terrain with a_w = 2.7 and $\sigma°_{50}$ = –39 dB at depression angle from 0° to 1° in high-relief terrain) This continuity suggests that the differences in the measured data have to do with illumination angle and terrain slope, not on intrinsically different backscattering properties between low- and high-relief terrain. In contrast, the Weibull coefficients of Table 5 indicate a significant intrinsic difference in backscattering properties between rural and urban terrain.

The Weibull mean clutter strength $\overline{\sigma°_w}$ (dB) and the Weibull median clutter strength $\sigma°_{50}$ (dB) are different from the actual mean and median clutter strengths in the measured Phase Zero ensemble distributions. The Weibull mean and median strengths are applicable to the analytic Weibull distribution that comes about by fitting a straight line to a measured ensemble distribution in plots like Figures 25 or 26. In particular, because of sensitivity limitations, the actual median strength in the measured ensemble distribution is often corrupted by radar noise. As such, it represents only an upper bound to the true ensemble median and is usually much greater than the approximating Weibull median. For this reason, actual median strengths in measured ensemble distributions are not tabulated.

The depression angle regimes are narrower and more numerous in Table 5 than in Figures 25 and 26. This reflects the fact that the parametric trend with depression angle is significant even for small steps of depression angle.

62

TABLE 5

Statistical Attributes of X-Band Ground Clutter Amplitude Distributions For Rural/Low-Relief Terrain, Rural/High-Relief Terrain, and Urban Terrain, by Depression Angle

Phase Zero X-band data, 75-m range resolution, horizontal polarization, 2- to 12-km range.
Also see Figs. 25 and 26.

Terrain Type	Depression Angle (deg)	Weibull Parameters			Ensemble Mean Clutter Strength $\overline{\sigma°F^4}$ (dB)	Percent of Samples above Radar Noise Floor	Number of Patches
		a_w	$\sigma°_{50}$ (dB)	$\overline{\sigma°_w}$ (dB)			
Rural/ Low-Relief	0.00–0.25	4.8	−60	−33	−32.0	36	413
	0.25–0.50	4.1	−53	−32	−30.7	46	448
	0.50–0.75	3.7	−50	−32	−29.9	55	223
	0.75–1.00	3.4	−46	−31	−28.5	62	128
	1.00–1.25	3.2	−44	−30	−28.5	66	92
	1.25–1.50	2.8	−40	−29	−27.0	69	48
	1.50–4.00	2.2	−34	−27	−25.6	75	75
Rural/ High-Relief	0–1	2.7	−39	−28	−26.7	58	176
	1–2	2.4	−35	−26	−25.9	61	107
	2–3	2.2	−32	−25	−24.1	70	44
	3–4	1.9	−29	−23	−23.3	66	31
	4–5	1.7	−26	−21	−22.2	74	16
	5–6	1.4	−25	−21	−21.5	78	9
	6–8	1.3	−22	−19	−19.1	86	8
Urban	0.00–0.25	5.6	−54	−20	−18.7	57	25
	0.25–0.70	4.3	−42	−19	−17.0	69	31
	0.70–4.00	3.3	−37	−22	−24.0	73	53

4.1.2 Overall Distribution

Figure 29 shows the overall cumulative clutter amplitude ensemble distribution resulting from combining individual measurements from all 2,177 Phase Zero clutter patches into one distribution. This overall distribution is plotted cumulatively in Figure 29 on a Weibull probability axis which shows much more of the top tail of the distribution, up to 0.999999 on the probability axis, compared to the upper limit defined by 0.995 on the probability axis for most of the other distributions shown in Section 4. For cumulative probabilities below about 0.995, the overall distribution is reasonably well fit by a linear

Weibull approximation with shape parameter a_w equal to about 3.9. However, this overall distribution has an upper tail at higher probabilities greater than 0.995 approximated by a much larger shape parameter a_w equal to about 7.
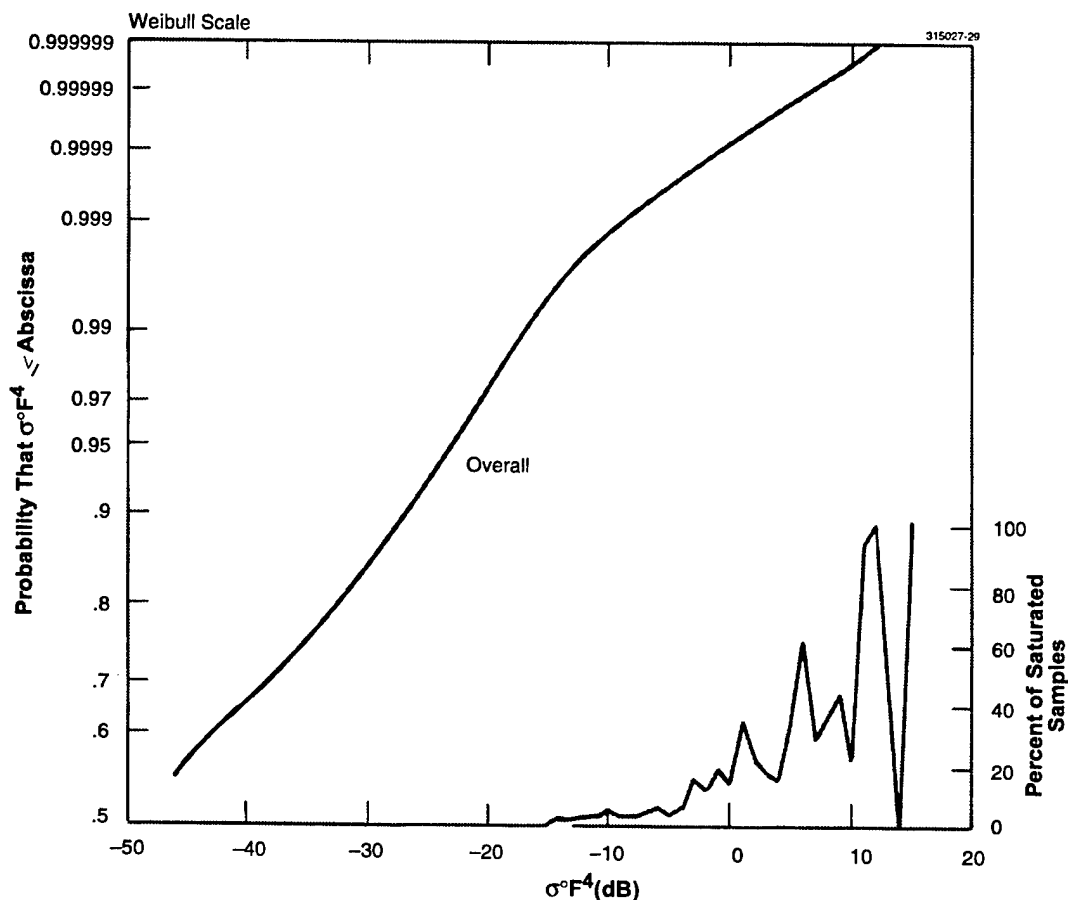
Figure 29. Overall cumulative ground clutter amplitude distributions. Phase Zero X-band data, 75-m range resolution, horizontal polarization, 2- to 12-km range, 2177 clutter patches, 96 sites.

This upper tail of strong clutter values of increased spread compared with the central part of the distribution is likely due to occasional strong localized discréte scattering sources on the landscape such as water towers and feed storage silos. Such objects are larger and of less frequent occurrence than the myriad smaller discrete objects acting as sources for the central part of the distribution. Thus, there exists some distinction between large and small discretes. Many of the empirical Phase Zero clutter amplitude distributions show evidence of containing an upper tail similar to that of the overall distribution of Figure 29. The basic Phase Zero clutter model does not contain this feature of a high tail of strong clutter values

with increased spread compared with the central part of the distribution. This high tail is very linear on the Weibull scale. The distribution of these relatively infrequent, widely ranging, strong clutter values, is well approximated for cumulative probability > 0.999 with Weibull parameters $a_w = 7$ and $\sigma°_{50} = -80$ dB.

The incidence of saturation in the Phase Zero measurements is shown in Figure 29. It is evident that the high-side tail in the overall distribution of Figure 29 is significantly affected by saturation, increasingly so with increasing clutter strength. The effect of saturation is to underestimate the high-side tail. The true uncontaminated high-side tail must extend to higher strengths and be of greater spread than indicated by the data of Figure 29.

A Weibull fit to the central part of the overall distribution of Figure 29 can be used to represent the general spatial amplitude distribution of low-angle X-band land clutter, irrespective of depression angle and terrain type. The Weibull parameters of this general distribution are given in Table 6. The relative linearity of the central part of the overall distribution in Figure 29 indicates that this Weibull approximation is reasonable, and this is borne out by the close comparison between the Weibull and actual ensemble mean clutter strengths in Table 6. Note that, in actuality, the central part of the overall distribution in Figure 29 is slightly concave upward, indicating that the a K-distribution might provide a slightly better fit. An approximating lognormal distribution would provide a worse fit.

TABLE 6

Statistical Attributes of Rural/Low-Relief, Rural/High-Relief, Urban, and Overall Ground Clutter Amplitude Distributions

Phase Zero X-band data, 75-m range resolution, horizontal polarization,
2- to 12-km range, 2177 patches. Also see Figs. 29 and 30.

Terrain Type	Weibull Parameters*			Ensemble Mean Clutter Strength $\overline{\sigma°F^4}$ (dB)	Percent of Samples above Radar Noise Floor	Number of Patches
	a_w	$\sigma°_{50}$ (dB)	$\overline{\sigma°_w}$ (dB)			
Overall	3.9	−48	−28.4	−27.6	53	2177
Rural/ Low-Relief	3.9	−51	−31.4	−29.7	52	1584
Rural/ High-Relief	2.3	−34	−26.1	−25.3	64	471
Urban	3.8	−41	−22.4	−19.7	68	122
*For cumulative probability < 0.999						

The overall amplitude distribution is now partitioned into component distributions corresponding to each of the three general terrain types, rural/low-relief, rural/high-relief, and urban. The resultant distributions are shown in Figure 30. Statistical attributes for these three ensemble distributions are also shown in Table 6. These three distributions can be used in non-site-specific ground clutter modeling where the overall terrain at a site is simply categorized as one of the three general types. The increased spread in the high tail of the overall distribution caused by large discrete objects is mirrored in both the rural/low-relief and high-relief distributions in Figure 30. At higher probabilities (>0.9999) in the high tails, there is no distinction between the rural/low-relief and rural/high-relief distributions, further supporting the conjecture that large discrete objects cause these tails. The urban distribution also has a high tail with increased spread that extends to lower probability levels than do the high tails in rural terrain. The effects of saturation cause an obvious break in slope in the high tail of the urban distribution.
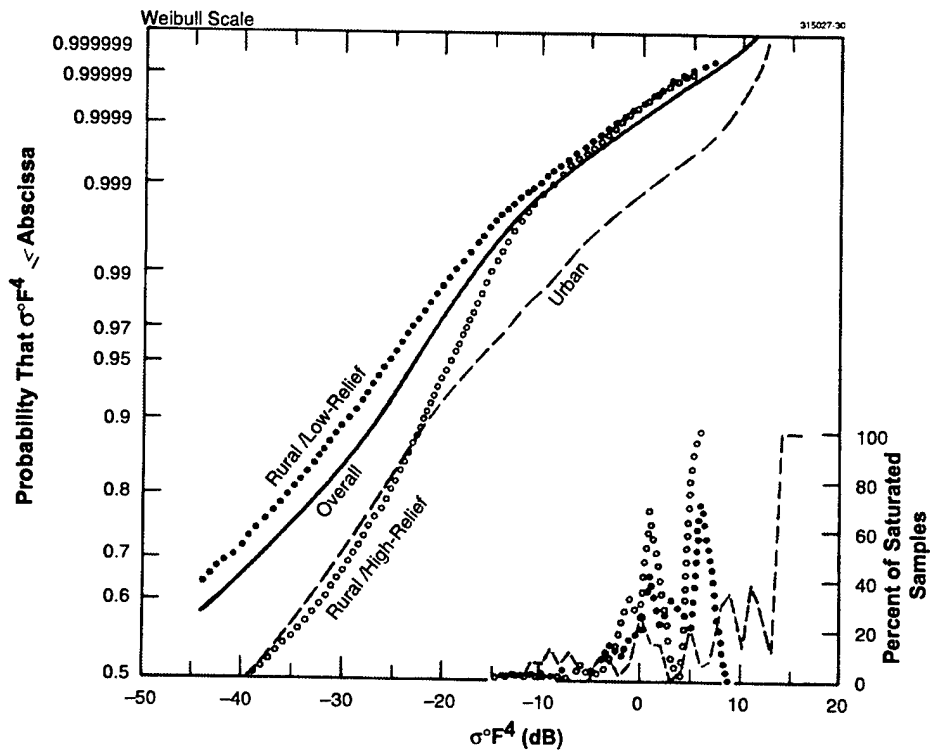
Figure 30. Cumulative ground clutter amplitude distributions for rural/low-relief terrain, rural/high-relief terrain, urban terrain, and the overall combination of all three terrain types. Phase Zero X-band data, 75-m range resolution, horizontal polarization, 2- to 12-km range, 2177 clutter patches. Also see Table 5.

66

4.1.3 High Distribution Tails

The high tails of the rural terrain amplitude distributions of the basic Phase Zero clutter model partitioned by depression angle are shown in Figure 31. The distributions by depression angle for low-relief terrain are shown at the top in Figure 31, and those for high-relief terrain are shown at the bottom. The data in Figure 31 are the high ends of the same distributions shown at lower probability levels in Figure 25. Linear extrapolation of the distributions in Figure 25 suggests a region of coalescence and cross-over at higher probability levels. For low-relief terrain, the upper part of Figure 31 shows that these distributions all roll to the right to assume the increased spread seen in the overall results of Figure 30, with little cross-over. For high-relief terrain, the lower part of Figure 31 shows that the distributions for zero to 2° and 2° to 4° also roll to the right with a cross-over, but the distributions for 4° to 6° and 6° to 8° do not roll to the right but stay relatively linear on the Weibull scale to the highest probability levels shown. This suggests that at low angles in high-relief terrain, effects of large discrete objects are still evident, but that at high enough angles effects of large discretes become much less evident. That is, at high angles in high-relief terrain, it is less probable to receive spectral-like broadside flashes from discrete vertical objects than is the case at lower angles in high-relief terrain or in low-relief terrain in general. The high tails shown in Figure 31 are of interest because of their effects in causing false alarms in surface-sited radar operating in ground clutter.

67
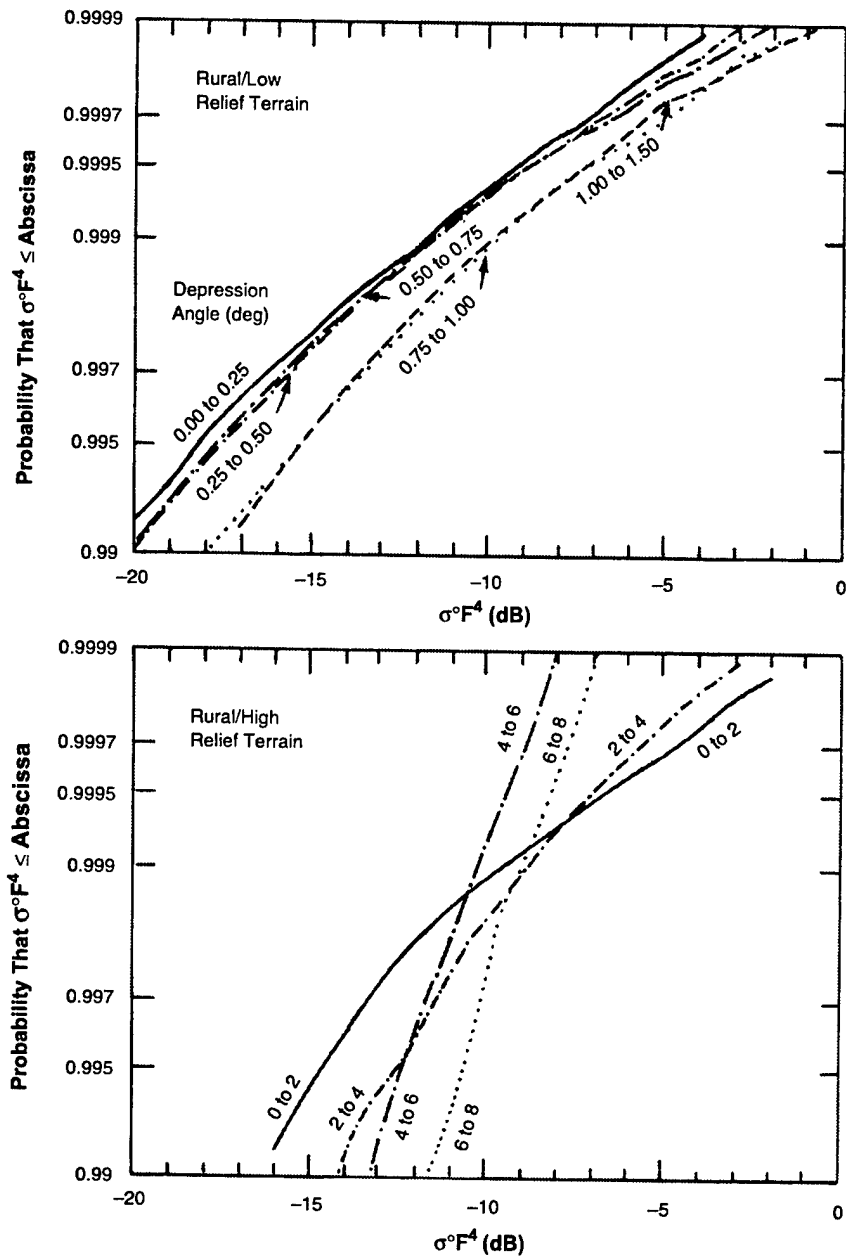
Figure 31. High tails of cumulative ground clutter amplitude distributions by depression angle for rural terrain of low- and high-relief. Phase Zero X-band data, 75-m range resolution, horizontal polarization, 2- to 12-km range, 1743 patches, 87 sites. Also see Figure 25.

4.2 CLUTTER RESULTS FOR MORE SPECIFIC TERRAIN TYPES

The basic Phase Zero ground clutter model of Section 4.1 is based on only three general terrain types. Although Weibull statistics and three terrain types are enough to show fundamental trends in low-angle clutter, the resultant basic construct cannot contain all the complex higher-order attributes of the real phenomenon. Section 4.2 illustrates how increasing fidelity in terrain descriptive information can reveal higher-order trends in clutter statistics.

4.2.1 Mountain Clutter

Besides needing information describing general clutter strengths, an analyst may also need to know something about worst-case situations. Provided here is additional specific information on how strong mountain clutter can become. Also discussed is the frequent existence of bi-modal amplitude distributions in high-relief terrain.

Clutter Patches at Plateau Mountain. The steepest roughest terrain from which Phase Zero ground clutter was measured was that of the Canadian Rocky Mountains. One site, Plateau Mountain, is a flat-topped mountain site high in the Rockies, to which road access was available for the truck-borne clutter measurement equipment. From Plateau Mountain, the view to the west is of steep barren rock faces from high peaks in the Rockies. The lower slopes of these mountains are often tree-covered with the trees gradually thinning out at the higher elevations. A photograph looking west from Plateau Mountain is shown in Figure 1(b). The measured Phase Zero clutter map for 12-km maximum range at Plateau Mountain is shown in Figure 32. The clutter patches selected within 12-km range at Plateau Mountain are also shown in Figure 32. Measured clutter amplitude distributions from the five strongest of these Plateau Mountain clutter patches are included in Figure 33. Descriptive information and mean clutter strengths for these five patches are provided in Table 7. In Figure 33, the regime of the rural distributions of the basic Phase Zero clutter model is shown lightly shaded for comparison. Also shown lightly shaded for comparison in Figure 33 is the strongest Phase Zero urban clutter patch amplitude distribution.

First consider patches 4/4, 4/5, 5/1, and 5/2. These four mountain patches represent very strong ground clutter. In terms of mean clutter strength, the strongest patch measured at Plateau Mountain was patch 4/4, at –9.6 dB, approximately 10-dB stronger than the strongest mean clutter from general rural terrain in Table 7. In perusing Table 7, it is seen that all four of these patches are of steep barren mountain peaks with various incidences of trees on their lower slopes and observed at various depression angles. Mean clutter strengths from these four patches range from –9.6 to –10.8 dB. Taken together, these four patches may be thought of as representing a worst-case (i.e., strongest clutter) for rural terrain.

Altogether at Plateau Mountain, there were 43 patches carrying primary landform classification of "steep." The average strength of these patches was –21.2 dB. Their average depression angle was +2.7°. The basic Phase Zero clutter model of Table 5 predicts mean clutter strength $\sigma^°$ of –24 or –25 dB for depression angle of 2.7° in high-relief terrain. Of course, steep terrain is the extreme case of high relief. A

69

3-dB increase in this predicted value of –24 or –25 dB comes very close to the average Plateau Mountain mean strength.

The other Phase Zero Rocky Mountain site was at Waterton, Alberta. At Waterton, the radar was set up on the high prairie in southern Alberta just a few kilometers east of steep mountain terrain. The area around Waterton is characterized by an abrupt transition from prairie to mountains without an intermediate forested foothills region. This situation is illustrated in the photograph of Figure 34. At this low Waterton site, the first range of mountains screened other peaks further west from view. As a result, only four patches carrying primary landform classification of steep existed at Waterton. Their average strength is –22 dB. The average depression angle to these four Waterton patches was –2.8° (i.e., the radar looked up to this steep terrain).

(a)
Phase Zero X-Band Clutter Map

(b)
Clutter Patch Selection
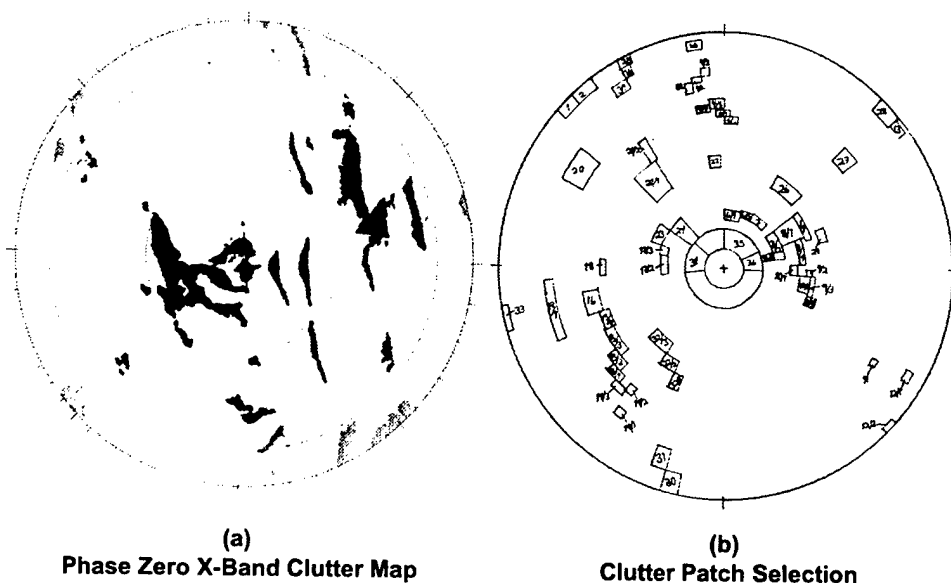
Figure 32. Measured ground clutter map and patches at Plateau Mountain. Maximum range = 11.8 km, north is zenith, clutter is black, clutter threshold is 3 dB from full sensitivity. See Figure 1(b), Figure 33, and Table 7.

70
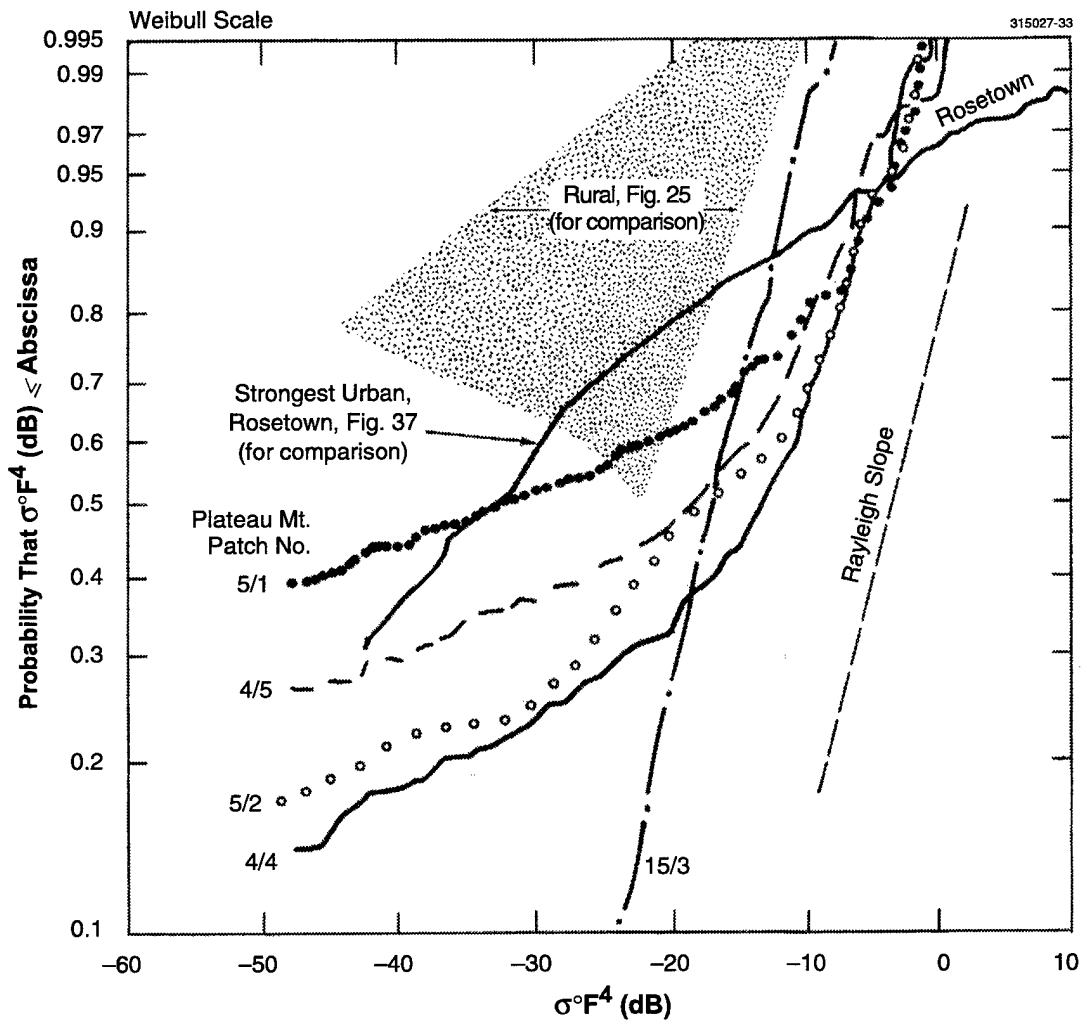
Figure 33. Ground clutter cumulative amplitude distributions for five patches containing strong clutter from the Rocky Mts. Phase Zero X-band data, Plateau Mt. site, 12-km maximum range experiment, 75-m range resolution, horizontal polarization. See Table 7.

71

TABLE 7

Descriptions and Statistical Attributes of the Five Strongest X-Band Clutter Patches* at Plateau Mt.

Phase Zero X-band data, 75-m range resolution, horizontal polarization. See Fig. 33.

Patch Number	Mean Clutter Strength of Patch $\overline{\sigma°F^4}$ (dB) Including Samples at Radar Noise Floor[4]	Excluding Samples at Radar Noise Floor[5]	Number of Spatial Samples in Patch	Percent of Samples above Radar Noise Floor	Depression Angle (deg)	Landform[1]	Land Cover[2]	Percent Tree Cover η [3]
4/4	−9.6	−9.0	264	86	1.6	8	7	$30 < \eta \le 50$
4/5	−10.8	−9.5	336	74	0.6	8	7	$30 < \eta \le 50$
5/1	−10.8	−8.7	216	62	1.2	8	7	$3 < \eta \le 10$
5/2	−9.8	−9.0	264	84	0.8	8	7	$1 < \eta \le 3$
15/3	−16.2	−16.1	784	99.5	2.2	8	41	$\eta > 50$

[1] 8 = steep, Table A-3
[2] 7 = barren, 41 = deciduous forest, Table A-2
[3] See Table 16
[4] "Shadowed upper bound," App. C
[5] "Shadowless," App. C

* Except for patch 15/3, these patches all include exposed rock and near vertical rock faces at mountain summits; in patch 15/3, the terrain constitutes forested slopes (still steep) at lower elevations.

72
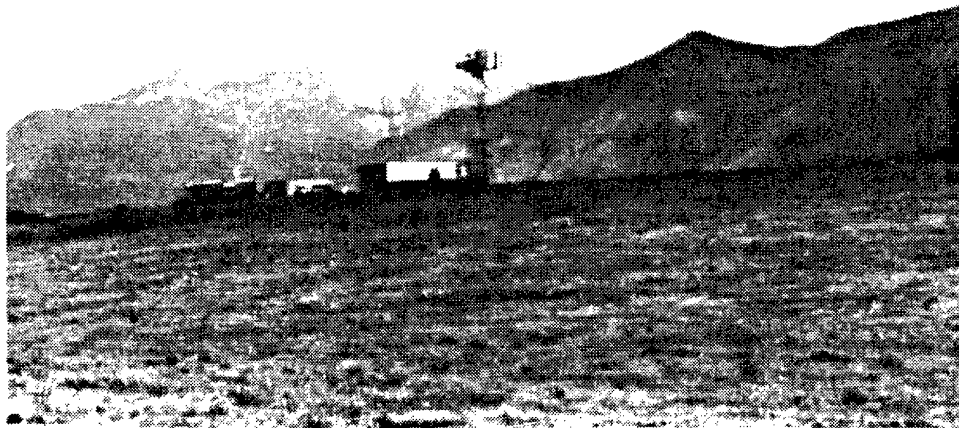
Figure 34. Mountainous terrain at Waterton, Alberta. Viewing direction is southwest. The Phase One equipment is visible on site. June.

The clutter amplitude distributions from the four Plateau Mountain patches, patches 4/4, 4/5, 5/1, and 5/2, in Figure 33 are bi-modal, by which is meant that each distribution is widely spread out over relatively weaker clutter strengths, but much tighter over the strongest clutter strengths. In the cumulative plots of Figure 33, each of these four distributions consists of two parts, a shallowly sloped part to the left and a steeply sloped part to the right. Mountain terrain is highly complex. Strong returns from relatively uniform rock faces oriented toward the radar are close to Rayleigh distributed. However, there are many other physical possibilities for the contents of visible resolution cells in mountain terrain, accounting for a large number of returns of widely spread out strength, all non-shadowed and well above minimum radar sensitivity. These returns from physically complex cells account for the shallow parts of the distributions to the left in Figure 33. Physically complex high-relief cells generally could not be distinguished from uniformly steep high-relief cells in Phase Zero patch specification. For example, at the terrain scale (1:50,000) at which Phase Zero terrain description work was performed, the four patches under discussion are quite small, of spatial dimensions from a few mm to a cm or so, on maps and air photos. But the preceding interpretation of high-relief bi-modal distributions was validated at one site, Blue Knob, where a steep ridge occurred running linearly across the field-of-view of the site. An original patch was specified in the region where the line-of-sight of the radar was normal to the line of the ridge and the contour lines rising up the ridge. The bi-modal amplitude distribution from this original patch specified on the steep side of the ridge at Blue Knob was separated under smaller, more precise, multiple patch specification into a

73

Rayleigh distribution from a central area of uniform steep planar surface and several highly spread out distributions from more complex surrounding areas.

Consider next the distribution for patch 15/3 in Figure 33. Patch 15/3 also has a left-side shallow portion in its distribution, but it appears at cumulative probabilities below 0.1. Table 7 indicates that patch 15/3 is a steep forested patch rather than a steep barren patch and that it was observed at a relatively high depression angle of 2.2 degrees. The mean strength of the clutter in patch 15/3 is −16.2 dB. The distribution for patch 15/3 in Figure 33 is seen to have a slope very close to the Rayleigh slope. Other indications that patch 15/3 provides close to Rayleigh statistics are that it has the following statistical attributes: ratio of standard deviation-to-mean = 0.15 dB; ratio of mean-to-median = 0.85 dB; ratio of 90 percentile-to-median = 4 dB; ratio of 99 percentile-to-median = 8 dB. Corresponding Rayleigh values are 0 dB, 1.6 dB, 5.2 dB, and 8.2 dB, respectively.

If more precise patch specification completely avoided shadowed cells, what then would be the worst-case clutter strengths that an analyst should assign to mountain terrain? A first answer is provided by the "shadowless" mean strengths given in the third column of Table 7. The shadowless mean clutter strength is computed as the mean strength from the subset of cells within the patch above radar noise level. It is seen that avoidance of shadowing raises mean strengths by less than one or two dB for the patches shown in Table 7. Generally, use of shadowless statistics must be approached cautiously since they are dependent on the particular sensitivity of the measurement radar.

Additional High-Relief Modeling Information. Many of the high-relief patches have bi-modal amplitude distributions like patches 4/4, 4/5, 5/1, and 5/2 in Figure 33. As a result, the high-relief cumulative ensemble clutter amplitude distributions in the basic clutter model of Figure 25 are also bi-modal. The high-relief ensemble distributions of Figure 25 only show the right-side steep parts of the distributions, and are truncated at the left, at the point of onset of the left-side shallow part of the distribution. In Table 5, the Weibull distributions approximating the right-side steep parts of the distributions in Figure 25 closely match the measured ensemble mean strengths inclusive of their shallow-sloped parts, indicating that mean clutter strength in high-relief terrain is controlled by the right-side steep parts of the amplitude distributions.

The complete rural/high-relief cumulative ensemble amplitude distributions for the basic Phase Zero clutter model are shown in Figure 35, including both the right-side steep parts of the distributions previously shown in Figure 25 (shown lightly in Figure 35) and the left-side shallow parts of the distributions at strengths greater than the maximum noise-contaminated $\sigma°F^4$ bin (shown heavily in Figure 35). As in the right-side steep parts of these distributions, the left-side shallow parts also continue to show a strong trend with depression angle. The data in Table 8 help to provide an understanding of this trend. These data show that, as angle increases, shadowing (i.e., percent of noise samples) decreases, but the proportion of samples in the right-side steep parts of the distributions increases at about the same rate, leaving the proportion of complex samples in the left-side shallow parts of the distributions at a relatively fixed value of about one-third, independent of depression angle. Approximating Weibull parameters for the left-side shallow parts of the rural/high-relief distributions of Figure 35 are given in Table 9.
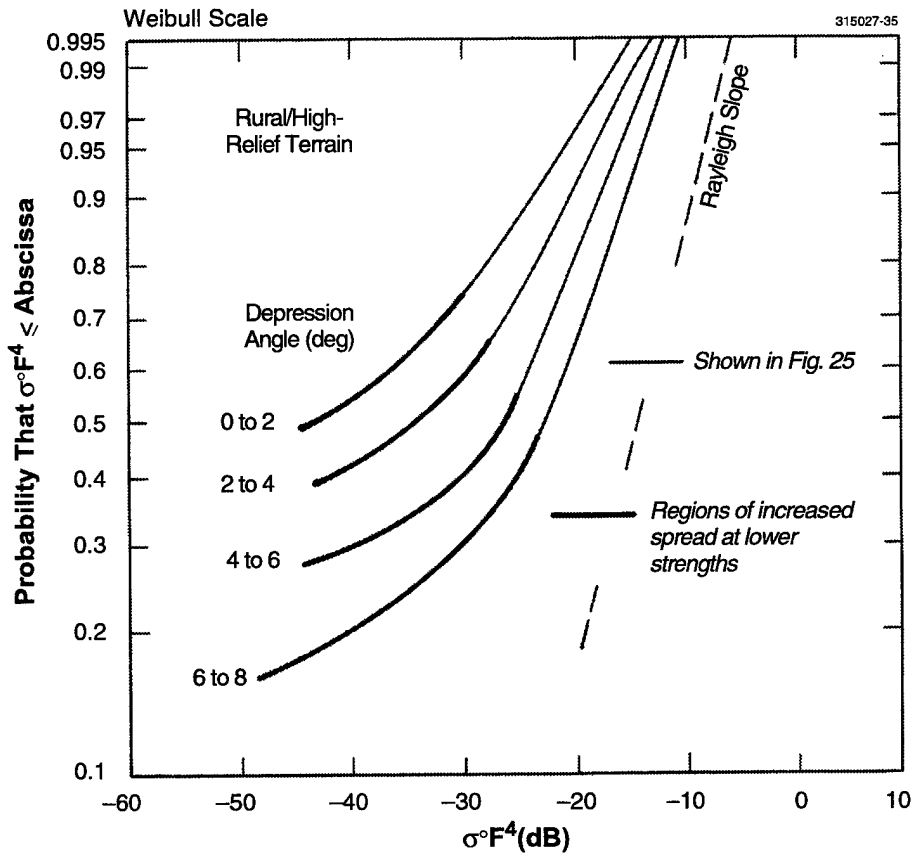
Figure 35. Cumulative ground clutter amplitude distributions by depression angle for rural/high-relief terrain showing regions of increased spread at lower clutter strengths. Phase Zero X-band data, 75-m range resolution, horizontal polarization, 2- to 12-km range, 391 patches, 52 sites.

75

TABLE 8

Relative Proportions of Samples in Noise, Right-Side Steep, and Left-Side Shallow Parts of High-Relief Clutter Amplitude Distributions

Depression Angle (deg)	Percent of Samples at Radar Noise Level = x (see Table 5)[1]	Percent of Samples in Right-Side Steep Part of Dist'n = y (see Fig. 35)[2]	Percent of Samples in Left-Side Shallow Part of Dist'n = z (see Fig. 35)[3]	Ratio of No. of Left-Side Shallow Samples to Total Number of Shadowless Samples[4]
0 to 2	40	27	33	0.55
2 to 4	32	34	34	0.50
4 to 6	24	43	33	0.43
6 to 8	14	52	34	0.40

[1] 100 minus "percent of samples above radar noise floor" = x
[2] (x minus break-point cumulative probability) x 100 = y
[3] [100 - (x + y)] = z
[4] z ÷ (z + y)

TABLE 9

Approximating Weibull Parameters for the Left-Side Shallow Parts* of High-Relief Clutter Amplitude Distributions

Depression Angle (deg)	Weibull Parameters		Applicable for Cumulative Probability < x
	a_w	σ°_{50} (dB)	
0 to 2	10	−42	x = 0.56
2 to 4	10	−28	x = 0.48
4 to 6	10	−10	x = 0.39
6 to 8	10	+1	x = 0.27

*These data assume piece-part Weibull fits in two parts, a left-side shallow part and a right-side steep part. Weibull parameters for the right-side steep parts for cumulative probability ≥ x are given in Table 5.

76

The ensemble distributions of Figure 35 include all of the samples within patches including these at radar noise level. Given that patch boundaries remain fixed as selected, these are current distributions. They show percentile levels independent of radar sensitivity. If sensitivity is imagined to increase without limit, the only effect in these distributions is to extend them further to the left; the parts above radar noise level shown in Figure 35 remain unaffected. In low-relief terrain, this is certainly the correct approach, since in low-relief terrain microshadow is distributed throughout the patch and is partly the result of low-reflectivity geometrically visible cells, and partly the result of actual fine-scaled geometric shadowing effects associated with fine detail in landform and land cover.

In high-relief terrain, however, it is much more the case that every geometrically visible cell contributes discernible clutter. Furthermore, in high-relief terrain, use of DTED to predict geometrically visible cells is more reliable because relative variations in terrain elevation are much greater (shadow boundaries are caused by macrofeatures, not microfeatures). Thus, it can be argued that more precise specification of patch boundaries, under the criterion that only geometrically visible cells be included, can rid high-relief amplitude distributions of noise-level cells, since the noise-level cells in such distributions largely come from the outer edges of patches near shadow boundaries.

Rather than attempting to respecify high-relief patches to more accurately avoid peripheral geometrical shadow, the same result can be obtained by removing measured noise level cells from the distributions. The resultant shadowless distributions are shown in Figure 36. The differences between the distributions of Figure 36 and those of Figure 35 are dramatic. Removing shadow has straightened the distributions on the Weibull scale. Each distribution in Figure 36 is well approximated by a single Weibull distribution, compared to the piece-part Weibull fits required of the distributions in Figure 35. Such approximations are provided in Table 10. In these shadowless Weibull approximations, a continuous trend of decrease in spread and increase in strength with increase in angle is observed. Figure 36 no longer shows a strong distinction between left-side shallow (physically complex) samples and right-side steep (uniform rock face) samples, although it is important to realize that the shadowless distributions still contain all of both kinds of samples. The cumulative probability level separating the two kinds of samples is computed in the right-most column of Table 8 and shown as a tic mark on each distribution in Figure 36. Airborne clutter measurements conducted at Lincoln Laboratory indicate that, at higher angles with essentially no shadowing, amplitude statistics from rural terrain become approximately Rayleigh. The shadowless distributions of Figure 36 are observed to be approaching continuity with the airborne results in that, as their shape parameters approach unity with increasing angle, they too approach Rayleigh distributions. On the whole, these shadowless high-relief ensemble distributions are more attractive for use in clutter modeling than the more complicated distributions of Figure 35.
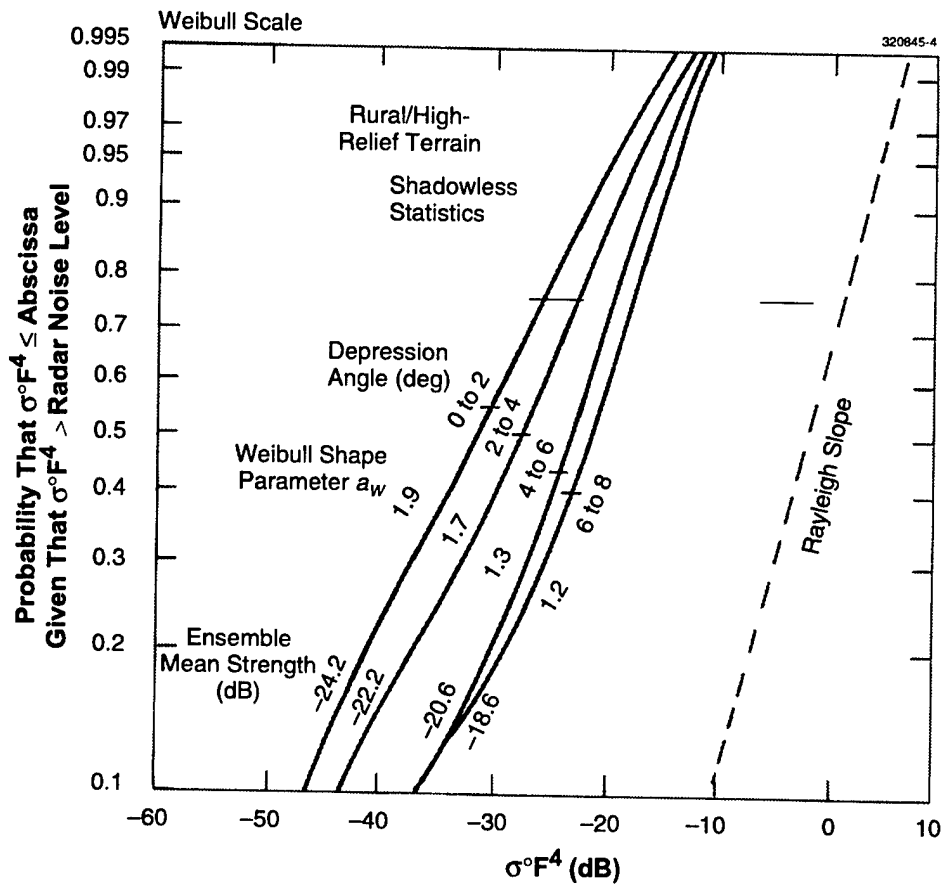
Figure 36. Shadowless cumulative ground clutter amplitude distributions by depression angle for rural/high-relief terrain. Phase Zero X-band data, 75-m range resolution, horizontal polarization, 2- to 12-km range, 391 patches, 32 sites.

78

TABLE 10

**Statistical Attributes of Shadowless Ground Clutter Amplitude Distributions for Rural/
High-Relief Terrain by Depression Angle**

Phase Zero X-band data, 75-m range resolution, horizontal polarization, 2- to 12-km range.
Also see Fig. 36 and Table 5.

Depression Angle (deg)	Weibull Parameters			Ensemble Shadowless Mean Clutter Strength* $\sigma°F^4$(dB)
	a_w	$\sigma°_{50}$	$\sigma°_w$	
0 to 2	1.9	−31	−25.4	−24.2
2 to 4	1.7	−28	−23.4	−22.2
4 to 6	1.3	−23	−20.3	−20.6
6 to 8	1.2	−21	−18.7	−18.6
*The mean of only those samples above radar noise level, computed in m^2/m^2 and subsequently converted to dB.				

The foregoing discussion has provided a deeper understanding of the distinction between low- and high-relief terrain in low-angle clutter. This distinction is not an arbitrary separation by terrain roughness and steepness as at first encountered in the mean clutter strengths presented in Figure 23. Rather, the distinction relates to shadowing. Low-relief terrain is characterized by large nearly-level regions of general geometric visibility, as would be predicted by standard DTED, in which cells containing discrete vertical sources causing strong returns are interspersed with weak cells—either shadowed or visible but discrete-free. In such circumstances, the idea of adjusting patch boundaries to avoid geometrically shadowed cells and predict every discrete is unrealistic. High-relief terrain is characterized by highly-sloped regions of general geometric visibility in which almost all cells return discernible clutter. In high-relief terrain, the distinction between cells with and without discretes is less apparent, and the idea of adjusting patch boundaries to contain only visible cells might become realistic with modest future improvements in DTED. Crossing the boundary between these two kinds of terrain actually crosses the classical boundary between the low-angle phenomenon traditionally associated with ground-based radar and the high-angle phenomenon traditionally associated with airborne radar. Of course, this boundary or transition region is gradual and should not be rigidly interpreted. But the boundary is clearly crossed in transitioning from the single-mode low-relief curves of Figure 25 to the bi-modal high-relief curves of Figure 35.

In modeling clutter amplitudes in high-relief terrain, the steep right-side parts of the distributions of Figures 25 and 35 illustrate the fundamental trend with depression angle that a basic model should incorporate.

This assumption is supported by the shadowless distributions of Figure 36 which indicate that more precise tailoring of patch boundaries to include only visible regions would largely remove the shallow left-side parts of these distributions shown in Figure 35.

4.2.2   Urban Clutter

The basic Phase Zero clutter model of Section 4.1 provides general information describing clutter amplitude distributions for urban terrain. Besides such general information, an analyst may wish to know how severe urban clutter might become in a worst-case situation. This section provides some information on this subject by showing clutter patch amplitude distributions for several of the strongest urban patches measured by Phase Zero. These strong urban patches are compared with the strong mountain patches discussed in Section 4.2.1.

Figure 37 shows measured cumulative amplitude distributions for three urban clutter patches. The regime of the general urban ensemble distributions from Figure 26 is shown lightly shaded in Figure 37 for comparison. Table 11 shows terrain descriptions, depression angles, and mean clutter strengths for these three patches. These three urban distributions constitute backscatter measurements made from the town of Rosetown, Saskatchewan (population 2,500); the city of Lethbridge, Alberta (population 55,000); and the city of Calgary, Alberta (population 600,000), respectively. All three urban areas exist on the relatively low-relief Canadian prairies. In each case, the patch was selected to include only relatively high commercial buildings within the urban complex, in contrast to lower outlying residential areas. Differences in clutter strength between commercial and residential urban clutter are discussed subsequently.

Although the data in Figure 37 are from three commercial patches, their physical differences are great. Rosetown is a small prairie town, providing services to the local agricultural community. Its commercial sector is physically very small but includes grain elevators illuminated at low depression angle. The mean clutter strength of –4.6 dB for the Rosetown patch is the single strongest mean clutter strength that exists within the database of 2,177 Phase Zero patch measurements. However, this Rosetown patch is not particularly exceptional—there are many other relatively small, relatively strong clutter patches from small prairie towns, often including grain elevators. The small Rosetown patch extended from 8,360 m to 8,740 m in range. Clutter strengths decreased relatively quickly with increasing range into the patch, from +3 dB in early range gates to levels between –25 and –30 dB in the last range gates.

Weibull Scale   315027-37
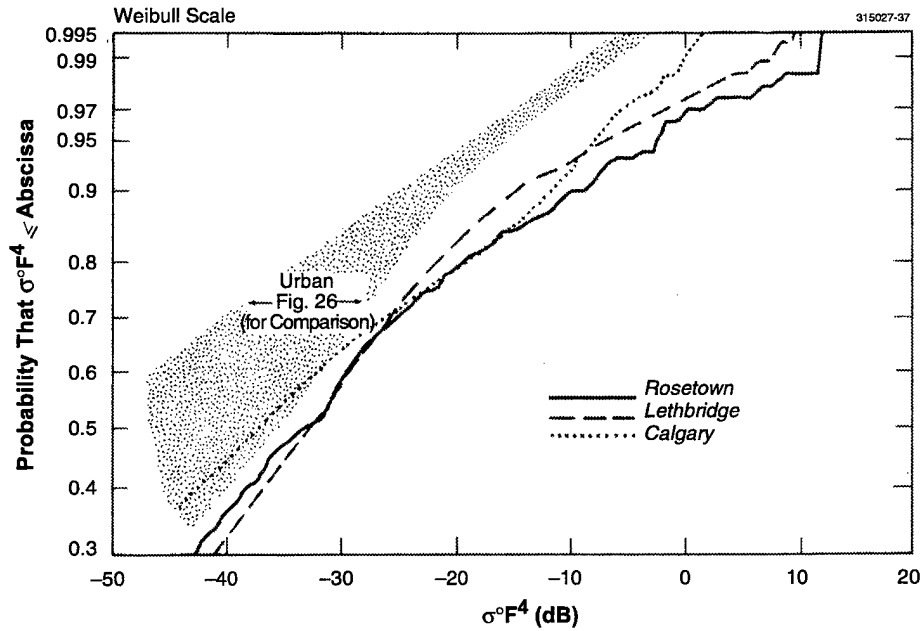
Figure 37. Ground clutter cumulative amplitude distributions for three patches containing strong urban clutter. Phase Zero X-band data, 75-m range resolution, horizontal polarization, 12-km maximum range experiment. See Table 11.

TABLE 11

Descriptions and Statistical Attributes of Three Urban Clutter Patches
at X-Band

Site	Patch Number	City or Town	Mean Clutter Strength of Patch $\overline{\sigma°F^4}$ (dB)[1]	Number of Spatial Samples in Patch	Percent of Samples above Radar Noise Floor	Depression Angle (Deg)	Landform[2]	Land Cover[3]	Percent Tree Cover η[4]
Rosetown North[5]	13/2	Rosetown	−4.6	384	77	0.18	1	12	$1 < \eta \le 3$
Lethbridge West[6]	12	Lethbridge	−5.1	3066	74	0.29	1	12	$1 < \eta \le 3$
Strathcona[7]	7	Calgary	−13.4	6328	70	1.21	1–3	12-11-51	$1 < \eta \le 3$

[1] "Shadowed upper bound," App. C
[2] 1 = level; 3 = undulating; Table A-3
[3] 12 = commercial; 11 = residential; 51 = streams, canals; Table A-2
[4] See Table 16
[5] Commercial sector of Rosetown.
[6] Industrial section, some open development land, TV tower
[7] Downtown Calgary, high rise buildings, Bow River and parks near river, railroad, some residential (minor)

81

With small enough specification of patch size, mean patch clutter strength can increase to arbitrarily high levels. Thus, it may be preferable to base the worst-case urban clutter strength estimate on larger urban patches than Rosetown, allowing for much more extensive statistical averaging to take place within the distributions. Lethbridge is a moderate-sized regional city in southern Alberta. The industrial area constituting its urban clutter patch is approximately ten times larger than Rosetown but, as was the Rosetown patch, is illuminated at quite low depression angle. Notwithstanding the substantial physical differences in these two patches, their clutter amplitude distributions and mean clutter strengths are very similar. The Calgary patch in Figure 37, extending from 5.9 to 10 km in range and 13 degrees in azimuth, is approximately twice as large as the Lethbridge patch. Calgary is a major city, and the Calgary patch was selected to include, for the most part, just its high-rise central urban core. Thus, the Calgary patch is quite different, physically, from both the Lethbridge and the Rosetown patches. At Calgary, the radar position was on a hill in the outskirts of the city, 490 ft higher than the average terrain height at the city center. Thus, the depression angle at which the radar viewed the ground at the city center was substantial, 1.2°, although the highest buildings in the city core were more than 500 ft high. The hill-top location may have resulted in less multipath augmentation and in many surfaces being illuminated at more oblique angles than the near-grazing-incidence illumination at Rosetown and Lethbridge, and may be the cause of the somewhat weaker mean clutter strength for Calgary compared with Rosetown and Lethbridge.

Taken together, these three distributions provide a reasonable indication of how strong urban clutter can become. Compared with the general urban distributions of Table 5, the data in Table 11 indicate that worst-case urban clutter can be 10-dB stronger in mean strength than general urban levels. This is approximately the same conclusion reached about severe mountain clutter compared with more general high-relief clutter. Severe urban mean clutter strength (Rosetown, Table 11) can be 5-dB stronger than severe mountain mean clutter strength (Plateau Mountain, patch 4/4, Table 7). The Rosetown urban clutter amplitude distribution is included lightly in Figure 33 to compare with mountain distributions.

In considering urban clutter, attention has been restricted to relatively strong urban clutter from commercial sectors. Considered now are the differences in urban clutter strength between residential sectors (expected to be weaker) and commercial sectors (expected to be stronger). Table A-2 indicates that within the general land cover class of urban, the more specific subclasses of residential and commercial are employed. All the measured clutter amplitude distributions from patches classified by land cover as residential were combined into one ensemble amplitude distribution, and all measured distributions from patches classified by land cover as commercial were combined into another ensemble amplitude distribution. These two clutter amplitude distributions for urban terrain of residential and commercial character, respectively, are shown in Figure 38. The regime of the rural amplitude distributions of the basic Phase Zero model is also shown lightly shaded in Figure 38 for comparison. Statistical attributes for the residential and commercial ensemble distributions are shown in Table 12. These two distributions are quite similar in shape but are horizontally displaced from one another indicating that clutter from commercial urban sectors is several dB stronger than clutter from residential urban sectors at most percentile levels. In terms of mean clutter strength, Table 12 indicates that clutter from commercial sectors is 3.4-dB stronger than clutter from residential sectors. This may be regarded as a general result based on measurements from many clutter patches.

82
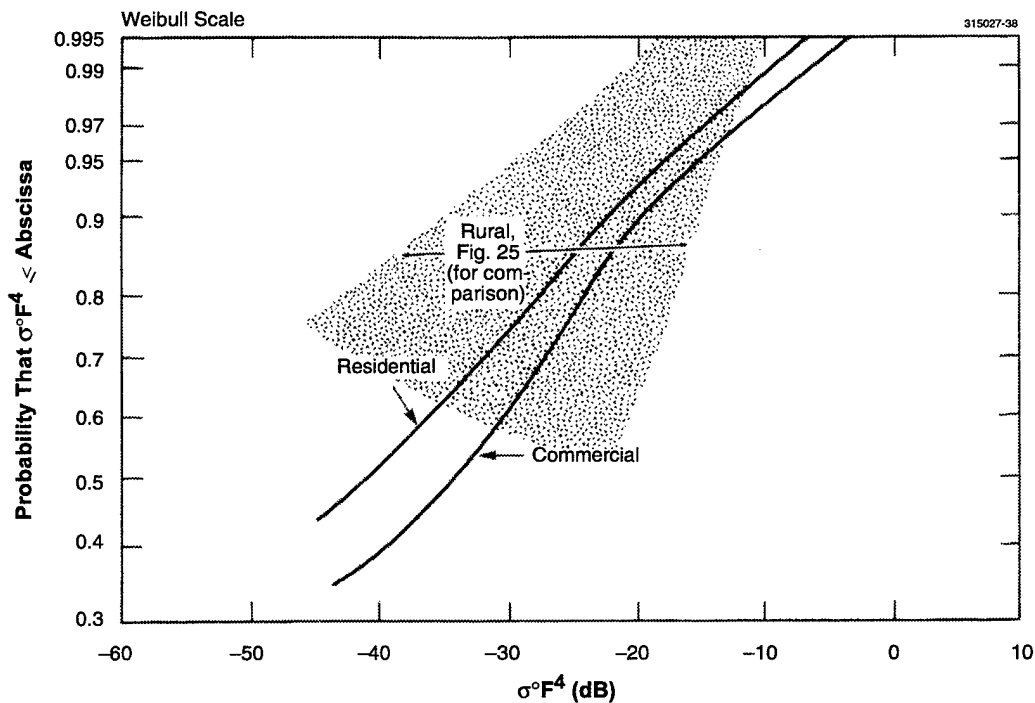
Figure 38. Comparison of cumulative ground clutter amplitude distributions for urban terrain of residential character and urban terrain of commercial character. Phase Zero X-band data, 75-m range resolution, horizontal polarization, 2- to 12-km range, 113 patches, 33 sites. Also see Table 9.

TABLE 12

Statistical Attributes of Urban Residential and Commercial Ground Clutter Amplitude Distributions

Phase Zero X-band data, 75-m range resolution, horizontal polarization, 2- to 12-km range. Also see Fig. 38.

Terrain Type	Weibull Parameters			Ensemble Mean Clutter Strength $\overline{\sigma°F^4}$ (dB)	Percent of Samples above Radar Noise Floor	Number of Patches
	a_w	$\sigma°_{50}$ (dB)	$\overline{\sigma°_w}$ (dB)			
Urban/ Residential	3.9	−42	−23	−21.1	67	85
Urban/ Commercial	3.6	−36	−19	−17.7	74	28

83

4.2.3 Wetland Clutter

Figure 39 shows cumulative distributions of mean clutter strength from measured Phase Zero patches for four distinctive terrain types, namely, wetland, rural/low-relief, mountains, and urban. Figure 39 shows distributions of mean strengths, not amplitude distributions within patches. The data in Figure 39 are reduced and displayed similarly to the data shown in Figure 23, which show distributions of mean clutter strength by landform. The data of Figure 39 strongly reinforce the position that mountain clutter and urban clutter stand significantly apart from most other clutter (i.e., rural/low-relief clutter). At the median position in Figure 39, mountain clutter and urban clutter are both about 10-dB stronger in clutter patch mean strength than rural/low-relief clutter. The distribution of mean clutter strength from wetland patches is included in Figure 39 with the expectation that wetland might be a terrain type for which clutter would be generally weaker than that provided by the basic Phase Zero model. Indeed, Figure 39 shows that, at the median level, wetland clutter patches are about 5-dB weaker in mean clutter strength than rural/low-relief patches. This decrease is less dramatic than the increases associated with mountain and urban clutter.
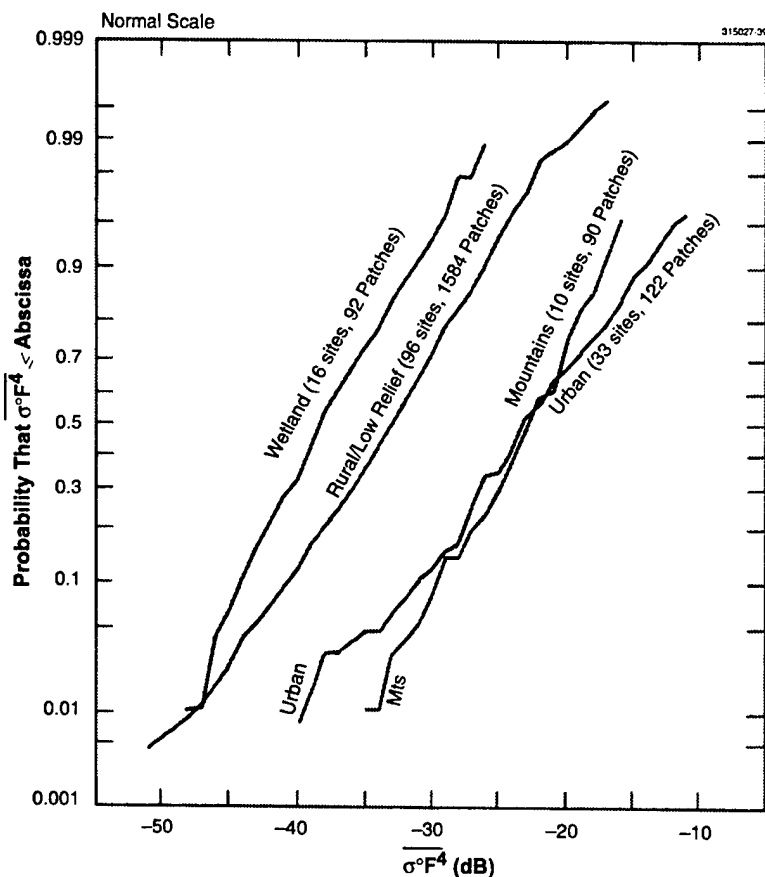
Figure 39. Cumulative distributions of mean ground clutter strength for four distinctive terrain types. Phase Zero X-band data, 75-m range resolution, horizontal polarization, 2- to 12-km range, 1796 patches, 96 sites. Each curve shows the cumulative distribution of mean clutter strengths from all patches of a given terrain type, one value of mean strength per patch.

84

Table A-2 indicates that wetland is separated into forested wetland (class 61) and non-forested wetland (class 62) in the land cover classification scheme utilized. Patches of trees often occur on wetland terrain. About half of Phase Zero wetland patches are mixtures of various proportions of forested and non-forested wetland. Only about one-quarter of all Phase Zero wetland patches are pure forested or pure non-forested. Thus, in thinking about backscatter from general wetland, it is necessary to think as much in terms of clumps of trees and tree lines as in terms of level reed- or sedge-covered marshland or open water conditions. As mentioned previously, the primary land cover category of wetland should not be overly-simplistically interpreted.

All of the Phase Zero wetland clutter patch amplitude distributions are now combined into ensemble amplitude distributions in four regimes of depression angle as shown in Figure 40. The regime of the rural amplitude distributions of the basic Phase Zero clutter model is shown lightly shaded in Figure 40 for comparison. Statistical attributes for these four wetland ensemble distributions are shown in Table 13. These four wetland ensemble distributions are now compared with the rural/low-relief distributions of the basic Phase Zero model (see Figure 25 and Table 5) at similar depression angles. There is considerable overlap of the wetland ensemble distributions with the rural/low-relief ensemble distributions, compared with the separation of the mean patch clutter strengths of these terrain types in Figure 39. In Figure 40, the wetland ensemble distributions only separate out as being substantially weaker than the rural/low-relief ensemble distributions at the higher percentile levels—it is the higher percentile levels that control the mean. Comparing ensemble mean clutter strengths (Tables 5 and 13), rural/low-relief terrain is about 5-dB stronger than wetland in the first three depression angle regimes. In the fourth depression angle regime, 0.75° to 1°, the ensemble mean clutter strength from wetland terrain is almost equal to that from rural/low-relief terrain.

In comparing the data of Figures 25 and 40, it is seen that the spreads in the wetland ensemble distributions are much less than those in rural/low-relief ensemble distributions at corresponding depression angles. This is quantified in comparing the Weibull shape parameter in Tables 5 and 13, which is about an integer or so higher for the rural/low-relief distributions than for the corresponding wetland distributions. Less spread in clutter amplitude statistics from wetland terrain indicates that wetland is more homogeneous than rural/low-relief terrain in general. This is partly due to the fact that wetland is predominantly level terrain. (See Gull Lake West discussion in Section 3.3.) The decreased spread in wetland amplitude statistics is also partly due to less heterogeneity of land cover.

All specific terrain types provide clutter distributions which, when studied in detail, show some differing attributes, and judgement is required as to whether such differences warrant separation of that specific terrain type within the wide variations that can occur within general terrain types. Because of the general overlap of wetland ensemble amplitude distributions with the corresponding rural/low-relief distributions, little motivation exists for separating wetland as a specific weak-clutter terrain category in the basic Phase Zero clutter model.

Figure 40. Cumulative ground clutter amplitude distributions by depression angle for wetland terrain. Phase Zero X-band data, 75-m range resolution, horizontal polarization, 2- to 12-km range, 75 patches, 16 sites. Also see Table 13.

TABLE 13

Statistical Attributes of Wetland Ground Clutter Amplitude Distributions, by Depression Angle

Phase Zero X-band data, 75-m range resolution, horizontal polarization, 2- to 12-km range. Also see Fig. 40.

Depression Angle (deg)	Weibull Parameters			Ensemble Mean Clutter Strength $\overline{\sigma°F^4}$(dB)	Percent of Samples above Radar Noise Floor	Number of Patches
	a_w	$\sigma°_{50}$ (dB)	$\overline{\sigma°_w}$ (dB)			
0.00 – 0.25	3.6	−56	−38	−37.0	49	35
0.25 – 0.50	3.1	−50	−37	−35.6	52	29
0.50 – 0.75	3.0	−47	−34	−34.7	63	6
0.75 – 1.00	2.3	−38.5	−31	−29.6	75	5

86

4.2.4 Level Terrain

The basic Phase Zero clutter model of Section 4.1 is based on separating terrain into only three general terrain types, rural/low-relief, rural/high-relief, and urban. It can be difficult to categorize terrain much more specifically than this in an X-band clutter model because terrain is so variable that spread within class can overwhelm separation between classes. However, level terrain as a specific landform category is a special simplifying case in which variability in land-surface form is not a factor. Level terrain represents a canonically simple landform that provides the opportunity to isolate and understand better the parametric dependencies generally at work in low-angle clutter. Since within level terrain only variability in land cover exists to introduce spread in clutter statistics, generality can be reached with the fewer samples within class that are available when the Phase Zero data are separated within a three-dimensional matrix consisting of a number of categories each of depression angle, landform, and land cover.

In what follows, clutter data are combined from all patches of a specified primary terrain classifier, landform or land cover, including those patches with variation occurring in second- and third-level classifiers. That is, the ensemble results shown include terrain that is heterogeneous in higher-order classifiers, not just pure terrain for which patches carry only primary classifiers. Twenty-six percent of Phase Zero patches have primary landform classification of level. Ensemble clutter amplitude distributions for level terrain formed from these level patches are now shown for two quite different commonly occurring land cover classes, forest and agricultural, each as a function of depression angle.

First consider level forest. All of the Phase Zero clutter measurements from patches of level forest (as classified at the primary level) were combined into ensemble amplitude distributions in three regimes of depression angle. The results are shown in Figure 41. Statistical attributes for these three level forest ensemble distributions are shown in Table 14. The regime of the rural ensemble distributions from Figure 25 is shown lightly shaded in Figure 41 for comparison. In the data of Figure 41 and Table 14, a strong trend with depression angle is observed, even over the small range (from 0 to 1.5°) of depression angle shown. With increasing depression angle, spreads in clutter amplitude statistics from level forest rapidly decrease, and mean strengths rapidly increase. Compared with clutter amplitude statistics from rural/low-relief terrain at similar depression angles, clutter statistics from level forested terrain have significantly less spread (i.e., much smaller Weibull shape parameters). This suggests that level forested terrain represents a much more homogeneous backscattering medium at X-band than rural/low-relief terrain in general, in spite of the fact that, within level forest patches, there exists considerable heterogeneity introduced by higher-order classifiers. For example, 71% of level forested patches carry some category of open terrain (agriculture, rangeland, etc.) as secondary land cover classification. Thus, the level forest under consideration contains secondary openings or "holes" of non-forested terrain that contribute forest edges as discrete clutter sources.

87
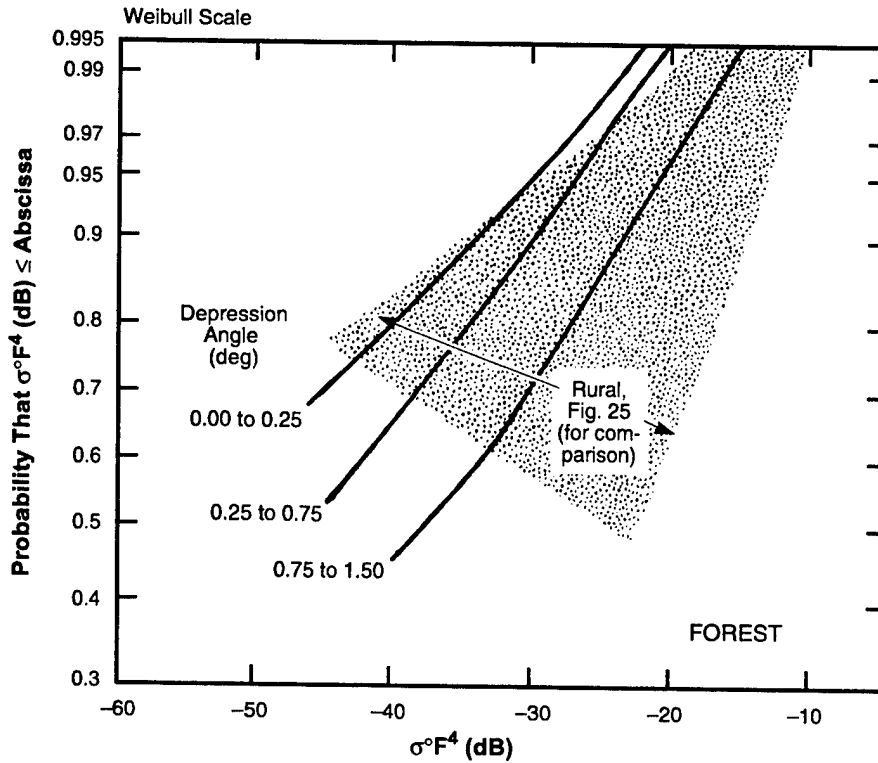
Figure 41. Cumulative ground clutter amplitude distributions by depression angle for level forested terrain. Phase Zero X-band data, 75-m range resolution, horizontal polarization, 2- to 12-km range, 88 patches. Also see Table 14.

TABLE 14

Statistical Attributes of Ground Clutter Amplitude Distributions for Level Forested Terrain, by Depression Angle

Phase Zero X-band data, 75-m range resolution, horizontal polarization, 2- to 12-km range. Also see Fig. 41.

Depression Angle (deg)	Weibull Parameters			Ensemble Mean Clutter Strength $\overline{\sigma^\circ F^4}$(dB)	Percent of Samples above Radar Noise Floor	Number of Patches
	a_w	σ°_{50} (dB)	$\overline{\sigma^\circ_w}$ (dB)			
0.00 – 0.25	3.6	–54	–37	–36.0	48	39
0.25 – 0.75	3.0	–46	–33	–31.8	63	36
0.75 – 1.50	2.3	–36	–28	–26.9	70	13

88

Compared with rural/low-relief terrain, mean clutter strengths from level forest are observed to be somewhat weaker (~4 dB) at very low angle (0° to 0.25°), but increase to be somewhat stronger (~1 or 2 dB) at higher angles (0.75° to 1.5°). However, it is the attribute of spread in clutter amplitude distributions in which level forest most significantly differs from rural/low-relief terrain.

Next consider level agricultural terrain. Ensemble amplitude distributions in four regimes of depression angle for level agricultural terrain are shown in Figure 42. Statistical attributes of these distributions are shown in Table 15. The regime of the rural ensemble distributions from Figure 25 is shown lightly shaded in Figure 42 for comparison. As with level forest, these level agricultural distributions show a strong dependence on depression angle. In other aspects, however, these level agricultural distributions are very different from level forest. The level agricultural distributions show a strong tendency to merge at the higher cumulative probability levels shown (around cumulative probability = 0.97), whereas at such levels the level forest distributions stay well separated. This suggests a dominating influence from discrete clutter sources at these probability levels on level agricultural terrain, from which backscatter would be expected to be less sensitive to depression angle. The spreads in the level agricultural distributions are extreme (much larger Weibull shape parameters), not only compared with level forest, but also, at very low depression angles (0° to 0.5°), with rural/low-relief terrain in general. At higher angles (0.75° to 10°), the spread in the level agricultural distribution becomes equal to that of the rural/low-relief distribution. Mean clutter strengths in level agricultural terrain show very little variation with depression angle (although median strengths rise quickly as the spread decreases with increasing depression angle) in contrast to the significantly increasing mean strength with depression angle of level forest. Of the level agricultural patches, 34% carry secondary land cover classification of forest. That is, similarly to level forest containing openings of non-forested terrain, so also does open level agricultural terrain contain closed patches of trees. Level agricultural terrain appears to be highly heterogeneous, because of strong localized discrete scattering sources (including patches of trees) in a weakly backscattering medium (the field surfaces themselves), so that amplitude distributions contain both many strong cells and many weak cells and hence a large degree of spread. As depression angle increases, the field surfaces backscatter more strongly, spreads decrease, and the resultant distributions begin to take on more of the characteristics expected from more homogeneous terrain such as shown by level forest.
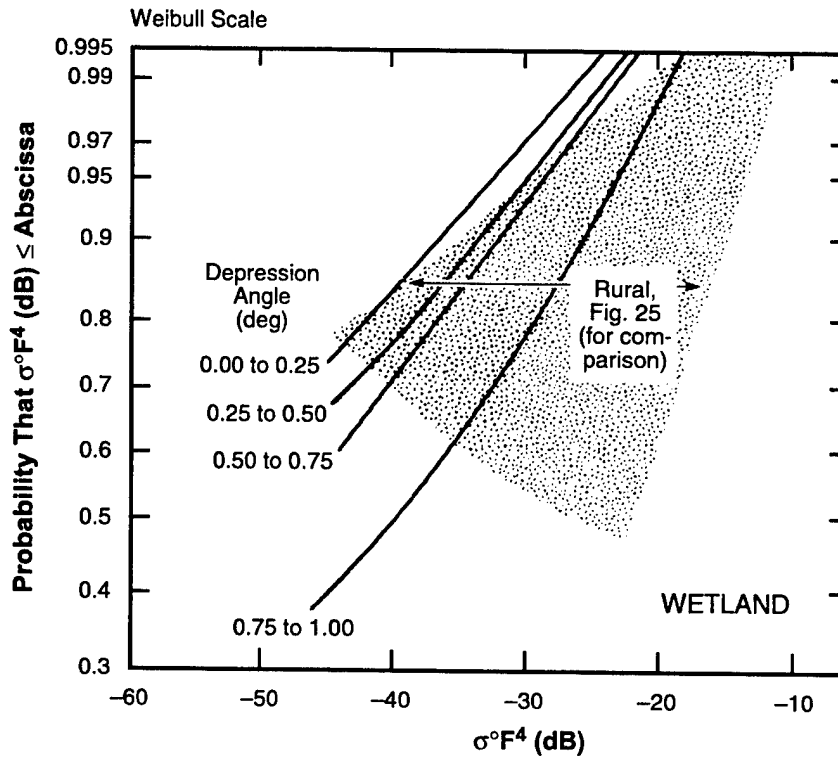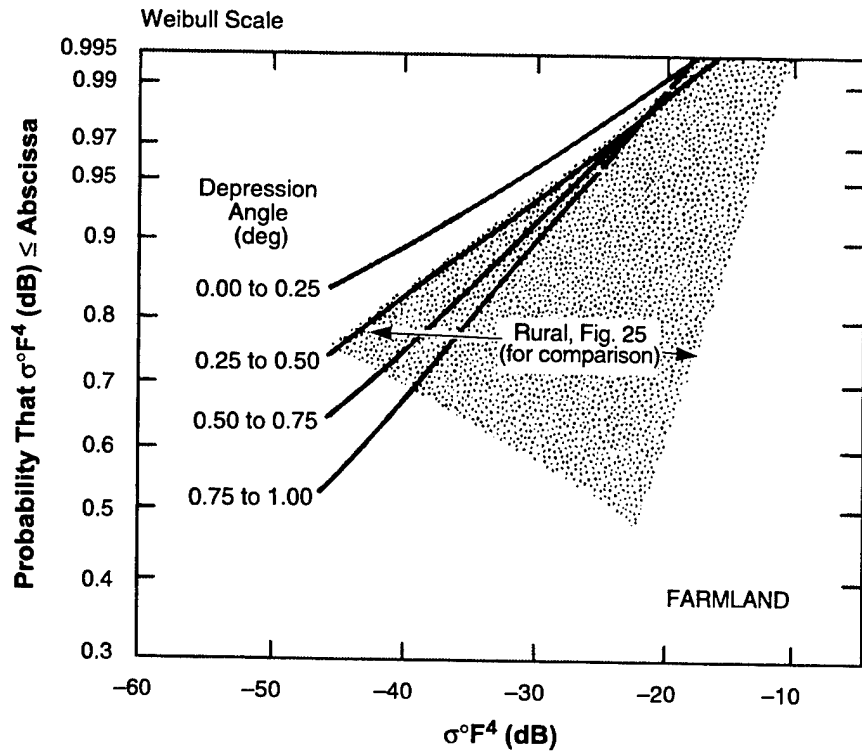
Figure 42. Cumulative ground clutter amplitude distributions by depression angle for level agricultural terrain. Phase Zero X-band data, 75-m range resolution, horizontal polarization, 2- to 12-km range, 245 patches. Also see Table 15.

TABLE 15

Statistical Attributes of Ground Clutter Amplitude Distributions for Level Agricultural Terrain, by Depression Angle

Phase Zero X-band data, 75-m range resolution, horizontal polarization, 2- to 12-km range. Also see Fig. 42.

Depression Angle (deg)	Weibull Parameters			Ensemble Mean Clutter Strength $\overline{\sigma°F^4}$(dB)	Percent of Samples above Radar Noise Floor	Number of Patches
	a_w	$\sigma°_{50}$ (dB)	$\overline{\sigma°_w}$ (dB)			
0.00 – 0.25	5.9	–69	–32	–31.8	25	94
0.25 – 0.50	5.0	–60	–32	–30.7	38	101
0.50 – 0.75	4.0	–52	–32	–31.2	54	36
0.75 – 1.00	3.4	–47	–32	–31.3	60	14

90

Next, the characteristics of wetland clutter (Figure 40, Table 13) are compared with those of level forest (Figure 41, Table 14). The wetland clutter patches were almost all level. Considered simplistically, both level forest and level wetland might be considered to constitute level vegetative backscattering mediums relatively free of discrete scattering objects. Hence, level forest and level wetland might be expected to backscatter relatively similarly, with perhaps wetland causing somewhat weaker clutter because of a possibly enhanced tendency for forward scatter as a result of increased wetness (i.e., increased reflection coefficient) in wetland. Considering next some of the complicating characteristics of real forest and wetland that have been previously discussed, it was indicated in previous discussions of terrain heterogeneity that the majority of wetland patches contained clumps of trees, and that many forested patches contained open areas of, for example, farmland or other open land cover types brought in through second- and third-order classifiers. Thus, from this point of view also, the backscattering characteristics of wetland and level forest might still be expected to be similar. It turns out that the clutter characteristics of wetland and level forest are, indeed, surprisingly similar. The distributions of Figures 40 and 41 almost exactly overlay one another in similar regimes of depression angle. (Since the level forest and level wetland depression angle regimes do not exactly coincide, some minor angular interpolation is required to see the match.) This almost exact overlay of the resultant two sets of three curves requires, however, a horizontal displacement of approximately 2 to 3 dB between the two sets of curves, such that the wetland curves are shifted to the right. Thus, these data suggest that wetland backscatters very similarly to level forest, except that wetland clutter is about 2- or 3-dB weaker. Thus, the initial simplistic speculation that wetland clutter might be like forest clutter, but weaker, is borne out. It is quite remarkable that such similarities should exist between two entirely different data sets, with the approximately 2- or 3-dB offset maintained throughout, depression angle regime by depression angle regime and percentile level by percentile level. The similarity in shapes (Weibull shape parameter a_w) and approximately 2- to 3-dB difference in strength between these two data sets is also evident in comparing Tables 13 and 14.

4.2.5   Effect of Trees

Trees are a dominant constituent of landscape. In examining any particular low-angle clutter measurement involving trees, the influence of the trees on the backscatter data is often paramount. When large numbers of trees exist as a forest, they cover many other potential sources of clutter on the ground including discrete cultural objects, so that a relatively homogeneous vegetative medium is presented to the radar. In partially cleared forested regions, the edges of forest can dominate the backscatter. On open agricultural land containing only small incidences of trees, either in isolated occurrence or in shelter belts around farmsteads, or in tree lots, or around ponds and along streams, even a small incidence of trees can dominate the landscape in terms of large vertical discrete objects and hence dominate the backscatter.

Because of the importance of trees in low-angle ground clutter, a procedure was implemented within the terrain classification system utilized whereby every clutter patch was classified by percent tree cover. This was done by moving a fine uniform dot pattern over the region of the patch on the air photo and counting the number of dots within the area of the patch containing trees. The categories of percent tree cover in which clutter statistics were separated are shown in Table 16. The criteria used for assigning

"forest" or "forested wetland" as the primary land cover classifier of any patch included the requirement that the percent tree cover within those patches be greater than 50%. Thus, in what follows, in separating clutter statistics by percent tree cover, all forest and forested wetland patch data were combined to represent greater than 50% tree cover, and, for the categories of percent tree cover less than 50%, patch data were combined from all patches specified to have percent tree cover within that category, irrespective of land cover class.

TABLE 16
Categories for Specification of Percent Tree Cover Within Clutter Patches

Category	Percent Tree Cover η	Primary Land Cover Classification*
1	no trees	not 4 and not 61
2	$0 < \eta \leq 3$	not 4 and not 61
3	$3 < \eta \leq 10$	not 4 and not 61
4	$10 < \eta \leq 30$	not 4 and not 61
5	$30 < \eta \leq 50$	not 4 and not 61
6	$\eta > 50$	4 or 61
*4 = forest, 61 = forested wetland		

Ensemble amplitude distributions by percent tree cover are shown in Figure 43 for patches of "level" primary landform classification (similar percent tree cover results are available for other landform classes). Statistical attributes of the ensemble distributions of Figure 43 are shown in Table 17. A significant trend is observed in these distributions, whereby the spread in the distributions as given by the Weibull shape parameter a_w strongly decreases with increasing percent tree cover, for percent tree cover between zero and 50%. The "no trees" distribution is a special case. Median clutter strengths gradually increase with increasing percent tree cover, also over the same range for percent tree cover between zero and 50%, but not enough to compensate for the decreasing spread, so to a lesser extent mean clutter strengths tend to decrease with increasing percent tree cover. The strength of this parametric variation with percent tree cover is observed in Figure 43 and Table 17 to be less than that resulting from depression angle in Figure 25 and Table 5. Spreads in these statistics decrease with increasing percent tree cover between zero and 50% because, with increasing percent tree cover, the sizes of individual stands of trees grow, resulting in fewer isolated trees, tree lines, and edges of stands (with their inherent wide variability in clutter strength) and larger areas covered more or less homogeneously with trees (within each of which the inherent variability in clutter strength is less). For the same reason, the percent of samples above noise level in these

ensemble distributions increases with increasing percent tree cover as shown in Table 17. In transitioning from the category with percent tree cover between 30% and 50% to the forest category (percent tree cover > 50%), the spread in the amplitude distributions remains about the same ($a_w = 3.4$), but the strengths at most percentile levels increase by about 2 dB.

Weibull Scale
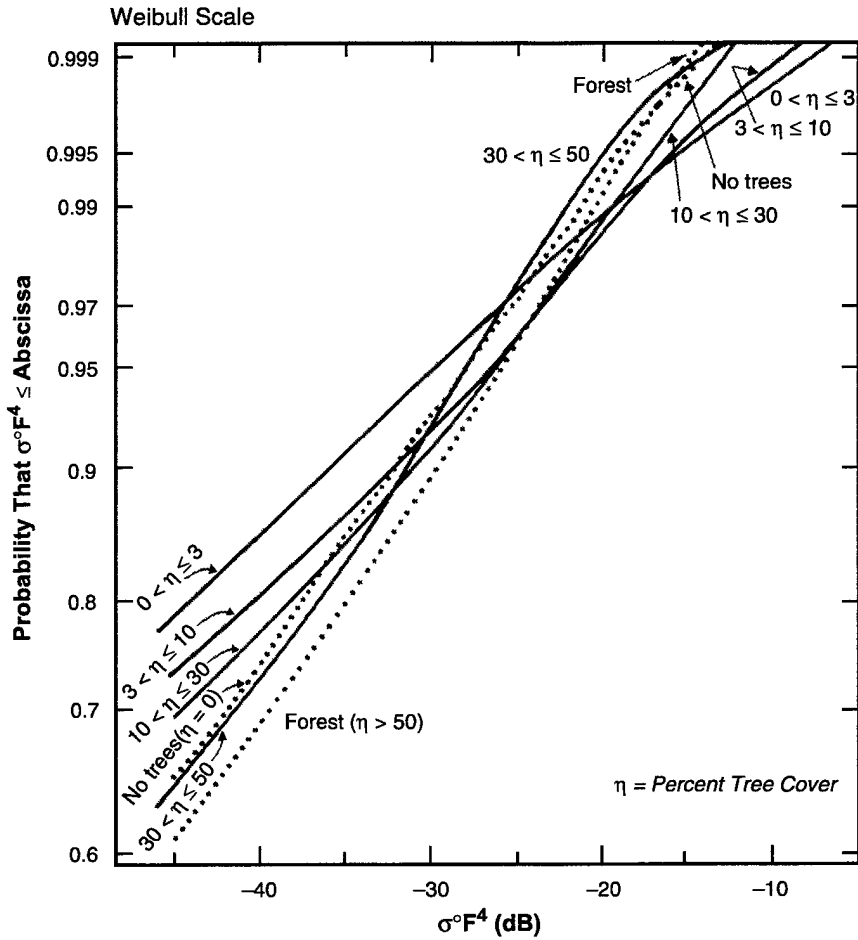
Figure 43. Ground clutter amplitude statistics by percent tree cover η on level terrain. Phase Zero X-band data, 75-m range resolution, horizontal polarization, 2- to 12-km maximum range, 530 clutter patches. Also see Table 17.

TABLE 17

Statistical Attributes of Ground Clutter Amplitude Distributions by Percent Tree Cover on Level Terrain

Phase Zero X-band data, 75-m range resolution, hoizontal polarization, 2- to 12-km range. Also see Fig. 43.

Percent Tree Cover η	Weibull Parameters			Ensemble Mean Clutter Strength $\sigma°F^4$(dB)	Percent of Samples above Radar Noise Floor	Number of Patches
	a_w	$\sigma°_{50}$ (dB)	$\overline{\sigma°_w}$ (dB)			
$0 < \eta \le 3$	5.3	−59	−28	−27.7	35	190
$3 < \eta \le 10$	4.9	−58	−31	−28.9	40	88
$10 < \eta \le 30$	4.4	−55	−31	−30.8	46	61
$30 < \eta \le 50$	3.4	−50	−34	−31.8	54	12
No Trees ($\eta = 0$)	3.5	−51	−34	−32.4	57	88
Forest ($\eta > 50$)	3.4	−48	−32	−31.4	57	91

The "no tree" distribution is a special case, standing outside the general trend of variation in the other distributions with percent tree cover. Simplistically interpreted, "no trees" means, to some extent, "no discretes" (or at least a de-emphasis of discretes). That is, treeless terrain brings out more the characteristics of area-extensive backscatter from a continuous medium. Forest terrain also begins to show more of the characteristics of a continuous medium, with a de-emphasis on discretes. Hence, simplistically, treeless terrain might be expected to backscatter like forested terrain. In fact, in Figure 43 the "no trees" distribution has abruptly swung away from the general trend of increasing spread with decreasing percent tree cover, and has abruptly assumed characteristics in strength and spread much more like the forest distribution at the other extreme of percent tree cover. The data of Figure 43 and Table 17 clearly show a considerable difference in low-angle clutter characteristics between terrain with absolutely no trees and terrain with "few trees" (where "few" means tree cover between 0 and 3%). This emphasizes the importance of isolated trees as the dominant type of discrete causing the wide spreads seen in low-angle clutter from agricultural land and other open terrain types.

4.2.6 Negative Depression Angle

A small portion of the Phase Zero clutter measurement sites are of negative effective site height. This is the result of terrain features in selected directions abruptly rising to elevations higher than the site elevation. Terrain higher than the antenna is observed by the radar at negative depression angle. Ten percent of our 2,177 Phase Zero clutter patches were observed at negative depression angle.

Patches observed at negative depression angle are now separated into three regions of negative depression angle, namely, zero to −0.25°, −0.25° to −0.75°, and −0.75° to −1.75°, irrespective of terrain

94

type. The clutter data from each of these three sets of patches is combined into an ensemble amplitude distribution. The resultant cumulative ensemble amplitude distributions for three regimes of negative depression angle are shown in Figure 44. Statistical attributes for these ensembles are given in Table 18. The regime of the rural terrain distributions of Figure 25 is shown lightly shaded in Figure 44 for comparison.
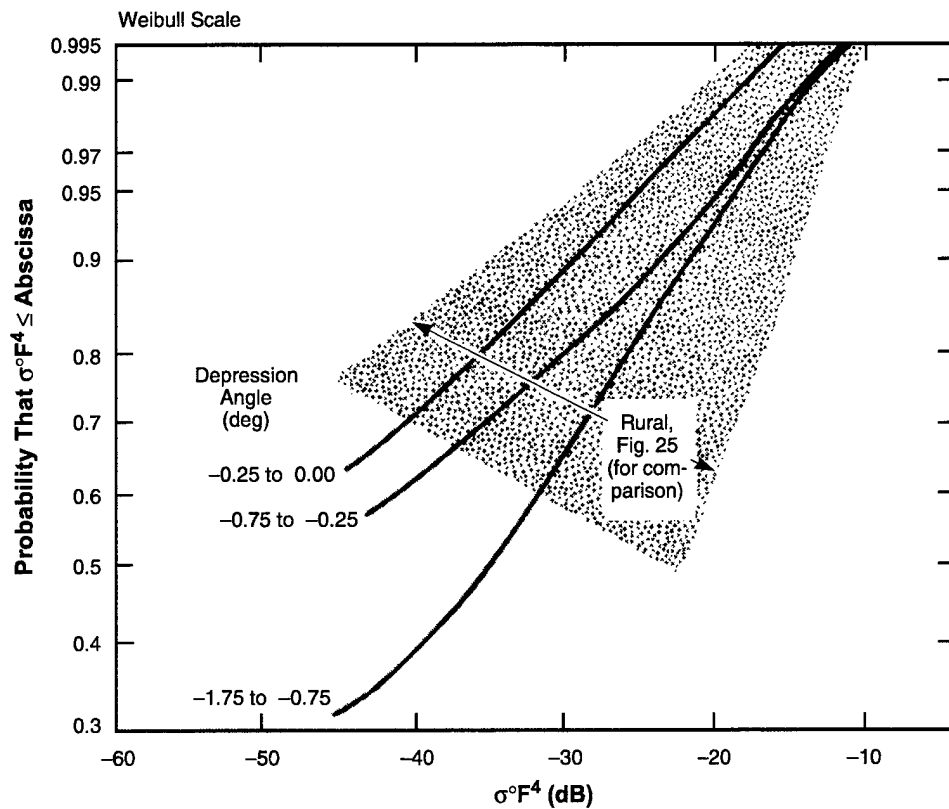
Figure 44. Cumulative ground clutter amplitude distributions in three regimes of negative depression angle. Phase Zero X-band data, 75-m range resolution, horizontal polarization, 2- to 12-km range, 194 patches. Also see Table 18.

TABLE 18

Statistical Attributes of Ground Clutter Amplitude Distributions in Three Regimes of Negative Depression Angle

Phase Zero X-band data, 75-m range resolution, hoizontal polarization, 2- to 12-km range. Also see Fig. 44.

Depression Angle (deg)	Weibull Parameters			Ensemble Mean Clutter Strength $\overline{\sigma°F^4}$ (dB)	Percent of Samples above Radar Noise Floor	Number of Patches
	a_w	$\sigma°_{50}$ (dB)	$\overline{\sigma°_w}$ (dB)			
0.00 to –0.25	3.9	–50	–31	–29.8	48	119
–0.25 to –0.75	3.8	–45	–27	–24.9	54	48
–0.75 to –1.75	2.6	–35	–26	–24.2	74	27

The negative depression angle clutter amplitude distributions of Figure 44 and Table 18 are not separated into two regions of relief, low-relief and high-relief, as are the positive depression angle data of Figure 25 and Table 5. To see terrain at negative depression angle from antennas of positive mast height implies a positive terrain slope greater than the absolute value of the particular depression angle involved. Indeed, the terrain occurring above a radar position was often observed to be inaccessibly rough and steep—otherwise, the radar would have been sited at the higher position. Thus, the data of Figure 44 and Table 18 are not separated into two regimes of relief because ground clutter measured at negative depression angle often emanates from relatively steep terrain.

These ideas are now considered as they affect the data in each of the three negative depression angle regimes in Figure 44 and Table 18. First, consider the data in the zero to –0.25° regime. Within this regime, there are a substantial number (119) of patch measurements. At this low angle, only 17% of these patches carry primary landform classification of high-relief. However, of the 83% that are low-relief, only 7% are level. Theoretically, of course, absolutely level terrain free of vertical objects cannot be observed at negative depression angle—this low incidence of level patches reflects this fact. Thus, the clutter data within this low negative depression angle regime are dominated by terrain in the undulating and inclined classes presenting slight positive slopes that are visible. In contrast, the clutter data at low positive depression angle from zero to +0.25° in Figure 25 and Table 5 are much more influenced by level terrain. As a result, the zero to –0.25° amplitude distribution is about 2-dB stronger in mean strength than the zero to +0.25° amplitude distribution, and is of less spread (a_w = 3.9 compared with 4.8). The highest positive depression angle data of Figure 25 and Table 5 (from +0.25° to +0.5° and from +0.5° to +0.75°) more closely match the zero to –0.25° distribution in mean strength and spread, indicating from another

96

perspective the dominant influence of small, non-zero terrain slopes in the low negative depression angle clutter data.

At slightly higher negative depression angles, the situation changes. In the data of Figure 44 and Table 18, in the –0.25° to –0.75° depression angle regime, about one-half of the patches are high-relief; of these that are low-relief, none are level. Most of these low-relief patches are inclined, many with secondary landform classification of moderately steep or steep. Also many of the high-relief patches are moderately steep or steep. Thus, as expected, with slightly increasing negative depression angle, the clutter-producing terrain was usually quite rough and steep. As a result, the clutter amplitude distribution in the –0.25° to –0.75° depression angle regime is about 5-dB stronger in mean strength than the corresponding low-relief distributions at positive depression angle. In terms of spread, however, the shape parameter a_w at –0.25° to –0.75° is very similar to that for low-relief terrain at corresponding positive depression angles. That is, in the clutter results of Figure 44 and Table 18, the high-relief component of terrain in the –0.25° to –0.75° depression angle regime appears to dominate the mean, whereas the low-relief component appears to dominate the spread.

For depression angles from –0.75° to –1.75°, these trends continue but with increasing domination by high-relief terrain. At the higher angles, the percentage of patches that are high-relief or carry primary any or secondary classifiers of moderately steep or steep is substantially higher. The clutter amplitude distribution in the –0.75° to –1.75° depression angle regime is similar to corresponding distributions in the 0° to 1° and 1° to 2° regimes in high-relief terrain. In comparing these data, the positive angle regimes (0° to 1° and 1° to 2°) are much less dominated by extreme high-relief landform classes than is the negative angle regime (–0.75° to 1.75°). The amplitude distributions in these positive and negative depression angle regimes bear some similarity only because the increased terrain slopes at negative angles offset the positive angles on less steeply sloped terrain. In moving from the –0.25° to –0.75° depression angle regime to the –0.75° to –1.75° regime, the increasing incidence of steep terrain has increased mean strength very little, but has reduced the spread in the amplitude distributions substantially.

In summary, clutter amplitude statistics at negative depression angles are, on the whole, relatively dissimilar to amplitude statistics at corresponding positive depression angles. At low negative angles (i.e., zero to –0.25°), strengths are somewhat higher and spreads are somewhat lower than corresponding positive angles because the generally low-relief terrain surfaces under observation at low negative angles have to be slightly more inclined towards the radar in order to be seen. At slightly higher negative angles (i.e., above –0.25°), the only terrain usually seen is for the most part quite rough and steep, with attendant increases in clutter strength. Once the terrain is high enough and steep enough to be observed at significant negative depression angles (i.e., depression angle <–0.25°), further increases in depression angle do not much increase the strongest returns received but do increase the weaker returns received through the central part of the distribution.

97

4.3 COMBINING STRATEGIES

Throughout Section 4, general understandings and general descriptions of the low-angle clutter phenomenon have been sought by combining measurement data from many individual, like-classified, clutter patches into ensemble amplitude distributions generally representative of that class. In combining clutter data, one can think in terms of individual spatial cells or samples as the elemental quantity being combined, or one can think in terms of clutter patches—each patch containing many cells—as elemental quantities. Both points of view have advantages and disadvantages.

First consider combination at the cell level. Imagine from a set of like-classified patches, a set of clutter amplitude histograms—one histogram per patch—that all have identical bell shapes but that have widely varying means so that there exists little overlap from histogram to histogram. Aggregation of the data in all of these elemental histograms, cell by cell, into one overall ensemble histogram, yields an ensemble histogram of quite different characteristics than any of the individual histograms. In particular, in these circumstances the ensemble histogram contains much more spread in its data than the individual histograms.

The failure of the above set of histograms as a proper ensemble is the failure of the classification system that grouped the patches together in the first place. Now from a set of like-classified patches, imagine a set of histograms of similar but not identical shape, with similar means and standard deviations, but with each histogram containing different specific higher-order attributes. Combining these histograms cell-by-cell into an ensemble histogram yields a useful general distribution in which individual differences are averaged out. The resultant ensemble distribution is generally representative of any of the individual histograms. This situation is the result of a classification system which successfully finds and groups together patches with similar amplitude statistics in the first place. In the real world of clutter patches, neither of the above positions is entirely true. The classification system utilized works usefully but not perfectly. As a result, aggregation of amplitude statistics from a set of patches sample by sample at the spatial cell level does provide much useful information, but it also introduces some extra spread into the resultant ensemble distributions.

The above discussion is now quantified around a specific example, namely, the ensemble of rural/low-relief terrain with depression angle from 0.25° to 0.5°. This ensemble contains 448 individual clutter patches giving rise to 448 individual clutter amplitude histograms. For each patch, the mean strength of its histogram is computed, and the distribution of 448 mean strengths is plotted cumulatively in Figure 45. Given this set of data, the task of modeling is to select an appropriate general value for representing mean clutter strength in rural/low-relief terrain at depression angles from 0.25° to 0.5°.

Observe that the cumulative distribution in Figure 45 is quite linear as plotted against the normal probability scale there. To the extent that it is linear, the distribution can be represented by a normal or Gaussian distribution. That is, the distribution of dB values of mean patch clutter strength (each mean computed in units of m^2/m^2 and subsequently converted to dB, as per equations C-3 and C-8) in Figure 45 is closely approximated by a well-behaved normal distribution. This being the case, a reasonable value to

select from this distribution as being generally representative of rural/low-relief, 0.25° to 0.5° depression angle, mean patch clutter strength is the median value in the distribution, –33.6 dB. If the distribution was exactly symmetrical, its mean, median, and modal measures of dB values would be identical. The mean value of the dB values of mean clutter strength (calculated similarly to equation C-12, although with y_i representing mean clutter strength of the i-th patch in dB as computed by equation C-8) in Figure 45 is –33.0 dB.
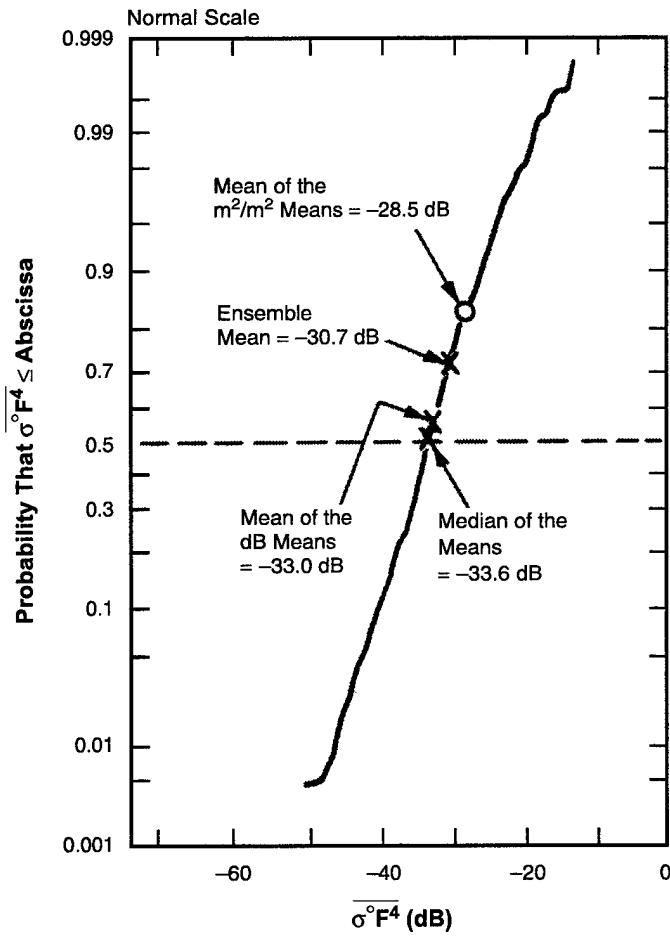
Figure 45. Cumulative distribution of mean ground clutter strength for rural/low-relief terrain with depression angle from 0.25° to 0.5°. Phase Zero X-band data, 75-m range resolution, horizontal polarization, 2- to 12-km range, 448 patches, 70 sites. The curve shows the distribution of mean strengths, one value of mean strength (Eq. C-8) per patch. See text for definitions of indicated central measures of the distribution.

99

If the distribution of dB values of mean clutter strength in Figure 45 is normal, then the distribution of the values of mean clutter strength in units of m^2/m^2 is lognormal. All of the percentile values in this fundamental m^2/m^2 distribution simply transform logarithmically to corresponding values in the dB distribution (e.g., the median position in the m^2/m^2 distribution is also the median position in the dB distribution). But mean and modal values in the m^2/m^2 distribution are not simply related to corresponding values in the dB distribution and do not occur at the same percentile positions in the m^2/m^2 distribution as they do in the dB distribution. The mean value of the m^2/m^2 values of mean patch clutter strength in the distribution of Figure 45 is –28.5 dB, 4.5-dB stronger than the mean value of the dB values of mean patch clutter strength in the same distribution. Note that this value of –28.5 dB occurs at the 82-percentile level in the distribution.

Finally, consider the overall ensemble histogram of individual cell-by-cell spatial samples assembled aggregatively from the 448 patches corresponding to the data of Figure 45. The mean value of this ensemble histogram computed in m^2/m^2 and converted to dB (by equations C-3 and C-8) is –30.7 dB. This value of –30.7 dB occurs at the 72-percentile level in the distribution. Let this value be called the cell-level "ensemble mean." Comparing it to the "mean of the m^2/m^2 means" = –28.5 dB, the "mean of the dB means" = –33.0 dB, and the "median of the means" = –33.6 dB, the "ensemble mean" lies between the "mean of the m^2/m^2 means" and the "mean of the dB means," 1.2-dB below the former and 2.3-dB above the latter. The "ensemble mean" is not equal to the "mean of the m^2/m^2 means" because the clutter patches are not all of equal size; if they were, these two quantities would be identically equal. In fact, smaller clutter patches have a slight tendency to be of greater mean strength, accounting for the higher value of the "mean of the m^2/m^2 means."

At this point in the discussion, three reasonable definitions of mean clutter strength exist to represent a patch of rural/low-relief terrain observed at 0.25° to 0.5° depression angle. There is no single correct definition. The clutter modeler wants to select a reasonable definition appropriate to the application of the model. The modeler wants to look for parametric trends in this defined quantity, and wants to stay aware of the extent to which the characteristics of such trends might be dependent on the quantity selected.

There is nothing in Figure 45 to discourage use of the ensemble aggregation of cell-level statistics to model clutter. The "ensemble mean" occupies middle ground between the "mean of the dB means" and the "mean of the m^2/m^2 means" at the 72-percentile level in the distribution. Thus, a model based on ensemble aggregations of cell-level statistics is biased somewhat towards more severe clutter leading to conservative estimates of radar capability. This is not necessarily undesirable. In overview, there are many patches with both stronger and weaker clutter strength than the ensemble mean value.

At the beginning of Section 4, the question was raised of whether cell values or patch values should be regarded as elemental statistical quantities to be combined in clutter modeling. The data in Figure 45 show the combination of all patch mean clutter strengths for a given ensemble of patches. Thus, within the distribution of Figure 45, the patch is the elemental quantity. The particular statistical attribute of the patch amplitude histogram that is quantified in Figure 45 is patch mean strength. Other statistical attributes of patch amplitude may be similarly plotted (see Figure 46). The advantage of regarding patches as elemental

statistical quantities is that it avoids cell-level aggregation of data from non-similar histograms. However, once the distribution of a particular patch attribute is plotted such as in Figure 45, the modeler still has to face up to selecting one value from a range of values. In the end, it still is an act of reasoned judgment to select the modeling quantity. If the argument against a cell-level aggregative approach to ensemble statistics is that it is too demanding of a terrain classification system, it is certainly true that a failed classification system also fails at the patch level. Under a failed system, collections of patch attributes will contain much spread and show no parametric variation. The advantage of forming cell-level aggregative ensemble distributions is that it is a convenient way to show resultant averaged or generalized amplitude distributions. That is, the general histogram is just the cell-by-cell sum of the data in the individual histograms. It is not so easy to provide an actual general histogram or cumulative distribution in a patch-oriented approach in which only various attributes of individual patch histograms are collected, as opposed to the histograms themselves.

One thing that can be done in this regard is to approximate the shape of each individual patch amplitude distribution with a Weibull shape parameter a_w. The distribution of all such values of a_w can then be formed for a particular ensemble of patches. Such a result is shown in Figure 46(a) for the same rural/low-relief, 0.25° to 0.5° depression angle ensemble for which data are shown in Figure 45. Three representative values for a_w are also indicated in Figure 46(a), the median value of a_w equal to 3.0, the mean value of a_w equal to 3.3, and the value of approximating shape parameter a_w for the cell-level aggregate distribution previously obtained (see Table 5) equal to 4.1. This last quantity is denoted as the cell-level ensemble value of a_w. The data of Figure 46(a) quantify the concern discussed at the beginning of Section 4, that cell-level aggregation can cause too much spread in resultant average distributions. The ensemble value of a_w is, indeed, greater than the mean or median values of a_w in Figure 46(a). The ensemble value of a_w is at the 80-percentile level in the distribution. Consider that the median level does not necessarily constitute a better modeling value than the 80-percentile level. There are many individual patches with both significantly greater spread and significantly less spread than that specified by the ensemble value of a_w in the data of Figure 46(a). However, use of the cell-level aggregation does provide a slight bias towards increased spread in clutter amplitude statistics in the modeling information of this report, as well as increased strength. Again, such a conservative bias from the point-of-view of radar capability is not necessarily undesirable. It does, however, need to be quantified and understood. In the data of Figure 46(a), this bias does not appear extreme. The bias is most extreme at the lowest depression angles, as in the depression angle regime of 0.25° to 0.5° for which data are shown in Figures 45 and 46. The bias decreases with increasing depression angle. Further quantification of differences between cell-level and patch-level characterization of clutter amplitude statistics, as a function of depression angle, is presented in Section 4.4. Comprehensive modeling information of clutter amplitude statistics based on patch-level expected-value characterization is the main approach taken in Phase One studies [1–3]. This was a more challenging empirical task than that based largely on cell-level aggregation, from which the information of this current Phase Zero report was derived.

101

Normal Scale

(a) Distribution of a_w

(b) Distribution of σ°_{50} (dB)
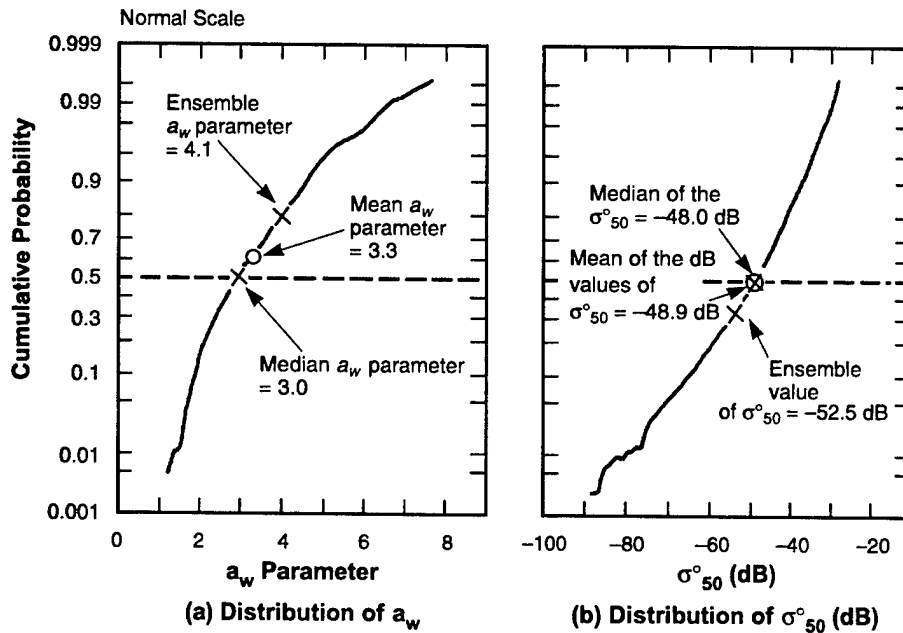
Figure 46. Cumulative distributions of approximating Weibull coefficients a_w and σ°_{50} (dB) for clutter patch amplitude distributions from rural/low-relief terrain with depression angle from 0.25° to 0.5°. Phase Zero X-band data, 75-m range resolution, horizontal polarization, 2- to 12-km range, 448 patches, 70 sites. The curves show distributions of Weibull shape parameter a_w and medium clutter strength σ°_{50}, one value of each per patch.

Besides the shape parameter a_w, a Weibull model requires specification of the σ°_{50} parameter. In approximating the clutter amplitude distribution of each of the 448 rural/low-relief patches observed at 0.25° to 0.5° depression angle with a Weibull distribution, besides collecting all of the patch values of a_w as shown in Figure 46(a), all of the patch σ°_{50} (dB) values were also collected as shown in Figure 46(b). It is observed that the ensemble value of σ°_{50} is 4.5 dB weaker than the median value. This also reflects the increased spread of cell-level aggregate models compared with aggregates of patch attributes. The increased spread of the cell-level distribution has driven σ°_{50} in the approximating Weibull distribution to somewhat lower levels (i.e., 33-percentile) in the distribution of patch-level σ°_{50} values. Again, compared to the overall range of this distribution, this value of –52.5 dB appears reasonable for a general model.

In the end, the relative goodness or badness of the "ensemble of cells" cell-level approach is the degree to which the ensemble distribution looks like a typical patch distribution. As indicated by the comparisons with constituent patch data shown in Figures 45 and 46, the rural/low-relief, 0.25° to 0.5° depression angle, ensemble of cells distribution on the whole does look satisfactorily like a clutter amplitude distribution from a typical clutter patch.

Consideration now is given to whether a given ensemble of like-classified patches contains enough patches to provide generality. A simple empirical test for whether a trial set of patches is sufficient to provide converged results[10] characteristic of the general set is to simply randomly partition the trial set any number of ways into two equal and independent subsets, each containing half as many patches as the original set, and to subsequently determine if the results obtained from the subsets agree with those of the original set [16]. Continuing with the rural/low-relief, 0.25° to 0.5° depression angle ensemble of 448 patches selected for previous discussion in Section 4, these patches are now randomly divided into two subsets, each containing 224 patches. This is done in three different ways. For each of these six subsets, the cell-level ensemble clutter amplitude distribution is formed and plotted cumulatively in Figure 47. It is apparent in Figure 47 that, within each partition generating two independent subsets, each independent pair of distributions are closely converged to one another. On the basis of these results, it would be expected that, if a new clutter measurement program were to be initiated, in which clutter was measured from 448 newly selected patches of similar classification, the new measurements would lead to a new cell-level ensemble clutter amplitude distribution well within the interval of uncertainty indicated in Figure 47.

---

[10] Also, consider the distribution of Figure 45 from the point-of-view of statistical estimation theory. Thus, sample size N = 448, sample mean $\bar{x}$ = –33.0 dB, and sample variance σ^2 = 25 dB. The rms error of $\bar{x}$ is $\left(\frac{\sigma^2}{N}\right)^{1/2}$ = 0.24 dB. Hence the quantity $\bar{x}$ = –33.0 dB is statistically "good" to –33.0 ± 0.24 dB.

103
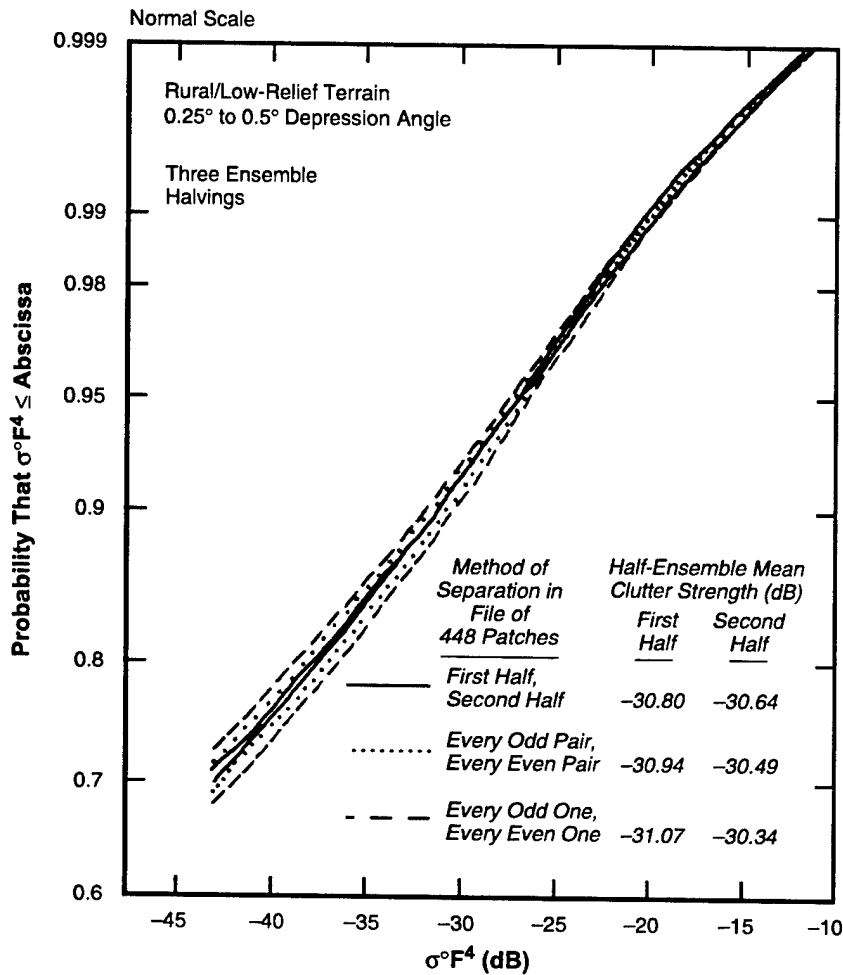
Figure 47. Three halvings of the 0.25° to 0.5° depression angle, rural/low-relief ensemble clutter amplitude distribution. Phase Zero X-band data, 75-m range resolution, horizontal polarization, 2- to 12-km range. Full ensemble mean clutter strength = −30.72 dB.

4.4 DEPRESSION ANGLE CHARACTERISTICS

A traditional approach to ground clutter modeling is to specify clutter strength as a simple characteristic of illumination angle. Following this approach, Figure 48 shows generalized mean and median clutter strengths as a function of depression angle, inclusive of all terrain types. The results of Figure 48 are based on Phase Zero measurements of 1,926 macropatches from 86 sites. First observe in Figure 48 that clutter strength increases with increasing angle. In the figure, spread in clutter amplitude

distributions is indicated by the mean-to-median ratio—heretofore in Section 4 spread has been characterized by the Weibull shape parameter a_w. Secondly, in Figure 48 observe that spread decreases with increasing angle. It is these two general observations, increasing strength and decreasing spread with increasing angle, that form the basis of the fundamental interpretation of the low-angle clutter phenomenon as provided in this report, and upon which is developed the clutter modeling information presented herein.
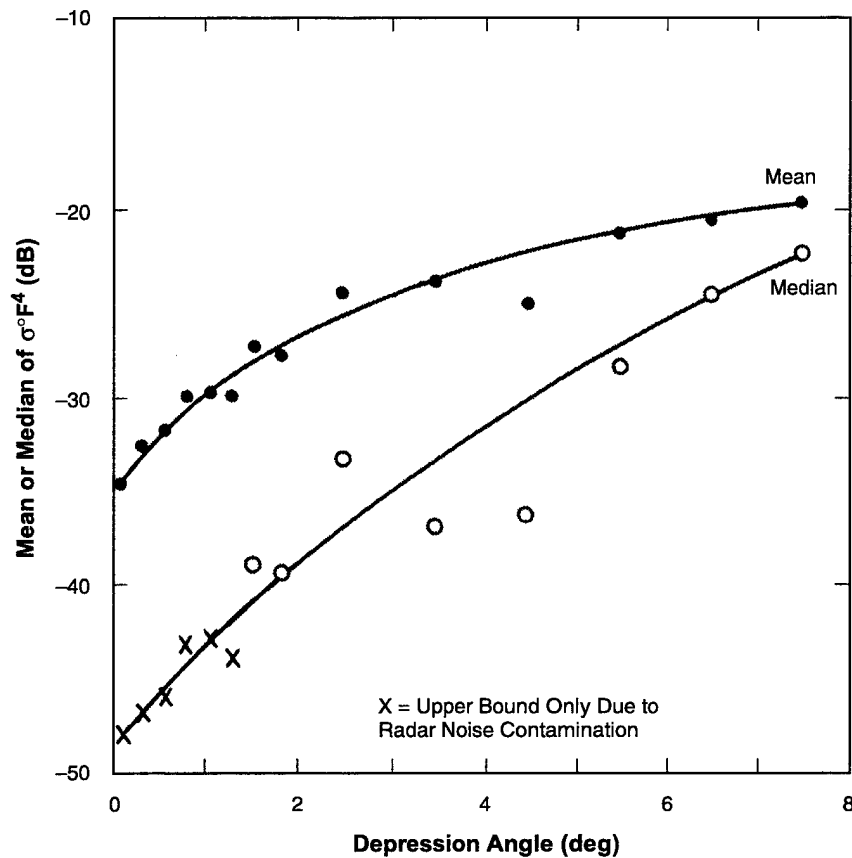
Figure 48. General variation of ground clutter strength with depression angle. Phase Zero X-band data, 75-m range resolution, horizontal polarization, 2- to 12-km range. All terrain types, 1926 patches from 86 sites. Data shown are expected values, see text.

Within visible patches, cells not providing discernible clutter are in microshadow (i.e., are at radar noise level). Figure 49 shows the general incidence of occurrence of microshadowing as a function of depression angle for the same set of Phase Zero data upon which the results of Figure 48 are based. At very low angles, clutter is caused to a very great extent by discrete sources distributed over a weakly

105

backscattering surface. Hence, at very low angles, less than half (38%) of cells within visible patches contain clutter discernible to the Phase Zero radar. As angle rises through the low-angle regime (depression angle <2°), the percent of cells containing discernible clutter rises very quickly, as the shadowed terrain between discrete sources rapidly comes into view. As a result, the median clutter strength, which was driven down by the large number of shadowed cells at very low angles, also rises relatively quickly with increasing depression angle. Median clutter strength does not rise quite as abruptly as the shadowing function, because even when terrain comes into visibility at very low angle, the area-extensive backscatter from the terrain surfaces themselves, as opposed to the discrete objects on them, is very weak. With increasing angle, however, as the shadowing function levels off, the median clutter strength continues to rise as area-extensive backscatter rises with increasing angle. Mean clutter strengths rise less rapidly than median clutter strengths, since the means are dominated more by the discrete vertical sources and less by the statistics of shadowing. The ratio of mean-to-median (i.e., spread) decreases strongly with increasing angle as the shadowed and weak samples at the low end of the distributions rise towards the stronger values that are dominating the mean. At the highest angle of between 7° and 8° in Figures 48 and 49, the mean-to-median ratio has dropped to only 2.7 dB, close to the Rayleigh value of 1.6 dB. This reflects the relatively low incidence of microshadowing (14%) and relatively full illumination prevailing at high angles.
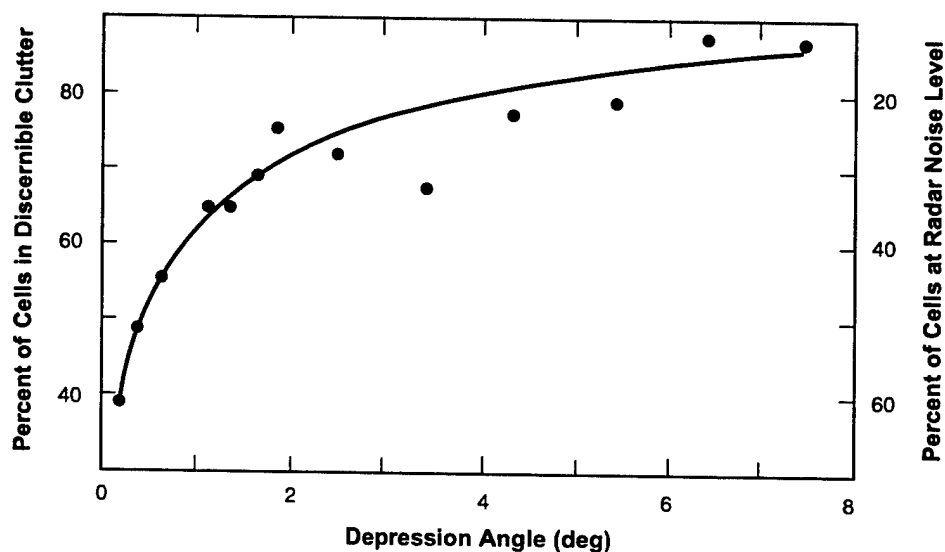
Figure 49. General incidence of microshadowing within clutter patches as a function of depression angle. Phase Zero X-band data, 75-m range resolution, horizontal polarization, 2- to 12-km range. All terrain types, 1926 patches from 86 sites. Each plotted point represents the overall percentage of all cells from all patches at a given depression angle.

In modeling ground clutter at the high depression angles associated with airborne platforms, clutter strength is often approximated as being directly dependent on the sine of the depression angle. Such a model is referred to as "constant γ," where $\sigma° = \gamma \cdot \sin\alpha$. Typical decibel values of γ (i.e., $10 \log_{10}\gamma$ in current use for rural terrain are -10 and -15 dB [13, 17, 18]. The mean clutter strength curve above $1°$ in Figure 48 is very accurately represented by $\sigma° = \gamma \cdot (\sin\alpha)^{1.2}$ with a decibel value of γ equal to -8.9 dB. Note that the exponent to which $\sin\alpha$ is raised in this latter expression is 1.2; that is, the $\sin\alpha$ dependence of the Phase Zero data in Figure 48 above $1°$ (457 macropatches) is somewhat stronger than the linear dependence often assumed [13, 17, 18]. Fitting the constant-γ model with linear $\sin\alpha$ dependence to the mean clutter strength data above $1°$ in Figure 48 leads to a decibel value of γ of approximately -11 dB, although doing so results in a poorer fit to the data. A summary of simple semiempirical clutter models such as the constant-γ model and its variations that have been utilized historically to fit various experimental data sets is provided in Ruck [19].

At lower angles, however, where most land clutter occurs in surface-sited radar, mean clutter strength is much stronger than would be predicted by the sine of the depression angle dependency, the latter becoming vanishingly small as depression angle approaches zero. Strong mean clutter at low angles is the consequence of domination of the low-angle phenomenon by discrete clutter sources. There has been occasional speculation in the clutter literature as to whether clutter strengths might "come back up" at very low angles because of possible specular incidence on discretes [20]. The data of Figure 48 indicate that although mean clutter strength remains relatively high at low angles, its general characteristic is to always decrease with decreasing angle, with no reversal occurring in this characteristic at very low angle.

Mean clutter strength is observed to vary over a range of 15 dB with depression angle in Figure 48, from -34.2 dB at grazing incidence in the $0°$ to $0.25°$ depression angle regime to -19.3 dB in the $7°$ to $8°$ regime. This mean strength variation of 15 dB with depression angle is the strongest general parametric variation observed of any single parameter in the Phase Zero X-band data. The effect of higher average terrain slopes at higher depression angles is implicit in this dependence. The dependence may be summarized by saying that it is depression angle as it influences shadowing on a sea of discretes that most directly effects strength in low-angle ground clutter.

The data in Figure 48 are expected-value results. Mean and median clutter strengths were computed for all patches within a given narrow regime of depression angle. A distribution of all the patch mean strengths for that particular depression angle regime was formed (like Figure 45). A similar distribution was formed of the corresponding set of patch median strengths. In each of these distributions, the expected value was computed, by which is simply meant the mean of the individual dB values of patch clutter strength (mean or median), each computed in m^2/m^2 and subsequently converted to dB.

In Figure 50, the expected-value data of Figure 48 are repeated, but also shown are the ensemble values of mean clutter strength in each angular regime. By ensemble value is meant the mean strength of the aggregate distribution obtained by combining individual patch histograms sample by sample. It is observed that the ensemble values of mean are somewhat higher than expected values of mean. The difference between expected and ensemble values diminishes with increasing angle. Because ensemble

107

values of mean are higher, so are the resulting mean-to-median ratios indicative of spread in amplitude distributions—this increase in spread also diminishes with increasing angle. The modeling information presented in Section 4 in terms of Weibull coefficients (a_w and σ°_{50}) is based on ensemble values. As a result, this modeling information has a slight bias towards increased mean strength and spread in clutter amplitude statistics compared with expected values as indicated in Figure 50. The trends revealed in the ensemble data are accurate. Similar multifrequency clutter modeling information based on Phase One measurement data and provided in subsequent reports [1, 3] is based on expected values. Expected values of median clutter strength are not included in Figure 50 because they are quite similar to the ensemble values of median clutter strength shown there. The microshadowing data in Figure 49 are ensemble values.
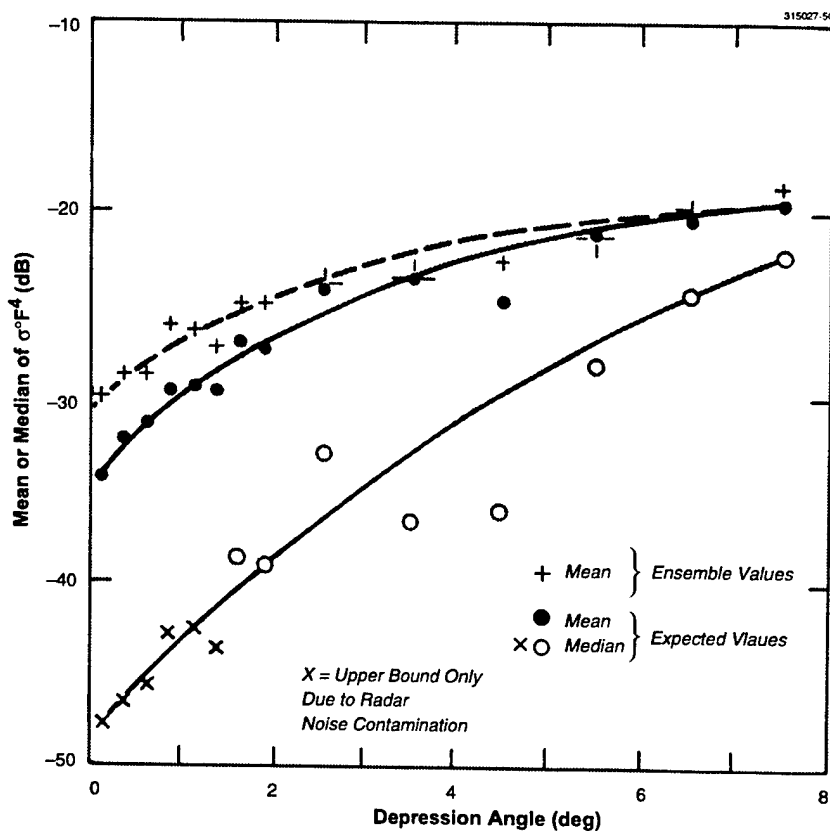
Figure 50. Differences between cell combination (i.e., ensemble values) and patch combination (i.e., expected values) on clutter strength versus depression angle. Phase Zero X-band data, 75-m range resolution, horizontal polarization, 2- to 12-km range. All terrain types, 1926 patches from 86 sites.

Most of the measured Phase Zero data occurs at low depression angle. For example, 95% of Phase Zero patches were observed at depression angles of <2.6°. Thus, in Figures 48, 49, and 50 in the 0° to 0.25° depression angle regime there are 456 patches contributing, but in the 7° to 8° depression angle regime

108

there are only three patches contributing. The major information content in these figures is at the low angles. Available data are included at higher angles in these figures only to show a more complete depression angle characteristic.

4.5 EFFECT OF RADAR SPATIAL RESOLUTION

Ensemble amplitude distributions were formed from ground clutter measured at each of the three Phase Zero pulse lengths over common spatial regions between 2 and 6 km in range from the radar at 14 sites of various terrain types. The three pulse lengths available were 60 ns, 0.5 μs, and 1.0 μs; corresponding range resolutions were 9, 75, and 150 m. The ratio of standard deviation-to-mean was computed as a measure of spread for each of these three ensemble distributions and plotted versus range resolution in Figure 51. The results in Figure 51 indicate a strong trend of increasing spread in low-angle clutter amplitude distributions with increasing range resolution, or in other words, with decreasing resolution cell size. In the discrete-dominated, heterogeneous process of low-angle clutter, increasing radar spatial resolution results in less averaging within cells, more cell-to-cell variability (i.e., more strong cells, more weak cells), and increasing spread in clutter amplitude distributions. A scale showing Weibull shape parameter a_w as it varies with ratio of standard deviation-to-mean in Weibull distributions is also shown in Figure 51. Thus, these results of Figure 51 may be used to nominally adjust values of Weibull shape parameter, provided as clutter modeling information heretofore in Section 4 and based on range resolution of 75 m, to apply to other range resolutions.
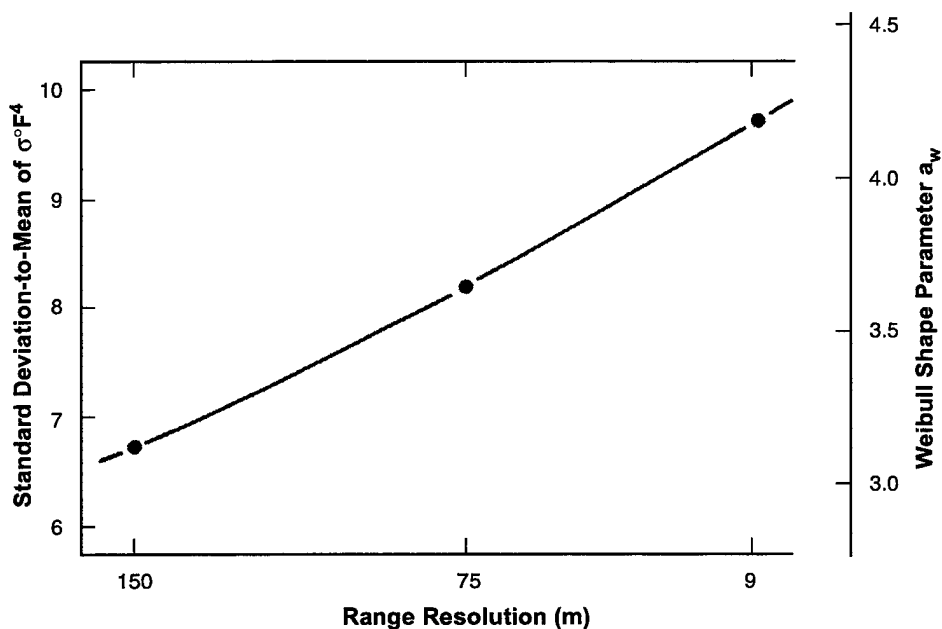
Figure 51. Spread in clutter amplitude statistics versus resolution. Phase Zero X-band data measured at each of the three Phase Zero pulse lengths over common spatial regions from 2 to 6 km in range at 14 sites of various terrain types.

109

The characterization of low-angle clutter strength by σ°, an area density function (i.e., σ° = radar cross section per unit area), implies spatial homogeneity of land clutter. If clutter were a constant single-valued quantity over the spatial field, all spatial cells in the field would provide identically equal values of clutter strength. In these circumstances, there would be no variation of σ° with resolution cell size, and in fact no statistical variation in the process. More realistically, if each clutter resolution cell in the spatial field contained a large number of elemental scatterers with no single scatterer dominating, cell-to-cell variations in clutter amplitudes would be Rayleigh distributed. In these circumstances, neither the mean strength of the distribution of clutter amplitudes over the whole spatial field (i.e., clutter patch) nor their spread would vary with resolution cell size. However, the conditions for Rayleigh statistics do not apply to low-angle clutter; strong discretes often dominate within resolution cells. In these circumstances, Phase Zero results indicate that the mean strength over the spatial field or clutter patch is still largely insensitive to the resolution cell area, which validates the basic characterization of low-angle clutter as properly being a density function σ°. However, as indicated in the results of Figure 51, the spreads in low-angle clutter amplitude distributions take on much greater values than Rayleigh (for Rayleigh statistics, $a_w = 1$; ratio of standard deviation-to-mean = 0 dB) and vary strongly with resolution cell size.

It is fundamentally important to accurately model the wide spreads that occur in low-angle land clutter. These spreads strongly affect radar performance in clutter through target detection and false alarm statistics. The results of Figure 51 provide a first indication of the effect of radar resolution cell size on spreads in low-angle clutter and a preliminary means to adjust the Phase Zero modeling information of this report to apply to other resolutions. In results based on Phase One multifrequency clutter measurements, the dependence of spread in low-angle clutter spatial amplitude distributions is developed as fundamentally dependent on radar spatial resolution within the basic parameterization of the modeling information provided [1–4].

5. SUMMARY

The data available from the Phase Zero program comprise calibrated clutter files covering all of the clutter within the field-of-view from 106 different sites. Extensive analyses of these data were conducted, incorporating terrain descriptive information obtained principally through detailed air photo interpretation. These analyses led to an understanding of a basic unifying mechanism underlying what appears at first consideration to be extreme variability and little predictability in low-angle clutter spatial amplitude distributions.

A surface-sited radar often experiences ground clutter interference over many kilometers in range. By and large, most of the relatively significant clutter comes from geometrically visible terrain. Geometric visibility is patchy at most places on the surface of the earth; high regions are visible and low regions are masked. Thus, clutter occurs within kilometer-sized macropatches of general geometric visibility illuminated at near-grazing incidence to ranges of 10's of kilometers. What has come to be understood in modeling investigations involving 2,177 measured clutter patch amplitude distributions obtained from 106 measurement sites is that within macroregions of general geometric visibility, at very low angles of illumination, what is being measured is backscatter from a sea of discrete clutter sources. That is, a wave is skimming over the landscape at grazing incidence, and backscatter is being measured from all of the sources of vertical discontinuity that rise up from the landscape. Such discrete vertical sources may be natural or cultural in origin and comprise such things as roads and field boundaries (or, more specifically, the vertical objects clustered along them); buildings (usually in clusters or complexes, for example, at farmsteads and industrial facilities, along road and rail lines, in towns and villages); trees (particularly tree lines, as at the edge of forest cover, or as shelter belts, or along river valleys); or even high points in terrain or breaks in terrain slope (for example, that occur in hummocky, hilly, or mountainous regions, or at edges of river valleys). All such clutter sources are spatially localized and thus discrete in nature. Numerous low reflectivity or shadowed cells occur between cells containing discrete clutter sources, even though the overall region from which the clutter amplitude distribution is being formed is under general illumination by the radar. In other words, at very low angles, small rises in terrain throw long ground shadows and even unshadowed terrain surfaces near grazing incidence backscatter very weakly. The combination of many shadowed or low-reflectivity weak cells together with many discrete-dominated strong cells causes a great deal of spread in the resultant low-angle amplitude distributions. As illumination angle increases, the low reflectivity areas between discrete vertical features become more strongly illuminated, resulting in less shadowing and a rapid decrease in the spread of the distributions. The upper tails of the clutter distributions, however, and the mean levels that are largely determined by the upper tails are still primarily caused by discrete sources and increase more slowly with increasing illumination angle.

Therefore, as a unifying mechanism, depression angle (i.e., the angle below the horizontal at which a clutter patch is observed at the radar) as it affects shadowing on a sea of discretes is the single most important parameter at work in low-angle ground clutter data, even at the very low angles of typically <1° that usually occur for surface radar. This basic parametric dependence in ground clutter spatial amplitude

distributions is such that strengths increase and spreads decrease with increasing depression angle. This parametric dependency with depression angle is strong enough to largely wash out many fine-scaled differences between similar terrain types. Attempts to refine this basic dependency through use of grazing angle (i.e., the angle between the tangent to the local terrain surface at the terrain point and the direction of illumination) have met with little additional success because of the extreme complexity that exists in terrain surfaces, the lack of detailed information defining these surfaces such that slopes (i.e., rates of change of elevation) are accurate, and difficulties in formulating a quantitative definition of terrain slope uniformly applicable across the various physical scales (cm to km) at which slopes exist in landscape. Over and above such considerations of scale and accuracy in terrain elevation data is the fact that the backscatter is frequently dominated by discrete elements of land cover rather than the underlying terrain itself.

This report presents general low-angle X-band ground clutter modeling information for clutter amplitude statistics within a construct that requires relatively detailed specification of depression angle, but only relatively coarse specification of terrain type, basically as one of only three types, rural/low-relief, rural/high-relief, or urban. Terrain slope enters the model explicitly through two categories of relief and implicitly through a general positive correlation between terrain slope and depression angle. Many additional results are provided for extending the general modeling information to more specific circumstances. The modeling information is presented largely in terms of Weibull coefficients, within a standard format in which spreads (i.e., shape parameter a_w, or mean-to-median ratio $\overline{\sigma^\circ_w}/\sigma^\circ_{50}$) may be observed to decrease, and strengths (i.e., $\overline{\sigma^\circ_w}$, σ°_{50}; and also measured ensemble mean strength) may be observed to increase, as depression angle rises and percent shadowing falls.

One of the most important attributes of low-angle ground clutter is the extremely broad spread that exists in amplitude distributions. Individual samples of clutter strength vary over orders of magnitude. The modeling information in this report reflects and highlights this element of extreme spread through Weibull coefficients. Low-angle clutter models which downplay the statistical nature of ground clutter and present clutter strength as, at best, just the mean or median of some Rayleigh-like process, or at worst, as a simple deterministic characteristic of range or angle do not do justice to the real phenomenon.

Throughout this report, the emphasis has been on the importance of spatially localized or discrete sources in low-angle clutter statistics. The dominant role of discrete sources is not, in itself, a new idea in the clutter literature (e.g., "...dominant land clutter signals are from discrete isolated targets...," [21]). Clutter models, however, have traditionally been developed, first, on a basis of area-extensive scattering from the statistically rough surface itself, as opposed to localized scattering from just the high points of that surface, or high objects on it. In such models, individual large discrete scatterers at specified incidences of RCS have sometimes been subsequently added in as a secondary feature of the model. One of the more valuable results to us of the extensive Phase Zero clutter measurements and analysis program is that we now imagine low-angle clutter as arising, first, from a sea of discrete vertical features or edges, separated by microshadow, and distributed over complex surfaces. The role of illumination angle in this construct is more as angle influences clutter strength through its effect on shadowing statistics between discrete features of vertical discontinuity, and less in its influence through grazing angle on area-extensive backscatter from tilted, statistically rough, terrain facets although both sorts of illumination angle effects

112

are at work in the real phenomenon. Examples of how the primary role of discretes affects many of the most important observable characteristics of low-angle clutter follow.

First, consider variations in clutter strength with radar frequency band. Although the results of this report are restricted to Phase Zero X-band data, analysis of the Phase One clutter data in all five Phase One frequency bands (VHF, UHF, L-, S-, and X-bands) shows that, in general, clutter strength is relatively independent of frequency band, VHF through X-band [1]. This reflects the fact that many dominant discrete clutter sources are large. For example, a tree line is a typical discrete vertical feature in landscape, and trees can be many RF wavelengths high, VHF (λ = 6 feet) through X-band (λ = 1 inch). By contrast, assumption of backscattering from a statistically rough surface (i.e., Rayleigh roughness model) results in a significant trend of increasing strength with frequency not generally seen in the Phase One data.

More specifically, however, the Phase One data show strong particular dependencies with radar frequency for specific terrain types. For example, on open agricultural land, the measurements are increasingly dominated by multipath propagation effects as frequency decreases, which increasingly prevent terrain illumination and result in a strong trend of increasing clutter strength with increasing frequency. As a counter-example, however, on forested land the Phase One measurements are dominated by the absorption characteristics of the forest, wherein the forest is not reflective and is increasingly absorptive with increasing frequency, resulting in a strong trend of decreasing clutter strength (i.e., decreasing strength of diffusely scattered radiation) with increasing frequency. In the X-band data of this report, variations in clutter strength with land cover are, on the whole, relatively minor, and the basic model only separates out "urban" land cover as being significantly different from all other land cover classes (which together are denoted as "rural"). The implication of strong opposite trends in clutter strength with frequency for different, more specific, land cover classes is that effects of more specific land cover on clutter strength are much more important at lower radar frequencies [1–4].

The strength of intrinsic backscattering—aside from propagation considerations on very open land or absorption characteristics on totally forested land—from general terrain (i.e., not completely open or completely forested) is relatively insensitive to variations in frequency band due to the discrete nature of the dominant clutter sources. Besides frequency, resolution is another fundamental parameter of any radar. If terrain were relatively homogeneous (as might be more expected in considering area-extensive backscatter from the terrain surfaces themselves as opposed to discrete sources on those surfaces), clutter statistics would be expected to be relatively insensitive to radar resolution. In fact, the clutter data show increasing spread in amplitude distributions with increasing resolution, a direct result of the granular nature of low-angle clutter in which cells containing discrete sources are interspersed with microshadowed cells.

Next, consider seasonal variations in clutter strength. Many of the measurement sites were on low-relief prairie farmland in western Canada. At the beginning of the measurement program, for example, when standing in an Alberta wheat field and seeing nothing but wheat to far horizons, clutter modeling was considered in terms of dielectric constant of wheat, moisture content of soil, and fields high in mature wheat versus harvested fields in stubble versus plowed or snow-covered fields, all of which led to

113

expectation of significant seasonal variations in clutter strength. Vertical discrete objects were not considered to be of foremost importance because, visually, they seemed relatively sparse. It turned out that when radar measurements were actually made at such sites to ranges of 25 or 50 km or more, the incidence of discrete sources was large and their effects were dominant. Not all discretes are evident visually. For example, when looking visually to a far horizon, what appears to be continuous terrain is often a series of discrete or localized hilltops, and furthermore, actual discrete land cover elements are often invisible at long range.

In the early days of radar, general acceptance of the idea that "angels" (i.e., non-zero Doppler echoes) were caused by birds came slowly because there did not appear to be that many birds, but over hundreds and thousands of square kilometers of radar coverage there can be enormous numbers of birds to account for angels, and similarly there are enormous numbers of stationary discrete or localized vertical scattering features dominating zero-Doppler ground clutter statistics. Thus, it is not so much the wheat field itself as the fence around it, the road and telephone line through it, and occasional storage granaries or trees around sloughs that are in it, that act as clutter sources. The dramatic seasonal variations that occur in the physical appearance of the surface of the wheat field have relatively little effect on the returned clutter statistics. The actual vertical sources tend to be relatively unchanged, summer and winter. Thus, in general, there is little seasonal variation in ground clutter strengths, usually on the order of 3 dB or so, with no noticeable trends. Occasionally when in specific situations there have been stronger seasonal variations in clutter strength (but always <10 dB), they have been the result of seasonal effects in multipath propagation, which is much more directly dependent on the state of the field surface itself.

Tree lines are very common discrete clutter sources. A tree line within a large regional clutter patch contributes strong clutter cells to the overall patch amplitude distribution, independent of whether the trees happen to be in leaf or bare, or wet or dry. Seasonal and weather effects only cause minor variations in these strong contributions. Of more significance in the distributions is whether the tree line exists or not, or more generally, the relative incidence of occurrence of tree lines on landscapes. This report provides information on how clutter amplitude distributions vary with percent tree cover, which indicates that the dominant sources causing much of the wide spread typically observed in these distributions for agricultural terrain are isolated trees.

General polarization effects, as observed with vertical and horizontal polarizations in the Phase One data, are very small. On the average, the vertically polarized data appear to be just slightly stronger (i.e., one dB or less) than the horizontally polarized data, an effect that may be due both to slightly higher forward scatter reflection coefficients at horizontal polarization, and a preferential vertical orientation of many sources. In sea clutter it has been generally reported, and data from the single Phase One sea clutter measurement site shows [22], that there is a much stronger variation in low-angle clutter strength with polarization than in land clutter, particularly at frequencies below X-band, with vertical being much stronger than horizontal.

The problem of making radar ground clutter understandable and predictable is as much one of statistics as of physics. Given enough time and effort, the backscattering processes within and

114

contributions from any particular clutter patch can be understood, but the heterogeneity of terrain often prevents useful generalization of such particular results. The ambiguous state of the historical clutter literature fundamentally reflects this problem. Hence the approach taken in Lincoln Laboratory studies is empirical and involves measuring clutter data within many patches and across many sites. This approach bounds the problem of clutter strengths for various terrain types by presenting generalized data with considerable averaging across sites and patches, and not data specific to some particular clutter scene that is nonrepresentative of other scenes. The resultant empirical modeling information contains all of the important trends observed in the measured data and thus constitutes a generally accurate predictive scheme for estimating low-angle ground clutter strength.

APPENDIX A

107 CLUTTER MEASUREMENT SITES

Table A-1 lists alphabetically the 107 sites at which Phase Zero or Phase One radar ground clutter measurements were made, and upon which clutter modeling investigations at Lincoln Laboratory were based. For each site, Table A-1 gives the site name, its location by province or state and in latitude and longitude, terrain descriptive information in terms of land cover and landform, and the effective site height.

Classes of land cover referred to in Table A-1 are briefly described in Table A-2. In the two-digit classifiers shown in Table A-2, the overall category given by the first digit is designated as general land cover, and the subcategory given by the second digit is designated as specific land cover. Also included in Table A-2 are the relative incidences of occurrence of each particular land cover class, in terms of the percent of the 2,177 Phase Zero patches carrying a particular primary general classifier. This land cover classification system is a slightly modified version of the United States Geological Survey land use and land cover classification system for remote sensor data [23]. Only first and second levels of this system are shown in Table A-2. The system includes higher order levels which extend to providing such particular information as vegetation species including height and density.

Classes of landform referred to in Table A-1 are briefly described in Table A-3. Also included in Table A-3 are the relative incidences of occurrence of each particular landform class, in terms of the percent of the 2,177 patches carrying a particular primary classifier. More complete descriptions of the landform classes are given in Table A-4. This system of landform classification is an extensively modified version of the geological landform classification system adopted by the Canadian Soil Survey Committee in 1976 [24].

In Table A-1, land cover and landform information is provided for each site in terms of the percent of occurrence of a particular category of classification across all of the clutter patches between 2 and 12 km from the radar at that site. The percent of occurrence of each classifier is shown in parentheses following that classifier. Examples of clutter patches at particular sites and their particular land cover and landform classifications may be seen in Figure 8 and, in Appendix C, Figures C-6, C-8, C-10, C-12, C-14, and C-16. As is indicated in these figures, three levels of land cover classification and two levels of landform classification were used, assigned in decreasing order of the amount of area involved, to deal with the heterogeneity of terrain within patches (even though at an overall level patches were selected so as to contain, in large measure, uniform terrain). In Table A-1, the percent of occurrence of a particular classifier at a site extends across and is inclusive of these second and third levels of classification. Thus, a great deal of specific information describing the terrain at each site is embedded in the land cover and landform numeric data of Table A-1. For example, Altona II is 100% level cropland. At Corinne, on the other hand, although 60% of the terrain is level and 70% is cropland, there is also 20% inclined terrain (along the Moose River) and 20% undulating terrain in terms of landform, and 15% residential (i.e., small prairie towns of Wilcox and Milestone) and 15% "river" (i.e., terrain dissected by Moose River and tributaries) in

117

terms of land cover. Such specific information describing land cover and landform was obtained after measurements were made at each site and correlated carefully with aerial photography and maps. These subsequent terrain studies occasionally provided surprises. Brief visual impressions did not always entirely reflect the contents of the 100's of square kilometers of landscape under radar coverage.

Effective site height is the difference between the terrain elevation of the radar position and the mean of the patch center elevations of all of the clutter patches (i.e., most of the visible terrain) between 2- and 12-km range that occurred at that site (see Appendix C for example of clutter patches at six sites). Effective radar height is equal to effective site height plus antenna mast height. All of the clutter data presented in this report were measured with Phase Zero antenna mast height equal to 15 m. It is clear that, by this definition, effective site height and effective radar height are with respect to illuminated terrain only. They indicate how high the site or antenna is above the terrain causing clutter backscatter between 2 and 12 km from the site. They are not influenced by masked or shadowed terrain. Extensive use of effective site height and radar height was made in non-site-specific clutter modeling investigations [4].

At four sites that were visited early in the measurements program and were not subsequently revisited, analog clutter measurements only (i.e., PPI scope photography in stepped levels of IF attenuation) were obtained. These four sites are indicated by footnote in Table A-1 as sites for which no digital data exist. A few other sites are indicated by other footnotes in Table A-1 as sites for which calibration is uncertain for one reason or another. Other reasons besides lack of or uncertain digital data prevent all 107 sites from being used in each of the modeling investigations that require averaging over many sites. For example, not all sites have positive effective radar heights. In the body of this report, 87 sites were used when assembling clutter amplitude distributions for positive depression angle (e.g., see Figure 25), and 96 sites were used when assembling distributions of average patch mean clutter strength (e.g., see Figure 23). Table A-5 shows which sites were deleted and why in arriving at these ensembles of 87 sites and 96 sites, respectively.

TABLE A-1

Location and Description of 107 Radar Ground Clutter Measurement Sites

Site Name	Province or State	Latitude (°N)	Longitude (°W)	LAND COVER Class Code (Percent Occurrence)	LANDFORM Class Code (Percent Occurrence)	Effective Site Height (m)
Altona[1]	Man.	49.32	97.70	—	—	
*Altona II	Man.	49.19	97.66	21(100)	1(100)	−2
Beausejour[3]	Man.	50.14	96.20	—	—	20
*Beiseker	Alta.	51.39	113.27	21(100)	3(43), 2(36), 9(9), 7(6), 1(4), 8(2)	76
*Beulah	N. Dak.	47.30	101.74	21(62), 31(34), 11(4)	2(33), 4(23), 3(21), 1(11), 7(11), 9(1)	47
*Big Grass Marsh	Man.	50.39	98.85	41(31), 62(20), 31(19), 21(17), 33(13)	1(100)	−3
Bisset	Man.	51.03	95.68	43(83), 52(17)	5(54), 3(17), 2(13), 6(8), 7(4), 8(4)	−20
*Blue Knob	Pa.	40.29	78.55	43(62), 21(31), 11(5), 70(2)	4(37), 7(37), 8(17), 6(7), 5(2)	338
*Booker Mt.	Nev.	38.10	117.19	33(46), 70(46), 12(8)	7(29), 8(24), 2(18), 1(12), 4(12), 3(5)	336
*Brazeau	Alta.	53.04	115.43	43(64), 51(13), 62(9), 21(4), 42(4), 61(4), 41(1), 52(1)	3(31), 1(21), 4(16), 7(14), 2(12), 8(5), 5(1)	142
Bromley Mt.	Vt.	43.21	72.94	43(88), 21(6), 44(6)	7(86), 2(7), 3(7)	74
Burnstick	Alta.	51.97	114.78	43(63), 21(21), 62(16)	3(25), 5(25), 2(21), 8(15), 7(14)	64
Calgary East	Alta.	50.98	114.18	11(29), 31(18), 41(16), 12(13), 21(13), 14(4), 52(4), 22(3)	3(35), 2(31), 7(21), 1(10), 4(3)	60
Calgary West	Alta.	51.00	114.23	41(41), 31(28), 11(13), 12(9), 21(9)	3(52), 4(35), 2(9), 7(4)	109
Cary Mound	Wis.	44.50	90.22	41(50), 21(47), 11(3)	3(50), 1(46), 2(4)	66
Casenovia	N.Y.	42.93	75.93	21(50), 41(50)	4(70), 2(10), 7(10), 3(5), 9(5)	12
Coaldale	Alta.	49.75	112.62	21(91), 11(9)	3(47), 1(37), 2(16)	−12
*Cochrane	Alta.	51.20	114.45	31(52), 21(36), 41(12)	2(33), 7(21), 3(17), 4(15), 5(8), 1(4), 6(2)	104

TABLE A-1 (Continued)
Location and Description of 107 Radar Ground Clutter Measurement Sites

Site Name	Province or State	Latitude (°N)	Longitude (°W)	LAND COVER Class Code (Percent Occurrence)	LANDFORM Class Code (Percent Occurrence)	Effective Site Height (m)
*Cold Lake	Alta.	54.43	110.18	21(39), 43(39), 11(5), 52(5), 61(5), 12(3), 31(2), 62(2)	1(40), 3(33), 1(12), 5(9), 7(6)	25
*Corinne	Sask.	50.05	104.62	21(70), 11(15), 51(15)	1(60), 2(20), 3(20)	1
Crystal[1]	N. Dak.	48.62	97.62	—	—	—
Cypress Hills[4]	Sask.	49.58	109.74	—	—	164
Dana	Sask.	52.28	105.77	21(69), 41(29), 11(2)	3(41), 5(34), 1(15), 2(10)	44
*Dundurn	Sask.	51.85	106.57	41(30), 21(23), 32(23), 52(8), 11(4), 14(4), 31(4), 51(4)	3(45), 5(35), 1(10), 2(10)	-3
Dutch Corner	Pa.	40.11	78.48	43(63), 21(34), 12(3)	4(32), 8(24)	41
Edson[3]	Alta.	53.84	116.82	—	—	177
Electronics Park	N.Y.	43.11	76.19	11(32), 24(26), 41(26), 12(16)	2(34), 1(20), 3(13), 5(13), 7(13), 6(7)	-30
Equinox Mt.	Vt.	43.16	73.12	43(91), 21(9)	7(65), 8(14), 5(11), 2(8), 6(2)	663
Gull Lake East	Man.	50.40	96.49	43(50), 21(38), 32(6), 52(6)	1(46), 3(31), 2(23)	5
Gull Lake East II	Man.	50.41	96.50	43(52), 21(33), 61(7), 32(4), 62(4)	1(45), 3(30), 2(25)	16
*Gull Lake West	Man.	50.40	96.53	43(49), 21(21), 33(8), 62(8), 61(6), 12(4), 52(4)	1(67), 3(27)	28
Hawk Hills	Alta.	57.65	117.40	43(88), 62(12)	2(45), 3(41), 5(7), 7(7)	212
Hay River	N.W.T.	60.75	115.86	43(40), 61(40), 11(20)	6(30), 1(14), 3(14), 4(14), 5(14), 8(14)	1
Hay River II	N.W.T.	60.69	115.92	61(31), 62(31), 43(19), 51(19)	1(50), 3(38), 5(6), 6(6)	—
*Headingley	Man.	49.88	97.40	21(30), 41(22), 51(12), 14(10), 16(8), 11(6), 24(6), 52(6)	1(69), 3(31)	3
High Knob	Pa.	41.30	75.13	43(60), 52(23), 61(10), 11(7)	4(46), 2(39), 7(15)	165
High Level	Alta.	58.60	117.14	41(40), 61(40), 62(10), 14(7), 10(3)	1(76), 2(12), 3(12)	-6

120

TABLE A-1 (Continued)

Location and Description of 107 Radar Ground Clutter Measurement Sites

Site Name	Province or State	Latitude (°N)	Longitude (°W)	LAND COVER Class Code (Percent Occurrence)	LANDFORM Class Code (Percent Occurrence)	Effective Site Height (m)
*Katahdin Hill	Mass.	42.46	71.27	43(55), 11(31), 12(8), 14(5), 21(1)	5(65), 3(22), 2(5), 4(5), 1(3)	31
Kindersley	Sask.	51.33	109.45	2(93), 31(7)	3(55), 5(21), 1(15), 3(9)	46
Kingston	Ont.	44.24	76.46	21(40), 43(26), 52(18), 11(5), 12(5), 32(2), 62(2), 70(2)	3(35), 2(30), 1(23), 6(8), 5(2), 7(2)	0
*Knolls	Utah	40.74	113.28	70(51), 33(49)	1(77), 4(9), 7(9), 5(5)	−1
Knolls East	Utah	40.73	113.14	33(50), 70(50)	1(78), 2(11), 7(11)	14
Lethbridge North	Alta.	49.76	112.86	21(38), 11(19), 31(16), 12(14), 41(11), 51(2)	1(42), 3(22), 9(22), 2(8), 8(6)	0
*Lethbridge West	Alta.	49.71	112.93	21(36), 31(33), 11(13), 12(9), 14(7), 41(2)	1(30), 3(26), 9(26), 8(10), 5(8)	25
Little America	Wis.	41.54	109.88	33(100)	3(42), 4(23), 7(19), 2(8), 5(4), 8(4)	15
*Magrath	Alta.	49.41	112.97	21(64), 31(19), 51(11), 11(3), 32(3)	2(25), 3(20), 7(15), 9(15), 1(13), 4(8), 5(2), 6(2)	79
Manigotagan	Man.	51.11	96.29	43(50), 62(33), 52(17)	3(75), 1(25)	—
Many Island	Alta.	50.18	110.54	31(68), 21(32)	2(29), 3(23), 7(14), 5(11), 4(9), 1(7), 9(7)	63
Mather	Wis.	44.24	90.31	43(34), 21(22), 61(22), 62(22)	1(80), 3(20)	−6
Mayville[1]	N. Dak.	47.49	97.23	—	—	—
Mayville II	N. Dak.	47.45	97.32	21(70), 41(22), 11(8)	1(74), 3(26)	−4
Meander River	Alta.	59.32	117.35	43(55), 62(30), 14(15)	5(57), 2(29), 3(14)	−12
Melrose	Iowa	41.00	93.02	21(52), 41(48)	3(38), 7(24), 2(18), 1(10)	15
Metropolis	Nev.	41.23	115.06	33(72), 21(14), 42(14)	4(21), 8(21), 7(18), 2(15), 3(15)	−62
Moose Mt.	Sask.	49.86	102.29	41(64), 52(36)	5(71), 3(29)	−10

121

Location and Description of 107 Radar Ground Clutter Measurement Sites

Site Name	Province or State	Latitude (°N)	Longitude (°W)	LAND COVER Class Code (Percent Occurrence)	LANDFORM Class Code (Percent Occurrence)	Effective Site Height (m)
*Neepawa	Man.	50.33	99.50	21(52), 41(46), 11(2)	3(35), 2(28), 7(15), 1(13), 5(7), 9(2)	-30
Nipawin	Sask.	54.11	104.52	44(34), 61(25), 62(22), 45(13), 41(3), 43(3)	6(25), 2(21), 1(18), 7(18), 5(12), 3(3), 4(3)	35
*North Truro[2]	Mass.	42.03	70.05	—	—	—
*Orion	Alta.	49.50	110.81	31(56), 21(38), 62(3), 33(1), 51(1), 52(1)	2(30), 3(21), 5(17), 7(14), 4(10), 9(6), 1(2)	41
*Pakowi Lake	Alta.	49.32	110.85	31(41), 21(26), 32(21), 33(9), 22(3)	1(50), 2(19), 3(19), 5(6), 4(3), 7(3)	11
Peace River North	Alta.	56.24	117.27	41(50), 21(36), 51(12), 43(2)	7(41), 3(29), 2(27), 8(3)	29
Peace River South	Alta.	56.21	117.27	41(44), 21(35), 33(10), 43(4), 51(4), 31(2)	3(45), 7(30), 2(12), 1(3)	19
*Peace River South II	Alta.	56.20	117.27	41(48), 21(40), 33(10), 51(2)	3(46), 7(24), 2(18), 5(6), 1(3), 4(3)	12
Penhold	Alta.	52.13	113.72	21(71), 41(20), 11(6), 31(3)	3(45), 5(16), 2(13), 7(11), 1(8), 6(5), 9(2)	92
*Penhold II	Alta.	52.18	113.97	21(64), 52(11), 41(8), 43(8), 11(3), 12(3), 62(3)	1(48), 3(28), 2(12), 7(7)	40
Picture Butte[1]	Alta.	49.89	112.97	—	—	—
*Picture Butte II	Alta.	49.92	112.82	21(83), 11(7), 14(7), 12(3)	3(57), 2(31), 7(6), 9(4), 1(2)	54
*Plateau Mt.	Alta.	50.22	114.52	42(35), 31(29), 70(26), 4(19), 32(1)	8(91), 2(4), 3(4), 7(1)	279
Pointe du Bois	Man.	50.30	95.55	43(54), 70(35), 52(11)	3(38), 5(31), 2(14), 1(7), 4(4), 6(3), 7(3)	-6
*Polonia	Man.	50.36	99.61	21(63), 41(35), 11(2)	2(38), 3(32), 5(15), 7(11), 1(4)	128
Port Austin	Mich.	44.03	83.00	21(33), 41(29), 61(21), 52(17)	1(57), 3(24), 6(19)	5
*Puskwaskau	Alta.	55.22	117.49	43(56), 21(15), 62(15), 41(7), 52(7)	2(50), 1(21), 3(21), 6(4), 7(4)	129
Rae	N.W.T.	62.50	116.47	62(36), 43(32), 61(23), 52(9)	1(41), 3(32), 5(27)	15

Location and Description of 107 Radar Ground Clutter Measurement Sites

Site Name	Province or State	Latitude (°N)	Longitude (°W)	LAND COVER Class Code (Percent Occurrence)	LANDFORM Class Code (Percent Occurrence)	Effective Site Height (m)
*Rosetown Hill	Sask.	51.54	107.93	21(95), 11(5)	3(45), 1(24), 2(14), 7(10), 5(7)	28
Rosetown North	Sask.	51.63	108.00	21(67), 32(17), 11(10), 51(4), 12(2)	3(40), 1(38), 9(11), 2(9), 7(2)	1
Rouleau	Sask.	50.23	104.87	21(90), 11(5), 51(5)	1(95), 3(5)	20
*Sandridge	Man.	50.61	97.51	41(52), 21(27), 33(13), 22(5), 14(3)	1(95), 3(5)	0
Saskatoon	Sask.	52.14	106.67	21(37), 11(32), 41(16), 12(5), 23(5), 51(5)	1(50), 2(33), 3(17)	-12
*Scranton	Pa.	41.38	75.59	43(56), 11(27), 12(11), 21(6)	4(43), 2(32), 5(13), 7(9), 3(3)	262
*Shilo	Man.	49.75	99.63	41(44), 21(26), 31(18), 32(6), 11(3), 12(3)	1(50), 3(36), 2(7), 5(7)	3
Simonette	Alta.	54.68	117.54	41(33), 43(31), 42(22), 45(8), 61(4), 62(2)	2(45), 4(28), 3(18), 7(7), 1(2)	111
*Spruce Home	Sask.	53.45	105.76	43(51), 21(42), 22(6), 11(1)	1(51), 3(37), 2(12)	25
Stahlville	Alta.	51.28	113.23	21(92), 31(4), 32(4)	3(47), 2(28), 7(21), 4(2), 5(2)	62
Stanley Mission[3]	Sask.	55.37	104.66	—	—	3
Stavely	Alta.	50.19	113.90	31(64), 41(24), 21(12)	4(54), 7(39), 2(7)	135
Steen River	Alta.	59.72	117.14	43(72), 62(14), 41(7), 42(7)	3(58), 6(25), 1(17)	5
*Strathcona	Alta.	51.03	114.17	11(33), 12(20), 41(15), 31(13), 51(11), 21(8)	7(33), 3(28), 4(19), 2(14), 1(3), 5(3)	72
*Suffield	Alta.	50.27	111.14	31(86), 12(7), 11(5), 52(2)	5(50), 3(42), 2(8)	20
Tennion	Alta.	49.96	112.55	21(60), 31(33), 51(7)	3(27), 7(21), 9(21), 1(13), 2(4), 5(4)	4
The Pas	Man.	53.66	101.27	62(36), 61(33), 21(17), 42(6), 41(5), 11(2), 43(1)	1(88), 3(12)	5
Thompson	Iowa	43.33	93.78	21(96), 11(4)	1(75), 3(25)	35

TABLE A-1 (Continued)
Location and Description of 107 Radar Ground Clutter Measurement Sites

Site Name	Province or State	Latitude (°N)	Longitude (°W)	LAND COVER Class Code (Percent Occurrence)	LANDFORM Class Code (Percent Occurrence)	Effective Site Height (m)
Tolstoi[5]	Man.	49.08	96.87	—	—	1
Tolstoi II	Man.	49.05	96.87	21(50), 41(50)	1(63), 3(37)	0
Tonopah	Nev.	37.60	116.45	70(52), 30(48)	2(30), 7(26), 3(21), 1(13), 8(10)	-115
*Turtle Mt.	Man.	49.06	100.18	52(46), 43(29), 41(25)	5(69), 3(31)	8
Vananda	Mont.	46.47	107.02	33(69), 21(19), 42(9), 31(2)	2(40), 4(37), 7(11), 3(9), 1(3)	66
*Vananda East	Mont.	46.45	106.98	33(87), 21(10), 61(3)	4(41), 7(24), 2(21), 3(12), 1(2)	94
*Wachusett Mt.	Mass.	42.49	71.89	41(55), 21(27), 11(9), 52(9)	4(59), 5(18), 7(15), 3(8)	333
*Wainwright	Alta.	52.82	111.06	41(47), 32(27), 21(22), 52(2), 12(1), 51(1)	3(48), 7(16), 1(14), 5(14), 2(8)	70
*Waterton	Alta.	49.15	113.83	31(27), 41(27), 33(16), 42(14), 70(8), 52(5), 40(3)	7(33), 4(26), 8(16), 2(10), 5(6), 1(3), 3(3), 6(3)	-88
*Westlock	Alta.	54.16	113.70	21(38), 41(27), 52(14), 11(8), 43(8), 33(5)	3(59), 1(24), 2(17)	24
Westray	Man.	53.50	101.39	61(50), 62(45), 43(5)	1(67), 3(28), 2(5)	28
White Sands	N. Mex.	33.50	106.33	33(49), 70(49), 11(2)	3(28), 2(19), 8(19), 7(16), 5(9), 4(7), 1(2)	-80
*Woking	Alta.	55.55	118.75	41(71), 21(29)	2(44), 4(26), 3(15), 7(15)	36
*Wolseley	Sask.	50.36	103.15	21(73), 41(21), 52(4), 11(2)	3(47), 5(33), 1(16), 2(4)	17
Yellowknife North[3]	N.W.T.	62.54	114.37	—	—	2
Yellowknife West	N.W.T.	62.30	114.46	43(38), 70(38), 52(24)	5(100)	9

1 No Phase Zero digital data
2 No Phase Zero measurements
3 Phase Zero azimuth calibration uncertainty
* Phase One measurements (in addition to Phase Zero measurements, except for North Truro)

4 Phase Zero azimuth alignment uncertainty
5 Phase Zero amplitude calibration uncertainty

124

TABLE A-2

Land Cover Classes

Land Cover Class	Relative Incidence of Occurrence* (%)
1. Urban or Built-up Land 11 Residential 12 Commercial	5.6
2. Agricultural Land 21 Cropland 22 Pasture	36.2
3. Rangeland 31 Herbaceous 32 Shrub 33 Mixed	17.1
4. Forest 41 Deciduous 42 Coniferous 43 Mixed	31.4
5. Water 51 Rivers, Streams, Canals 52 Lakes, Ponds, Sloughs	0.2
6. Wetland 61 Forested 62 Non-Forested	4.2
7. Barren Land	5.3
	100.0

*Percentage of primary classified patches out of the 2177 patches between 2- and 12-km range from the radar.

TABLE A-3
Landform Classes and Descriptions

Landform Class		Terrain Relief (ft)	Terrain Slope (deg); Comments	Relative Incidence of Occurrence* (%)
1	Level (LEV)	< 25'	< 1°	26.2
2	Inclined (INC)	> 50'	1° – 2°; Unidirectional	15.5
3	Undulating (UND)	25' – 100'	< 1°; Regular sequences of gentle slopes; wavelike	25.6
4#	Rolling (ROL)	> 150'	2° – 5°; Regular to irregular sequences of moderate slopes	9.9
5	Hummocky (HUM)	25' – 150'	< 2°; Complex sequences of slopes	9.8
6#	Ridged (RID)	50' – 500'	2° – 10°; Sharp breaks in slope at tops and bottoms of terrain features	0.7
7#	Moderately Steep (MST)	> 100'	2° – 10°; Unidirectional	7.0
8#	Steep (STP)	> 100'	10° – 35°; Frequently unidirectional	4.3
9	Broken (BRK)	> 50'	1° – 5°; Short dissected slopes	1.0
				100.0

*Percentage of primary classified patches out of the 2177 patches between 2- and 12-km range from the radar.

#Classes so indicated are "high-relief;" classes not so indicated are "low-relief."

TABLE A-4

More Complete Descriptions of Landform Classes

Terrain Descriptions	LANDFORM CLASS			
	1 Level	2 Inclined	3 Undulating	4 Rolling
Relief	Generally >25', may contain contour microphotography	>50', 2 or more contours, intermediate between level and moderately steep	25'–100', intermediate between level, rolling, and hummocky	>150', greater relief than undulating or hummocky
Slope	<1°, constant not broken by marked irregularities, least slope of all classes	1°–2°, constant often unidirectional, not broken by marked irregularities, greater slope than level or undulating	>1° overall slope, regular sequence of gentle slopes, some local slopes >1°, wavelike convexities and cavities	2°–5°, regular to irregular sequences of moderate slopes, overall slope greater than hummocky class
Contour Pattern	No pattern with contour interval of 25' or greater	Equal spaced or parallel contours common	Semiparallel to highly convoluted	Convoluted, curved contours around low or broad hills. Irregular when gullied
Associated Features	Wetlands, depression contours	Frequently occurs with gullies or stream channels, lacks wetlands	Temporary or permanent standing water bodies, wetlands	Frequently gullied
Topographic Position	Occupies uplands, lowlands, plains	Lower, mid, and upper slope positions	Lower slopes, pediments, plains, uplands	Mid to upper slope positions
Secondary Modifier	Most common with undulating terrain	Common with undulating or moderately steep terrain	Common with inclined or hummocky terrain	Common with inclined, less frequent with moderately steep and steep classes
Landform Origin	Glacial drift, erosional surface, lacustrine or alluvial deposits	Glacial drift, erosional surface, lacustrine or alluvial deposits, rock structure	Glacial drift, lacustrine or alluvial deposits, erosional surface	Rock structure or glacial drift
Additional Comments	Commonly occurs with 25' contour interval	Mapped using various contour intervals (i.e., 25' or 50')	Commonly occurs with 25' contour interval	Occurs with 25' or 50' contour intervals

127

TABLE A-4 (Continued)
More Complete Descriptions of Landform Classes

Terrain Descriptions	LANDFORM CLASS				
	5 Hummocky	6 Ridged	7 Moderately Steep	8 Steep	9 Broken
Relief	25'–150', usually greater relief than undulating, less than rolling	Micro ridges 25'–50', macro ridges 50'–500', sharp created linear morphology	>100'	>100'	>50'
Slope	<2°, complex sequence of slopes, some local slopes >2°, knobs and kettles	2°–10°, generally sharp break in slope at top and bottom of feature	2°–10°, intermediate between inclined and steep, unidirectional	10°–35°, greater slope than moderately steep, frequently unidirectional	1°–5°, short dissected slopes
Contour Pattern	Irregular, broken, numerous closed contours, rarely linear or parallel	Linear or parallel (finger-like), can be irregular or broken	Convoluted to parallel, indented from gullies and spurs	Convoluted to parallel, indented from gullies and spurs	Indented, convoluted from gullies and spurs
Associated Features	Sloughs or ponded water, depression contours	Often occurs with adjacent ridges, shoreline ridges associated with water	River valleys, escarpments, foothills, mountains	River valleys, escarpments, foothills, mountains	Frequently occupies river valleys, stream channels
Topographic Position	Lower slopes, plains, uplands	Lower, mid, and upper slope positions	Mid to upper slope positions	Mid to upper slope positions	Mid to upper slope positions
Secondary Modifier	Common with undulating or inclined	Common with moderately steep or rolling terrain	Commonly forms single modifier, also occurs with inclined, ridged, steep	Commonly forms single modifier, also occurs with moderately steep class	Occurs with undulating and rolling terrain
Landform Origin	Predominately glacial drift, less frequent erosional surfaces	Shoreline deposit, glacial drift, rock structure, erosional surface	Rock structure, erosional surfaces, glacial drift	Rock structure, erosional surfaces	Erosional surface, rock structure
Additional Comments	Not always visible from maps, may require air photo interpretation to identify pattern	Not always visible from maps, may require air photo interpretation to identify pattern	Occurs with 25', 50', or 100' contour intervals	Occurs with 100" contour intervals, typical of mountainous bedrock terrain	Not always visible from map, dissection pattern may require air photo interpretation

TABLE A-5

Sites Deleted in Clutter Strength Ensembles

	Number of Sites with Problem	Number of Remaining Available Sites
Number of sites in Table A-1	—	107
No digital clutter data (Altona I, Crystal, Mayville Picture Butte)	4	103
No Phase Zero data; Phase One measurement only (North Truro)	1	102
Azimuth calibration uncertainty (Beausejour, Edson, Stanley Mission, Yellowknife North)	4	98
Azimuth alignment uncertainty (Cypress Hills)	1	97
Amplitude calibration uncertainty (Tolstoi)	1	96*
Negative effective radar height, including 15-m mast height (Bissett, Electronics Park, Metropolis, Neepawa, Tonopah, Waterton, White Sands)	7	89
No terrain elevation information, no topographic maps (Hay River II, Manigotagan	2	87**
No 48-km maximum range experiment (Dutch Corner)	1	86

* Number of sites contributing to distributions of patch mean clutter strengths, e.g., Fig. 23.
**Number of sites contributing significantly at positive depression angle.

129

APPENDIX B

PHASE ZERO RADAR

B.1 BACKGROUND

The radar ground clutter results presented in the body of this report are based on clutter measurements that were obtained with the Phase Zero radar ground clutter measurement instrument. This instrument and its program of measurements are referred to as Phase Zero because of the precursor or pilot role in which they served in site selection, clutter measurements, and data analysis and modeling development prior to the full-scale program of multifrequency measurements which subsequently came to be known as Phase One. The principal purpose of this appendix is to provide some additional information describing the Phase Zero radar and what was required in terms of hardware modifications and software processing to enable this commercial-grade radar to be used as a calibrated measurement instrument. Some ancillary information describing the Phase One radar is also provided here.

The programmatical context in which clutter measurements were undertaken at Lincoln Laboratory required quantifying the performance of surface-sited radars against low-flying aircraft. Ground clutter often limits the system performance of surface radars as they attempt to detect and track low-altitude targets in a background of ground clutter interference over ranges from as close as a few kilometers to as great as 25 or 50 kilometers. The objective of the clutter measurements program was to develop clutter modeling capabilities that provide accurate predictions of clutter effects in typical surface-sited radars for a variety of terrain types. Thus, of principal interest is ground clutter as it affects such radars, typically at grazing incidence over many square kilometers of composite heterogeneous terrain.

To develop clutter modeling capabilities, clutter measurements were required at many sites. Thus, both the Phase Zero and Phase One clutter measurement instruments were mobile, with erectable towers on truck platforms. As with typical surface-sited surveillance radars, the antennas for these instruments had beams which in elevation were wide, fixed, and boresight-directed at the horizon, and in azimuth were narrow and positionable. Thus, azimuth resolution is given by beam position. For a given azimuth beam position, the terrain at all ranges from one to many kilometers was usually illuminated within the elevation beamwidth as it existed with its boresight fixed to be locally horizontal. No elevation beam control was available. Both Phase Zero and Phase One radars were uncoded pulsed systems, so that range resolution was given by RF pulsewidth. Of course the clutter results, although measured with radars emulative of surveillance radars, are also applicable to tracking radars with pencil beams, when those beams are low, as they are when tracking very low altitude targets and clutter power is entering the receiver through the main lobe. In fact, the clutter results, being absolute measures of ground clutter reflectivity, are generally applicable to any system as long as the frequency, polarization, resolution, and terrain scale (i.e., amount of terrain illuminated and over which statistical averaging is performed) match those of the measurements. Brief summaries of the Phase Zero and Phase One instruments are provided in Table 1 in the body of this report. In all of this, it is well to remember that the Phase Zero instrument provided only a relatively crude

131

(i.e., slow) measurement of amplitude only, whereas the Phase One instrument was (for its day) a modern computer-controlled instrumentation radar which recorded highly coherent and stable (i.e., specified to provide 60 dB of clutter improvement factor from a hypothetical two-pulse canceller MTI circuit) in-phase and quadrature samples of the raw clutter return signal from 13-bit A/D converters at a 10-MHz sampling rate.

Later, Section B.3 discusses Phase Zero calibration. However, before beginning that specific discussion, a brief general discussion is provided here concerning the effects of antenna pattern gain variation both in elevation and azimuth on ground clutter measurements with either the Phase Zero or Phase One radars. For both Phase Zero and Phase One radars, the backscatter from a clutter patch was measured at some angular position on the fixed elevation antenna pattern. Although this angle was usually small and usually within the one-way 3-dB points on the free-space elevation pattern, it was of course rigorously zero (i.e., on-boresight) only if the source of clutter backscatter was at the same elevation as the antenna phase center. Since this was seldom rigorously true, computations of clutter strength were corrected for elevation gain variations. To do this required knowledge of the relative difference in terrain elevation between the radar and the clutter patch (i.e., conversion from a raw measurement of clutter signal strength to an absolute measure of clutter reflectivity cannot be performed on the basis of the radar measurement and radar instrumentation parameters only). This relative difference in mean height above sea level between the radar position and the clutter patch, as well as antenna mast height, range to the clutter patch, and the decrease in the effective elevation of the clutter patch due to a 4/3 radius spherical earth, were used to compute the off-axis angle on the elevation pattern at which the clutter measurement was made. The two-way gain adjustment due to this non-zero off-axis angle was accounted for in computation of absolute clutter reflectivity, even when the angle was within the one-way 3-dB elevation beamwidth. Note that this off-axis angle, which is defined in a Cartesian coordinate system locally centered and horizontal at the antenna phase center (see Appendix D), is slightly different from the depression angle (also, see Appendix D) used in the body of this report as a major parameter in clutter modeling. Depression angle is rigorously defined in a Cartesian coordinate system locally centered and horizontal at the terrain point from which backscatter is emanating. These two angles differ by the amount that the two Cartesian reference frames (i.e., local horizontals) in which they are respectively defined are rotated with respect to each other due to the spherical earth (see Appendix D). Since this elevation gain correction requires terrain elevation information specific to each site and measurement, it was often not known in advance and was not automatically included in the calibration algorithms by which the raw measurement data were converted to calibrated clutter files (see Figure B.12). To include it would have required correlation of clutter measurement data with digital terrain elevation data at calibration time, a rather large undertaking for what was usually a small, if not zero, correction. Rather, this correction was made subsequently in the application programs (particularly, the patch program and software in which ensembles of patch results were combined; see Figure B.12) which accessed the calibrated clutter files. The usually small correction was made globally on a patch basis rather than on a pulse by pulse or individual sample basis. Terrain descriptive information, including relative terrain elevations, was included as input with these patch application programs.

The accuracy of a clutter measurement with either the Phase Zero or Phase One radar requires that the azimuth sidelobe levels be low. That is, the clutter power received from strong clutter sources through sidelobes must be enough weaker than main lobe clutter power, even from relatively weak main lobe clutter sources, so as not to significantly degrade the main lobe measurement. There was little evidence in the measured data (i.e., a continuous ring of clutter in a range gate) to suggest significant sidelobe contamination. Occasionally, a very strong discrete clutter source would smear itself out over a few additional azimuth samples as it continued to be received a bit beyond the one-half power point on the main lobe. However, for energy to actually enter through sidelobes, it would have had to overcome, in the Phase Zero radar, 65 dB of pattern selectivity (see Table B-4), and this almost always puts the return below noise level.

The history of use of the Phase Zero and Phase One clutter measurement instruments is as follows. The requirement for a large-scale ground clutter measurement program became defined in 1977–78. A measurement equipment procurement cycle was initiated which led to a contract being let to the General Electric Company, Syracuse, New York, for the development and fabrication of the full-scale, multifrequency Phase One equipment. The Phase One equipment was delivered to Lincoln Laboratory late in 1981. Meanwhile, to avoid delay in the overall program while the Phase One equipment was in procurement, in 1979 a commercial, X-band, marine navigation radar was acquired and installed in an all-wheel drive one-ton truck. The truck was equipped with a 50-ft pneumatically extendable antenna mast and self-contained prime power. An on-board clutter data digital recording capability was implemented. The resultant clutter measurement instrument was referred to as Phase Zero. A photograph of the Phase Zero clutter measurement instrument is shown in Figure B-1.
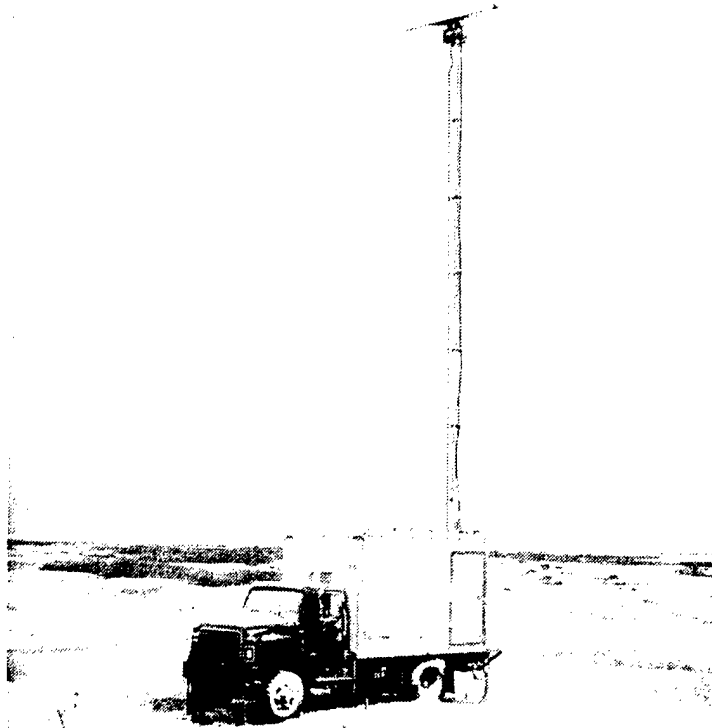
Figure B-1. Phase Zero equipment at Dundurn, Saskatchewan. Camera viewing direction is north. October.

The Phase Zero instrument made its first clutter measurement tour in October 1979. Following that, it also made measurements in 1980, 1981, 1982, and 1983, and accessed 106 of the 107 sites listed in Table A-1. (Phase Zero did not measure the North Truro site at which sea clutter measurements were conducted with Phase One equipment; see Ref. 22.) A map of these 106 sites is shown in Figure B-2. The schedule of Phase Zero ground clutter measurements is shown in Table B-1 The Phase Zero instrument continued to be in use subsequently in other systems-related aspects of overall program activities at Lincoln Laboratory. The initial primary purpose fulfilled by Phase Zero in clutter measurements and modeling was in site selection and access, in setting up the initial liaison with landowners, and in the overall establishment of a measurement program involving mobile radar equipment accessing many sites widely dispersed throughout the United States and Canada. Beyond this, however, the resulting extensive data base of digital X-band clutter measurements was utilized to develop approaches to clutter modeling. As a result, these approaches were well defined when Phase One measurements were begun late in 1981. Therefore, much of the effort in dealing with the much more extensive multifrequency Phase One data was associated with

reducing it, calibrating it, and processing it through terrain classification modeling procedures already established in the Phase Zero program.
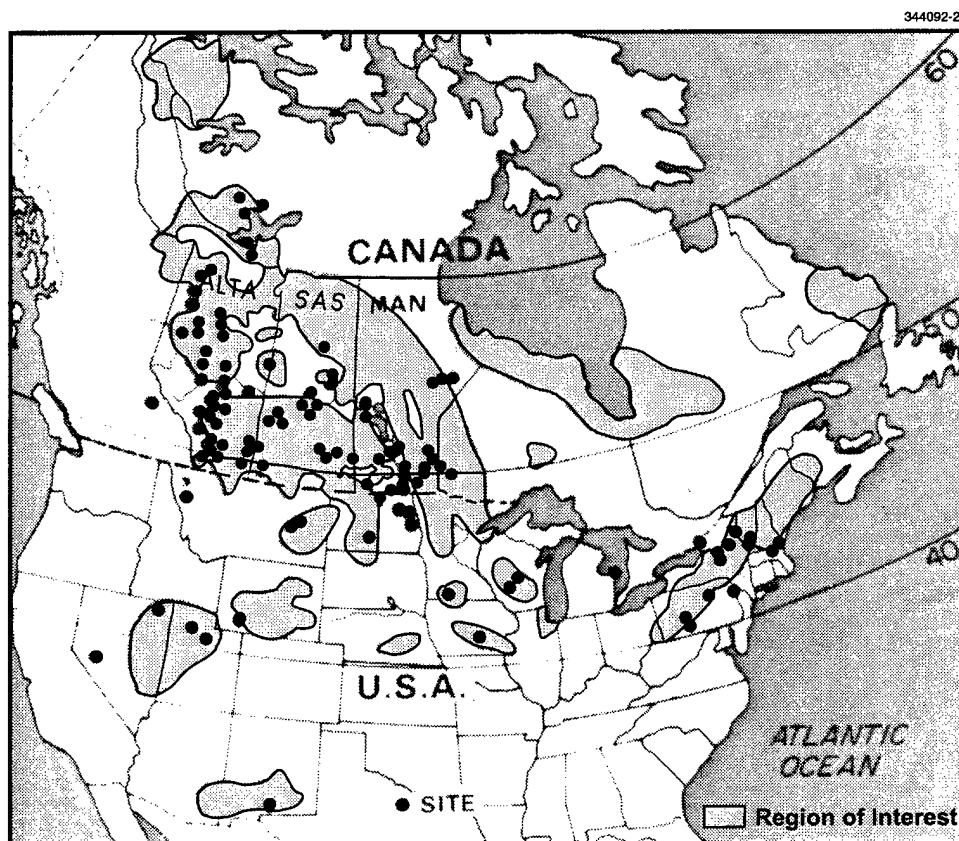
Figure B-2. Map of 106 Phase Zero sites. See Table A-1.

Summary Schedule of Phase Zero Ground Clutter Measurements

Calendar Year	Active Measurement Period	Location	Duration (days)	No. of Sites Measured		
				Analog Data Only	Digital Data	
					First	Repeated
1979 Autumn	12 Oct – 29 Oct	N. Dak., Man., Sask., Alta.	18	20		
1980 Winter/ Spring/ Summer	18 Feb – 11 Mar	Man., Sask.	23		23	
	2 Apr – 14 Apr	Sask., Alta.,	13		13	
	13 May – 7 Jun	Alta, N.W.T.	26	1	18	
	8 Jul – 12 Jul	Alta.	5		6	
	30 Jul – 2 Aug	Nev.	4		1	
	11 Dec – 16 Dec	N. Mex.	6		1	
1981 Summer	14 May – 4 Jun	Mass.	2		1	1
	9 Jun – 27 Jun	Mass., Vt., N.Y., Ont., Penna, Mich., Iowa, Wisc., N. Dak., Man.	19		18	2
	25 Jul – 5 Aug	Man., Sask., Alta., N.W.T.	12		12	1
1982 Summer/ Autumn	26 Jun – 7 Jul	Nev., Utah, Wyo., Mont., N. Dak., Man., Sask.	12		8	4
	28 Jul – 31 Jul	Alta.	4		1	2
	27 Oct – 14 Nov	Alta., Sask., Man.	15			14
1983 Summer/ Autumn	10 Aug	Alta.	1			1
	16 Nov – 20 Nov	Sask., Alta.	5			3
1984 Summer/ Autumn	23 Jun	Utah	1			1
	30 Aug	Mass	1			1
				Totals	102*	30

*See Table A-5, row 3

The Phase One program involved an essentially continuous sequence of clutter measurements at many sites over the three-year period between October 1981 and October 1984. A photograph of the Phase One equipment is shown in Figure B-3. The overall Phase One radar system block diagram is shown in Figure B-4. A schematic diagram of the Phase One receiver and signal processor is shown in Figure B-5. A summary of Phase One system capabilities is shown in Table B-2.

315027-54
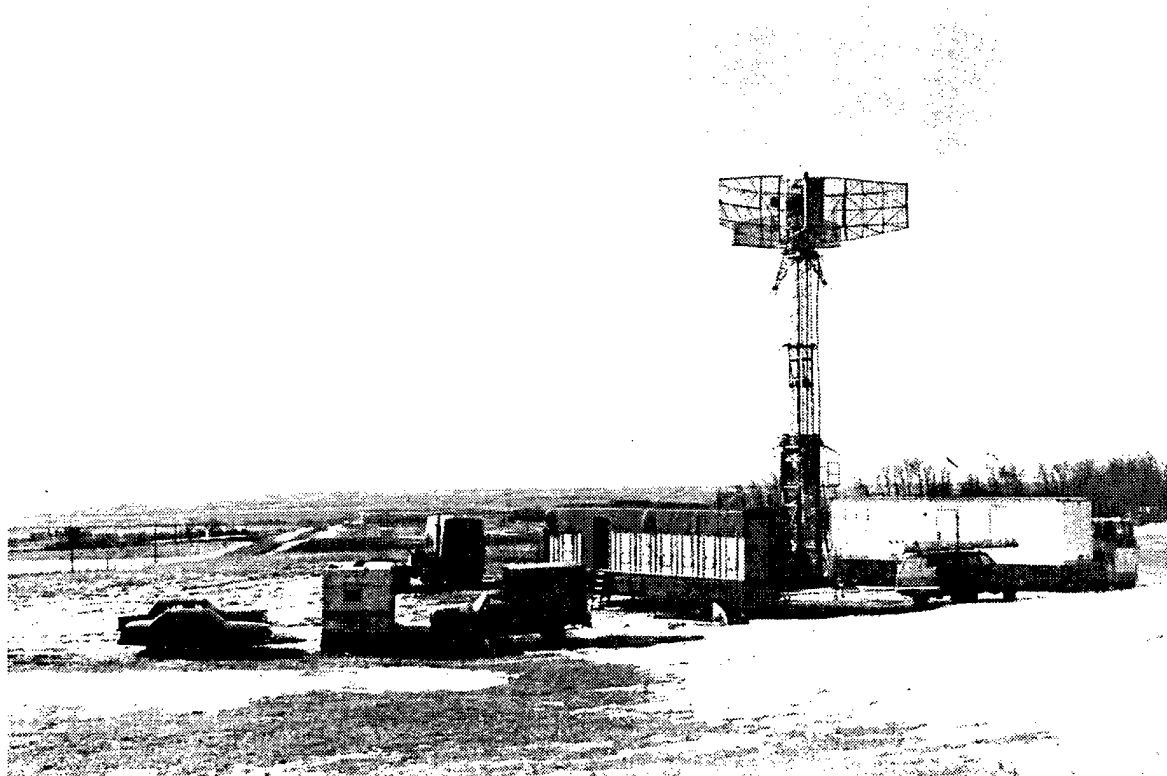
Figure B-3. Phase One equipment at Polonia, Manitoba. Camera viewing direction is south. Antenna tower is erected to 60 feet. March.
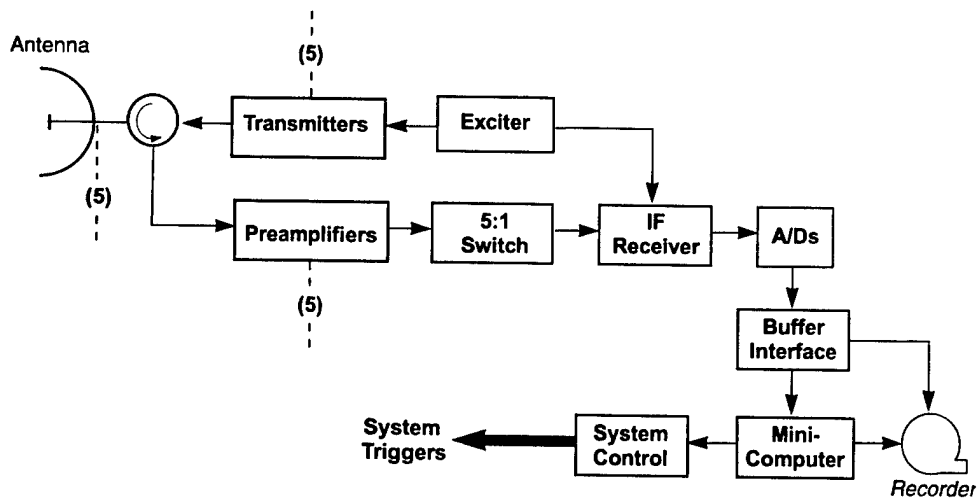
Figure B-4. Phase One instrument block diagram.
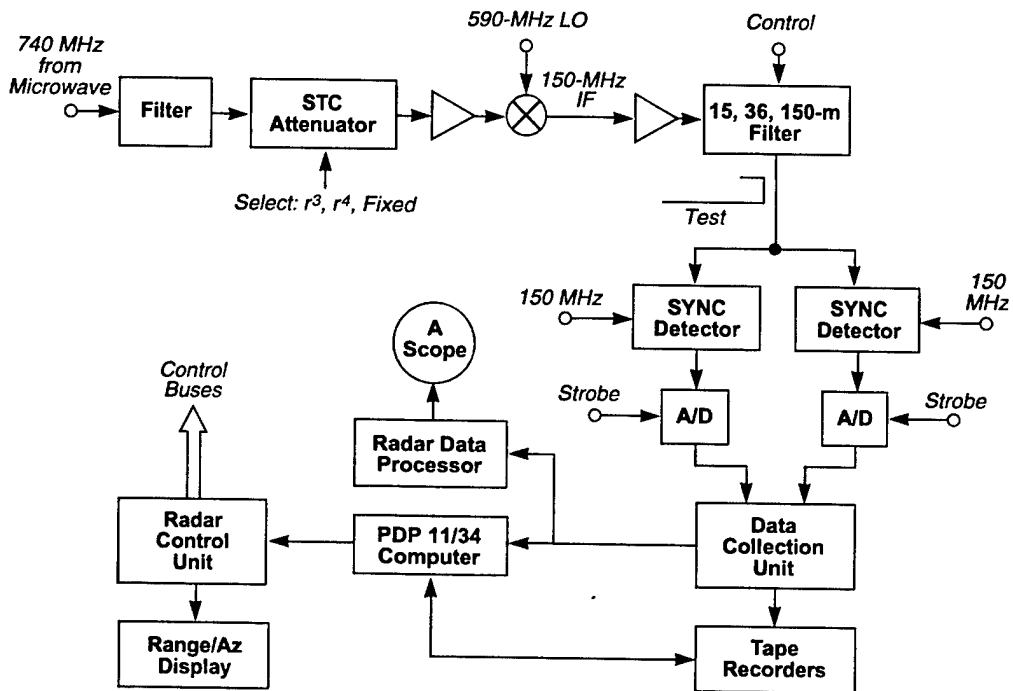
Figure B-5. Phase One receiver and signal processor.

138

TABLE B-2

Phase One System Capabilities

	VHF	UHF	L-	S-	X-Band
Frequency Limits (MHz)	162–173	420–450	1220–1280	3220–3380	8900–9300
Beamwidth (deg)					
Azimuth	13	5	3	1	1
Elevation	42	16	10	4	3
Range Resolution (m)					
Low	150	150	150	150	150
High	36	36	15	15	15
System Sensitivity					

Signal-to-Noise (dB) with:
    single pulse,
    $\sigma°F^4 = -60$ dB,
    10 km range,
    150 m waveform
	9	14	9	8	12

Clutter Improvement Factor (dB)	60	60	60	55	55
Polarization	HH or VV				
A/D Sampling Rate	1, 2, 5, or 10 MHz				
A/D Number of Bits	13				
Data Recording Rate	625 Kbytes/sec				
Output Data	I and Q				
RCS Accuracy	2 dB rms				
Minimum Range	1 km				
Dynamic Range					
Instantaneous	60 dB				
Attenuator Controlled	40 dB				
Data Collection Modes	Beam Scan, Parked Beam, Beam Step				
Azimuth Scan Rate	0 to 3 deg/sec				

A summary schedule of Phase One measurement activities during its data acquisition period is shown in Table B-3. During this period, the Phase One radar was set up and measurements were obtained 49 times on 42 different sites. A map of these 42 sites is shown in Figure B-6. There were seven repeated set-ups at previously accessed sites in order to provide data for the determination of seasonal dependencies in ground clutter. All of the Phase One sites measured (except one, North Truro) had been previously measured by Phase Zero. Phase One sites are indicated in Table A-1 with a preceding asterisk. At two sites, Beiseker and Knolls, Phase Zero and Phase One obtained measurements at (or very nearly at) the same time in order to obtain temporally and spatially coincident (or nearly coincident) data for the purposes of calibration comparison.
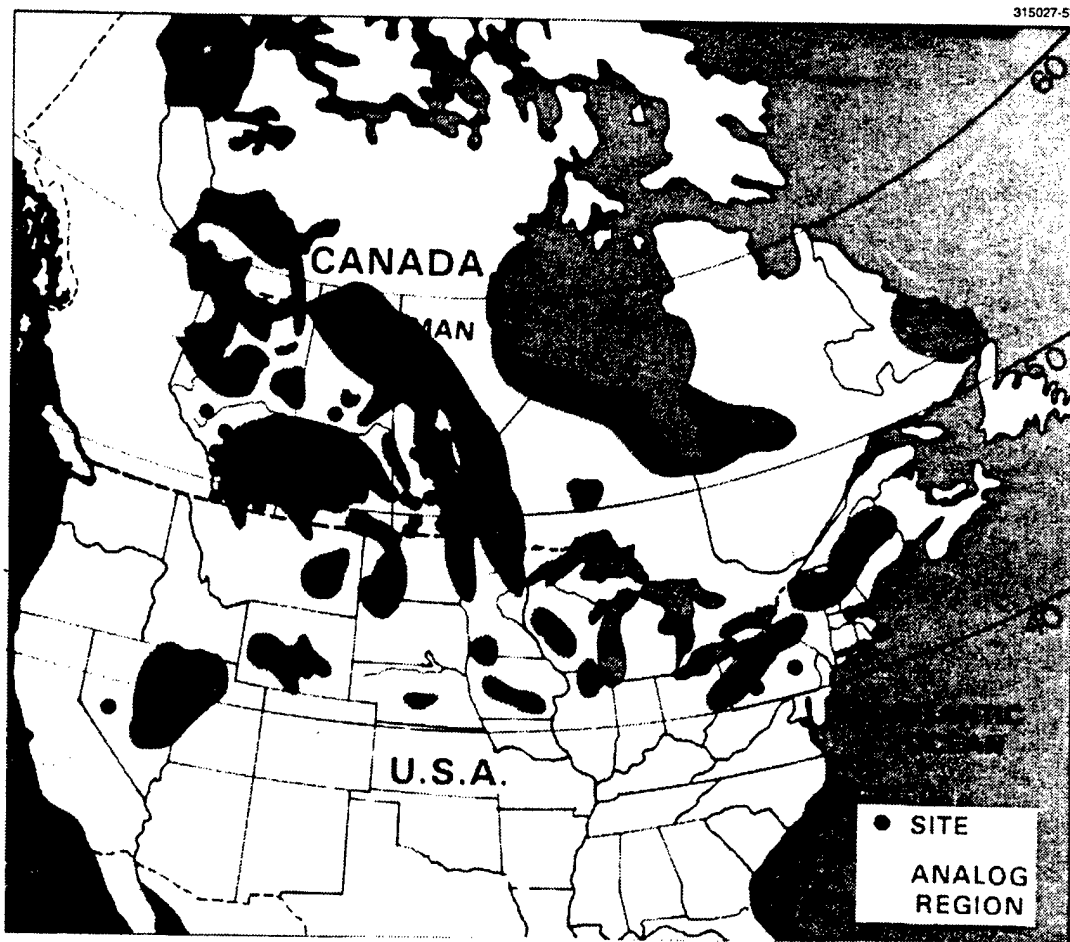

Figure B-6. Map of 42 Phase One sites. See Table A-1.

TABLE B-3
Summary Schedule of Phase One Ground Clutter Measurements

Set Up No.	Site Name	Dates Visited		Days on Site
1.	Katahdin Hill, Mass.	2 Oct – 17 Dec	1981	77
2.	Shilo, Man.	1 Feb – 2 Mar	1982	30
3.	Neepawa, Man.	3 Mar – 18 Mar	1982	16
4.	Polonia, Man.	19 Mar – 30 Mar	1982	12
5.	North Truro, Mass.	23 Jun – 21 Jul	1982	29
6.	Cochrane, Alta.	11 Aug – 31 Aug	1982	21
7.	Strathcona, Alta.	1 Sep – 25 Sep	1982	25
8.	Penhold II, Alta.	27 Sep – 16 Oct	1982	20
9.	Beiseker, Alta.	18 Oct – 13 Nov	1982	27
10.	Westlock, Alta.	15 Nov – 25 Nov	1982	11
11.	Cold Lake, Alta.	27 Nov – 9 Dec	1982	13
12.	Suffield, Alta.	11 Dec – 21 Jan	1983	42
13.	Pakowki Lake, Alta.	22 Jan – 2 Feb	1983	12
14.	Orion, Alta.	2 Feb – 11 Feb	1983	10
15.	Beiseker (2), Alta.	12 Feb – 24 Feb	1983	13
16.	Cochrane (2), Alta.	24 Feb – 18 Mar	1983	23
17.	Brazeau, Alta.	26 Mar – 13 Apr	1983	19
18.	Lethbridge West, Alta.	29 Apr – 17 May	1983	19
19.	Magrath, Alta.	17 May – 6 Jun	1983	21
20.	Waterton, Alta.	6 Jun – 16 Jun	1983	11
21.	Plateau Mountain, Alta.	17 Jun – 24 Jun	1983	08
22.	Picture Butte II, Alta.	20 Jul – 6 Aug	1983	18
23.	Beiseker (3), Alta.	6 Aug – 24 Aug	1983	19
24.	Brazeau (2), Alta.	25 Aug – 13 Sep	1983	20
25.	Puskwaskau, Alta.	28 Sep – 11 Oct	1983	14
26.	Peace River South II, Alta.	12 Oct – 3 Nov	1983	23

TABLE B-3 (Continued)
Summary Schedule of Phase One Ground Clutter Measurements

Set Up No.	Site Name	Dates Visited		Days on Site
27.	Woking, Alta.	5 Nov – 14 Nov	1983	10
28.	Beiseker (4), Alta.	16 Nov – 26 Nov	1983	11
29.	Wolseley, Sask.	29 Nov – 5 Dec	1983	07
30.	Headingley, Man.	7 Dec – 21 Dec	1983	15
31.	Altona II, Man.	5 Jan – 31 Jan	1984	27
32.	Big Grass Marsh, Man.	1 Feb – 14 Feb	1984	14
33.	Gull Lake West, Man.	15 Feb – 25 Feb	1984	11
34.	Spruce Home, Sask.	27 Feb – 10 Mar	1984	13
35.	Rosetown Hill, Sask.	12 Mar – 21 Mar	1984	10
36.	Wainwright, Alta.	23 Mar – 2 Apr	1984	11
37.	Dundurn, Sask.	3 Apr – 13 Apr	1984	11
38.	Corinne, Sask.	13 Apr – 30 Apr	1984	18
39.	Gull Lake West (2), Man.	2 May – 12 May	1984	11
40.	Sandridge, Man.	12 May – 21 May	1984	10
41.	Turtle Mountain, Man.	22 May – 4 Jun	1984	14
42.	Beulah, N. Dak.	6 Jun – 15 Jun	1984	11
43.	Knolls, Utah	18 Jun – 25 Jun	1984	08
44.	Booker Mountain, Nev.	17 Jul – 27 Jul	1984	11
45.	Vananda East, Mont.	30 Jul – 4 Aug	1984	06
46.	Wachusett Mountain, Mass.	15 Aug – 25 Aug	1984	11
47.	Scranton, Penn.	27 Aug – 12 Sep	1984	17
48.	Blue Knob, Penn.	12 Sep – 22 Sep	1984	11
49.	Katahdin Hill (2), Mass.	25 Sep – 19 Oct	1984	25
(n) n-th repeated visit to a site to establish seasonal variations				

As an example of Phase One data, Figure B-7 shows Phase One multifrequency clutter measurements at Cochrane. These data were obtained using on-board quick-look Site Assessment Control software, through which PPI displays of clutter at close to full radar sensitivity could be quickly displayed prior to the actual acquisition of clutter measurement data. The most obvious feature that varies with frequency in the data of Figure B-7 is azimuth beamwidth, which tends to introduce azimuth smearing with decreasing frequency (see Table B-2 for azimuth beamwidths). Strobes of RF interference are also visible at VHF in these raw data; such interference is usually removable in the coherent processing of actual measurement data. Otherwise, what is striking about the five measured displays at five different frequencies in Figure B-7 is their basic similarity. Observable through the decreasing azimuth resolution with decreasing frequency is a basic arrowhead shape in all of these plots showing the spatial occurrence of the clutter as it generally arises from terrain within line-of-sight visibility. At the scale viewed here, VHF ground clutter does not appear to be a completely different phenomenon from microwave ground clutter. This point-of-view is enlarged upon in subsequent Phase One analyses [1–4]. As a further note of similarity, the raw Phase One data of Figure B-7 may by compared with the long-range (94.2 km) plot of raw Phase Zero data in Figure B-9(g) in the next section, in which the same arrowhead shape is evident.

The ground clutter data presented in this report are Phase Zero data. In what follows in this appendix, the Phase Zero instrument and its calibration are described in more detail.

a) X-Band

24 Aug 82   18:17: 30
X-Band   : 9200.0
Wfrm (m) : 150H
PRF (Hz) : 500
INT   : 1 (NC)
Att   : 0R3 Amp

315027-58

18 Aug 82   13:40: 41
UHF   : 435.0
Wfrm (m) : 150H
PRF (Hz) : 500
INT   : 1 (NC)
Att   : 0R3 Amp

d) UHF

10 Aug 82   09:45: 47
S-Band   : 3240.0
Wfrm (m) : 150H
PRF (Hz) : 500
INT   : 1 (NC)
Att   : 0R3 Amp

b) S-Band

23 Aug 82   05:04: 09
VHF   : 168.0
Wfrm (m) : 150H
PRF (Hz) : 500
INT   : 1 (NC)
Att   : 0R3 Amp

e) VHF

10 Aug 82   10:18: 30
L-Band   : 1230.0
Wfrm (m) : 150H
PRF (Hz) : 500
INT   : 1 (NC)
Att   : 0R3 Amp

- 150 m Range Resolution
- Horizontal Polarization
- Top and bottom halves of each PPI
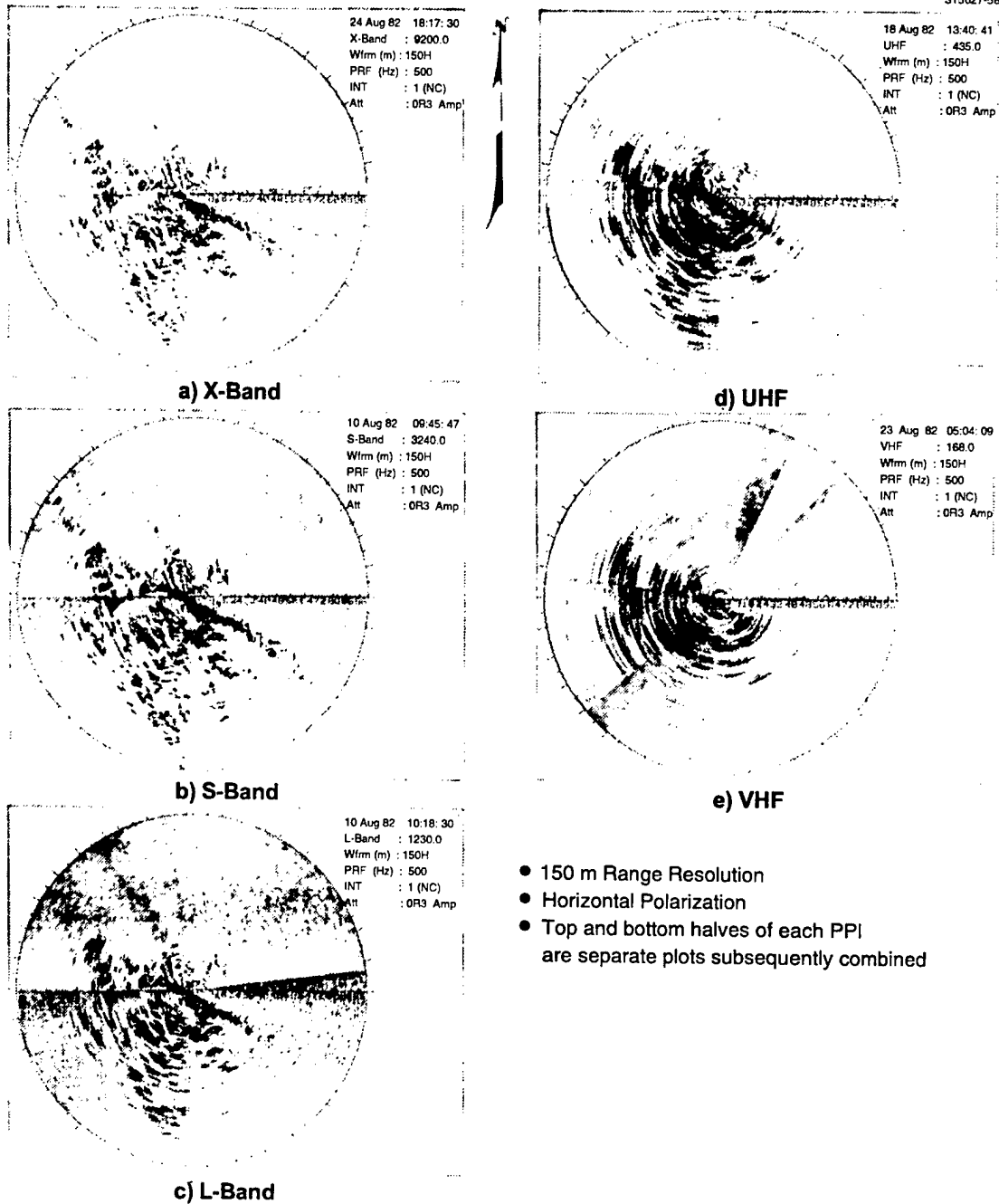 are separate plots subsequently combined

c) L-Band

Figure B-7. Phase One clutter maps from Cochrane for all five frequency bands. In each plot, maximum range is 101 km. Clutter is black, and the clutter threshold is near full sensitivity.

144

B.2 PHASE ZERO RADAR

The Phase Zero clutter measurement radar was an X-band commercial marine navigation radar, namely, the Raytheon Mariners Pathfinder Model 1650/9XR. The salient characteristics of this radar are displayed in Table B-4. A precision IF attenuator was installed in the Phase Zero receiver in order to measure clutter strength by recording sequential 360 degree azimuth scans in stepped levels of IF attentuation. Clutter strength was determined from these data subsequently using thresholding techniques. This procedure was facilitated by the fact that the large, 16-inch diameter, primary PPI display unit of the radar was digitally driven. For each attenuator setting, each pixel in the PPI display was either lit (i.e., above the minimum detectable signal) or unlit (i.e., below the minimum detectable signal). The lit/unlit state of each pixel was set by determining if the corresponding signal strength exceeds a threshold (i.e., single-bit A/D converter). The results of this thresholding process for all 320 range gates in each range sweep of the radar were stored as ones and zeros in its binary buffer unit. Hence the binary buffer unit controlling the contents of the PPI could be unloaded onto tape to provide a direct digital record of each scan of data. This entire scheme was brought under control of a surplus minicomputer which was installed in the box of the Phase Zero truck. A simple schematic diagram for the computer-controlled Phase Zero radar system is shown in Figure B-8. In this manner a digital (binary) record of a PPI stack of azimuth scans in stepped levels of attenuation (usually about 45 or 50 dB in 1 dB steps) was obtained at each site. These raw data were later processed at Lincoln Laboratory to provide calibrated clutter data. Also under control of the minicomputer was PPI scope photography to provide a back-up analog record.

The Phase Zero data set collected at each site is shown in Table B-5. The radar operated under mode control where the only parameter normally set by the operator was the maximum range. The maximum range was selected from the set indicated in the first column of Table B-5 with a nob on the face of the PPI console. The underlying important parameters which changed with maximum range setting are indicated in the other columns of Table B-5 (also, see Table B-4). Each maximum range setting is referred to as a Phase Zero experiment. At each measurement site, Phase Zero recorded stepped attenuation data for all seven experiments shown in Table B-5 (200×10^6 binary samples on two tape reels). This was a fairly large set of data to process and assimilate. Figure B-9 shows computer-generated PPI polar plots of raw Phase Zero clutter data near maximum sensitivity (i.e., with 3 dB of IF attenuation) for all seven experiments at the Cochrane, Alberta site. This data may be compared with Phase One multifrequency data from Cochrane in Figure B-7.

145

TABLE B-4
Phase Zero Radar Parameters

Transmitter

Frequency	9375 ± 30 MHz
Power	50 kW peak; 45 W average
Operating Modes	

Max Range (nmi)*	0.75, 1.5, 3	6, 12	24, 48
Pulsewidth (μs)	0.06	0.5	1
Transmit PRF (pps)	3600	1800	900

Receiver

Type	Noncoherent (amplitude only)
Intermediate Frequency	45 MHz
IF Amplifier Bandwidth	24 MHz (0.06 μs pulsewidth)
	4 MHz (0.5, 1 μs pulsewidth)
Noise Figure	10 dB
Nominal Sensitivity	$\sigma°F^4 = -45$ dB at 10 km
	(0.5 μs pulsewidth)
IF Attennuation (dB)**	0 to 50 in 1 dB steps
Recording**	Digital recording of stepped attenuation PPI displays
Record PRF (pps)	450

Antenna

Type	9-ft, end fed, slotted array
Polarization	Horizontal
Mast Height	50 feet
Scan	Continuous azimuth scan only (horizontal beam)
Rotation	17.6 rpm
Beamwidth	0.9° Az; 23° El
Gain	32.5 dB
Sidelobes	32.5 dB below peak

---

* Manually set by operator
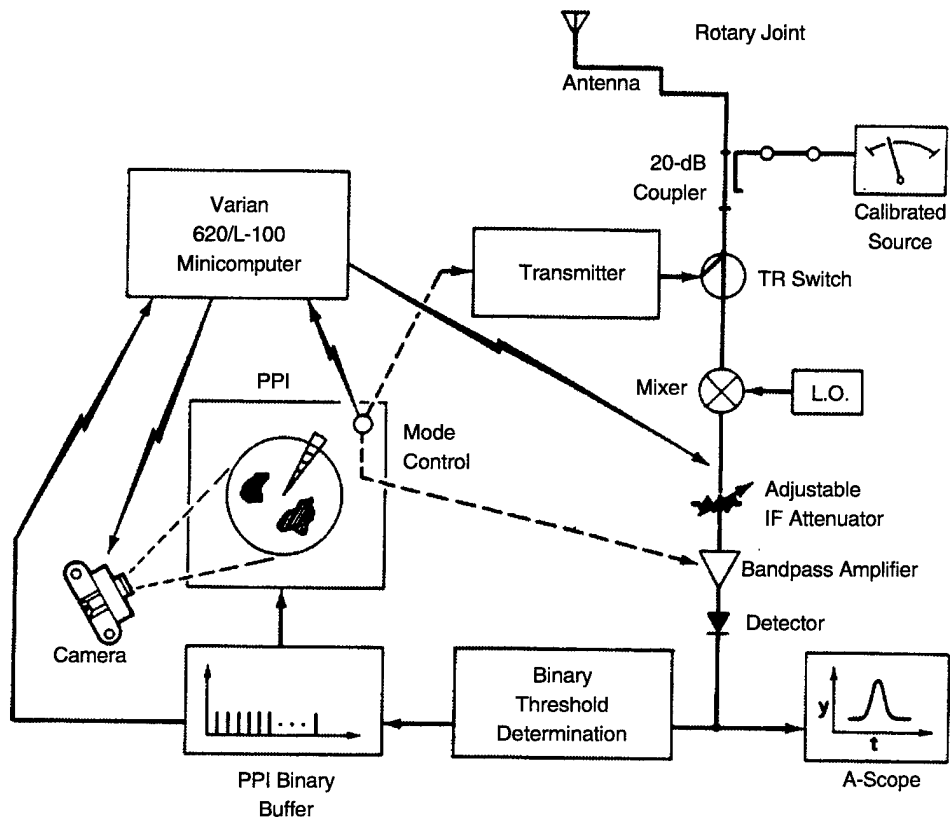**Computer controlled

*Figure B-8. Phase Zero radar schematic.*

TABLE B-5
Phase Zero Experiment Set

| PPI Nominal Maximum Range Setting* (nmi)	PPI Binary Buffer Unit**			Pulse Length	
	Actual Maximum Range (km)	Range Origin (range gate number)	Sampling Interval (m)	(m)	(μs)
0.75	1.47	4	4.6379	9	0.06
1.5	2.94	3	9.2758		
3.	5.88	3	18.5515		
6.	11.76	4	37.1030	75	0.5
12.	23.52	3	74.2061		
24.	47.05	3	148.4121	150	1.0
48.	94.09	3	296.8243		

* Manually set by operator.
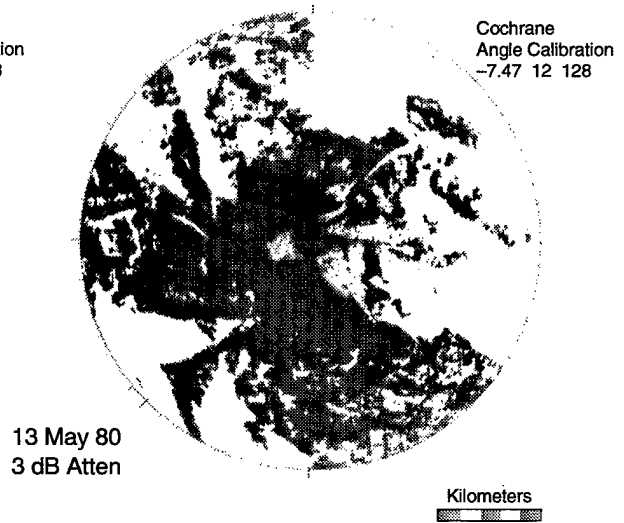** 320 range gates per pulse.

315027-60
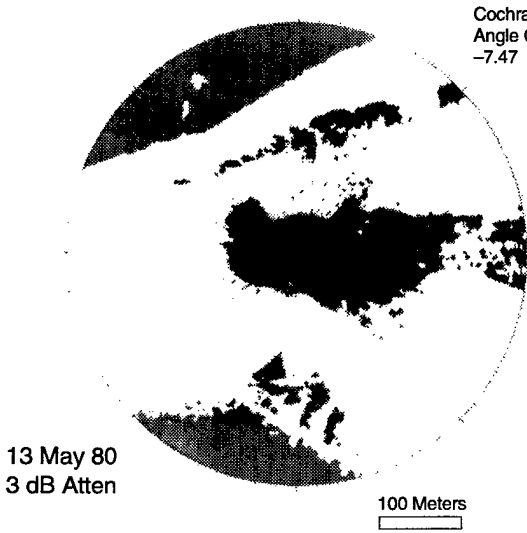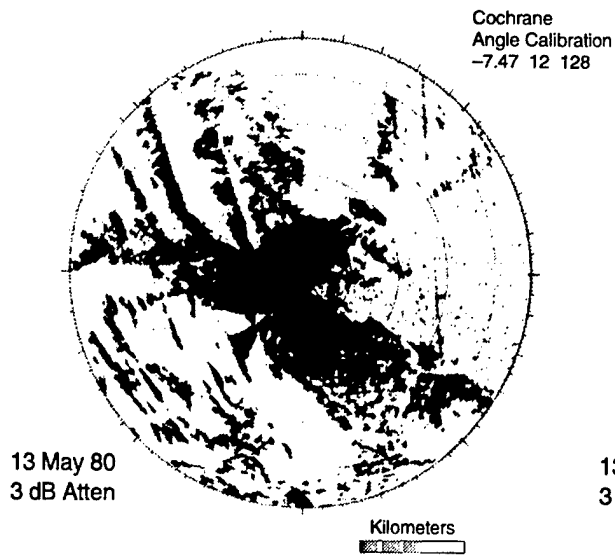
a) 1.5 km Maximum Range
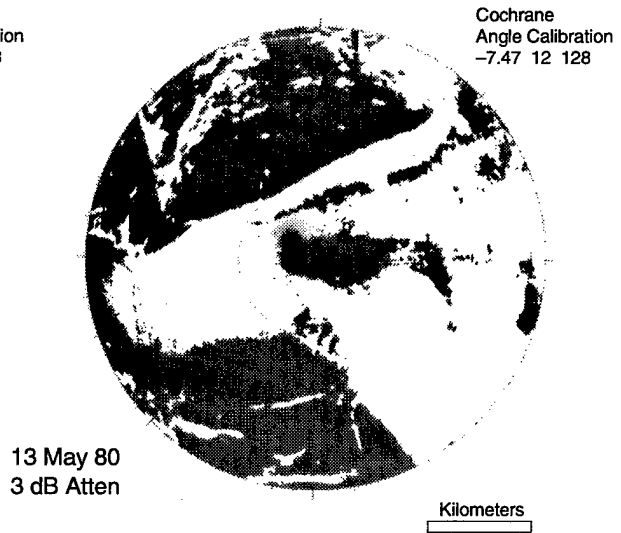
b) 2.9 km Maximum Range
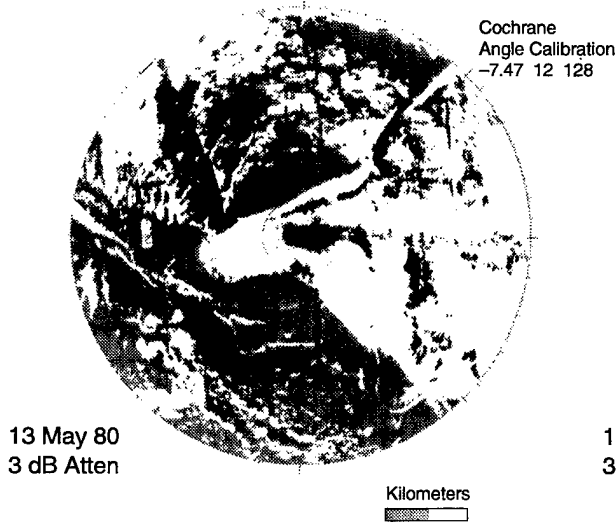
c) 5.9 km Maximum Range

d) 11.7 km Maximum Range

Figure B-9(a-d). Phase Zero clutter maps from Cochrane for all seven maximum range settings. In each map, north is zenith, clutter is black, and the clutter threshold is 3 dB from full sensitivity. Figure continued on next page.

149

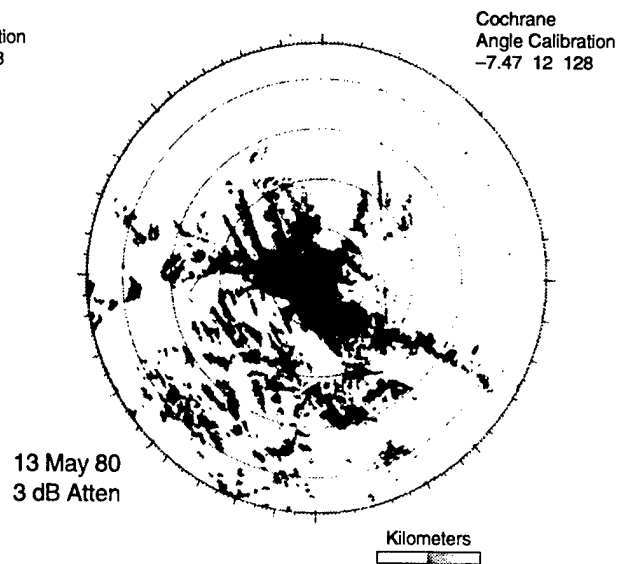**e) 23.5 km Maximum Range**

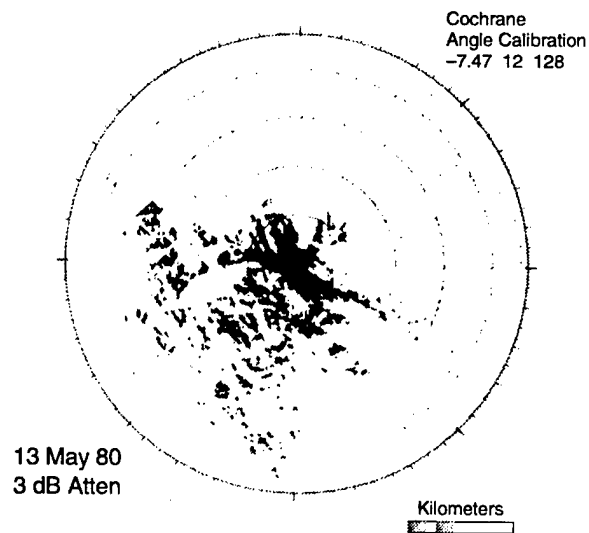**f) 47.1 km Maximum Range**

g) 94.2 km Maximum Range

Figure B-9(e-g). Phase Zero clutter maps from Cochrane for all seven maximum range settings. In each map, north is zenith, clutter is black, and the clutter threshold is 3 dB from full sensitivity. Figure concluded.

150

B.3 PHASE ZERO CALIBRATION

Calibration requires both accurate computation of absolute signal strength from a given resolution cell on the ground and accurate knowledge in range and angle of where that cell actually is on the ground. Section B.3 provides a general discussion of what was done to calibrate the commercial Phase Zero marine navigation radar with respect both to spatial position (range and angle) and signal strength, so that it could be utilized as a scientific ground clutter measurement instrument. More detailed information describing the specific processes involved in the signal strength calibration of this radar is available.

Phase Zero angle calibration was performed as follows. At each attenuation level, 14 angular sectors of data were recorded, each consisting of 128 radials, with 320 range gates recorded per radial. Each radial corresponded to one recorded pulse repetition interval (pri) of the radar. The nominal rate at which pulses were recorded was 450 Hz in all operating modes. (The emitted rate of pulses was higher than this (see Table B-4); however, not all emitted pulses were recorded.) A sector was 30 degrees wide, and 14 sectors covered 420 azimuth degrees. The angle interval per radial (or per pulse) was thus 0.2344 degrees. The end of an azimuth sweep provided about 60 degrees of data which overlapped with and repeated the beginning of an azimuth sweep. Correlation procedures were used in the overlap region to determine the exact radial where the data started to repeat (i.e., corresponding to 360 degrees azimuth). This radial varied slightly from site to site, experiment to experiment, and azimuth sweep to azimuth sweep due to such things as wind loads on the antenna, power loads on the generator, and so on. In early calibration techniques, this angle calibration was done once per experiment on a single azimuth sweep in the PPI stack (Ref. 21 was based on this early calibration). Later, in improved techniques, every sweep in the stack was calibrated, and in addition angle information recorded from shaft encoders at the beginning of each sector was used to reduce variations within a sweep and ensure uniform initial alignment from sweep to sweep. An indication of the improvement in data quality that resulted is illustrated in Figure B-10. This figure gives a sectional view into the raw PPI stack. Thus, it shows 50 levels of attenuation versus 320 range gates for a given radial. It is at the resolution of the data; a black dot indicates an above-threshold (or lit) sample, the absence of a black dot indicates a below-threshold (or unlit) sample. The data shown at the top are unaligned. There are obvious anomalies in these data. The data at the bottom have been aligned by means of angle calibration processing. A clear improvement in data quality has been realized with the investment in processing. The particular radial shown in the top of Figure B-10 may not exactly correspond with the data shown in the bottom of Figure B-10, because the relative position in the stack of a particular radial varies slightly from azimuth sweep to azimuth sweep during alignment. All of the Phase Zero clutter data in this report were obtained using the improved angle alignment procedures. The plots shown in Figure B-10 are referred to as range sweeps. These plots were made by software utilizing raw Phase Zero data tapes as source. In standard data reduction procedures, several range sweeps were routinely generated at various azimuth angles for each experiment recorded (see Figure B-12). These plots provided basic visual assurance on the underlying quality of the raw data. This assurance was also provided through digitally generated PPI displays of clutter, which were also generated for each experiment. Examples of PPI displays are shown in Figure B-9. Occasionally erratic or anomalous behavior was discovered both with

respect to range and angle in the Phase Zero radar through inspection and/or automatic assessment (see Figure B-12) of range sweeps and PPIs.
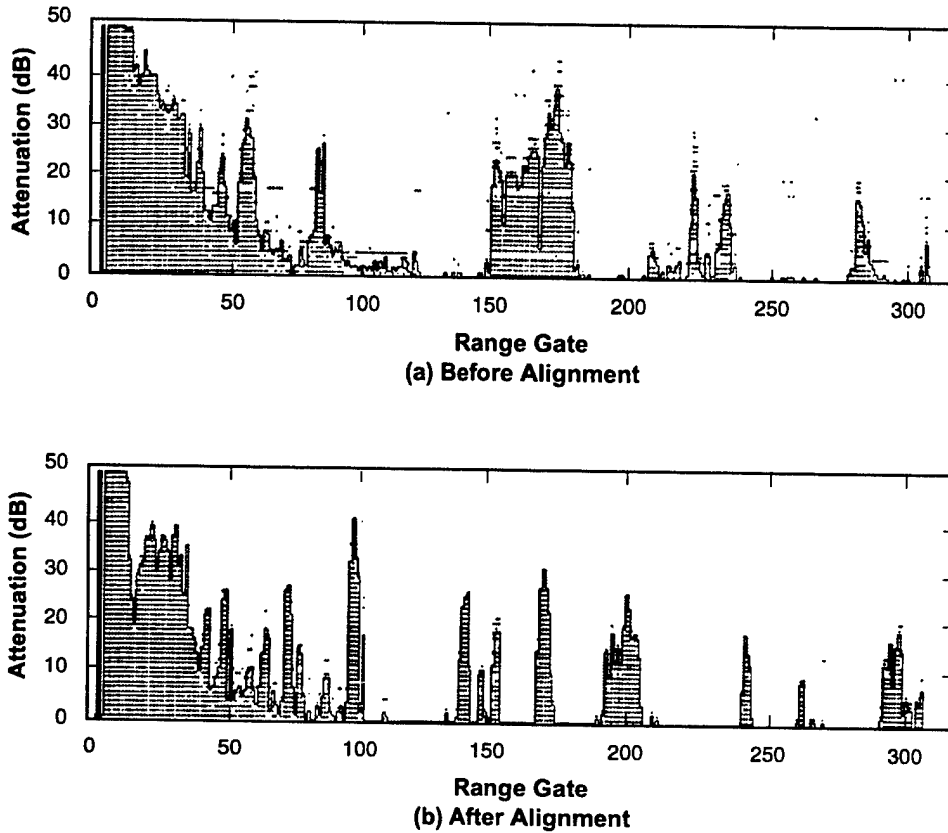

Figure B-10. Angle alignment of the Phase Zero data. The data are from sector 11, radial 64 (i.e., 315° azimuth) of the 12 km maximum range experiment at Shilo, Manitoba. See also Figure 18.

Experiments were conducted with the Phase Zero radar to determine range calibration, or, in other words, the actual position in range from the radar of the 320 range gate positions in the receiver. Special range calibration experiments were conducted using oil drums deployed on flat terrain, and telephone poles, power pylons, and road markers along roads. Also, from time to time, when highly discrete and recognizable targets of opportunity were available within the standard set of clutter measurements at a measurement site, they were analyzed to obtain range calibration. The details of range calibration were experiment dependent, but in general it was determined that there was an initial, negative, 3 or 4 range gate positional bias (i.e., the radar position was in the 3rd or 4th range gate; see Table B-5), with a subsequent gate sampling interval also as indicated in Table B-5.

152

The method for thresholding in the PPI stack to determine signal strength is indicated in Figure B-11. The step function thresholding algorithm illustrated there determines the threshold at a given pixel location by counting the number of lit samples at that location (sometimes thought of as "shaking down" the lit samples) and taking the attenuation corresponding to the top of the shaken-down stack as the threshold level. The continuous line shown in both top and bottom data sets in Figure B-10 is the step function threshold. Experimentation with various thresholding algorithms led to a "top-down, 2-out-of-3" algorithm as most representative. Note that thresholding in a binary PPI stack of stepped levels of attenuation is essentially a slow A/D conversion process in which the clutter signal varies over the conversion period, and hence no clear-cut conversion or thresholding algorithm is definable. Thoughts to bear in mind in considering how clutter can scintillate during the conversion period are that:

1. the scan period for one azimuth rotation was about 3.4 s;

2. every data-recording azimuth scan was followed by a buffer scan in which IF attenuation was switched;

3. assembling the entire 50-dB stack of PPIs thus took about 6 minutes; and

4. data recording over several scans near the threshold level where scintillation has most effect in the binary result took about one-half minute.

This slow A/D process dictated by instrumenting the Phase Zero radar may be contrasted with the fast, 10 MHz, A/D converters of the Phase One system. All of the Phase Zero calibrated data presented in this report were reduced using the top-down, 2-out-of-3 thresholding algorithm. In this algorithm, for each PPI pixel location, a sliding attenuation window 3-dB wide was first positioned at the maximum attenuation level (nominally 50 dB) and then allowed to move in 1-dB steps toward lower attenuations, with the threshold set at the first position where two of the three windowed levels were lit.

With the thresholded attenuation value in hand, computation of received signal strength followed from knowledge of the minimum detectable signal, which was measured and recorded by injection of a calibration RF test signal at the input to the Phase Zero receiver for each experiment (see Figure B-8). The calibration procedures incorporated correction in this process for gain compression in the IF amplifier. Received power was converted to clutter strength using a calibration equation. A first indication of what was involved in this conversion is shown by the equation illustrated in Table B-6. Table B-6 also shows nominal values of parameters. Of course actual data reduction involved conversion to clutter strength, not using nominal radar values, but rather using a calibration constant relating received signal strength to radar cross section obtained through Phase Zero backscatter measurements from an external test target of known radar cross section. Information about these tests and the radar calibration constant resulting from them is available. However, at a first level, the equation in Table B-6 can be used to understand the basic parameters involved. Combined with the nominal parameters shown in Table B-4, and a required minimum output signal-to-noise ratio for detection of 7 dB for narrowband experiments, they lead to the approximate clutter sensitivity of the Phase Zero radar shown in Table B-4.

153

1. Raw Data
• 51 Binary (r, θ) PPI Maps

0 dB   1 dB   • • •   50 dB
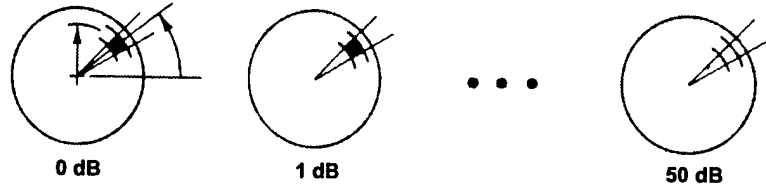
2. Thresholding Process
• Establish threshold attenuation α
for each (r, θ) sample cell
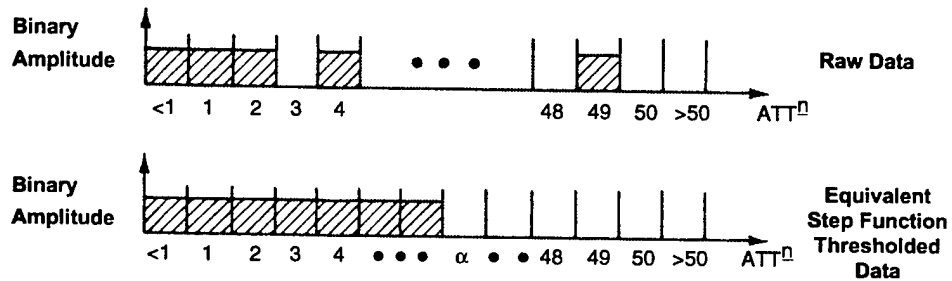
3. Calibrated Clutter Data
• Convert threshold attenuation α to $\sigma°F^4$ for each (r, θ) sample cell
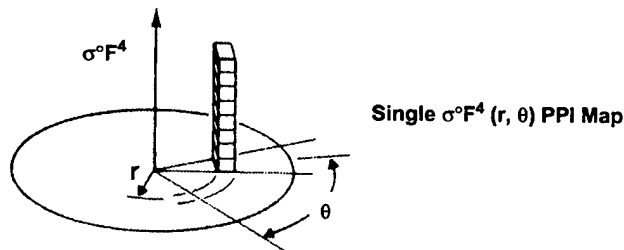

Single $\sigma°F^4$ (r, θ) PPI Map

Figure B-11. Thresholding of the Phase Zero raw data.

154

In particular, note in Table B-6 that clutter strength is shown in terms of $\sigma°F^4$, where $\sigma°$ is the clutter coefficient and F is the pattern propagation factor. The clutter coefficient $\sigma°$ is the radar cross section per unit of ground area. The pattern propagation factor F is the ratio of the incident field that actually exists at the clutter cell being measured to the incident field that would exist there if the clutter cell existed by itself in free space and on the axis of the antenna beam. In low-angle clutter measurements, the intervening terrain between radar and clutter cell can strongly influence both the transmitted radiation illuminating the cell and the backscattered radiation received by the radar. These terrain effects are caused by multipath reflections and diffraction from the terrain. By definition, the pattern propagation factor F includes all such effects. The propagation factor is raised to the fourth power as it enters into clutter strength because clutter strength (actually, clutter intensity) is proportional to power (i.e., the square of the field strength), and a two-way propagation path is involved. It is usually not possible to measure the propagation factor separately (it requires a field strength measurement at the clutter cell) in order to separate $\sigma°$ and F in clutter measurements, although the measurement and separation was made occasionally in the Phase One measurements. Therefore, all of the calibrated clutter data in this report include effects of propagation. This fact is generally kept in mind by using the explicit notation $\sigma°F^4$ to refer to clutter strength. To ensure unambiguous language, $\sigma°$ itself (i.e., the backscattering coefficient separated from propagation effects) is referred to as the clutter coefficient.

The determination of the overall calibration constant that the various terms in the equation in Table B-6 lead to is a very difficult matter with radars that always illuminate the ground (i.e., the elevation beams were not controllable but fixed horizontally for both the Phase Zero and Phase One systems). External calibration experiments sometimes involving balloon-borne spheres, and other times involving tower-mounted calibrated repeaters, were conducted in the Phase Zero program to ensure that the calibration factors were accurate. Two methods for minimizing competing ground clutter were developed for such experiments. The first involved deploying the target in a shadowed area behind a hill; in this case diffraction from the hilltop made data extraction difficult. The second involved deploying the target in a smooth level area where forward scatter was enhanced and hence backscatter was minimal; in this case foreground terrain reflection and multipath made data extraction difficult. These external calibration tests were difficult to perform and interpret. However, perserverance with them uncovered several significant problems over the history of the Phase Zero measurements. It is believed that relatively consistent and accurate calibrations finally existed across the entire Phase Zero data set.

A flow chart illustrating the processing performed on the raw Phase Zero data tapes to generate calibrated clutter tapes is shown in Figure B-12. Through all of the improvements in Phase Zero data quality, it should be borne in mind that the Phase Zero radar was an off-the-shelf commercial radar. Substantial gains were made in improving its calibration accuracy with bootstrapped, after-the-fact, procedures, but further efforts along these lines would have yielded diminishing returns and in any event could never have practicably reached accuracies comparable to a scientific measurement radar such as the Phase One radar.

TABLE B-6

Phase Zero Clutter Strength Calibration Equation

$$\sigma°F^4 = \frac{2 \cdot (4\pi)^3 \cdot P_r \cdot R^3 \cdot L_p}{P_t \cdot G^2 \cdot \lambda^2 \cdot \Delta\theta \cdot c \cdot \Delta\tau}$$

where

$\sigma°F^4$ = clutter strength ,

$\sigma°$ = clutter coefficient (theoretical backscattering coefficient with free space illumination and no terrain multipath effects.

F = propagation factor (ratio of incident field that actually exists at clutter cell being measured to the incident field that would exist there if the clutter cell existed by itself in free space).

P_r = received power,

R = range to clutter cell,

L_p = two-way waveguide plumbing loss (nominally 6 dB),

P_t = transmitted power (nominally 50 kw),

G = one-way antenna gain (nominally 32.5 dB),

λ = RF wavelength (nominally 0.032 m),

$\Delta\theta$ = azimuth beamwidth (nominally 0.9°),

c = velocity of light

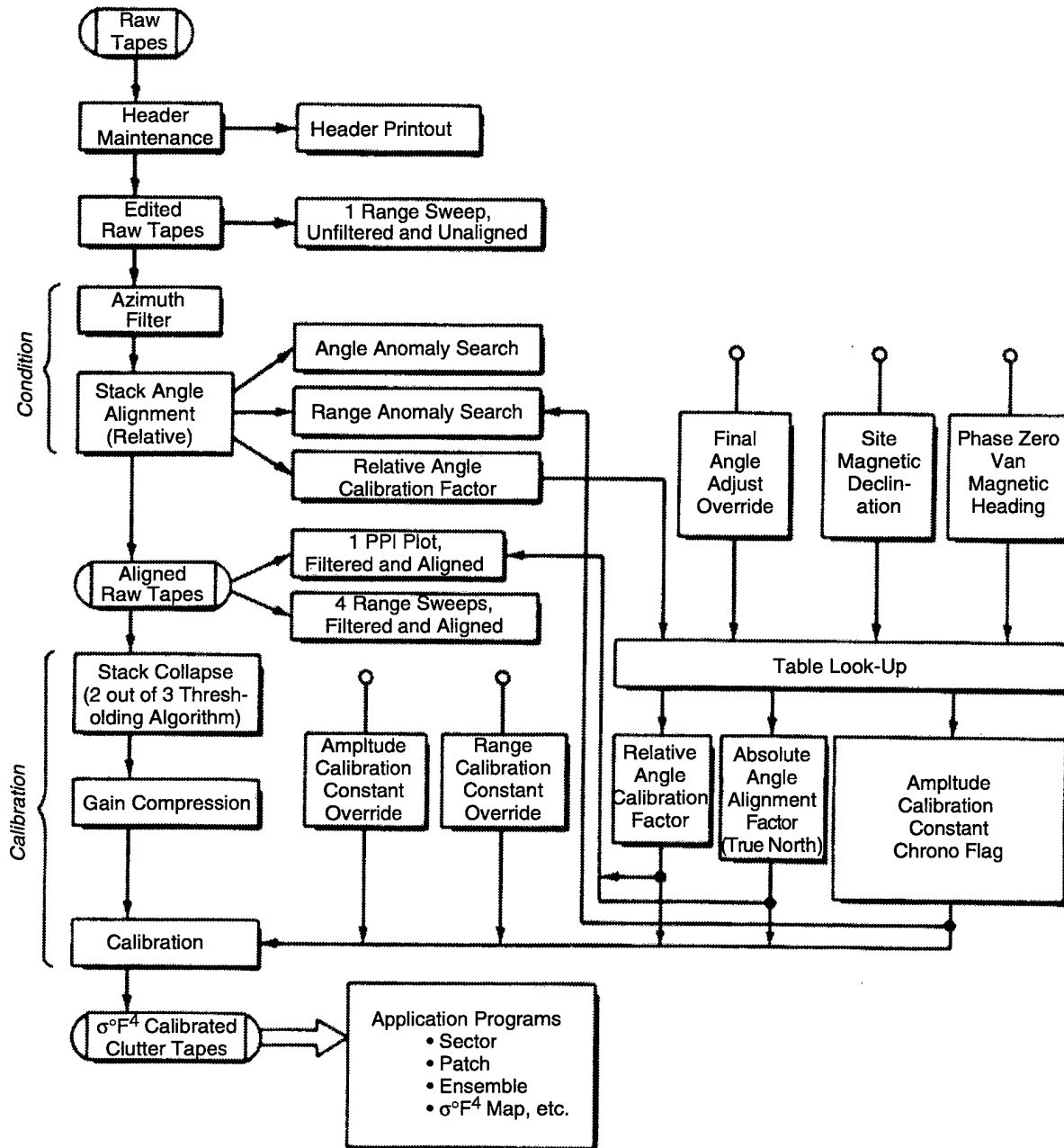$\Delta\tau$ = RF pulsewidth (see Table B-5)

Figure B-12. Phase Zero data reduction flow chart.

APPENDIX C

FORMULATION OF CLUTTER STATISTICS

C.1 OVERVIEW OF PATCH DATA

Modeling investigations of clutter amplitude statistics were based on the concept of a clutter patch. A clutter patch is a local region selected in a clutter map in which substantial clutter visibility is discernible above the radar noise level, and in which the terrain is in large measure uniform. In order to provide detailed and accurate terrain descriptive information for the process of patch specification and description, measured clutter maps were overlain and carefully registered onto stereo air photos and topographic maps of the terrain. This was done by means of a Bausch and Lomb stereo zoom-transfer scope. For convenience, clutter patches were selected in a polar grid centered at the radar, such that each patch was specified by beginning and ending limits on both range and azimuth.

For each clutter patch selected, the distribution of clutter strengths that occurred within the patch was formed. That is, within a clutter patch, typically from several thousands to several tens of thousands of samples of clutter strength $\sigma°F^4$ were obtained, one sample per spatial cell or pixel, as range and azimuth position varied throughout the patch. The histogram of all the spatial samples of $\sigma°F^4$ measured within the patch was formed, and various statistical attributes of this histogram or distribution were computed. The histogram together with its statistical attributes and associated terrain descriptive information for the patch was then stored in a computer file.

This file contained data for 2,177 clutter patches selected from all Phase Zero measurement sites. For each site, patches were selected from the nominal 6-nmi Phase Zero experiment utilizing a 0.5 µs-pulse length (i.e., in patch specification, beginning range $\geq$ 2 km, ending range $\leq$ 11.8 km; see Table B-5). Subsequent patch specification occurred out to 47 km in range utilizing the nominal 24-nmi experiment with a 1-µs pulse length (i.e., beginning range $\geq$ 1 km, ending range $\leq$ 47 km) at each site, but this report does not analyze these data at longer ranges. The median patch size of the 2,177 patches between 2 and 12 km from the radar is 5.3 km^2, or about 2.3 km on a side for an approximately curvilinear square patch. Such a patch typically contains about 5,000 spatial samples of $\sigma°F^4$.

The purpose of this appendix is to show some examples of clutter patches. Six sites were selected from which to show patches. These six sites are shown in Table C-1. They were selected to cover the range of effective radar height that was experienced in the measurements (see Table A-1). At each of these sites, six patches are shown as examples in this appendix. This is done by providing a pair of figures for each site. In the first figure, the locations of the patches are shown on a 12-km clutter map. Then, in the second figure, terrain descriptions and amplitude statistics for each patch are shown. These pairs of figures are presented together at the end of this section, as Figures C-5 through C-16 consecutively. Typically, about 20 patches in total at each site are specified to substantially cover most of the visible clutter between 2- and 12- km range, but not all of the patches selected at each site are shown in this appendix.

TABLE C-1

Six Clutter Measurement Sites

Site Name*	Land Cover**	Landform	Effective Radar Height[#] (m)
Coaldale, Alta.	21	3-1	3
Shilo, Man.	41-21-31	1-3	18
Cold Lake, Alta.	21-43	1-3	40
Magrath, Alta.	21-31	2-3-7	94
Calgary West, Alta.	41-31-11	3-4	124
Equinox Mt., Vermont	43-21	7-8-5	678

* See Table A-1

**General overview, not comprehensive; see Table A-1

[#] Includes 15 m Phase Zero antenna mast height; see Table A-1

Figure C-1 shows Phase Zero clutter maps to 47-km maximum range for the six sites of this appendix. The effective radar height[1] at each site is also shown in Figure C-1. These long range clutter maps are shown in Figure C-1 partly to provide context and perspective for the 12-km maximum range patches shown subsequently in Figures C-5, C-7, C-9, C-11, C-13, and C-15 (i.e., the first range ring in the 47-km clutter maps of Figure C-1 is at 10 km), and partly to indicate how clutter visibility increases with effective radar height. Figure C-2 further quantifies this latter point by showing plots of percent circumference in discernible clutter versus range for the six sites. It is clear in Figure C-2 that visibility to clutter increases strongly with increasing effective radar height. Quantification of this plays an important part in non-site-specific clutter model investigations.
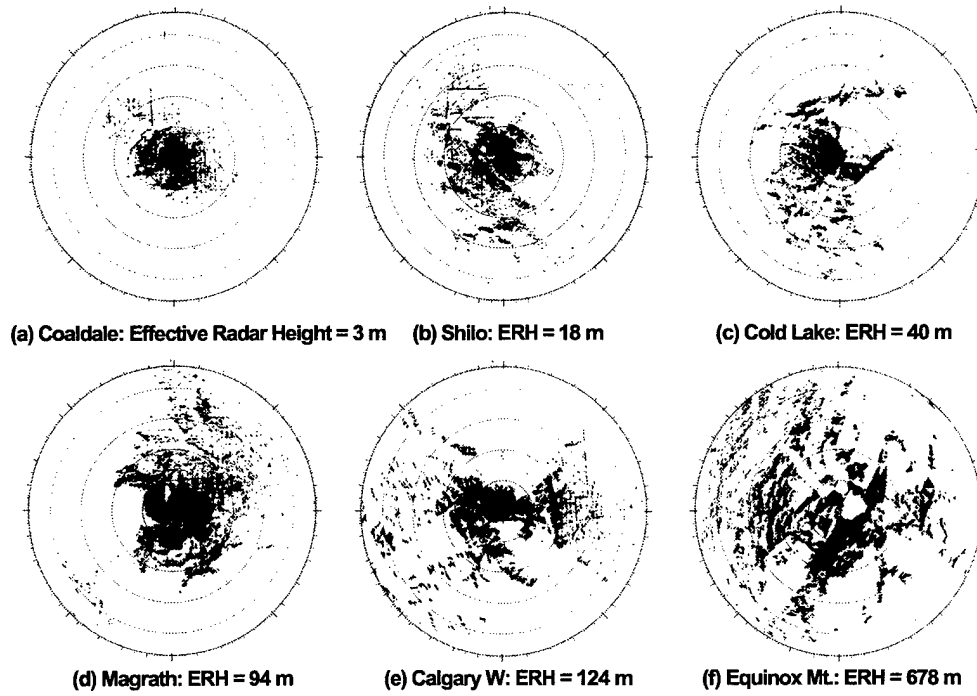
---

[1] See Appendix A.

Figure C-1. Phase Zero clutter maps for six sites. In each map maximum range = 47 km, north is zenith, range resolution = 150 m, clutter is black, clutter threshold is 3 dB from full sensitivity.
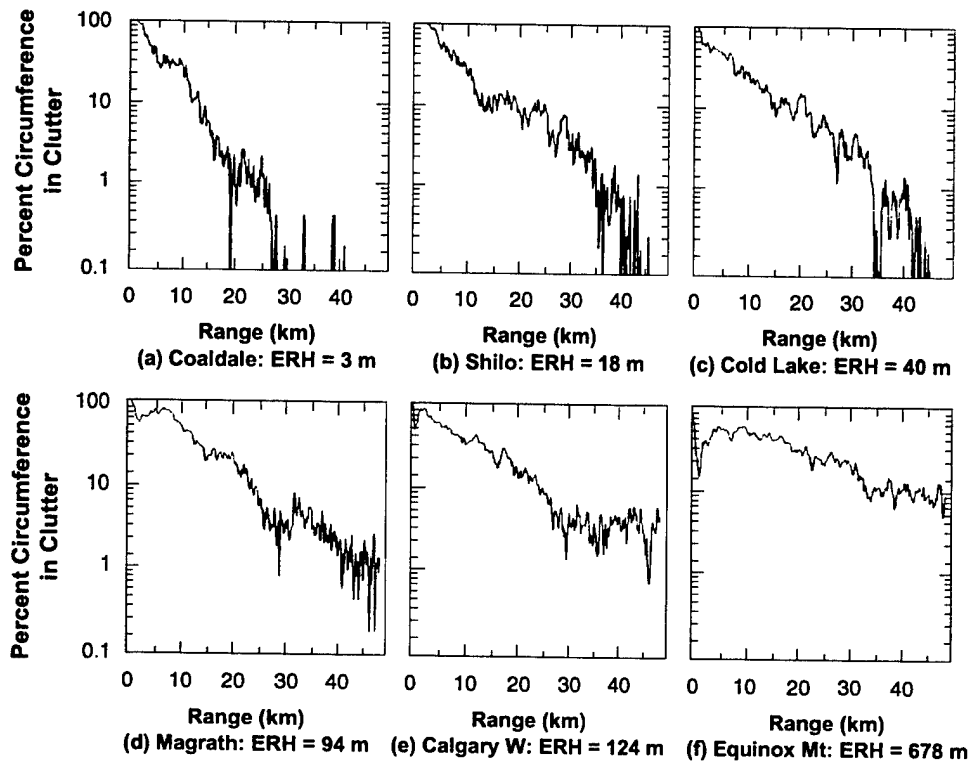
161

Figure C-2. *Percent circumference in clutter versus range for six sites. Phase Zero data, 47-km maximum range, 150-m range resolution, clutter threshold is 3 dB above full sensitivity.*

Effective radar height is not only the basic parameter directly affecting visibility, but it also indirectly affects strength through depression angle. It is for this reason that sites spanning the total available range of effective radar height were selected for inclusion in this appendix. By this means, most of the total range of depression angles occurring across all of the sites was also effectively spanned. Depression angle directly affects and dominates clutter strength distributions as is shown in Figure 48. As a result, the six sites of this appendix may be thought of as an interesting canonical set, although they have not been used as such beyond this appendix.

In order to see the effect of depression angle on strength across these six sites, the histograms and cumulative distributions of $\sigma°F^4$ from all six sites need to be perused together as shown in Figures C-6, C-8, C-10, C-12, C-14, and C-16. Although there is considerable variety in land cover and landform across these six sites, what is striking is how the histograms and cumulatives are frequently quite similar for any given site, but vary considerably from site to site. The considerable variations in amplitude distributions from site to site show a trend with increasing effective radar height. As an aid in seeing this site-to-site

trend, Figure C-3 shows one representative histogram selected from each of the six sites, and Figure C-4 shows the corresponding cumulative distribution from each site plotted together on a Weibull nonlinear ordinate. The reason for this trend is that, as our attention moves progressively across these six sites from low to high effective radar height, the depression angle regimes in effect are generally much the same at any given site but increase substantially site by site from Coaldale to Equinox Mountain. The principal effect observed in the trend of variation in amplitude distributions across these six sites is the decreasing spread in the distributions as our attention moves from low to high depression angle regimes. Decreasing spread is observed in the histograms as a progression from histograms characterized by long spread-out high tails at low effective radar heights to histograms of more and more bell-shape which become increasingly narrow and peaked as effective radar height increases. This decreasing spread in the histograms is also indicated by the decreasing separation of the percentile lines (i.e., 50, 90, and 99 percentiles are shown as vertical dotted lines in the histograms) with increasing effective radar height and depression angle. Decreasing spread is observed in the cumulative distributions as a continual increase in slope from site to site with increasing effective radar height. At the highest effective radar heights and depression angles, some of the histograms and cumulative distributions are approximated by Rayleigh statistics (generally expected as shadowing approaches zero) with mean and standard deviation approaching equality and mean-to-median ratio approaching 1.6 dB.

Increasing strength as depression angle regimes increase with increasing effective radar height is also evident in reviewing the patch amplitude distributions for the six sites in this appendix, but it is not as striking at first glance in the way the data are displayed and requires a more detailed site-to-site comparison to discern. What is more striking in terms of strength is that occasional patches stand apart as being much stronger than the other patches at any given site. This effect is most easily seen as a cumulative distribution positioned much further to the right than the others, especially at the higher percentile levels (>0.99, say). Such occasional strong clutter patches are often urban (e.g., Coaldale, patch #5; Shilo, patch #4; Cold Lake, patch #7 and #8; Calgary West, patch #5/2). Other occasional clutter patches, less strong than urban but still stronger than others, are often of more extreme landforms (e.g., Cold Lake, patch #5 and #6, and Calgary West, patch #2 and #3, are all of landform = 7, moderately steep).

Thus, these data in this appendix substantiate statements made in the body of this report to the effect that depression angle as it affects shadowing represents the single strongest parametric dependence at work in the measured clutter data, strong enough to wash out most distinctions between similar terrain types. However, occasional specific terrain types, particularly urban and to a lesser extent extreme landform categories (e.g., "mountains"), stand significantly apart.
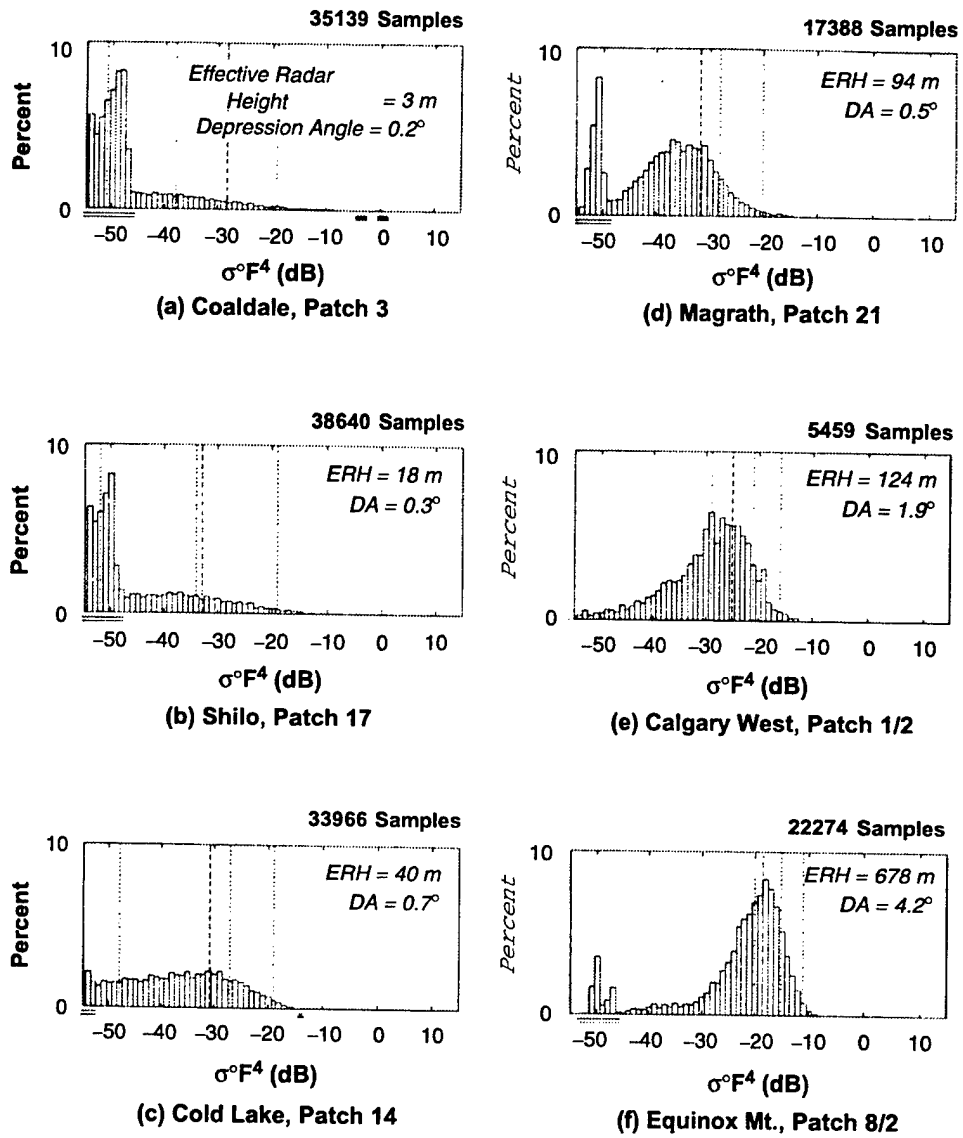
Figure C-3. Clutter strength histograms for six patches selected from sites in different regimes of effective radar height. Phase Zero data, 75-m range resolution.

164
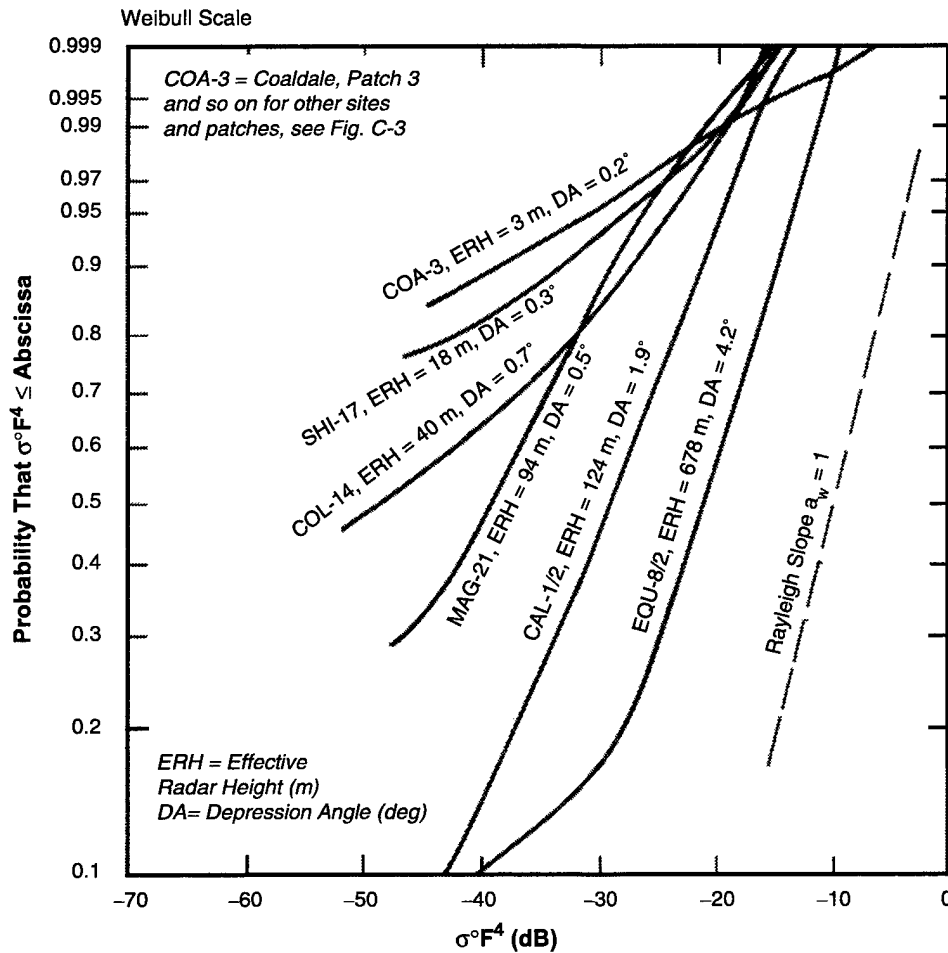
Figure C-4. Six clutter patch cumulative amplitude distributions from sites in different regimes of effective radar height. Phase Zero data, 75-m range resolution.

C.2 DEFINITION OF TERMS

Section C.1 presents two clutter patch figures for each of six sites in Figures C-5 through C-16. The first figure shows patch positions. The second figure shows patch statistics. This section describes more specifically what is shown in these two figures.

Phase Zero PPI Display
Received Power: 3-dB attenuation
Radius: 12 km

Land Cover Map
1. Urban
2. Agricultural
3. Rangeland
4. Forest
5. Water
6. Wetland
7. Barren

Landform Map
1. Level
2. Inclined
3. Undulating
4. Rolling
5. Hummocky
6. Ridged
7. Moderately steep
8. Steep
9. Broken

Figure C-5. Radar ground clutter visibility and terrain classification maps with selected clutter patches for Coaldale site.

Figure C-6. Phase Zero clutter statistics and terrain classification for selected patches at Coaldale site.

167

Phase Zero PPI Display
Received Power: 3-dB attenuation
Radius: 12 km

Land Cover Map
1. Urban
2. Agricultural
3. Rangeland
4. Forest
5. Water
6. Wetland
7. Barren

Landform Map
1. Level
2. Inclined
3. Undulating
4. Rolling
5. Hummocky
6. Ridged
7. Moderately steep
8. Steep
9. Broken

Figure C-7. Radar ground clutter visibility and terrain classification maps with selected clutter patches for Shilo site.

168

Figure C-8. Phase Zero clutter statistics and terrain classification for selected patches at Shilo site.

Phase Zero PPI Display
Received Power: 3-dB attenuation
Radius: 12 km

Land Cover Map
1. Urban
2. Agricultural
3. Rangeland
4. Forest
5. Water
6. Wetland
7. Barren

Landform Map
1. Level
2. Inclined
3. Undulating
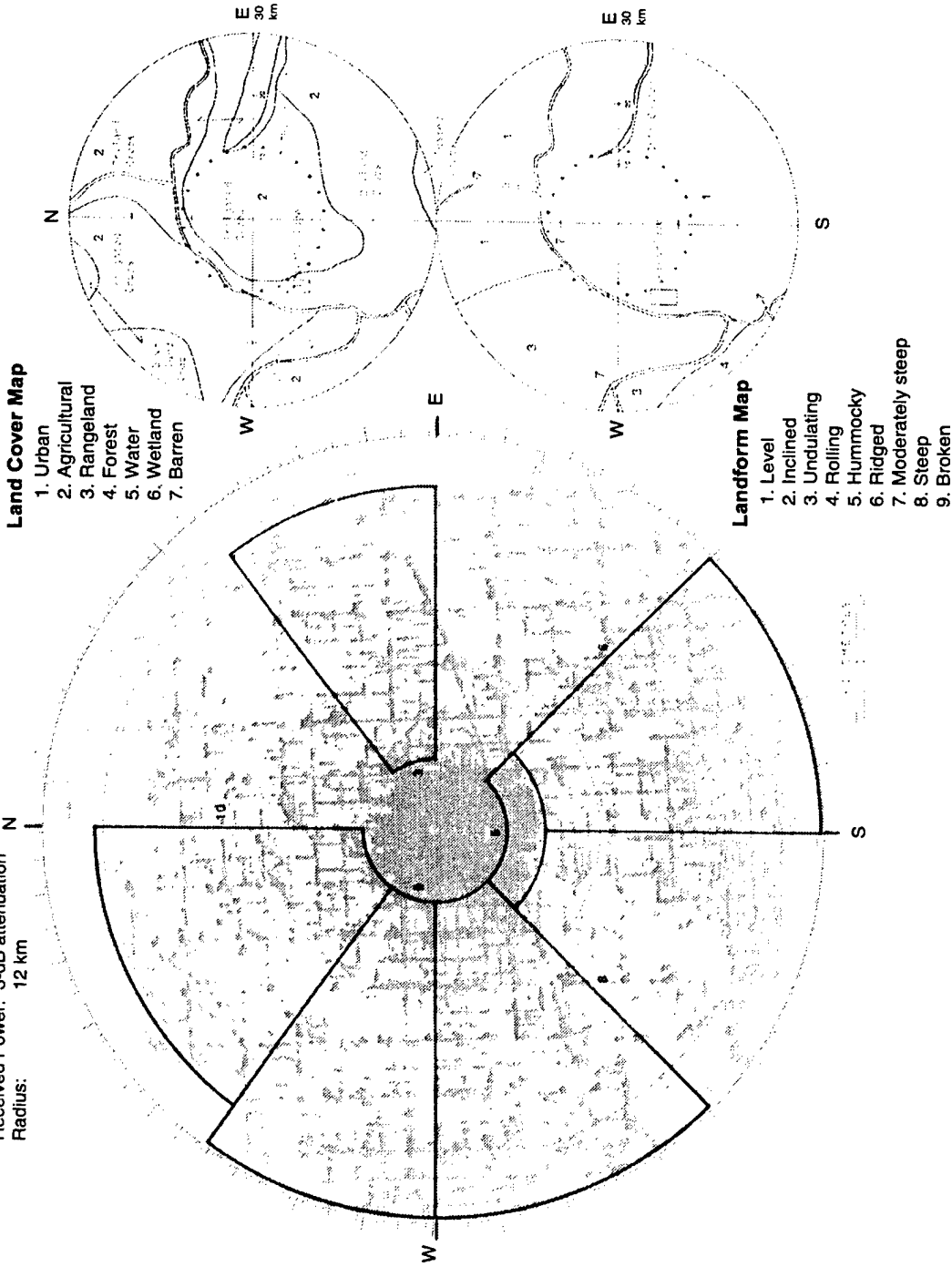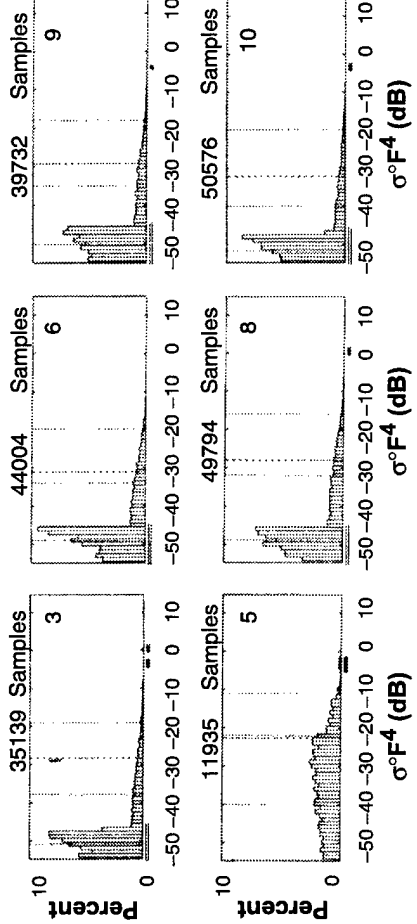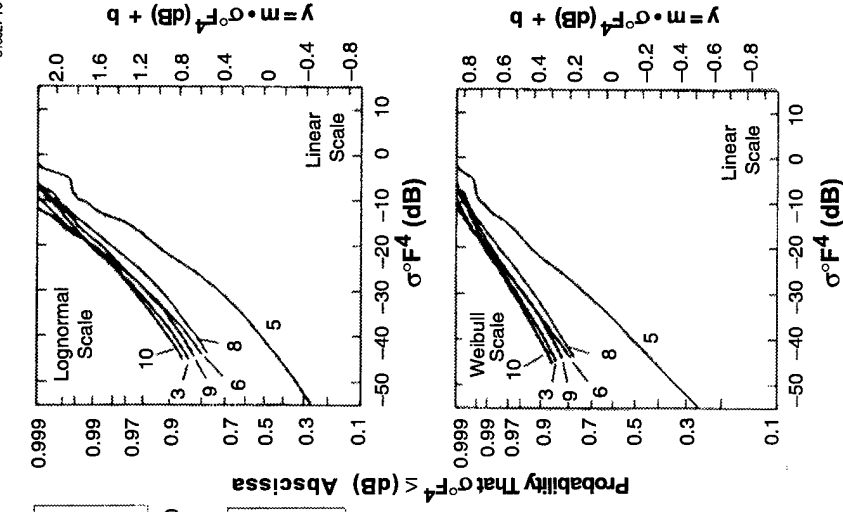4. Rolling
5. Hummocky
6. Ridged
7. Moderately steep
8. Steep
9. Broken

Figure C-9. Radar ground clutter visibility and terrain classification maps with selected clutter patches for Cold Lake site.

Histograms (Percent vs σ°F⁴ (dB)) for Samples: 9168 (5), 8580 (7), 33966 (14), 4998 (6), 10260 (8), 22496 (15).

Probability plots: Lognormal Scale and Weibull Scale (Probability That σ°F⁴ (dB) ≤ Abscissa vs σ°F⁴ (dB)), with Linear Scale and Rayleigh Slope references; y = m · σ°F⁴ (dB) + b.

Patch Number	Terrain Classification		Depression Angle (deg)	Tree Cover (%)	Supplementary Terrain Descriptors
	Land Cover	Landform			
5	43-21	7	0.02	>50	Major Road
6	43-52	7	0.08	>50	Heavy Forest, Major Road, Railway
7	11-21	1-3	0.88	1-3	Cropland Surrounds Town, Major Road, Railway
8	11-43	3-2	0.45	11-30	Town Patch Contains part of CFB Cold Lake, Major Roads, Railway
14	21-43	1-3	0.65	4-10	Major Highway, Sewage Plant, Sloughs, Trees along Creek
15	21-43	3-1	0.26	11-30	Major Highway, Roads, Creek

σ°F⁴ (dB)*

Patch Number	Mean	Standard Deviation	Skewness	Kurtosis
5	-25.9 (-34.7)	-22.9 (11.0)	7.59 (0.18)	18.2 (1.63)
6	-28.8 (-33.7)	-24.7 (9.6)	4.92 (0.25)	12.0 (1.66)
7	-23.0 (-32.3)	-16.7 (11.2)	7.34 (0.66)	15.9 (3.17)
8	-23.3 (-39.2)	-14.5 (11.8)	12.91 (0.23)	27.0 (2.46)
14	-30.8 (-46.0)	-25.4 (13.5)	10.62 (0.31)	24.5 (1.85)
15	-37.0 (-45.6)	-30.9 (7.1)	10.07 (1.28)	21.8 (3.98)

Patch Number	Percentiles			Y= m · σ°F⁴(dB)+b		Regression Coefficients †	
	50	90	99	Slope (m)	Intercept (b)	Coefficient of Determination	Sum of Squared Deviations
5	-32	-21	-16	0.042 (0.078)	1.30 (2.71)	0.968 (0.906)	0.192 (2.060)
6	-31	-22	-18	0.049 (0.089)	1.49 (3.06)	0.959 (0.883)	0.208 (2.100)
7	-30	-20	-11	0.046 (0.074)	1.25 (2.45)	0.997 (0.974)	0.031 (0.782)
8	-38	-25	-10	0.030 (0.057)	1.02 (2.29)	0.982 (0.996)	0.147 (0.135)
14	-48	-27	-19	0.026 (0.057)	1.17 (2.61)	0.977 (0.926)	0.080 (1.070)
15	-48††	-34	-25	0.030 (0.073)	1.42 (3.51)	0.994 (0.975)	0.008 (0.200)

* Of Linear Values (of dB Values)   † Weibull (Lognormal)   †† Upper Bound

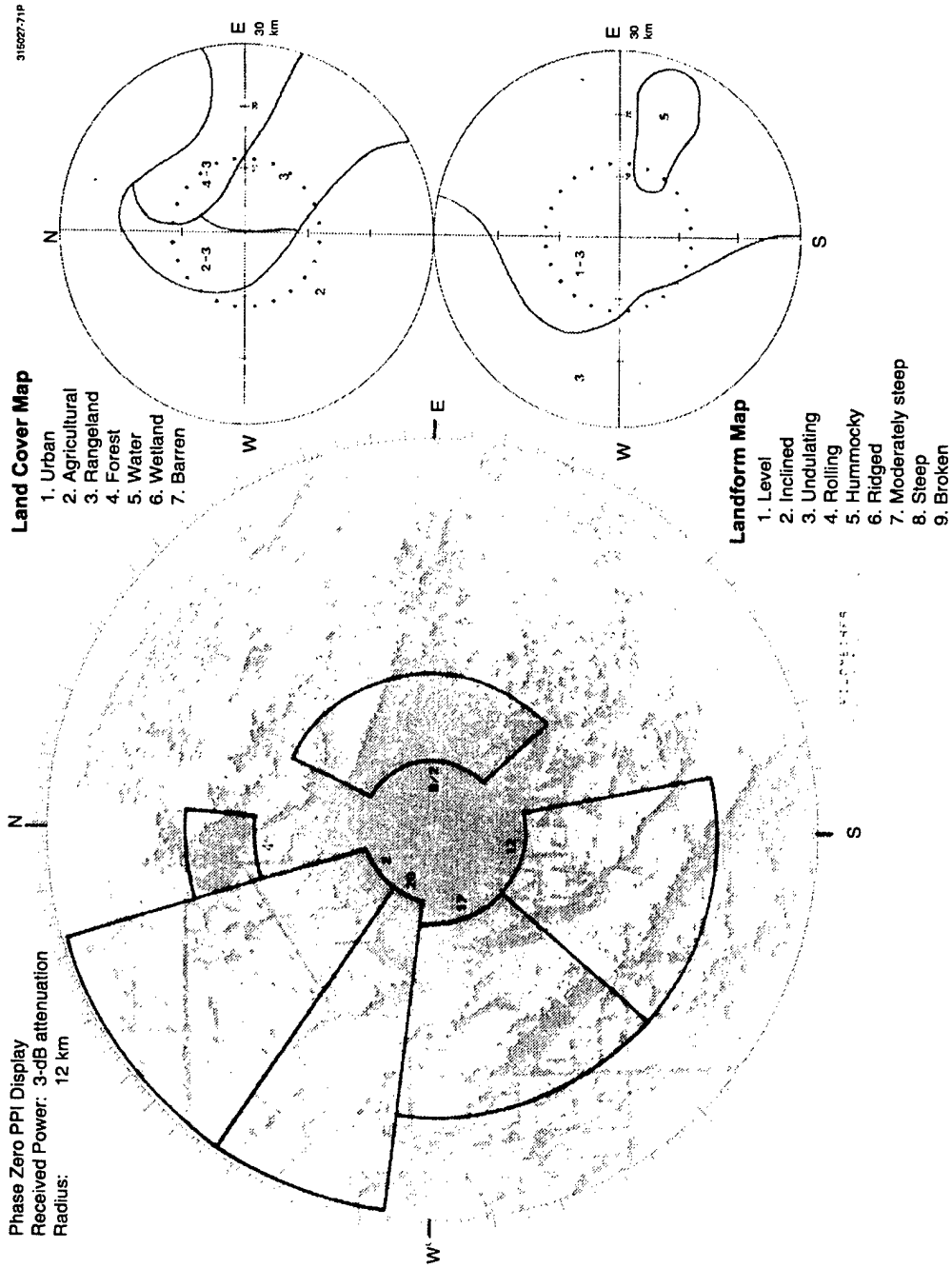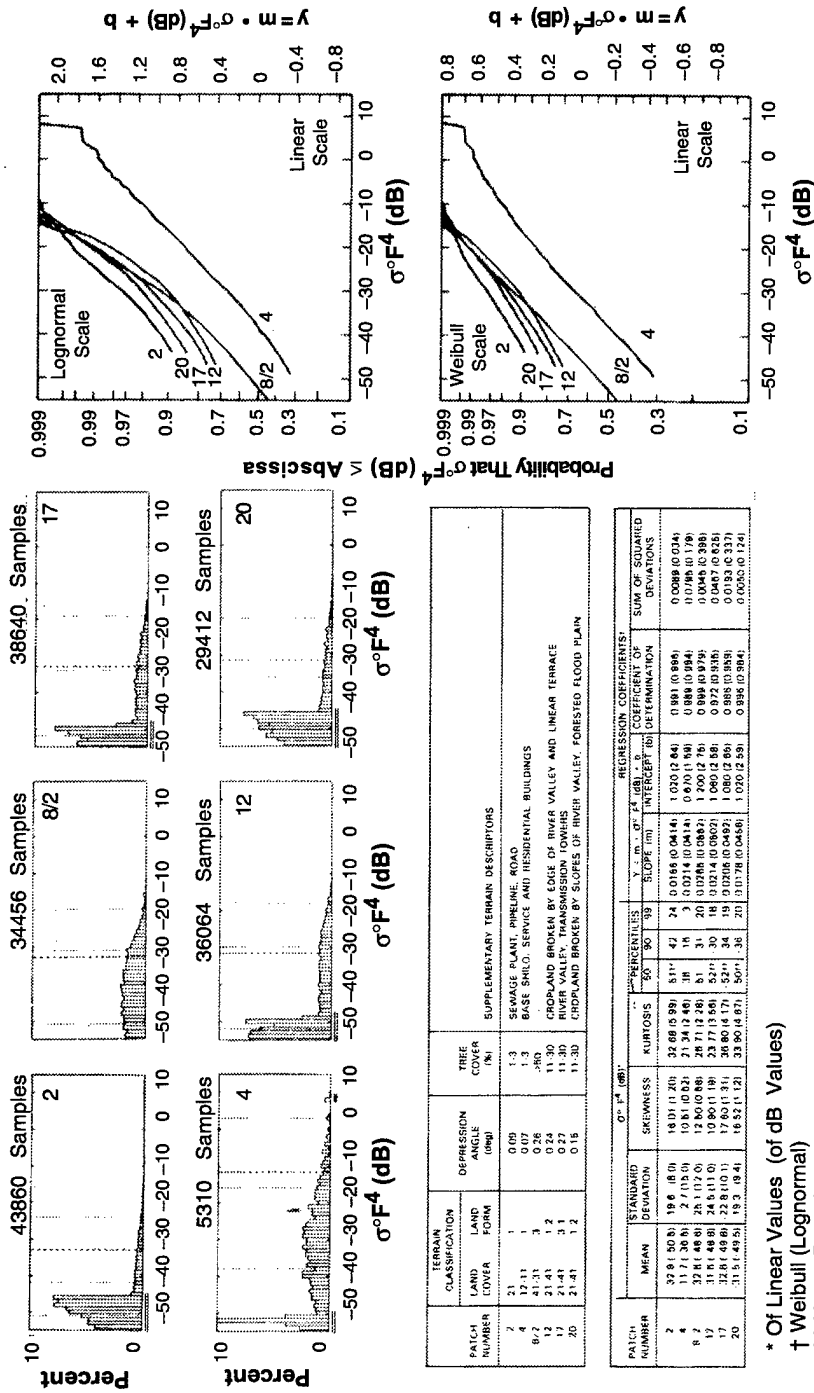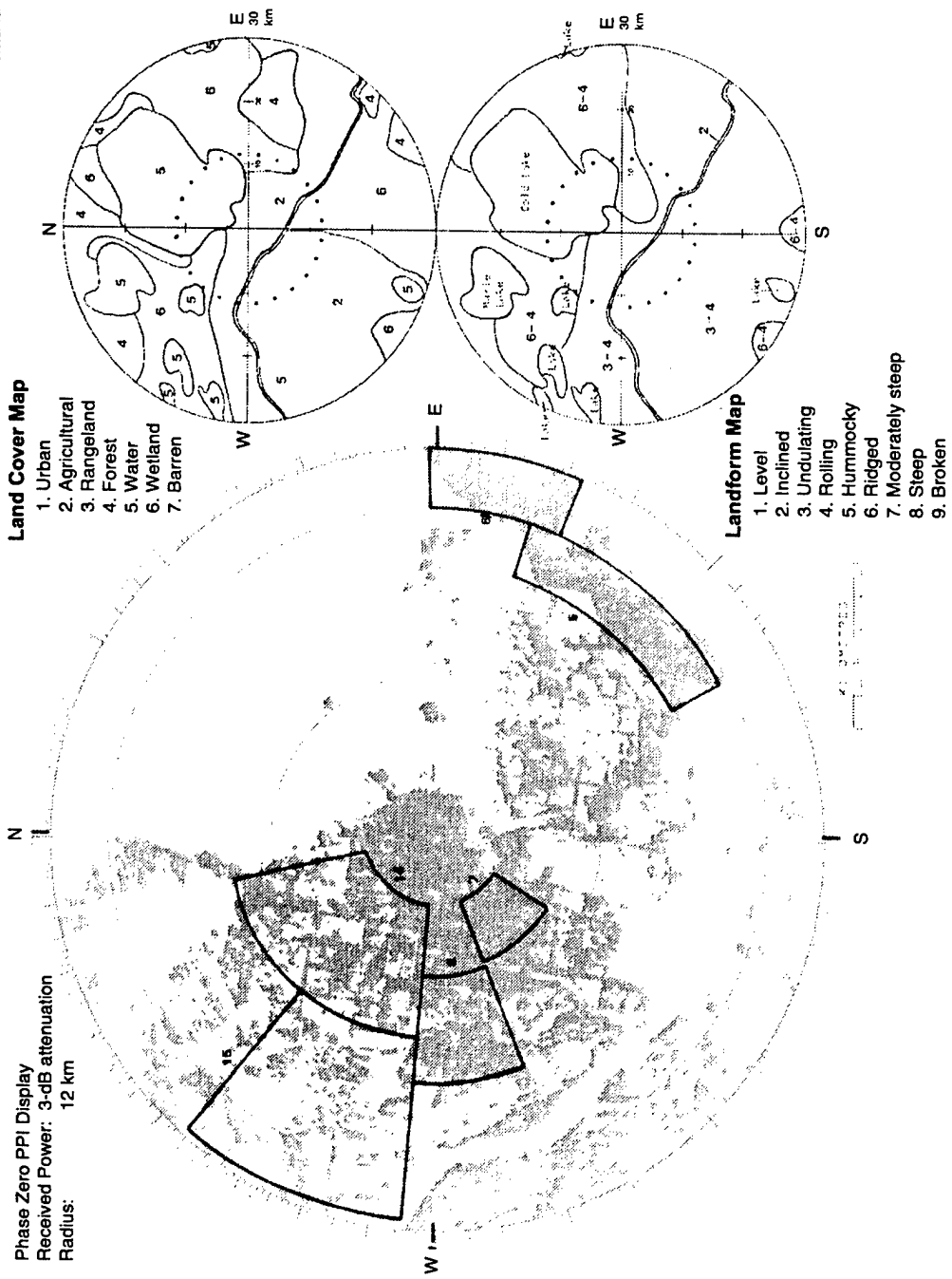*Figure C-10. Phase Zero clutter statistics and terrain classification for selected patches at Cold Lake site.*

Phase Zero PPI Display
Received Power: 3-dB attenuation
Radius: 12 km

Land Cover Map
1. Urban
2. Agricultural
3. Rangeland
4. Forest
5. Water
6. Wetland
7. Barren

Landform Map
1. Level
2. Inclined
3. Undulating
4. Rolling
5. Hummocky
6. Ridged
7. Moderately steep
8. Steep
9. Broken

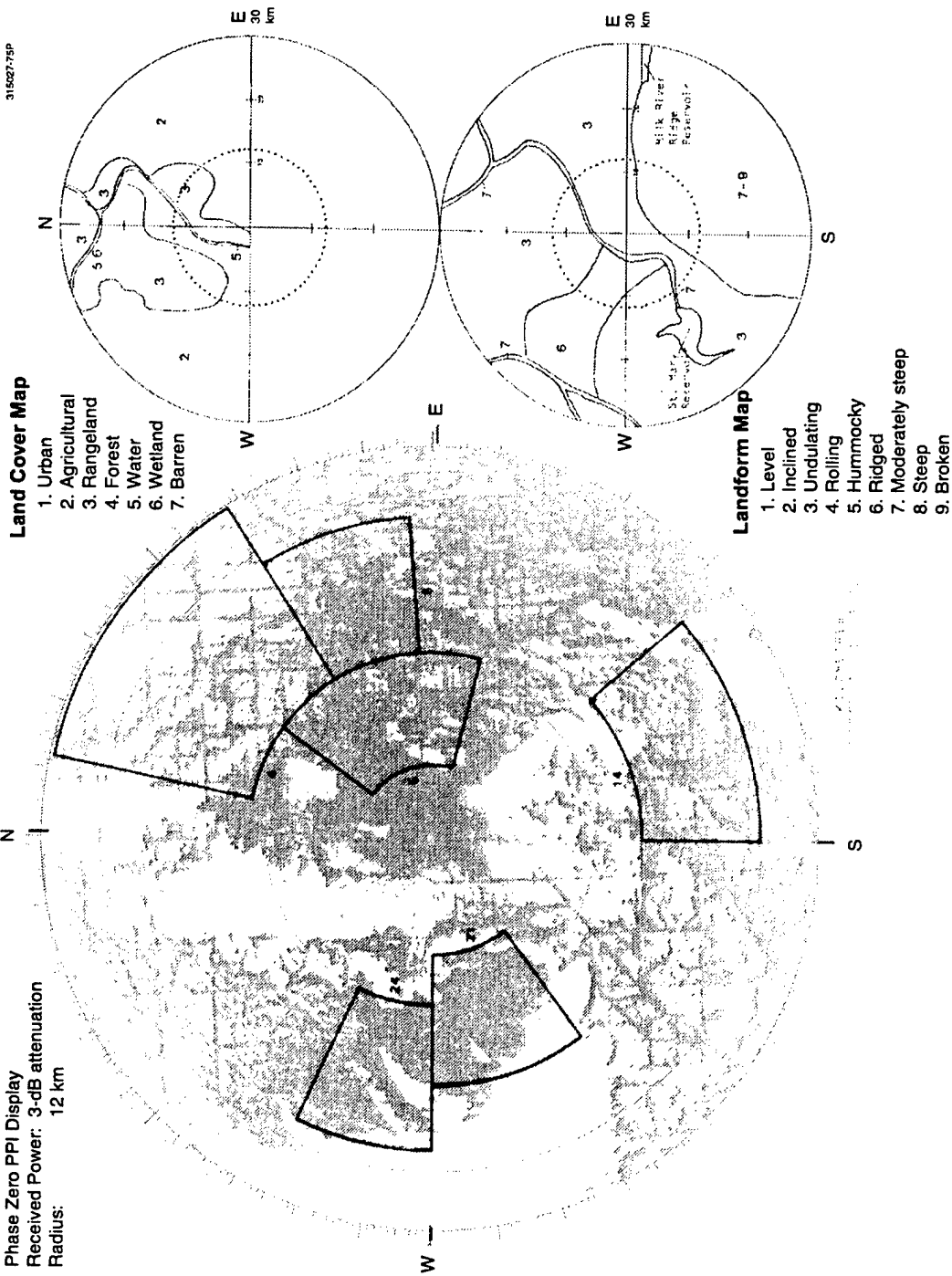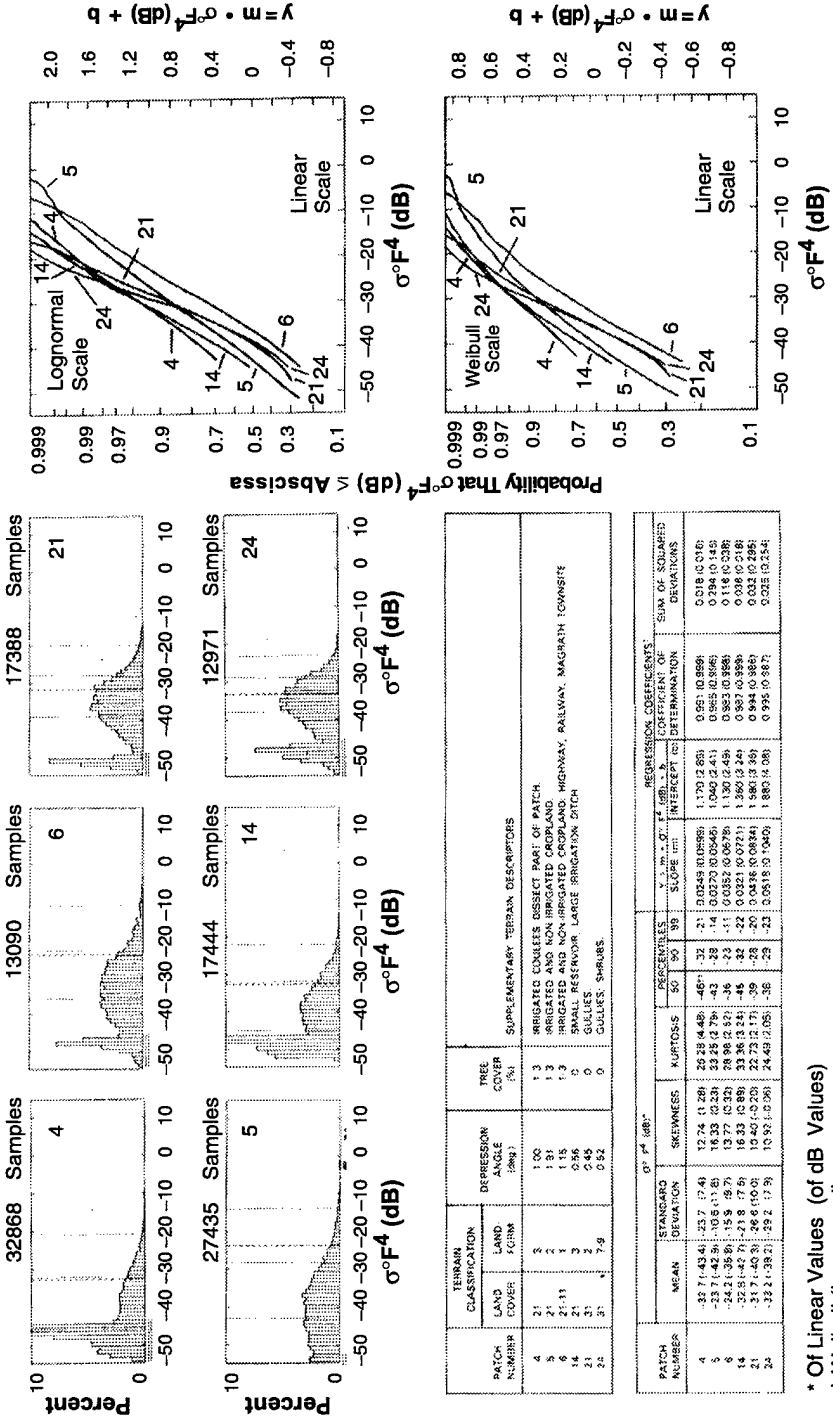*Figure C-11. Radar ground clutter visibility and terrain classification maps with selected clutter patches at Magrath site.*

172

Figure C-12. *Phase Zero clutter statistics and terrain classification for selected patches at Magrath site.*

Phase Zero PPI Display
Received Power: 3-dB attenuation
Radius: 12 km

Land Cover Map
1. Urban
2. Agricultural
3. Rangeland
4. Forest
5. Water
6. Wetland
7. Barren

Landform Map
1. Level
2. Inclined
3. Undulating
4. Rolling
5. Hummocky
6. Ridged
7. Moderately steep
8. Steep
9. Broken

Figure C-13. Radar ground clutter visibility and terrain classification maps with selected clutter patches for Calgary West site.

174

Figure C-14. Phase Zero clutter statistics and terrain classification for selected patches at Calgary West site.

Land Cover Map
1. Urban
2. Agricultural
3. Rangeland
4. Forest
5. Water
6. Wetland
7. Barren

Landform Map
1. Level
2. Inclined
3. Undulating
4. Rolling
5. Hummocky
6. Riged
7. Moderately steep
8. Steep
9. Broken

Phase Zero PPI Display
Received Power: 3-dB attenuation
Radius: 12 km

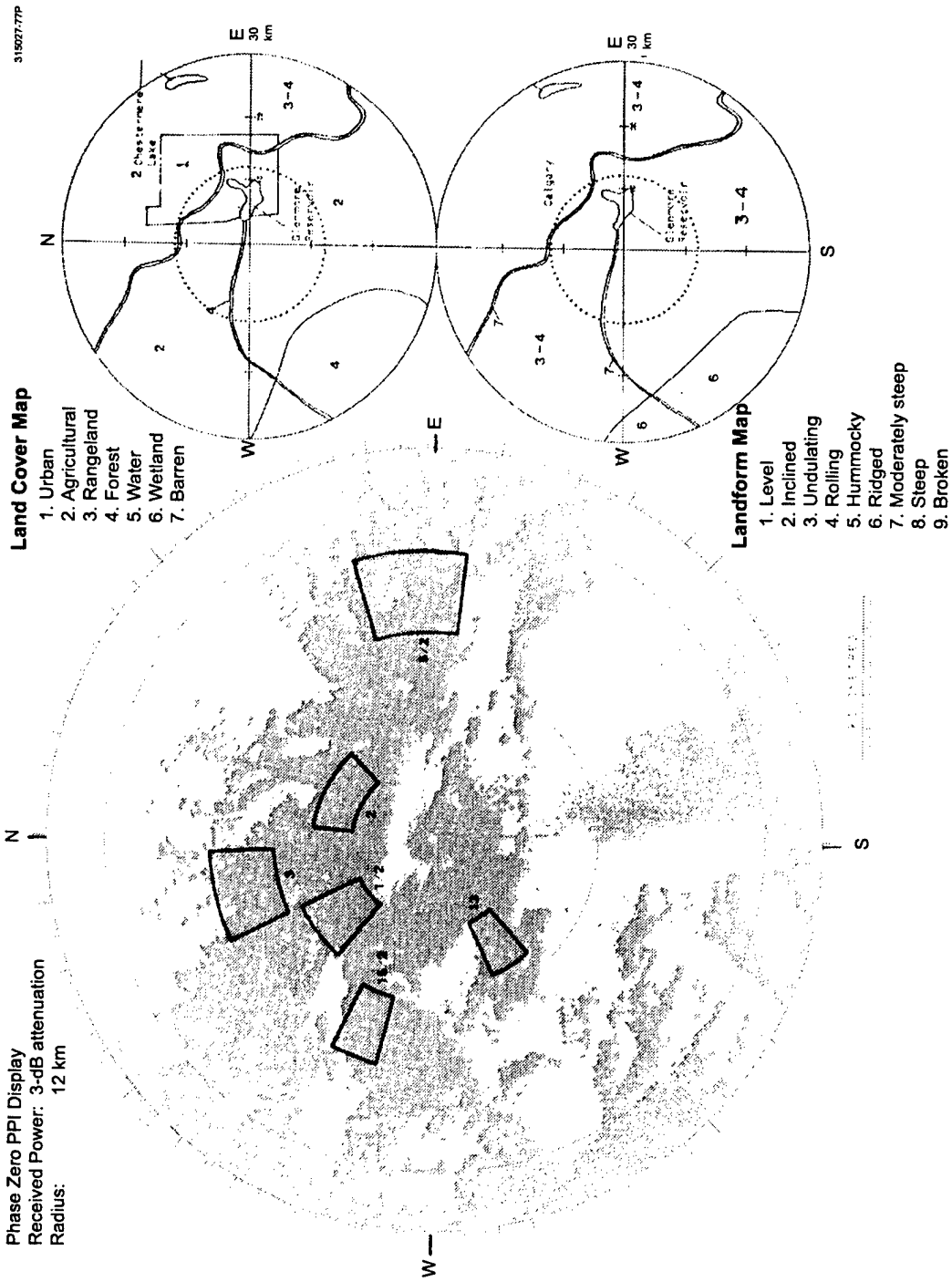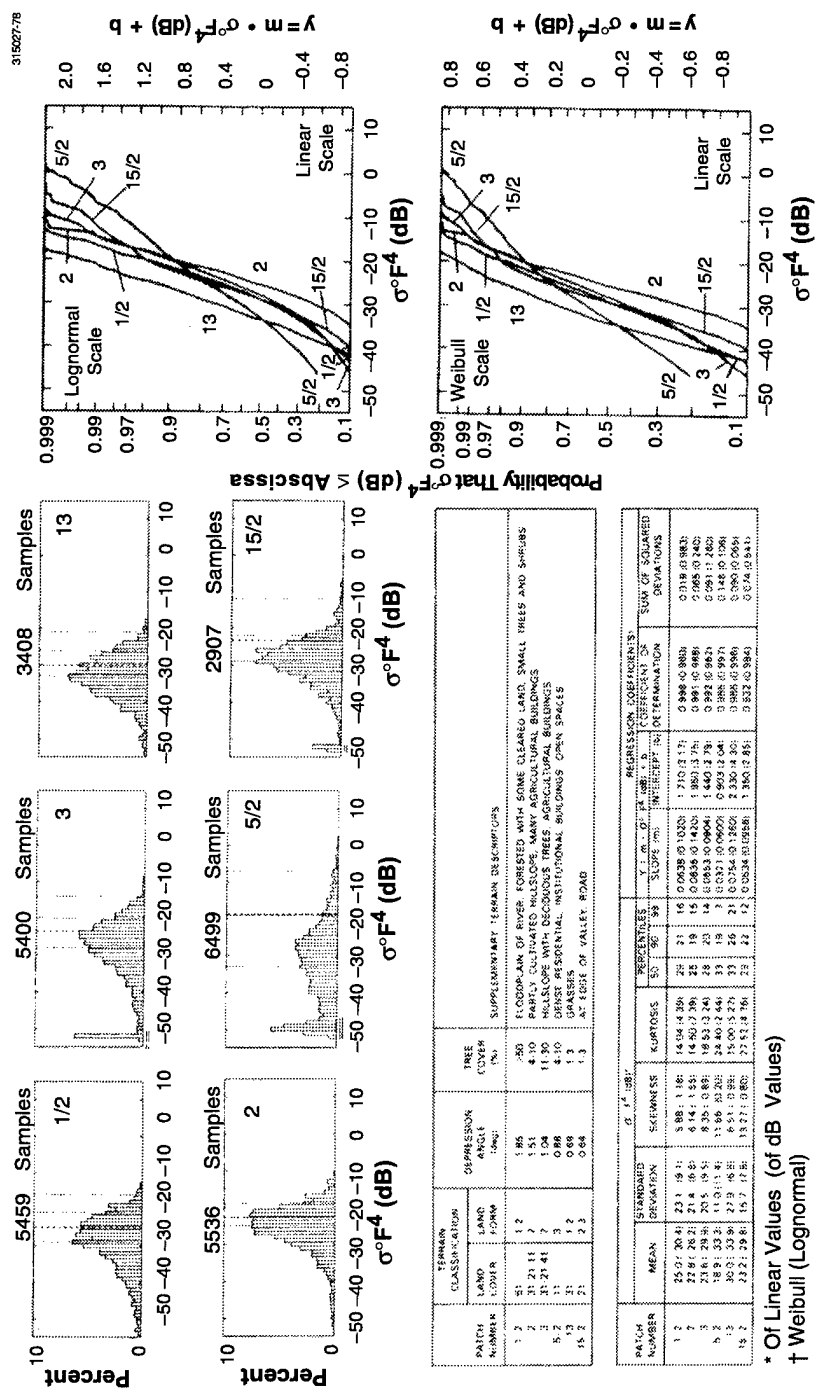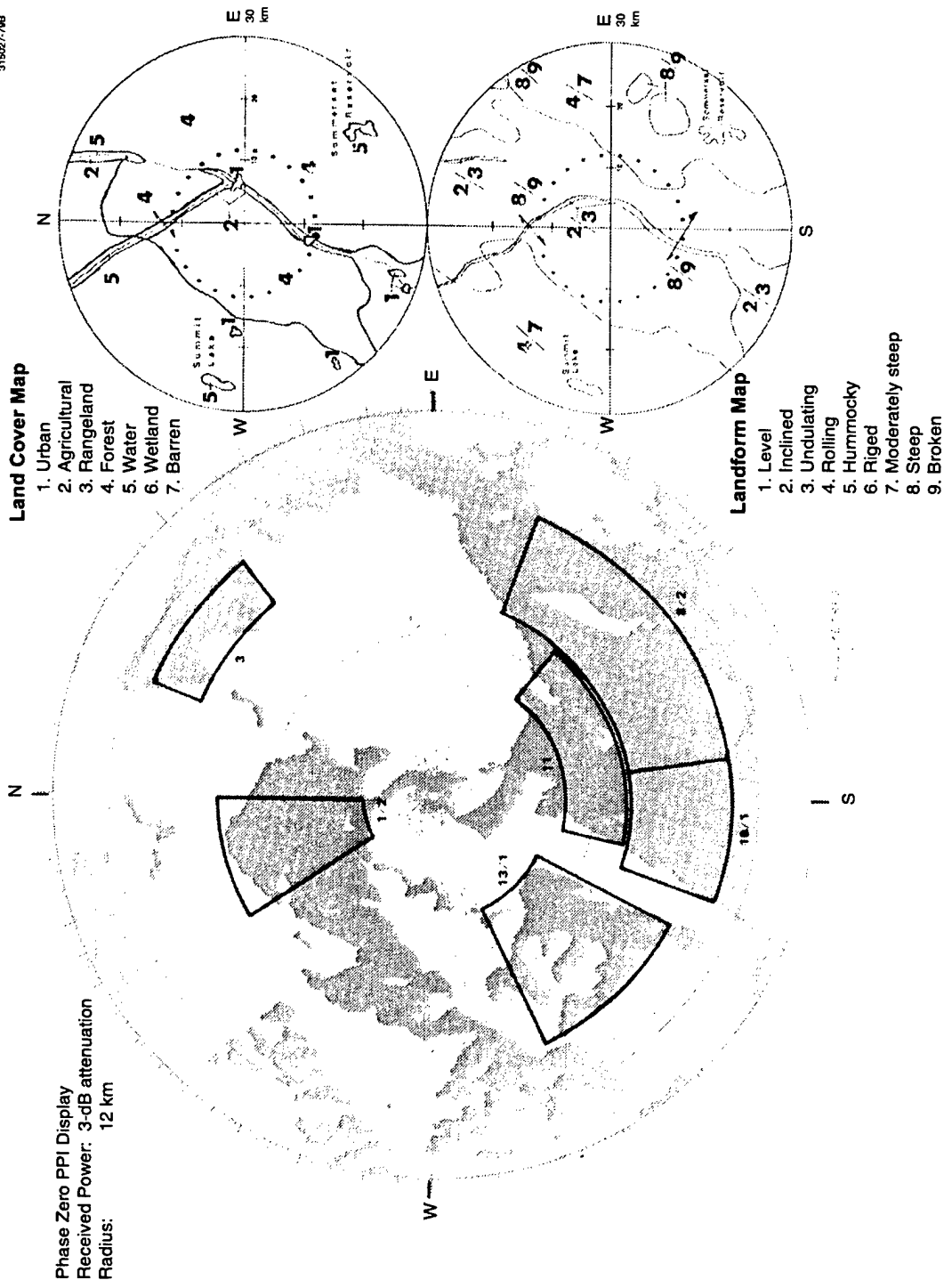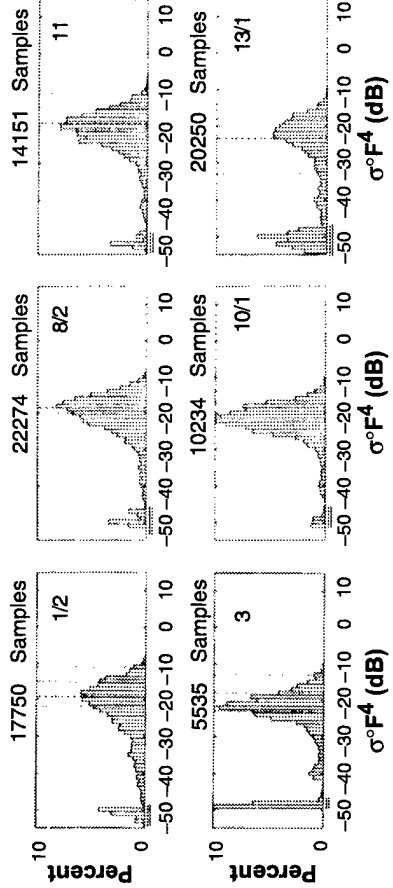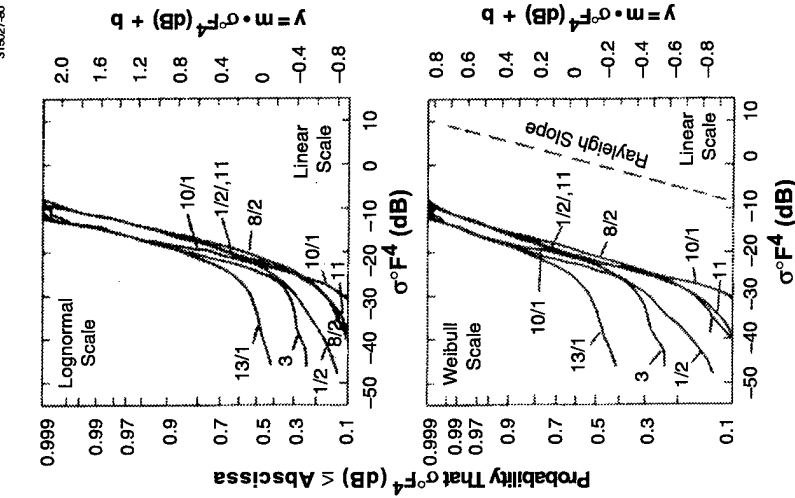*Figure C-15. Radar ground clutter visibility and terrain classification maps with selected clutter patches for Equinox Mt. site.*

176

Figure C-16. Phase Zero clutter statistics and terrain classification for selected patches at Equinox Mt. site.

The first figure for each site shows a Phase Zero measured clutter map at 12-km maximum range, upon which an overlay is superimposed showing the outlines and identifying numbers of six patches. This clutter map shows discernible clutter as dark gray where a discernible clutter signal is defined to be greater than or equal to 3 dB above the radar noise level. Signal levels at or slightly (i.e., 2 dB or less) above the noise floor are shown as white. Thus, these maps are thresholded in received power 3 dB above the noise floor. The noise floor power level increases with the third power of the range (e.g., see Figures 10 and 18).

The $\sigma°F^4$ statistics presented for each patch in the second figure for each site are all with the Phase Zero radar set at 12-km maximum range (see Table B-5). At this maximum range setting, the range resolution was 75 m and the range sampling interval was 37.5 m (i.e., approximately 2:1 oversampling). Other Phase Zero parameters are presented in Table B-4. In particular, the azimuth resolution (i.e., one-way 3-dB beamwidth) was 0.9° and the azimuth sampling interval was about 0.23° (i.e., approximately 4:1 oversampling). That is, individual spatial sample cells or pixels in the clutter map are 37.5 m × 0.23°, but individual resolution cells are 75 m × 0.9° (i.e., about 8:1 oversampling). If 8:1 oversampling were rigorously true, pixels would always light in groups of eight, and, in fact, this is not nearly the case. In each map, it is not difficult to find a number of single pixels that light alone. There is some degree of independence in the strength estimates of adjoining pixels, partly due to beamwidth effects (i.e., 6 dB two-way from center to edge), but possibly more importantly, due to thresholding effects as strength is determined through sequential steps of IF attenuation. Both of these effects introduce desirable variations, both spatial and temporal, into the amplitude distributions. To the extent that they do so, the influence of both is to reduce the nominal 8:1 oversampling down to lower levels. Nevertheless, there does remain a significant degree of oversampling, difficult to quantify, in these Phase Zero distributions, and this should be borne in mind when considering the number of samples (i.e., pixels) that are shown to be contained in each patch.

Also shown in the first figure for each site, in addition to the measured clutter map, is a simple land cover map and a simple landform map which together provide a complementary overview of terrain description as an aid in interpreting the measured clutter map. These simple, line drawing, terrain description maps were prepared relatively quickly from 1:250,000 scale topographic maps and Landsat images, and do not reflect the level of terrain descriptive detail provided for each patch in the second figure for each site. The terrain descriptive information in the second figure for each site was obtained from much larger scale (e.g., typically 1:50,000) air photos and maps. The line drawing terrain maps in the first figure for each site are of 30-km radius; the 12-km radius of the clutter map is shown in each as a dotted circle.

The second figure for each site shows $\sigma°F^4$ statistics and terrain descriptions for each of the six patches shown in the first figure. Histograms of $\sigma°F^4$ are shown for each patch at the top of the figure. The identifying patch number is shown in the upper right corner of each histogram box. Fifty, 90, and 99 percentile levels are shown as three vertical dotted lines in each histogram, progressing left to right, respectively, across the histogram. The n-th percentile level of $\sigma°F^4$ indicates that n percent of the samples (n = 50, 90, or 99) in the histogram lie to the left of the dotted line at $\sigma°F^4$ levels less than or equal to that indicated by the dotted line. The mean value (upper bound, of linear values) of clutter strength $\sigma°F^4$ within each patch is shown as a vertical dashed line in the corresponding histogram. The number of samples

178

(individual sample pixels, not spatially independent resolution cells) in each histogram including samples at radar noise level is printed above each histogram box. The resolution of $\sigma°F^4$ in each histogram is in one dB increments or bins. Bins which contain one or more samples at radar noise level are doubly underlined between the $\sigma°F^4$ scale and the bottom edge of the histogram window to indicate radar noise contamination. They usually occur to the left side of the histogram. Bins which contain one or more saturated samples are triply underlined. When they occur, which is infrequently, they are to the right side of the histogram. The histograms are stored in computer files as three-dimensional arrays containing: 1) the total number of samples per bin; 2) the number of noise samples per bin; and 3) the number of saturated samples per bin for each 1-dB bin in $\sigma°F^4$.

Obviously not all samples in noise-contaminated bins are at noise level. Histograms and statistics with noise samples removed were also collected. These so-called "shadowless" measures of clutter are sensitivity dependent and are not absolute measures of reflectivity. They are tempting to use, but can easily be misinterpreted in analysis. Further discussion concerning shadowless statistics is given in Section 4.3.2. No shadowless statistics are shown in this appendix.

To the right of the histograms, cumulative distributions are shown obtained by integrating (i.e., cumulatively summing) across each histogram from left to right. These cumulative distributions are shown both on a nonlinear lognormal scale and a nonlinear Weibull scale. If an empirical distribution is rigorously lognormal or Weibull, it plots as a straight line on a nonlinear lognormal or Weibull scale, respectively. To the extent that empirical distributions are approximately linear on either of these scales, they may be approximated analytically by Weibull or lognormal statistics. On the whole, but not without exception, the empirical clutter distributions tend to be somewhat more linear on the Weibull scale than the lognormal scale, as may be observed in the plots of cumulative distributions in this appendix. Lognormal statistics tend to overemphasize the spreads that actually occur in low-angle clutter.

Percentile levels for any $\sigma°F^4$ value may be read directly from the left-hand, nonlinear vertical scale on either the lognormal or Weibull plot. Of course, for a given distribution the same levels are read on either plot. These cumulative distributions are absolute measures independent of noise contamination at $\sigma°F^4$ levels above the maximum (i.e., strongest) noise-contaminated bin. The percentile level only indicates the relative proportion of samples below a given strength. As long as the given strength is above the noise, it does not matter whether samples below that are at noise level or not. That is, the true levels for samples measured at noise level must be less than or equal to the noise level. The cumulative plots shown in this appendix are only shown as they emerge above (i.e., to the right of) the maximum noise-contaminated bin. However, their formation includes the samples at radar noise level to the left of this point of emergence. As a result, to the right of the point of emergence, over the region where the cumulative is displayed in the plots, the cumulatives in this appendix are absolute measures of reflectivity independent of sensitivity.

In the box immediately below the histograms in the statistics figures, terrain descriptive or ground truth information is provided as stored in the computer files for each patch. Terrain classification by land cover and landform is indicated. Three levels of land cover are allowed (primary, secondary, and tertiary),

179

and two levels of landform are allowed (primary and secondary), where the higher levels indicate decreasing relative incidence of those terrain types within the patch. These various levels of classification reflect efforts to grapple with and capture the complexity and heterogeneity of actual terrain within kilometer-sized patches, even though a criterion in patch specification is by and large to maintain similarity in the overall type of terrain within the patch. Patches with only first level classifiers are referred to as pure patches. Only 592 (or 27.2%) of the 2,177 Phase Zero patches are pure. Specialized studies were done with these patches of more homogeneous terrain but they did not lead to markedly better understanding of the overall low-angle clutter phenomenon. Patches with one or more higher level classifications are referred to as hybrid patches. The fact that shadowing is a more important influence in low-angle amplitude statistics than fine distinctions in terrain type resulted, fortunately, in de-emphasis of these classification nuances in later studies.

Next, the ground truth box shows depression angle. In practical terms, at the ranges of less than 12 km that apply to the patches of this appendix, depression angle is just the angle below the horizontal at which the center of the patch is viewed at the antenna. However, the rigorous definition and computation of depression angle is in a reference system centered at the terrain point, in which depression angle is the complement of incidence angle at the terrain point (i.e., point of backscatter) on the spherical earth (see Appendix D). Incidence angle is the angle between the direction of illumination from the radar and the local earth radius through the terrain point in question. Thus, the actual computation of depression angle takes into account sphericity of the earth.

Perhaps a better term than depression angle could be coined for this angle. However, the term grazing angle is ambiguous and therefore not appropriate. Grazing angle carries for many people the connotation of inclusion of local terrain slope (i.e., grazing angle = angle between direction of illumination and the tangent to the local terrain surface; see Figure 20). Elsewhere, this report discusses the fact that implementation of grazing angle as so defined, or even definition of what it means over large composite landscape, has not proven very useful in improving observed correlations with illumination angle. Effects of terrain slope on amplitude distributions are instead captured through landform classification.

Grazing angle carries for other people, generally of the airborne community, just the connotation of inclusion of spherical earth effects, without consideration of local terrain slope. Thus, whether the terminology of grazing angle or depression angle is used to describe the measure of illumination angle used herein—which includes spherical earth effects but not local terrain slope effects—there is susceptibility to misinterpretation. Thus, the term depression angle is used, and made the best of.

Next, the ground truth box shows the percentage of the spatial area of the patch occupied by trees. This was obtained by overlaying a uniform pattern of dots over the air photo within the patch and counting the relative proportion of dots overlaying trees. Five tree cover classes were used, as: 1) no trees; 2) $1 <$ percent treed area ≤ 3; 3) $3 <$ percent treed area ≤ 10; 4) $10 <$ percent treed area ≤ 30; and 5) $30 <$ percent treed area ≤ 50 (see Table 16). When trees exist at relatively low incidence of occurrence, they often dominate as discrete sources of backscatter. Effects of varying incidence of trees on amplitude statistics are

180

discussed in Section 4.3.6. Patches that are classified as forest (land cover = 41, 42, or 43) or forested wetland (land cover = 61) have tree cover greater than 50 percent.

Finally, in the ground truth box, supplementary terrain descriptors are included as were provided in the stereo air photo interpretation. These were not stored in the computer files.

Below the ground truth box is a box containing a number of computed statistical characteristics of the clutter amplitude distribution for each patch. These are all computed from the stored, three dimensional, patch histogram in which the $\sigma°F^4$ bin size is always 1 dB. The differences between statistics computations based on the actual array of non-rounded-off, individual, pixel-level, samples of $\sigma°F^4$, and the more efficient computations based on the rounded-off, binned groups of the histogram, were shown to be insignificant. In what follows, each quantity in the statistics box is defined in turn.

First, let x represent clutter strength $\sigma°F^4$ in units of m^2/m^2. Let y represent the dB value of $\sigma°F^4$, such that

$$y = 10\log_{10} x \qquad \text{(C-1)}$$

As discussed above, in forming a histogram of spatial samples of clutter strength within a clutter patch, measured values of y are sorted into bins 1-dB wide. A sketch of such a histogram is shown in Figure C-17. In this histogram, let i be the bin index, which runs in increasing order from $i = 1$ at the minimum value of y, $y = y_{min}'$, in the histogram, to $i = I$ at the maximum value of y, $y = y_{max}'$, in the histogram. Let $i = i'$ represent the bin containing the maximum value of y that is noise contaminated, $y = y'$. Let the number of samples in the i-th bin be n_i. Let the total number of samples in the histogram be N. Then

$$N = \sum_{i=1}^{I} n_i \qquad \text{(C-2)}$$

The sketch of Figure C-17 shows these relationships.
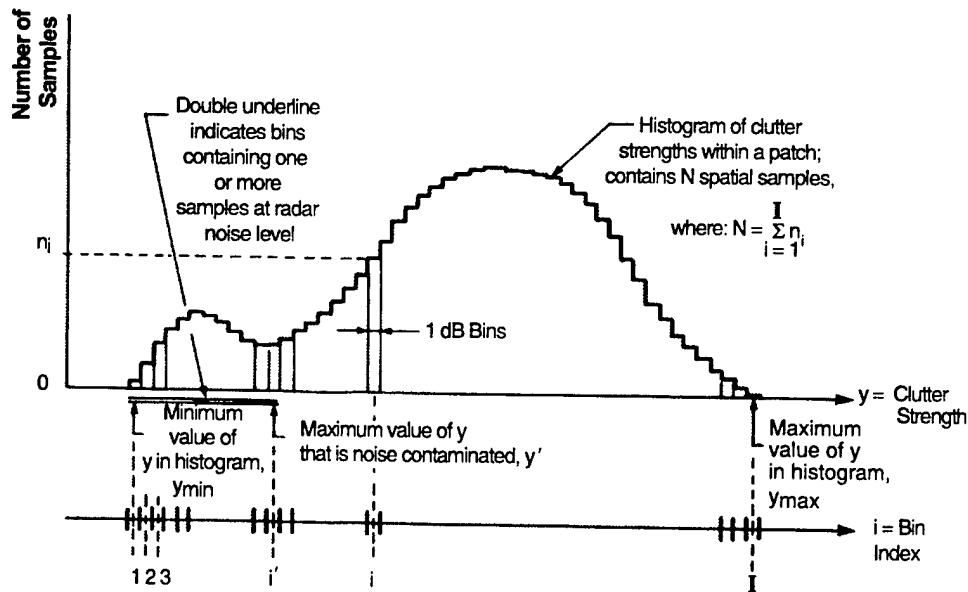
Figure C-17. Sketch of patch clutter strength histogram showing nomenclature. Here, $y = 10 \log_{10} (\sigma°F^4)$.

Some of the samples in the histogram are at noise level. In all moment computations, upper bounds were computed assigning noise power values to these samples, and lower bounds were computed assigning zero power values to these samples. Both upper and lower bounds for each moment-derived quantity were stored for each patch in a computer file. This was done both for computations of moments of linear values, x_i, and dB values, y_i. Only upper bounds are shown in the statistics boxes of Figures C-6, C-8, C-10, C-12, C-14, and C-16. Upper and lower bounds for the mean of linear values only, and the percent of cells at radar noise level, are shown for all six patches at all six sites in Table C-2. It is clear in Table C-2 that the amount of microshadowing within a patch, which is extensive for some patches (e.g., 80.5 percent for patch 10 at Coaldale), has very little effect on the estimate of the mean of linear values for the patch (i.e., upper and lower bounds are very close to each other). The upper bound to the mean of linear values within a patch is used extensively in the body of this report as clutter strength modeling information.

Next, the moment-dependent quantities in the statistics box are defined. These moment-dependent quantities were first computed from linear values x_i and subsequently converted to dB. The same set of moment-dependent quantities were secondly computed from dB values y_i. These latter quantities dependent on the moments of dB values y_i are shown in the statistics box within parentheses.

182

TABLE C-2

Effects of Microshadowing* on Mean Clutter Strength

Site	Effective Radar Height (m)	Clutter Patch Number	Percent of Cells at Radar Noise Level	Mean Clutter Strength $\sigma°F^4$ (dB)[†]	
				Upper Bound[‡]	Lower Bound**
Coaldale	3	3	74.4	−24.332	−24.346
		5	15.9	−18.624	−18.624
		6	70.0	−27.030	−27.068
		8	64.9	−24.004	−24.021
		9	72.5	−25.307	−25.331
		10	80.5	−28.815	−28.878
Shilo	18	2	74.4	−28.938	−28.998
		4	27.5	−7.726	−7.726
		8/2	30.3	−28.825	−28.828
		12	59.8	−27.599	−27.615
		17	62.7	−28.808	−28.831
		20	70.2	−27.470	−27.510
Cold Lake	40	5	25.2	−21.889	−21.894
		6	24.0	−22.843	−22.853
		7	2.7	−19.105	−19.105
		8	19.8	−19.477	−19.478
		14	34.5	−26.781	−26.784
		15	65.2	−33.030	−33.212
Magrath	94	4	56.4	−28.841	−28.928
		5	14.7	−19.784	−19.784
		6	18.1	−20.489	−20.492
		14	42.0	−28.929	−28.974
		21	25.2	−27.770	−27.778
		24	23.1	−29.282	−29.306
Calgary West	124	1/2	2.3	−21.270	−21.270
		2	0.3	−18.991	−18.991
		3	6.8	−19.617	−19.618
		5/2	16.5	−15.005	−15.006
		13	0.6	−26.076	−26.076
		15/2	3.9	−19.356	−19.356
Equinox Mt.	678	1/2	11.1	−17.901	−17.901
		3	23.0	−18.933	−18.935
		8/2	8.3	−15.499	−15.499
		10/1	3.8	−18.678	−18.678
		11	6.8	−20.084	−20.084
		13/1	39.0	−20.922	−20.924

* Microshadowed cells are defined to be cells within patches at radar noise level

† Computed in units of m^2/m^2 and subsequently converted to dB

‡ Assign noise power level to noise cells

**Assign zero power level to noise cells

Quantities dependent on the first four moments of linear values x_i are defined as follows:

$$\text{mean} = \bar{x} = \frac{1}{N} \sum_{i=1}^{I} n_i x_i \qquad \text{(C-3)}$$

$$\text{Standard Deviation} = \text{sd}(x) = \left[\frac{1}{N-1} \sum_{i=1}^{I} n_i (x_i - \bar{x})^2 \right]^{\frac{1}{2}} \qquad \text{(C-4)}$$

$$\text{coefficient of skewness} = g_3(x) = \frac{M_3(x)}{[M_2(x)]^{3/2}} \qquad \text{(C-5)}$$

$$\text{coefficient of kurtosis} = g_4(x) = \frac{M_4(x)}{[M_2(x)]^2} \qquad \text{(C-6)}$$

where

$$\text{q-th moment about the mean} = M_q(x) = \frac{1}{N} \sum_{i=1}^{I} n_i (x_i - \bar{x})^q \; ; q = 2, 3, 4. \qquad \text{(C-7)}$$

In clutter amplitude statistics, these quantities dependent on the first four moments of x_i are almost always much less than unity. For convenience, these quantities shown in Eqs. C-3 through C-6 were converted to dB units as:

$$\bar{x}\big|_{dB} = 10 \log_{10}(\bar{x}) \qquad \text{(C-8)}$$

$$\text{sd}(x)\big|_{dB} = 10 \log_{10}[\text{sd}(x)] \qquad \text{(C-9)}$$

$$g_3(x)\big|_{dB} = 10 \log_{10}[g_3(x)] \qquad \text{(C-10)}$$

$$g_4(x)\big|_{dB} = 10 \log_{10}[g_4(x)] \qquad \text{(C-11)}$$

184

It is these quantities dependent on the first four moments of x_i and converted after computation to dB units as defined in Eqs. C-8 through C-11 that are shown to the left (i.e., not within parentheses) in the 2nd, 3rd, 4th, and 5th columns from the left, respectively, in each of Figures C-6, C-8, C-10, C-12, C-14, and C-16. These quantities dependent on the moments of linear values x_i are regarded as primary quantities fundamentally representative of the clutter amplitude distributions.

Next, quantities dependent on the first four moments of the dB values y_i are defined as follows:

$$\text{mean of dB values} = \bar{y} = \frac{1}{N} \sum_{i=1}^{I} n_i y_i \tag{C-12}$$

$$\text{standard deviation of dB values} = sd(y) = \left[\frac{1}{N-1} \sum_{i=1}^{I} n_i (y_i - \bar{y})^2 \right]^{1/2} \tag{C-13}$$

$$\text{coefficient of skewness of dB values} = g_3(y) = \frac{M_3(y)}{[M_2(y)]^{3/2}} \tag{C-14}$$

$$\text{coefficient of kurtosis of dB values} = g_4(y) = \frac{M_4(y)}{[M_2(y)]^2} \tag{C-15}$$

where

$$M_q(y) = \frac{1}{N} \sum_{i=1}^{I} n_i (y_i - \bar{y})^q ; q = 2, 3, 4 \tag{C-16}$$

It is these quantities dependent on the first four moments of dB values y_i as defined in Eqs. C-12 through C-15 that are shown to the right (i.e., within parentheses) in the 2nd, 3rd, 4th, and 5th columns from the left, respectively, in each of Figures C-6, C-8, C-10, C-12, C-14, and C-16. These quantities dependent on moments of dB values y_i are regarded as adjunct quantities occasionally useful in working with lognormal statistics. They are included in this appendix for completeness, but are not referenced or their use implied anywhere else in this report.

The interpretation of the quantities dependent on the first four moments of linear values x_i in the statistics box is next briefly commented on. The standard deviation is meaningful only with respect to the mean. That is, it is the ratio of standard deviation-to-mean (i.e., $sd(x)|_{dB} - \bar{x}|_{dB}$) that is meaningful. For example, for Rayleigh statistics $sd(x) = \bar{x}$, and $10 \log_{10}(sd(x)/\bar{x}) = sd(x)|_{dB} - \bar{x}|_{dB} = 0$. Thus, the quantity $sd(x)|_{dB} - \bar{x}|_{dB}$ (i.e., left value in 3rd column minus left value in 2-nd column of the statistics box)

indicates the degree of spread in the amplitude distribution beyond Rayleigh. Low-angle clutter amplitude distributions are usually characterized by wide spreads. Occasional patch amplitude distributions may be found, almost always at higher depression angles, that are close to Rayleigh, to the extent that $sd(x)|_{dB}$ approaches $\bar{x}|_{dB}$. Again, Rayleigh may be taken as a point-of-departure in interpreting coefficient of skewness and kurtosis. Skewness is a measure of asymmetry in the distribution. Kurtosis is a measure of concentration about the mean. For Rayleigh statistics, $g_3(x) = 2$ and $g_4(x) = 9$, so that $g_3(x)|_{dB} = 3.01$ and $g_4(x)|_{dB} = 9.54$. Usually the values listed for $g_3(x)|_{dB}$ and $g_4(x)|_{dB}$ as the left-most quantities in the 4th and 5th columns, respectively, of the statistics box are considerably greater than 3 and 9.5, respectively, again the result of a widely dispersed high-side tail in low-angle clutter amplitude distributions.

By these measures of $g_3(x)|_{dB}$ and $g_4(x)|_{dB}$ also, as well as $sd(x)|_{dB} - \bar{x}|_{dB}$, occasional patch amplitude distributions may be found close to Rayleigh. For example, the high depression angles at Equinox Mountain resulted in some of the empirical statistics there beginning to approach Rayleigh. This is indicated in Figure C-16 by the fact that the quantities dependent on the first four moments of linear values for patch numbers 1/2, 3, 8/2, and 13/1, which all reference patches which substantially have homogeneous forest as land cover, all in rough measure approach Rayleigh values. On the other hand, patch numbers 10/1 and 11 in Figure C-16, which reference patches which include cropland on the valley floor as a secondary component of land cover in addition to forest, remain far from Rayleigh. In Table C-3, two patches at Equinox Mountain, patch numbers 1/2 and 8/2, are selected for detailed comparison of attributes of their spatial amplitude statistics with theoretical Rayleigh values. Most of the empirical attributes shown for these two patches in Table C-3 are within 1 or 2 dB (or at most 3 dB for attributes sensitive to the high tail, such as the ratio of 99-percentile to median, and kurtosis) of theoretical Rayleigh values. If a similar comparison is made of such empirical attributes with Rayleigh values for other patches at other sites shown in this appendix, it is generally observed that the empirical patch attributes are much further (i.e., many dB) removed from Rayleigh than the forested patches at Equinox Mountain. Other examples of patches with approximately Rayleigh spatial amplitude statistics are patch numbers 19/1 and 19/2 at Gull Lake West, Manitoba, discussed in Section 3.3 in the body of this report. These Gull Lake West patches provide near matches in their approach to Rayleigh with patch number 8/2 at Equinox Mountain (see Table C-3), although they are separated by 10 dB or so in mean strength. Another very Rayleigh-like patch is patch 15/3 at Plateau Mountain, discussed in Section 4.3.2. No systematic search for Rayleigh patches has been made in the Phase Zero database.

TABLE C-3

Approximately Rayleigh Spatial Amplitude
Statistics for Two Patches at Equinox Mountain, Vermont
Phase Zero X-band data, range resolution = 75 m

Statistical Attribute of Spatial Amplitude Distribution	$\sigma°F^4$ (dB)		
	Measured Values		Theoretical Rayleigh Values
	Patch No. 1/2*	Patch No. 8/2**	
Mean	−17.9	−15.5	–
Standard Deviation-to-Mean	1.5	0.6	0
Skewness	4.3	4.3	3
Kurtosis	11.1	12.4	9.5
Mean-to-Median	3.1	1.5	1.6
90 Percentile-to-Median	7	5	5.2
99 Percentile-to-Median	11	9	8.2

* Moderately steep mixed forest. Depression angle = 7.6°. Range limits are from 2.0 to 6.6 km. Azimuth limits are from 327° to 360°.

** Moderately steep to steep mixed forest. Depression angle = 4.3°. Range limits are from 6.2 to 9.3 km. Azimuth limits are from 110° to 171°.

Next, in the 6th, 7th, and 8th columns from the left of the statistics boxes in Figures C-6, C-8, C-10, C-12, C-14, and C-16 are shown the 50, 90, and 99 percentile levels of $\sigma°F^4$, respectively, of the six patch amplitude distributions for each site. That is, in Figure C-17 let P_i represent the probability that $y < y_i$ (or, equivalently, that $x \leq x_i$).

Then

$$P_i = \frac{1}{N} \sum_{j=1}^{i} n_j \qquad \text{(C-17)}$$

187

and the corresponding percentile level is $100 \cdot P_i$.[2] The 50, 90, and 99 percentile levels, besides being tabulated in the statistics box, may be read directly from the histograms (as vertical dotted lines), or from the cumulatives (as the $\sigma°F^4$ values for probabilities of 0.5, 0.9, and 0.99, respectively). In the statistics box, if the median (i.e., 50 percentile) is at a level of $\sigma°F^4$ contaminated by noise, it is indicated by footnote as only representing an upper bound to the true median. Otherwise, the percentile levels tabulated are uncontaminated by noise, unlike the four moment-dependent quantities which, theoretically at least, are all upper bound approximations (see Table C-2).

The right-most four columns of the statistics box in Figures C-6, C-8, C-10, C-12, C-14, and C-16 provide linear regression and goodness of fit coefficients to either Weibull (left entry in each column) or lognormal (right entry in each column within parentheses) approximations to each of the six actual empirical patch amplitude distributions at each site. That is, if an empirical patch amplitude distribution is approximately linear in the lower Weibull graph or in the upper lognormal graph the regression coefficients provide the best fitting straight line approximation to the empirical distribution. In what follows, information is provided defining the regression coefficients and goodness of fit parameters. To do this definitively, the Weibull and lognormal analytic distributions also need to be defined.

The Weibull probability density function may be written

$$p(x) = \frac{(\xi) \cdot \ln 2 \cdot x^{\xi - 1}}{x_{50}^{\xi}} \cdot e^{-\frac{\ln 2 \cdot x^{\xi}}{x_{50}^{\xi}}} \tag{C-18}$$

where

x_{50} = median value of x,

ξ = $1/a_w$,

a_w = Weibull shape parameter,

and, as before, x represents $\sigma°F^4$ in units of m^2/m^2. The Weibull distribution degenerates to a Rayleigh[3] distribution when $a_w = 1$. The Weibull cumulative distribution function is

$$P(x) = 1 - e^{-\frac{\ln 2 - x^{\xi}}{x_{50}^{\xi}}} \tag{C-19}$$

---

[2] If the n-th percentile level ($0 \le n \le 100$) occurs at $x_i = x_{i_n}$ in the distribution of x_i, it occurs at $y_{i_n} = 10 \log_{10}(x_{i_n})$ in the distribution y_i, since percentile level only indicates relative position in the distribution. This is not true of moment-dependent quantities. That is, $M_q(y) \neq 10 \log_{10} M_q(x)$.

[3] That is, voltage-like quantities are Rayleigh-distributed, power-like quantities are exponentially distributed. Here, x is a power-like quantity.

where $\quad P(x) = \int\limits_{o}^{x} p(\xi)d\xi$

Equation C-19 may be rearranged, as

$$\cdot \log_{10}\left\{\ln\left(\frac{1}{1-P}\right)\right\} = \frac{1}{10a_w} \cdot 10\log_{10}x + \left\{\log_{10}(\ln 2) - \frac{1}{10a_w} \cdot 10\log_{10}x_{50}\right\} \qquad \text{(C-20)}$$

In Eq. C-20, if we let

$$Y = \log_{10}\left[\ln\left(\frac{1}{1-P}\right)\right] \qquad \text{(C-21)}$$

and recall that $y = 10 \log_{10}x$, we obtain

$$Y = m \cdot y + b \qquad \text{(C-22)}$$

where

$$m = \frac{1}{10a_w} \qquad \text{(C-23)}$$

$$b = \log_{10}(\ln 2) - \frac{1}{10a_w} \cdot y_{50} \qquad \text{(C-24)}$$

and

$$y_{50} = 10\log_{10}(x_{50}) \qquad \text{(C-25)}$$

That is, Eq. C-22 is a linear relationship between Y and y.

189

Equation C-17 shows that for each patch there exists an empirical cumulative amplitude distribution given by an ordered pair (P_i, y_i), $i = 1, 2, ... I$. In this ordered pair, the dependent variable P_i is transformed to Y_i by Eq. C-21. The cumulative distributions (Y_i, y_i) are then plotted, as shown in Figures C-6, C-8, C-10, C-12, C-14, and C-16 in the Weibull graph to the lower right. The abscissa of this graph, shown as $\sigma^\circ F^4$ (dB) (i.e., $\sigma^\circ F^4$ (dB) = $10 \log_{10} (\sigma^\circ F^4)$), is what is represented here as y. The linear ordinate on the right side of this graph is Y given by Eq. C-22. The nonlinear ordinate on the left side of this graph is P, obtained from the corresponding value of Y by Eq. C-21.

A standard linear regression fit to the plot of (Y_i, y_i) is now performed for each patch shown in the Weibull graph to the lower right of Figures C-6, C-8, C-10, C-12, C-14, and C-16. That is, for each patch the slope m and Y-intercept b of the best-fitting straight line to (Y_i, y_i) is obtained. This regression analysis was performed only over the region that (Y_i, y_i) is shown in the graph. This region is defined to be above (i.e., to the right of) the maximum noise-contaminated bin (i.e., $y_i > y'$; see Figure C-17) and within the limits of probability shown in the graph (i.e., $0.1 \le P_i \le 0.999$). As the standard measure of goodness of fit in regression analysis, the coefficient of determination (i.e., the square of the correlation coefficient) is obtained. Also obtained is the sum of the squared deviations which is a subsidiary quantity in the computation of coefficient of determination. These regression computations are defined by the following standard formulas [25]:

$$m = \frac{\frac{1}{I} \sum_{i=1}^{I} (y_i Y_i) - \bar{y}\bar{Y}}{\sigma_y^2} \tag{C-26}$$

$$b = \bar{Y} - m\bar{y} \tag{C-27}$$

$$\text{coefficient of determination} = \left(\frac{m\sigma_y}{\sigma_Y}\right)^2 \text{; and} \tag{C-28}$$

$$\text{sum of squared deviations} = \sum_{i=1}^{I} [Y_i - (my_i + b)]^2 \tag{C-29}$$

where

$$\bar{y} = \frac{1}{I} \sum_{i=1}^{I} y_i \tag{C-30}$$

$$\bar{Y} = \frac{1}{I} \sum_{i+1}^{I} Y_i \tag{C-31}$$

190

$$\sigma_y^2 = \left(\frac{1}{I} \sum_{i=1}^{I} y_i^2 \right) - y^2 \tag{C-32}$$

and

$$\sigma_Y^2 = \left(\frac{1}{I} \sum_{i=1}^{I} y_i^2 \right) - Y^2 \tag{C-33}$$

The regression quantities m, b, coefficient of determination, and sum of squared deviations were tabulated for each of six clutter patches as the left-most entries in the 4th, 3rd, 2nd, and 1st columns from the right in the statistics box of Figures C-6, C-8, C-10, C-12, C-14, and C-16.

A rigorously exact Weibull distribution would plot as a straight line in the lower right-hand graph of Figures C-6, C-8, C-10, C-12, C-14, and C-16 as shown by Eqs. C-20 and C-22. To the extent that any particular patch amplitude distribution is observed to be fairly linear in this graph, it can be reasonably approximated by a Weibull distribution over the range indicated, with Weibull coefficients m and b as given by the left-hand entries in the 4-th and 3-rd columns from the right in the statistics box. This approximating Weibull distribution may be quickly drawn in the lower right graph as a straight line with slope m and Y-intercept b using the right-hand ordinate in the graph. This direct qualitative comparison of the empirical curve with its approximating straight line was found to be the most useful method of assessing goodness of fit; the coefficient of determination and the sum of the squared deviations provided as the 2-nd and 1-st columns from the right in the statistics box also quantify the goodness of fit, but in practice it was found that interpreting these quantities was not as useful as the direct comparison of the curves themselves. The parameters a_w and x_{50} in the analytical Weibull distribution of Eqs. C-18 and C-19 may be quickly obtained from Eqs. C-23, C-24, and C-25. Weibull random variates distributed according to this approximating best-fit distribution may be obtained by generating uniformly distributed random variates P_k, $k = 1,2,3,...$ and using Eq. C-20 to convert each to a corresponding Weibull distributed variate x_k, $k = 1,2,3,...$, where the parameters a_w and x_{50} in Eq. C-20 are obtained as discussed above. The mean-to-median ratio of Weibull distribution is given by

$$\frac{\bar{x}}{x_{50}} = \frac{\Gamma(1 + a_w)}{(\ln 2)^{a_w}} \tag{C-34}$$

where Γ is the Gamma function. The ratio of standard deviation-to-mean of a Weibull distribution is given by

$$\frac{\mathrm{sd}(x)}{\bar{x}} = \frac{[\Gamma(1 + 2a_w) - \Gamma^2(1 + a_w)]^{1/2}}{\Gamma(1 + a_w)} \tag{C-35}$$

191

In Eq. C-34 one may substitute empirical values of $\bar{x}$ (2nd column from the left) and x_{50} (6th column from the left) from the statistics box and solve for the Weibull spread parameter a_w. Similarly, in Eq. C-35 one may substitute empirical values of x (2nd column from the left) and sd(x) (3rd column from the left) and solve for a_w. In this manner either of these equations can be used to obtain alternative Weibull approximations to a patch distribution. Such alternative characterizations generally do not agree well with one another or with the characterization obtained by the regression fit to the cumulative distribution for $y_i > y'$ and $0.1 \leq P_i \leq 0.999$ discussed above. In other words, the approximating Weibull distribution obtained by the regression fit often will not have median levels or moment-dependent quantities that agree well with those shown in the statistics box. The reason for poor agreement in moment-dependent quantities is that the high tail of the empirical distributions (i.e., $P_i > 0.999$), although beyond the range and often poorly approximated by the regression fit for $0.1 \leq P_i \leq 0.999$, strongly influences the empirically derived higher moments. The reason for poor agreement between median levels is that the empirical median value tabulated in the statistics box sometimes just represents an upper bound due to noise contamination (in which case it is beyond the regression range), and even when not noise contaminated and within the regression range, it is usually to the extreme left of the regression range where the deviation from the linear approximation can be severe. Any several-point fit of a Weibull line to a patch distribution, whether including the median point or not, is less reliable than the regression fit which involves all points $y_i > y'$ within $0.1 \leq P_i \leq 0.999$. Since, in this manner, the regression fit utilizes all but the highest 1/10 percent of the measured data, it is regarded as the best first step in obtaining an empirically approximating analytic distribution. The deviation of high tails from this approximation and their characterization is discussed in Section 4.3.1.

In Figure C-16 it is observed that many of the patch cumulative distributions for Equinox Mountain appear to be piece-wise linear in two pieces. The first piece at low percentile levels has relatively low slope, and the second piece at higher percentile levels has relatively high slope. Both pieces exist well above noise contamination. The applicable region of each piece is observable in the histograms, where the low-sloped piece represents a long low tail reaching to the left in the histogram, and the high-sloped piece represents a tight bell-shaped distribution to the right in the histogram. These two-piece Equinox Mountain patch distributions are generally characteristic of mountain clutter data. The distribution of high-sloped returns come from steep, well-illuminated mountain slopes facing the radar at high grazing angles where the backscatter is essentially a Rayleigh process (the Rayleigh slope is indicated in the Weibull graph of Figure C-16). The low-sloped distribution of returns comes from the complexes of terrain at lower elevations and lower grazing angles between the steep mountain faces themselves. Mountain terrain is not generally uniform enough to allow the selection of reasonably large-sized patches on individual mountain faces. When increasingly smaller-sized patches were selected on one well-illuminated mountain face in which the direction of illumination was approximately broadside to the ridge line in a separate detailed study, we did move more towards being able to specify a single meaningful grazing angle, and we did increasingly obtain a single piece distribution of approximately Rayleigh statistics as the patch got smaller. Other analyses of Phase zero mountain clutter data are discussed in Section 4.3.2.

In clutter analyses involving shape parameters a_w, values obtained from the Weibull regression slope coefficient were not blindly used over the complete range $y_i > y'$, $0.1 < P_i < 0.999$ (by Eq. C-23) for cases

where a single-piece Weibull approximation was very poor over this range (for example, most of the Equinox Mountain patches). Although the regression coefficients over this complete range were generally provided as part of the standard patch analysis software package, more specific subjective piece-wise Weibull fits were performed, where appropriate, to patch amplitude distributions.

As with the information provided on regression fits to measured amplitude distributions with Weibull statistics, similar information for lognormal statistics is now provided. As before, let $y = 10 \log_{10} x$, and let $x = \sigma^\circ F^4$ in units of m^2/m^2. Suppose y is normally distributed with variance s^2. Then x is lognormally distributed, with probability density function

$$p(x) = \left[\frac{N}{4\pi \log_{10} \rho} \right]^{1/2} \cdot \frac{1}{x} \cdot e^{-\frac{\log_{10}\left(\frac{x}{x_{50}}\right)^2}{4N\log_{10}\rho}} \qquad \text{(C-36)}$$

where

x_{50} = median value of x,

x = mean value of x,

$$\rho = \frac{\bar{x}}{x_{50}} \qquad \text{(C-37)}$$

$$10\log_{10}\rho = \frac{s^2}{20N} \qquad \text{(C-38)}$$

and

$$N = \log_{10} e = 0.4343$$

The lognormal cumulative distribution function is

$$P(x) = \frac{1}{2}\left[1 + \text{erf}\frac{\log_{10}\left(\frac{x}{x_{50}}\right)}{2(N\log_{10}\rho)^{1/2}} \right] \qquad \text{(C-39)}$$

where

erf = error function

Equation C-39 may be rearranged as

$$\mathrm{erf}^{-1}\{2P(x)-1\} = \frac{\log_{10}\left(\frac{x}{x_{50}}\right)}{2(N\log_{10}\rho)^{1/2}} \qquad (C\text{-}40)$$

where

erf^{-1} = inverse error function.

In Eq. C-40, if we let

$$Y = \mathrm{erf}^{-1}\{2P(x)-1\} \qquad (C\text{-}41)$$

we obtain

$$Y = m \cdot y + b , \qquad (C\text{-}42)$$

where

$$m = \frac{1}{20(N\log_{10}\rho)^{1/2}} \qquad (C\text{-}43)$$

and

$$b = \frac{\log_{10}(x_{50})}{2(N\log_{10}\rho)^{1/2}} \qquad (C\text{-}44)$$

Equation C-42 indicates that Y is linearly dependent on y, with slope equal to m and Y-intercept equal to b. In the empirical cumulative amplitude distribution (P_i,y_i), $i = 1, 2,...I$, of each patch, the dependent variables P_i were transformed to Y_i by Eq. C-41, the resultant distribution (Y_i,y_i) was plotted in the lognormal graph to the upper right in Figures C-6, C-8, C-10, C-12, C-14, and C-16, and a standard linear regression fit to the plot of (Y_i,y_i) was performed for each patch over the range given by $y_i > y'$ and $0.1 < P_i < 0.999$. As with the Weibull regression analyses, lognormal regression computations were performed

using Eqs. C-26 through C-33 to yield lognormal regression quantities m, b, coefficient of determination, and sum of squared deviations. These were tabulated as the right-most entries (i.e., within parentheses) in the 4th, 3rd, 2nd, and 1st columns from the right in the statistics boxes of Figures C-6, C-8, C-10, C-12, C-14, and C-16. The approximating lognormal distribution to any empirical patch distribution may be quickly drawn in the upper right lognormal graph as a straight line with slope m and Y-intercept b using the right-hand ordinate in the graph. The parameters ρ and x_{50} in the analytical lognormal distribution of Eqs. C-36 and C-39 may be quickly obtained from Eqs. C-43 and C-44. Lognormal random variates distributed according to the lognormal approximation to the empirical patch amplitude distribution may be obtained by generating uniformly distributed random variates $P_k(x)$, $k = 1,2,3...$ and using Eq. C-37 to convert each to a corresponding lognormal distributed variate X_k, $k = 1,2,3,...$, where the parameters ρ and x_{50} in Eq. C-40 are obtained as discussed above. The mean-to-median ratio of a lognormal distribution is given by ρ (see Eq. C-37 and C-38). The ratio of standard deviation-to-mean is given by $(\rho^2 - 1)^{1/2}$. The coefficient of skewness is given by $(\rho^2 - 1)^{1/2}(\rho^2 + 2)$. The coefficient of kurtosis is given by $\rho^8 + 2\rho^6 + 3\rho^4 - 3$. The approximating log-normal distribution obtained by regression may not provide other statistical attributes such as higher moments in very close agreement with the empirical values tabulated in the statistics box. This is because the high tail in the region $P_i > 0.999$ often does not closely follow the lognormal approximation obtained over the regression range defined by $y_i > y'$ and $0.1 \leq P_i \leq 0.999$.

APPENDIX D

DEPRESSION ANGLE COMPUTATION

Figure D-1 shows geometrical relationships involved in considerations of depression angle on a spherical earth. Range from radar to backscattering terrain point is "*r.*" Effective earth's radius (i.e., actual earth's radius times 4/3 to account for nominal atmospheric refraction) is "*a.*" The actual earth's radius is approximately 6370 km. Effective radar height (i.e., site elevation above mean sea level plus radar antenna mast height minus terrain elevation above mean sea level at backscattering terrain point) is "*h.*" The quantity "*h*" is small compared to "*r*" and "*a.*" For solidly forested sites, effective radar height should be reduced by the average tree height.
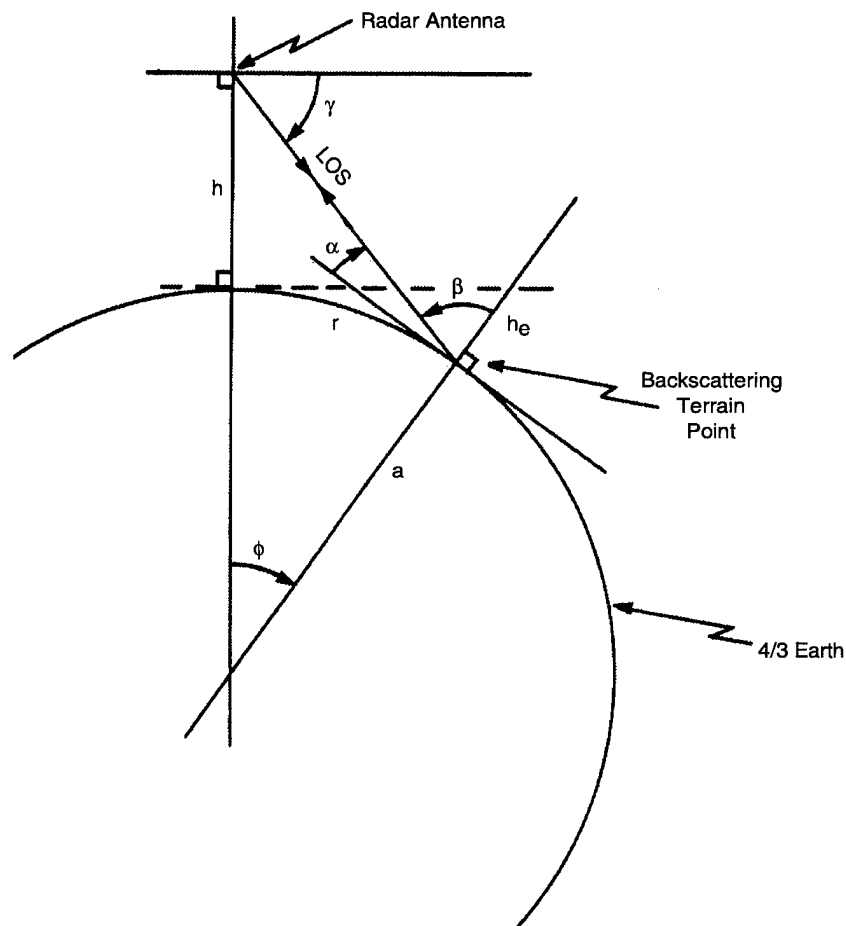

Figure D-1. Geometrical relationships involving depression angle on a spherical earth.

Depression angle α on a spherical earth is defined to be the complement of incidence angle β at the backscattering terrain point. Incidence angle β is the angle between the outward projection of the earth's radius at the backscattering terrain point and the direction of illumination (or line-of-sight to the radar antenna phase center) at the backscattering terrain point. The spherical earth may be thought of as having two effects in the computation of depression angle. The first effect is the effective decrease in terrain elevation of the backscattering terrain point due to the sphericity of the earth, whereby the surface of the earth (i.e., an imaginary sphere with height above mean sea level constant and equal to that of the backscattering terrain point) drops off with increasing range from the radar. This effective decrease in terrain elevation of the backscattering terrain point is denoted as "h_e." On a spherical earth of radius equal to 4/3 times the actual earth's radius, h_e is computed as

$$h_e = \frac{r^2}{2a} \qquad \text{(D-1)}$$

Including h_e, the angle below the local horizontal at the radar antenna at which the backscattering terrain point is observed, denoted γ, is computed as

$$\gamma = \tan^{-1}\left(\frac{h + h_e}{r}\right) \qquad \text{(D-2)}$$

Angle γ is referred to as the off-axis angle. It is the angle for which elevation gain correction on the elevation pattern of the radar antenna was performed in computation of absolute clutter strength $\sigma°F^4$.

The second effect of the spherical earth on depression angle is the rotation of the local Cartesian reference frame at the backscattering terrain point with respect to that at the radar antenna. This angle of rotation, denoted by φ, is computed as

$$\varphi = \frac{r}{a} . \qquad \text{(D-3)}$$

That is, the depression angle to be associated with the clutter measured from the backscattering terrain point should be the angle as seen by an observer at the backscattering terrain point, not an observer[4] at the radar. However, the off-axis angle used for elevation gain correction is that seen by an observer at the radar.

---

[4] To the observer at the backscattering terrain point, the quantity α is actually an elevation angle above the local horizontal.

Incorporating both effects, depression angle α is computed as

$$\alpha = \gamma - \phi \, . \tag{D-4}$$

It is depression angle α that was computed for each Phase Zero clutter patch and associated thereafter with the measured amplitude distribution of the clutter patch. In practice, α was computed once per patch, using the mean terrain elevation over the area of the patch as the elevation of the backscattering terrain point referred to in the above discussion.

How significant are these spherical earth effects? All of the clutter patches for which measurements are presented in this report lie between 2 and 12 km in range from the radar. At 12 km, $h_e = 8.48$ m, and $\phi = 0.081$ degrees. At longer ranges, for which clutter results have subsequently been reported [1, 3, 5], these quantities increase. Additional discussion concerning depression angle is presented in Section B.1 of Appendix B.

REFERENCES

1. J. B. Billingsley, *Low-Angle Radar Land Clutter: Measurements and Empirical Models*, Norwich, New York: William Andrew/SciTech Publishing, 703 pp. (2002).

2. J. B. Billingsley, "Radar ground clutter measurements and models," *AGARD Conf. Proc. Target and Clutter Scattering and Their Effects on Military Radar Performance*, Ottawa, AGARD-CP-501, 1991; DTIC AD-P006 373.

3. J. B. Billingsley and J. F. Larrabee, "Multifrequency Measurements of Radar Ground Clutter at 42 Sites," Lexington, MA: MIT Lincoln Laboratory, Technical Rep. 916, Volumes 1, 2, 3; 15 November 1991; DTIC AD-A246710.

4. J. B. Billingsley, "Ground Clutter Measurements for Surface-Sited Radar," Lexington, MA: MIT Lincoln Laboratory, Technical Rep. 786, Rev. 1, 1 February 1993; DTIC AD-A262472.

5. J. B. Billingsley, A. Farina, F. Gini, M. V. Greco, and L. Verrazzani, "Statistical analyses of measured radar ground clutter data," *IEEE Trans. AES*, Vol. 35, No. 2, pp. 579-593 (April 1999).

6. J. B. Billingsley and J. F. Larrabee, "Measured Spectral Extent of L- and X-Band Radar Reflections from Windblown Trees," Lexington, MA: MIT Lincoln Laboratory, Project Rep. CMT-57, 6 February 1987; DTIC AD-A179942.

7. J. B. Billingsley, "Exponential Decay in Windblown Radar Ground Clutter Doppler Spectra: Multifrequency Measurements and Model," Lexington, MA: MIT Lincoln Laboratory, Technical Report 997, 29 July 1996; DTIC AD-A312399.

8. P. Lombardo, M. V. Greco, F. Gini, A. Farina, and J. B. Billingsley, "Impact of clutter spectra on radar performance prediction," *IEEE Trans. AES*, Vol. 37, No. 3, pp. 1022-1034 (July 2001).

9. D. A. Hill and J. R. Wait, "Ground wave propagation over a mixed path with an elevation change," *IEEE Trans. Ant. and Prop*, Vol. AP-30, No. 1, pp. 139-141 (January 1982).

10. L. Tsang, J. A. Kong, and R. T. Shin, *Theory of Microwave Remote Sensing*, New York: Wiley, 1985.

11. K. D. Ward and S. Watts, "Radar sea clutter," *Microwave J.*, Vol. 28, No. 6, pp. 109-121, June 1985.

12. E. Jakeman, "On the statistics of K-distributed noise," *J. Physics A; Math. Gen.*, vol. **13**, 31-48 (1980).

13. D. K. Barton, "Land clutter models for radar design and analysis," *Proc. IEEE*, vol 73, no. 2, pp. 198-204 (February 1985).

14. C. J. Oliver, "A model for non-Rayleigh scattering statistics," *Opt. Acta.* Vol. <u>31</u>, pp. 701-722 (1984).

15. R. R. Boothe, "The Weibull Distribution Applied to the Ground Clutter Backscatter Coefficient," U.S. Army Missile Command Rept. No. RE-TR-69-15, Redstone Arsenal, AL, June 1969; DTIC AD-691109.

16. J. S. Bendat and A. G. Piersol, *Random Data: Analysis and Measurement Procedures*, (2nd ed.), New York: Wiley, 1986.

17. D. K. Barton, *Modern Radar System Analysis*, Norwood, Mass.: Artech House, Inc. (1988),pp. 124-128.

18. F. E. Nathanson, *Radar Design Principles* (2nd ed.), New York: McGraw-Hill (1991), pp. 329-332.

19. G. T. Ruck, D. E. Barrick, W. D . Stuart, and C. K. Krichbaum, *Radar Cross Section Handbook*, New York: Plenum Press (1970), p. 676.

20. M.I. Skolnik, *Introduction to Radar Systems* (2nd ed.), New York: McGraw-Hill (1980), p. 490.

21. M. P. Warden and E. J. Dodsworth, "A Review of Clutter, 1974," Royal Radar Establishment Technical Note No. 783, Malvern, U.K., September 1974; DTIC AD A014421.

22. H. C. Chan, "Radar sea clutter at low grazing angles," *IEE Proc*. Pt. F, Vol. 137, No. 2, pp. 102-112 (1990).

23. J. R. Anderson, et al., "A land use and land cover classification system for use with remote sensor data," Professional Paper 964, Geological Survey, U.S. Department of the Interior (1975).

24. J. A. McKeague, et al., *The Canadian System of Soil Classification*, Canadian Department of Agriculture Publ. 1646, Supply and Services, Ottawa, Canada (1978).

25. G. W. Snedecor and W. G. Cochrane, *Statistical Methods* (7th ed.), Iowa State University Press, Ames, Iowa, 1980.

REPORT DOCUMENTATION PAGE

Public reporting burden for this collection of information is estimated to average 1 hour per response, including the time for reviewing instructions, searching existing data sources, gathering and maintaining the data needed, and completing and reviewing the collection of information. Send comments regarding this burden estimate or any other aspect of this collection of information, including suggestions for reducing this burden, to Washington Headquarters Services, Directorate for Information Operations and Reports, 1215 Jefferson Davis Highway, Suite 1204, Arlington, VA 22202-4302, and to the Office of Management and Budget, Paperwork Reduction Project (0704-0188), Washington, DC 20503.

1. AGENCY USE ONLY (*Leave blank*)	2. REPORT DATE 20 December 2002	3. REPORT TYPE AND DATES COVERED Technical Report

4. TITLE AND SUBTITLE

Low-Angle X-Band Radar Ground Clutter Spatial Amplitude Statistics

5. FUNDING NUMBERS

C—F19628-00-C-0002

6. AUTHOR(S)

J. Barrie Billingsley

7. PERFORMING ORGANIZATION NAME(S) AND ADDRESS(ES)

Lincoln Laboratory, MIT
244 Wood Street
Lexington, MA 02420-9108

8. PERFORMING ORGANIZATION REPORT NUMBER

TR-958

9. SPONSORING/MONITORING AGENCY NAME(S) AND ADDRESS(ES)

SAF/AQLR
1500 Wilson Blvd., Suite 1500
Arlington, VA 22209

10. SPONSORING/MONITORING AGENCY REPORT NUMBER

ESC-TR-2000-066

11. SUPPLEMENTARY NOTES

None

12a. DISTRIBUTION/AVAILABILITY STATEMENT

Approved for public release; distribution is unlimited.

12b. DISTRIBUTION CODE

13. ABSTRACT (*Maximum 200 words*)

A large volume of X-band radar ground clutter measurement data was collected from many sites widely dispersed over the North American continent. This program of measurements involved a wide variety of terrain types, where at each site backscatter was recorded from all of the terrain within the field of view, through 360 degrees in azimuth and to ranges typically extending to 25 or 50 km. As a result, in most of these measurements the angle of illumination of the earth's surface was usually very low, typically within a degree or so of grazing incidence, with much intermittent shadowing of low regions occurring within the field of view. This report examines the nature of low-angle radar ground clutter as it has come to be understood through analysis of this extensive base of measurements. Depression angle, that is, the angle below the horizontal at which the backscattering terrain point is observed at the radar antenna, is shown to be the principal parametric influence on clutter amplitude statistics, even for the very low angles and small (typically fractional) variations in angle that occur in surface-sited radar. This principal role of depression angle is the result of its effect on shadowing in a sea of patchy visibility and discrete or localized scattering sources. Following this understanding, a general predictive model for X-band ground clutter spatial amplitude statistics is developed based on specific computation of depression angle but on only relatively general specification of terrain type. The report goes on to illustrate how increasing information about terrain type allows more precise prediction of clutter statistics.

14. SUBJECT TERMS

radar ground clutter	terrain reflectivity	backscatter
clutter measurements	land clutter	
clutter models	low angle	

15. NUMBER OF PAGES
222

16. PRICE CODE

17. SECURITY CLASSIFICATION OF REPORT Unclassified	18. SECURITY CLASSIFICATION OF THIS PAGE Unclassified	19. SECURITY CLASSIFICATION OF ABSTRACT Unclassified	20. LIMITATION OF ABSTRACT Same as Report